



**HAL**  
open science

# Improvement of the thermal and epithermal neutron scattering data for the interpretation of integral experiments

Juan Pablo Scotta

► **To cite this version:**

Juan Pablo Scotta. Improvement of the thermal and epithermal neutron scattering data for the interpretation of integral experiments. Nuclear Experiment [nucl-ex]. Université d'Aix-Marseille (AMU), 2017. English. NNT: . tel-01835720

**HAL Id: tel-01835720**

**<https://theses.hal.science/tel-01835720>**

Submitted on 11 Jul 2018

**HAL** is a multi-disciplinary open access archive for the deposit and dissemination of scientific research documents, whether they are published or not. The documents may come from teaching and research institutions in France or abroad, or from public or private research centers.

L'archive ouverte pluridisciplinaire **HAL**, est destinée au dépôt et à la diffusion de documents scientifiques de niveau recherche, publiés ou non, émanant des établissements d'enseignement et de recherche français ou étrangers, des laboratoires publics ou privés.

# UNIVERSITE D'AIX-MARSEILLE

CEA Cadarache/ DEN / DER / SPRC / Laboratoire d'Etudes de Physiques

Thèse présentée pour obtenir le grade universitaire de docteur

Discipline : ED352 – PHYSIQUE ET SCIENCES DE LA MATIERE

Spécialité : Energie, Rayonnement et Plasma

Juan Pablo SCOTTA

Amélioration des données neutroniques de diffusion  
thermique et epithermique pour l'interprétation des mesures  
intégrales

Soutenue le 26/09/2017 devant le jury :

Luiz LEAL	IRSN	Examineur
Cyrille DE SAINT JEAN	CEA Cadarache	Examineur
Jose BUSTO	Université d'Aix Marseille	Examineur
Florent REAL	Université de Lille	Rapporteur
Florencia CANTARGI	Centro Atomico Bariloche (ARG)	Rapporteur
Gilles NOGUERE	CEA Cadarache	Directeur de thèse
Yoann CALZAVARA	ILL Grenoble	Invité

# Abstract

In the present report it was studied the neutron thermal scattering of light water for reactors application. The thermal scattering law model of hydrogen bounded to the water molecule of the JEFF-3.1.1 nuclear data library is based on experimental measures performed in the sixties. The scattering physics of this latter was compared with a model based on molecular dynamics calculations developed at the Atomic Center in Bariloche (Argentina), namely the CAB model.

In the frame of this work, experimental measurements of the double differential cross sections were done at room temperature. The new microscopic data were used to analyze the performance of the CAB model and JEFF-3.1.1. The CAB model exhibits an improvement over JEFF-3.1.1.

The impact of these models was evaluated on application on reactor calculations at cold conditions. The selected benchmark was the MISTRAL program (UOX and MOX configurations), carried out in the zero power reactor EOLE of CEA Cadarache (France). The contribution of the neutron thermal scattering of hydrogen in water was quantified in terms of the difference in the calculated reactivity and the calculation error on the isothermal reactivity temperature coefficient (RTC).

For the UOX lattice, the calculated reactivity with the CAB model at 20 °C is +90 pcm larger than JEFF-3.1.1, while for the MOX lattice is +170 pcm because of the high sensitivity of the thermal scattering to this type of fuels. In the temperature range from 10 °C to 80 °C, the calculation error on the RTC is  $-0.27 \pm 0.3$  pcm/°C and  $+0.05 \pm 0.3$  pcm/°C obtained with JEFF-3.1.1 and the CAB model respectively (UOX lattice). For the MOX lattice, is  $-0.98 \pm 0.3$  pcm/°C and  $-0.72 \pm 0.3$  pcm/°C obtained with the JEFF-3.1.1 library and with the CAB model respectively. The results illustrate the improvement of the CAB model in the calculation of this safety parameter.

Finally, the uncertainties on the thermal scattering data were quantified creating covariance matrices between the parameters of the CAB model and the JEFF-3.1.1 library. The uncertainties were propagated to produce covariance matrices for the thermal scattering function and for the scattering cross section of hydrogen bounded to the light water. The uncertainty on the calculated reactivity of the MISTRAL benchmark (UOX fuel) is  $\pm 125$  pcm for JEFF-3.1.1 and  $\pm 71$  pcm for the CAB model (20 °C).

Keywords: neutron thermal scattering, light water, covariance matrix.

# Résumé

Dans ces travaux de thèse, la diffusion thermique des neutrons pour l'application aux réacteurs à eau légère a été étudiée. Le modèle de loi de diffusion thermique de l'hydrogène lié à la molécule d'eau de la bibliothèque de données nucléaires JEFF-3.1.1 est basée sur des mesures expérimentales réalisées dans les années soixante. La physique de diffusion de neutrons de cette bibliothèque a été comparée à un modèle basé sur les calculs de dynamique moléculaire développé au Centre Atomique de Bariloche (Argentine), à savoir le modèle CAB.

Dans le cadre de ce travail, des mesures expérimentales de la section doublement différentielle ont été faites à température ambiante. Les nouvelles données microscopiques ont été utilisées pour analyser la performance du modèle CAB et du JEFF-3.1.1. Le modèle CAB présente une amélioration par rapport à JEFF-3.1.1.

L'impact de ces modèles a également été évalué sur le programme expérimental MISTRAL (configurations UOX et MOX) réalisé dans le réacteur de puissance nulle EOLE situé au CEA Cadarache (France). La contribution de la diffusion thermique des neutrons sur l'hydrogène dans l'eau a été quantifiée sur le calcul de la réactivité et sur l'erreur de calcul du coefficient de température isotherme (reactivity temperature Coefficient en anglais - RTC).

Pour le réseau UOX, l'écart entre la réactivité calculée à 20 °C avec le modèle CAB et celle du JEFF-3.1.1 est de +90 pcm, tandis que pour le réseau MOX, il est de +170 pcm à cause de la sensibilité élevée de la diffusion thermique pour ce type de combustible. Dans la plage de température de 10 °C à 80 °C, l'erreur de calcul sur le RTC est de  $-0.27 \pm 0.3$  pcm/°C avec JEFF-3.1.1 et de  $+0.05 \pm 0.3$  pcm/°C avec le modèle CAB pour le réseau UOX. Pour la configuration MOX, il est de  $-0.98 \pm 0.3$  pcm/°C et  $-0.72 \pm 0.3$  pcm/°C obtenu respectivement avec la bibliothèque JEFF-3.1.1 et avec le modèle CAB. Les résultats montrent l'apport du modèle CAB dans le calcul de ce paramètre de sûreté.

Enfin, les incertitudes sur les données de diffusion thermique ont été quantifiées en calculant des matrices de covariance entre les paramètres du modèle CAB et ceux de la bibliothèque JEFF-3.1.1. Les incertitudes liés aux paramètres de modèle ont été propagées afin de calculer des matrices de covariance pour la loi de diffusion thermique et pour la section efficace de diffusion de l'hydrogène lié à l'eau légère. L'incertitude sur la réactivité calculée pour MISTRAL (réseau UOX) est de  $\pm 125$  pcm pour JEFF-3.1.1 et  $\pm 71$  pcm pour le modèle CAB (20 °C).

Mots clés : loi de diffusion thermique, eau légère, matrice de covariance

# Contents

1-Introduction.....	18
1.1-Context .....	18
1.2-Motivations .....	19
1.3-Objectives.....	21
1.4-Report description.....	21
2-Thermal neutron scattering.....	23
2.1-Introduction to thermal scattering theory.....	23
2.2- The coherent and incoherent cross sections.....	25
2.3-The coherent and incoherent scattering functions.....	27
2.4-The approximations of scattering in light water .....	29
2.4.1-The incoherent approximation.....	29
2.4.2-The Gaussian approximation.....	29
2.5-The evaluation of the scattering law with the LEAPR module of NJOY.....	31
2.5.1-The phonon expansion .....	32
2.5.2-Molecular translations.....	33
2.5.2.1-The free gas model .....	33
2.5.2.2-The Egelstaff and Shofield diffusion model.....	33
2.5.3-The intramolecular vibration modes .....	34
2.5.4-The short collision time approximation .....	35
2.6-Preliminary conclusions.....	36
3-Neutron thermal scattering models for light water .....	37
3.1-The IKE model.....	37
3.2- Molecular dynamic simulations.....	40
3.2.1-Molecular dynamic simulations for reactor applications.....	40
3.2.2-Introduction to molecular dynamic simulations .....	41
3.2.3-The velocity autocorrelation function .....	42
3.3-The CAB model .....	43
3.3.1-The water potential of CAB model .....	43
3.3.2-The frequency spectrum of CAB model.....	44
3.3.3-Implementation in LEAPR module.....	46

3.4-Comparison between JEFF-3.1.1 and CAB model .....	48
3.4.1- The scattering function.....	48
3.4.2- The double differential cross section .....	50
3.4.3- The H1 in H2O scattering cross section .....	52
3.4.4- The H2O total cross section.....	53
3.5-impact of the O16 in H2O thermal scattering law in the microscopic data .....	54
3.5.1- The double differential cross section .....	54
3.5.2-The O16 in H2O scattering cross section.....	54
3.6-Preliminary conclusions.....	56
4-Light water double differential cross section measurements at 300 K and 350 K.....	57
4.1-TOF spectrometers .....	57
4.1.1-IN4c spectrometer.....	57
4.1.2-IN6 spectrometer .....	58
4.2-Experimental set up conditions.....	59
4.3-Analysis of the resolution function of the spectrometers .....	61
4.4-Data post-processing.....	63
4.4.1-Data reduction routine .....	63
4.4.2-Background subtraction.....	65
4.5-Results and discussions .....	67
4.5.1-IN4c spectrometer.....	67
4.5.2-IN6 spectrometer .....	67
4.6-Monte Carlo simulations .....	69
4.6.1-Simplified tof experimentl model in TRIPOLI4 .....	69
4.6.2-Results for IN4C spectrometer .....	71
4.6.3-Results for IN6 spectrometer .....	72
4.6.4-Origin of the differences between the calculations and the data.....	73
4.6.4.1-Experimental problems .....	73
4.6.4.2-Theoretical problems .....	74
4.6.4.3-Problems induced by using the LEAPR module of NJOY .....	75
4.7-Preliminary conclusions.....	76
5-Impact of the thermal scattering law of H1 in H2O in MISTRAL experiments .....	77
5.1-The MISTRAL experimental program .....	77

5.2-Interpretation of the mistral experiments using the Monte Carlo code TRIPOLI4 .....	79
5.2.1-Processing of the thermal scattering law with TRIPOLI4 code.....	80
5.2.2-Considerations about the crystal lattice effect on the fuel.....	80
5.2.3-Material thermal expansion effects .....	81
5.2.4-Validation of the calculation scheme .....	83
5.2.5-Energy treatment for the thermal scattering libraries in TRIPOLI4.....	84
5.2.5.1-Thermal energy cut-off.....	84
5.2.5.2-Study of the discontinuity of the H1 scattering cross section.....	85
5.2.6-Interpolation of the leapr module parameters of JEFF-3.1.1.....	86
5.3-Reactivity excess as a function of the temperature in the MISTRAL experiments .....	89
5.4-Analysis and discussions of the reactivity excess in the MSITRAL experiments .....	93
5.4.1-Analysis of the H1 reaction rates.....	94
5.4.2-Analysis of the fissile isotopes U235, Pu239 and Pu241 .....	95
5.5-Calculation errors on the isothermal reactivity temperature coefficients .....	96
5.5.1-Previous works .....	96
5.5.2-Present results with TRIPOLI4 .....	97
5.6-Impact of new evaluations on the MISTRAL benchmark .....	100
5.6.1-Am241 (JEFF-3.2).....	100
5.6.2-O16 (JEFF-3.3 T3).....	102
5.7-Impact of the O16 in H2O thermal scattering law on the MSITRAL benchmark.....	104
5.8-Preliminary conclusions.....	105
6- Thermal scattering function uncertainties .....	106
6.1-Introduction to uncertainty quantification .....	106
6.1.1-Classification of the uncertainties .....	106
6.1.2-Uncertainties propagation .....	106
6.2-The generalized least square method .....	108
6.3-The systematic uncertainties.....	109
6.4-Covariance matrix of the thermal scattering law of the CAB model.....	110
6.4.1-parameters of the CAB model .....	110
6.4.2-Experimental data for the fit in the generalized least square method .....	111
6.4.3-The nuisance parameters .....	113
6.4.3.1-The experimental parameters.....	113

6.4.3.2-The fixed model parameters .....	114
6.4.4-The derivative matrices .....	115
6.4.5-Results .....	116
6.4.5.1-Results after the fitting procedure .....	116
6.4.5.2-Results after the marginalization technique .....	117
6.5-Covariance matrix of the thermal scattering law of JEFF-3.1.1.....	118
6.5.1-Parameters of the TSL .....	118
6.5.2-Experimental data for the fit in the generalized least square method .....	120
6.5.3-The nuisance parameters .....	121
6.5.3.1-The experimental parameters.....	121
6.5.3.2-The diffusion constant c .....	121
6.5.3.3-The fixed model parameters .....	122
6.5.4-The derivative matrices .....	123
6.5.5-Results .....	124
6.5.5.1-Results after the fitting procedure .....	124
6.5.5.2-Results after the marginalization technique .....	124
6.6-Preliminary conclusions.....	126
7- Thermal scattering uncertainties propagation .....	127
7.1-Introduction.....	127
7.2-Uncertainty propagation to the scattering function of CAB model.....	128
7.2.1-Sensitivities of the scattering function to the CAB model parameters.....	128
7.2.2-Covariance matrix of the scattering function of the CAB model.....	128
7.3-Uncertainty propagation to the H1 in H2O scattering cross section of CAB model .....	131
7.3.1-Sensitivities of the scattering cross section to the CAB model parameters.....	131
7.3.2-Covariance matrix of the scattering cross section of the CAB model .....	132
7.4-Uncertainty propagation average cosine of the scattering angle of CAB model .....	132
7.4.1-Sensitivities of the $\bar{\mu}$ to the CAB model parameters.....	132
7.4.2-Covariance matrix of the $\bar{\mu}$ of the CAB model .....	132
7.5-Uncertainty propagation to the scattering function of JEFF-3.1.1.....	135
7.6-Uncertainty propagation to the H1 in H2O scattering cross section of JEFF-3.1.1 .....	136
7.7-Uncertainty propagation to the mistral experiments .....	138
7.8-Uncertainty propagation using the ifp method of the monte carlo code TRIPOLI4 .....	139

7.8.1-Uncertainty on the calculated reactivity by direct propagation of the leapr parameters of JEFF-3.1.1 .....	139
7.8.2-Uncertainty propagation on the calculated reactivity using the ifp method.....	139
7.9-Preliminary conclusions.....	143
General conclusions and perspectives.....	144
List of references.....	147
Appendix A: MISTRAL-2 core used to compensate the reactivity loss due to the temperature .....	151
Appendix B: List of publications.....	156

# List of tables

1.1- Differences in reactivity $\Delta\rho = C - E$ (pcm) obtained with the thermal scattering laws of JEFF-3.1.1, CAB model and with the free gas approximation for the MISTRAL-1 configuration. The statistical uncertainty due to the Monte Carlo calculations is 2 pcm. The magnitude of the experimental uncertainties ranges 200 pcm.....	21
3.1- IKE (JEFF-3.1.1) and CAB model parameters introduced in the LEAPR module for $^1\text{H}$ in $\text{H}_2\text{O}$ at 294 K.....	38
3.2- Parameters of the TIP4P/2005f water potential .....	46
3.3- Water diffusion mass $M_{diff}$ and molecular diffusion coefficient $D$ used in the CAB model at 294 K.....	47
4.1- Measured thermodynamic experimental conditions of water for the spectrometers IN4c ( $E_0 = 14$ meV) and IN6 ( $E_0 = 3$ meV) and the acquisition time in hours .....	60
4.2- Temperature and acquisition time measured at IN4c and IN6 spectrometers for the empty cell .....	61
5.1- Summary of the main characteristics of the three MISTRAL configurations .....	79
5.2- Excess of reactivity calculated with the TRIPOLI4 code for the MISTRAL-1 configuration at 20 °C. $\Delta$ is the impact relative to the reference case of the official T4 library. The statistical uncertainty of calculations is 4 pcm .....	84
5.3- Excess of reactivity calculated with the TRIPOLI4 code for the MISTRAL-1 configuration at 20 °C for three cases. The statistical uncertainty of the calculations is 3 pcm.....	85
5.4- Differences in reactivity $\Delta\rho = C - E$ (pcm) obtained with the thermal scattering laws of JEFF-3.1.1 and CAB model for the MISTRAL-1, MISTRAL-2 and MISTRAL-3 configurations. In MISTRAL-1, the reactivity differences do not include the correction due to thermal expansion effects. The statistical uncertainty due to the Monte Carlo calculations is 2 pcm.....	90
5.5- Polynomial coefficients $a_i$ provided by the CONRAD code after the least-square adjustment of the $\Delta\rho$ values reported in Table 4 with eq. (5). A quadratic polynomial fit was done for MISTRAL-1, while a linear fit was proposed for MISTRAL-2 and MISTRAL-3.....	91
5.6- Comparison of the polynomial coefficients $a_i$ provided by the CONRAD code after the least-square adjustment of the $\Delta\rho$ values calculated for MISTRAL-1 with and without the thermal expansion effects corrections. A linear fit is obtained when the reactivity corrections are taken into account .....	93
5.7- Ratio of JEFF-3.1.1 to CAB model of the absorption and scattering $^1\text{H}$ in $\text{H}_2\text{O}$ reaction rates at 20°C calculated in the MISTRAL experiments .....	95
5.8- Ratio of JEF-3.1.1 to CAB model of the capture to fission ratio of the three main fissile isotopes at 20 °C calculated in the MISTRAL-1 and MISTRAL-2 experiments. The ratios are measured in pcm .....	96

5.9- Summary of the calculation errors $\Delta\alpha_{iso}(T)$ for the MISTRAL experiments obtained with the deterministic code APOLLO2 in association with the JEF-2.2 and JEFF-3.1.1 nuclear data libraries.....	97
5.10- Summary of the calculation errors $\Delta\alpha_{iso}$ (in pcm/°C) for the MISTRAL experiments obtained with the Monte Carlo code TRIPOLI4. The present results are compared with those obtained with the deterministic code APOLLO2 [51]. The experimental uncertainties are also given in pcm/°C. The contribution of the statistical uncertainties due to the Monte Carlo calculations is negligible ( $\pm 0.02$ pcm/°C) .....	98
5.11- Comparison of the calculation errors $\Delta\alpha_{iso}$ (in pcm/°C) for the MISTRAL-1 experiment applying the thermal expansion corrections to the reactivity difference $\Delta\rho$ and to the reactivity temperature coefficient difference $\Delta\alpha_{iso}$ .....	99
5.12- Differences in reactivity $\Delta\rho = C - E$ (pcm) obtained with the thermal scattering laws of JEFF-3.1.1 and CAB model and the $^{241}\text{Am}$ evaluations of JEFF-3.1.1 and JEFF-3.2 libraries for the MISTRAL-2 and MISTRAL-3 configurations at 20 °C and 80 °C. The statistical uncertainty due to the Monte Carlo calculations is 3 pcm .....	101
5.13- Differences in reactivity $\Delta\rho = C - E$ (pcm) obtained with the thermal scattering laws of JEFF-3.1.1 and CAB model and the $^{16}\text{O}$ evaluations of JEFF-3.1.1 and JEFF-3.3 libraries for the MISTRAL-1, MISTRAL-2 and MISTRAL-3 configurations at 20 °C and 80 °C. The statistical uncertainty due to the Monte Carlo calculations is 3 pcm .....	103
5.14- Excess of reactivity calculated with the TRIPOLI4 code for MISTRAL-1 at 20 °C for oxygen bound to light water molecule and as a free gas. The statistical uncertainty of the calculations is 3 pcm.....	104
6.1- Parameters of the TIP4P/2005f water potential .....	111
6.2- Nuisance parameters for the experimental measures used in the retroactive analysis.....	115
6.3- Prior and posterior relative uncertainties and correlation matrix of the parameters of the TIP4P/2005f water potential.....	116
6.4- Relative uncertainties and correlation matrix of the parameters of the TIP4P/2005f water potential after the marginalization .....	118
6.5- JEFF-3.1.1 model parameters introduced in the LEAPR module for $^1\text{H}$ in $\text{H}_2\text{O}$ at 294K .....	119
6.6- Relative uncertainties and correlation matrix of the LEAPR parameters of JEFF-3.1.1 after the marginalization .....	125
7.1- Differences in reactivity $\Delta\rho = C - E$ (pcm) obtained with the thermal scattering laws of JEFF-3.1.1 and CAB model for the MISTRAL-1 and MISTRAL-2 configurations. In MISTRAL-1, the reactivity differences include the correction due to thermal expansion effects. The reported uncertainties on	

each case are due to the CAB model parameters and to the LEAPR module parameters, in the case of JEFF-3.1.1, which were propagated with the CONRAD code. The combined statistical uncertainty due to the Monte Carlo calculations is 25 pcm for the CAB model and 18 pcm for JEFF-3.1.1..... 138

7.2- Comparison of the calculated uncertainty on the keff value of the PST-001.1 benchmark using different uncertainty propagation methods. The reference case corresponds to the direct perturbation of the LEAPR parameters ..... 141

# List of figures

1.1- Total H <sub>2</sub> O cross section calculated with the CAB model and with the JEFF-3.1.1 library at 294 K.....	20
1.2- Radial cross section of MISTRAL-1 core from EOLE reactor .....	20
2.1- Hydrogen scattering and capture cross sections as a function of the neutron energy from JEFF-3.1.1 library .....	24
2.2- Continuous frequency spectra and intramolecular vibration modes of <sup>1</sup> H H <sub>2</sub> O at 294 K for JEFF-3.1.1 nuclear data library.....	31
3.1- Frequency spectra of <sup>1</sup> H in H <sub>2</sub> O at 294 K measured by Haywood and modified by Koppel.....	39
3.2- Continuous frequency spectra of <sup>1</sup> H in H <sub>2</sub> O at 294 K and 550 K as a function of the vibration energy used in IKE model (ENDF/B-VII.1 and JEFF-3.1.1 nuclear data libraries) .....	39
3.3- Continuous component of the frequency spectrum of <sup>1</sup> H in H <sub>2</sub> O at 294 K of the nuclear data libraries ENDF/B-VII.1 and JEFF-3.1.1 .....	40
3.4- Simulation of 512 H <sub>2</sub> O molecules with GROMACS code in a cubic box of side a = 2.48 nm .....	42
3.5- VACF of H(H <sub>2</sub> O) (continuous red line) and O(H <sub>2</sub> O) (dash blue line) at 294 K generated with the molecular dynamic simulations code GROMACS and the water potential TIP4P/2005f .....	45
3.6- Generalized frequency spectrum of H(H <sub>2</sub> O) (left scale), O(H <sub>2</sub> O) (right scale) and H <sub>2</sub> O (left scale) at 294 K .....	45
3.7- Low energy detail of the generalized frequency (continuous line), continuous (dash line) and diffusive spectrum (dotted line) from Egelstaff-Schofield model of <sup>1</sup> H H <sub>2</sub> O at 294 K .....	47
3.8- CAB model (continuous red line) and JEFF-3.1.1 (dash blue line) continuous frequency spectra and intramolecular vibration modes of <sup>1</sup> H H <sub>2</sub> O at 294 K as a function of the excitation energy (lower scale) and dimensionless energy transfer (upper scale).....	48
3.9- S( $\alpha,\beta$ ) as a function of the momentum transfer for CAB model and JEFF-3.1.1 nuclear data library at 294 K .....	49
3.10- Symmetric S( $\alpha,\beta$ ) as a function of the momentum transfer for CAB model and JEFF-3.1.1 nuclear data library at 294 K.....	49
3.11- Double differential scattering cross section for light water calculated with CAB model and JEFF-3.1.1 compared with data measured by Novikov (1986), for E <sub>0</sub> = 8 meV, $\theta$ = 37° and T = 294 K. The energy resolution is 7%.....	51

3.12- Double differential scattering cross section for light water calculated with CAB model and JEFF-3.1.1 compared with data measured by Bischoff (1967), for $E_0 = 231$ meV, $\theta = 25^\circ$ and $T = 294$ K. The energy resolution is 5%.....	51
3.13- $^1\text{H}$ in $\text{H}_2\text{O}$ scattering cross section calculated with CAB model and JEFF-3.1.1 at 294 K (upper plot). The ratio between JEFF-3.1.1 and CAB model is in the bottom plot.....	52
3.14- Total $\text{H}_2\text{O}$ cross section calculated with CAB model and JEFF-3.1.1 at 294 K.....	53
3.15- Double differential scattering cross section calculated with $^1\text{H}$ in $\text{H}_2\text{O}$ of CAB model and $^{16}\text{O}$ in the free gas approximation compared with $^1\text{H}$ in $\text{H}_2\text{O}$ and $^{16}\text{O}$ in $\text{H}_2\text{O}$ of CAB model, for $E_0 = 231$ meV, $\theta = 25^\circ$ and $T = 294$ K.....	55
3.16- Scattering cross sections of $^{16}\text{O}$ in $\text{H}_2\text{O}$ calculated with CAB model and $^{16}\text{O}$ calculated in the free gas approximation of JEFF-3.1.1 at 294 K (upper plot). The ratio between JEFF-3.1.1 and CAB model is in the bottom plot.....	55
4.1- The IN4c time-of-flight spectrometer.....	58
4.2- The IN6 time-of-flight spectrometer.....	59
4.3- Characteristics of the Cu-Be sample holder.....	59
4.4- Water pressure – temperature diagram showing the thermodynamic states measured for IN4c (blue full squares) and IN6 (red squares) spectrometers.....	60
4.5- Vanadium intensity measured at IN4c spectrometer for $\theta = 14^\circ$ (upper plot) and $\theta = 120^\circ$ (lower plot).....	62
4.6- Vanadium intensity measured at IN6 spectrometer for $\theta = 11^\circ$ (upper plot) and $\theta = 115^\circ$ (lower plot).....	62
4.7- Half-width at half-maximum of the vanadium elastic peak as a function of the scattering angle $\theta$ .....	63
4.8- Intensity of the water signal and empty cell as a function of $\theta$ and $E'-E_0$ (upper plot) and intensity of the empty cell measure (lower plot) for IN4c at 300 K.....	64
4.9- Intensity of the water signal and empty cell as a function of $\theta$ and $E'-E_0$ (upper plot) and intensity of the empty cell measure (lower plot) for IN6 at 350 K.....	65
4.10- Intensity of the “ $\text{H}_2\text{O}$ +sample holder” and “sample holder” as a function of $E'-E_0$ for $\theta = 15^\circ$ measured in IN4c spectrometer at 300 K (left plot). Detail of the quasi-elastic peaks (right plot).....	66
4.11- Intensity of the “ $\text{H}_2\text{O}$ +sample holder” and “sample holder” as a function of $E'-E_0$ for $\theta = 15^\circ$ measured in IN6 spectrometer at 350 K (left plot). Detail of the quasi-elastic peaks (right plot).....	67
4.12- Water double differential scattering cross section at $E_0 = 14$ meV and $\theta = 15^\circ$ and $45^\circ$ , measured in IN4c spectrometer at 300 K. Detail of the quasi-elastic peaks (right plot).....	68

4.13- Water double differential scattering cross section at $E_0 = 3$ meV and $\theta = 15^\circ$ and $45^\circ$ , measured in IN6 spectrometer at 350 K. Detail of the quasi-elastic peaks (right plot) .....	69
4.14- Simplified ToF model implemented in TRIPOLI4 code. $E_0$ designated the incident neutron energy, $\theta$ the scattering angle, $L$ the flight path distance and $E'$ the secondary energy.....	70
4.15- Comparison between the unbroadened (dashed curve) and broadened (continuous curve) double differential cross sections calculated with the Monte Carlo code TRIPOLI4 for $E_0 = 14$ meV, $\theta = 15^\circ$ and 300 K. The convolution was done with the experimental vanadium measures.....	71
4.16- Double differential scattering cross section at $E_0 = 14$ meV, $\theta = 15^\circ$ and 300 K calculated with JEFF-3.1.1, CAB model and Free gas model compared with the experimental data .....	71
4.17- Double differential scattering cross section at $E_0 = 3$ meV, $\theta = 15^\circ$ and 350 K calculated with JEFF-3.1.1 and CAB model compared with the experimental data .....	72
4.18- Comparison of two convolution options for $E_0 = 14$ meV (IN4c), $\theta = 15^\circ$ and $T = 300$ K. The dashed line was obtained convoluting the double differential cross section with a Gaussian function of 1.44% of resolution. The continuous line was obtained convoluting with the vanadium measures .....	73
4.19- Double differential scattering cross section at $E_0 = 3$ meV, $\theta = 45^\circ$ and 350 K calculated with CAB model compared with the experimental data .....	74
4.20- $S(\bar{q}, \omega)$ for $\bar{q} = 1.6\text{\AA}^{-1}$ at 294 K (left hand plot) obtained using the quantum correction (GAAQC) and the Gaussian approximation. In the right hand plot it was calculated the double differential cross section for $E_0 = 3$ meV, $\theta = 71^\circ$ and 294 K using both approaches .....	75
5.1- Radial cross section of MISTRAL-1 core.....	78
5.2- Radial cross section of MISTRAL-2 core. The configuration corresponds to $20^\circ\text{C}$ .....	78
5.3- Radial cross section of MISTRAL-3 core.....	78
5.4- Flowchart of the calculation scheme used to produce the thermal scattering libraries for TRIPOLI4 .....	81
5.5- Effective temperature correction to the temperature for taking into account the crystal lattice effects in the fuel matrix.....	81
5.6- Reactivity corrections as a function of the temperature due to the thermal expansion of the MISTRAL-1 core. The reference corresponds to reactivity at $20^\circ\text{C}$ . The solid line represents the linear fit .....	83
5.7- Energy ranges for the tests performed over MISTRAL-1 configuration at $20^\circ\text{C}$ .....	85
5.8- $^1\text{H}$ scattering cross sections bound to $\text{H}_2\text{O}$ at 294 and in the free gas approximation at 294 K and 1250 K from JEFF-3.1.1 library .....	86
5.9- Interpolation of the model parameters established by Mattes and Keinert between $6^\circ\text{C}$ and $80^\circ\text{C}$ .....	87
5.10- Continuous frequency spectra for $^1\text{H}$ in $\text{H}_2\text{O}$ interpolated over a fine temperature mesh.....	88

5.11- Total cross section of $^1\text{H}$ in $\text{H}_2\text{O}$ calculated with the broad temperature mesh of the JEFF-3.1.1 library (20 °C, 50 °C and 100 °C) and interpolated over a fine temperature mesh (from 6 °C to 80 °C).....	88
5.12- Differences in reactivity $\Delta\rho(T)$ obtained with the thermal scattering laws of JEFF-3.1.1 and CAB model for the MISTRAL-1, MISTRAL-2 and MISTRAL-3 configurations. The solid lines represent the best fit curves calculated with the CONRAD code.....	92
5.13- Differences in reactivity $\Delta\rho(T)$ obtained with the thermal scattering laws of JEFF-3.1.1 and CAB model for the MISTRAL-1 with (empty points) and without (filled points) the thermal expansion effects.....	93
5.14- $\text{H}_2\text{O}$ cross section calculated with CAB model and JEFF-3.1.1 at 293.6 K, together with the MISTRAL-2 neutron spectrum at the same temperature .....	95
5.15- Calculation errors on the reactivity temperature coefficient as a function of the temperature for the MISTRAL-1 experiment. The uncertainty bands accounts for the statistical uncertainty of the Monte Carlo calculations .....	99
5.16- Comparison between the $^{241}\text{Am}$ capture cross sections as a function of the energy of JEFF-3.1.1 and JEFF-3.2 libraries at 294 K, together with the MISTRAL-2 neutron spectrum at 20 °C and 80 °C .....	101
5.17- Comparison between the $^{241}\text{Am}$ capture cross sections as a function of the energy of JEFF-3.1.1 and JEFF-3.2 libraries at 294 K, together with the MISTRAL-2 neutron spectrum at 20 °C and 80 °C .....	103
6.1- Total cross section measurements at 294 K used in the fitting procedure of the GLSM .....	112
6.2- Average cosine of the scattering angle measurements at 294 K used in the fitting procedure of the GLSM .....	112
6.3- Transmission data measured at 294 K.....	114
6.4- Full correlation matrix between the model and the experimental parameters after marginalization.....	117
6.5- Continuous distribution and discrete oscillators used in JEFF-3.1.1 at 294 K .....	118
6.6- Effect on the $\text{H}_2\text{O}$ total cross section of the scaling factor applied to the vibration energy grid used to reconstruct the frequency distribution at 294 K.....	120
6.7- $\text{H}_2\text{O}$ total cross section measurements at 294 K from the EXFOR database compared to the cross section of JEFF-3.1.1 (upper plot) and the transmission data converted using a generic areal density of $0.017 \text{ barn}^{-1}$ .....	121
6.8- Modifications of the low energy part of a given theoretical transmission of a thick water sample according to the diffusion constant $c$ .....	122
6.9- Bending and stretching modes calculated at 294 K with the molecular dynamic code GROMACS and parameters used in reference [5]. The mean energies of the two modes (205.2 meV and 415.5 meV) are	

compared with the energies of the first and second oscillators introduced in JEFF-3.1.1 (205.0 meV and 436.0 meV).....	123
7.1- $S(\alpha, \beta_0)$ and the multigroup $\bar{S}(\alpha, \beta_0)$ as a function of the momentum transfer for $\beta_0 = 1.0$ calculated with the CAB model at 294 K.....	129
7.2- Sensitivities of the $\bar{S}(\alpha, \beta_0)$ function (dashed line) to the CAB model parameters as a function of the momentum transfer for $\beta_0 = 1.0$ calculated with the CAB model at 294 K.....	129
7.3- Relative uncertainties and correlation matrix of the $\bar{S}(\alpha, \beta_0)$ function for $\beta_0 = 1.0$ (upper plot) and $\beta_0 = 10.0$ (bottom plot) calculated with the CAB model at 294 K .....	130
7.4- Sensitivity of the $^1\text{H}$ in $\text{H}_2\text{O}$ scattering cross section at 294 K to the TIP4P/2005f water potential parameters. The dashed line represents the scattering cross section of $^1\text{H}$ in $\text{H}_2\text{O}$ .....	131
7.5- Relative uncertainties and correlation matrix of the $^1\text{H}$ in $\text{H}_2\text{O}$ scattering cross section calculated with the CAB model at 294 K. The left hand plot shows the results after the fitting procedure and the right hand plot the results after the marginalization. For both cases the calculated cross section and the uncertainty bands are plotted with the experimental data used in the retroactive analysis .....	133
7.6- Sensitivity of the $\bar{\mu}$ the TIP4P/2005f water potential parameters. The dashed line represents the calculation done with CAB model at 294 K.....	134
7.7- Relative uncertainties and correlation matrix of average cosine of the scattering angle $\bar{\mu}$ calculated with the CAB model at 294 K. The right plot represents the calculated $\bar{\mu}$ and the uncertainty bands compared with the experimental data used in the retroactive analysis.....	134
7.8- Relative uncertainties and correlation matrix of the $\bar{S}(\alpha, \beta_0)$ function for $\beta_0 = 1.0$ (upper plot) and $\beta_0 = 10.0$ (lower plot) calculated with the JEFF-3.1.1 library at 294 K.....	136
7.9- Relative uncertainties and correlation matrix of the $^1\text{H}$ in $\text{H}_2\text{O}$ scattering cross section calculated with the JEFF-3.1.1 library at 294 K after the marginalization.....	137
7.10- Comparison of the total cross section calculated with the CAB model and the JEFF-3.1.1 library at 294 K around the thermal neutron energy.....	137
7.11- Sensitivity profiles of the keff value to the multigroup $\bar{S}(\alpha_0, \beta)$ for $\alpha_0 = 0.5$ (left hand plot) and to the $\bar{S}(\beta)$ (right hand plot) calculated at 294 K .....	140
7.12- Relative uncertainties and correlation matrix of the scattering function $\bar{S}(\beta)$ averaged in one momentum transfer group at 294 K.....	141
A.1- MISTRAL-2 configuration at 10 °C and 15 °C .....	151
A.2- MISTRAL-2 configuration at 20 °C .....	151
A.3- MISTRAL-2 configuration at 25 °C .....	152

A.4- MISTRAL-2 configuration at 30 °C .....	152
A.5- MISTRAL-2 configuration at 40 °C .....	152
A.6- MISTRAL-2 configuration at 45 °C .....	153
A.7- MISTRAL-2 configuration at 50 °C .....	153
A.8- MISTRAL-2 configuration at 60 °C .....	153
A.9- MISTRAL-2 configuration at 65 °C .....	154
A.10- MISTRAL-2 configuration at 70 °C .....	154
A.11- MISTRAL-2 configuration at 75 °C .....	154
A.12- MISTRAL-2 configuration at 80 °C .....	155

# Chapter 1

## Introduction

### 1.1 Context

The knowledge of the neutron distribution in space, energy and time is crucial to understand the behavior of a nuclear reactor and critical systems as well. In principle, the time-dependent Boltzmann's neutron transport equation predicts the distribution of the neutrons with the appropriate initial and boundary conditions [1]:

$$\frac{1}{v} \frac{\partial}{\partial t} \varphi(\vec{r}, \Omega, E, t) = \iint \Sigma_s(E', \Omega' \rightarrow E, \Omega) \varphi(\vec{r}, \Omega', E', t) dE' d\Omega' + \frac{\chi(E)}{4\pi} \int \nu(E') \Sigma_f(E') \varphi(\vec{r}, \Omega', E', t) dE' + Q(\vec{r}, \Omega, E, t) - \Sigma_t \varphi(\vec{r}, \Omega, E, t) - \Omega \cdot \bar{\nabla} \varphi(\vec{r}, \Omega, E, t) \quad (1)$$

where  $v$  is the neutrons velocity,  $\varphi$  is the angular flux,  $\Sigma_s$ ,  $\Sigma_f$  and  $\Sigma_t$  are the macroscopic scattering, fission and total cross sections,  $\chi$  is the fission spectrum,  $\nu$  is the mean number of neutrons emitted per fission and  $Q$  is the external source factor.

This integral-differential equation reflects the balance of neutrons at any time, energy and space due to their appearances and disappearances. The first term of the right part of the equation, are the scattered neutrons from an energy and solid angle  $E', \Omega'$  to  $E, \Omega$ . The second term reflects the neutrons created by fission. The third term describes a neutron source. The fourth term defines the neutrons disappearance due to absorption or to scattering. The last term expresses the neutrons lost by leakages.

The neutrons produced by the fission of fissile isotopes have a very high energy (typically of 2 MeV). In order to increase the probability of producing more fissions, they need to be lose energy in a process called slowing-down. The first term of the right part of the equation models this physical process.

The materials used as moderators, consist of atoms bonded together chemically or in a crystalline structure. For neutron energies higher than the bonding energy of these atoms the interaction of neutrons with the material can be approximated by a free gas interaction. For smaller energies (typically below 1 eV), the target molecule motion must be accounted as a whole in order to reproduce correctly the physics of the scattering process.

The light water is one of the most used materials as moderators and coolants for nuclear reactors and critical systems in general. From a safety point of view, the correct understanding of the interaction of the neutron with the water molecule is very important to predict their transport. The neutron scattering process in light water is the object of study in the present work.

## 1.2 Motivations

When performing neutron transport calculation, reactor calculation codes need the microscopic cross sections of the isotopes involved in the system to predict the nuclear reactions. The nuclear data information is obtained through cross section libraries that are carefully constructed on the basis of nuclear data evaluation process. These libraries are commonly referred as the Evaluated Nuclear Data files (ENDF).

The nuclear data libraries ENDF/B-VII.1 [2] and the JEFF-3.1.1 library [3] contain a model that describes the thermal neutron scattering with the light water. This model, namely IKE model [4] is based on experimental measurements done in the sixties (almost 50 years ago).

Nowadays, the calculation power of computers enables producing more accurate and reliable theoretical models with a completely different approach like molecular dynamic simulation. The methodology consists of simulating in a microscopic scale the interaction forces between the water molecules. In this context, a new model was developed by the neutron physics research group of Centro Atomico Bariloche (Argentina): the CAB model [5].

Figure 1.1 compares the H<sub>2</sub>O total cross section calculated with the CAB model (continuous line), with the JEFF-3.1.1 nuclear data library (dashed line), and in the free gas approximation (dotted line) for an energy range of 10<sup>-5</sup> eV to 5 eV at 294 K.

The importance of taking into account the chemical bond of the hydrogen with the oxygen, at this energy range, is pointed out when one compares the cross section of <sup>1</sup>H as a free gas with the experimental data. The agreement is poor. The cross sections calculated with a model describing the scattering of a neutron with the <sup>1</sup>H bounded to the H<sub>2</sub>O molecule are represented by the JEFF-3.1.1 and the CAB model. In both cases, the trends of the total cross sections are consistent with the experimental data up to approximately 0.1 meV. Below this energy, the differences between JEFF-3.1.1 and the CAB model are clearly marked. The ratio between the cross sections is close to 1.54 at 10<sup>-5</sup> eV.

The impact of such differences in the total cross sections between the free gas approximation and the thermal scattering models is illustrated in a reactor calculation. As a matter of comparison, we chose the MISTRAL-1 experiment at 20 °C, which was carried out in the EOLE reactor at CEA Cadarache. The MISTRAL-1, shown in Figure 2.1, is a homogeneous UO<sub>2</sub> configuration moderated and cooled by light water (a detailed analysis of this experiment will be described in the present report). It was calculated the reactivity with the Monte Carlo code TRIPOLI4, replacing the evaluated file of <sup>1</sup>H in H<sub>2</sub>O of JEFF-3.1.1 library by the <sup>1</sup>H in H<sub>2</sub>O of CAB model and the <sup>1</sup>H in the free gas approximation. The reactivity difference,  $\Delta\rho$ , between the calculated (C) and the experimental (E) reactivity for each case are listed in table 1.1.

The reactivity difference between the JEFF-3.1.1 and CAB model cases is 90 pcm. The origin of such discrepancy will be studied further. The remarkable outcome of this analysis is the overestimation of the reactivity by the <sup>1</sup>H free gas approximation in almost 1000 pcm. The difference with respect to JEFF-3.1.1 yields 770 pcm. Recalling that the target accuracy in a reactivity calculation is approximately

200 pcm, it is confirmed the significance of taking into account the hydrogen bounded to water molecule in thermal scattering.

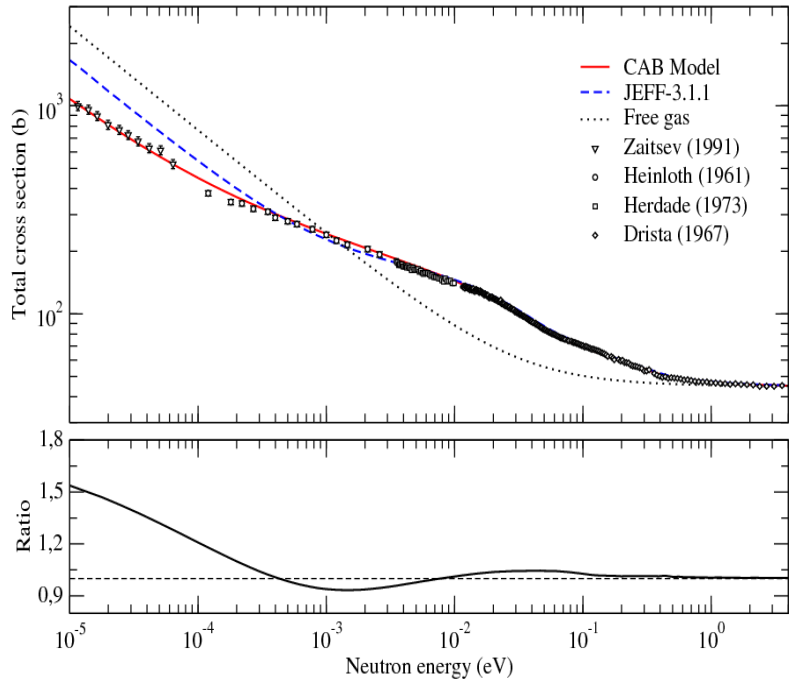


Fig. 1.1 Total H<sub>2</sub>O cross section calculated with the CAB model and with the JEFF-3.1.1 library at 294 K.

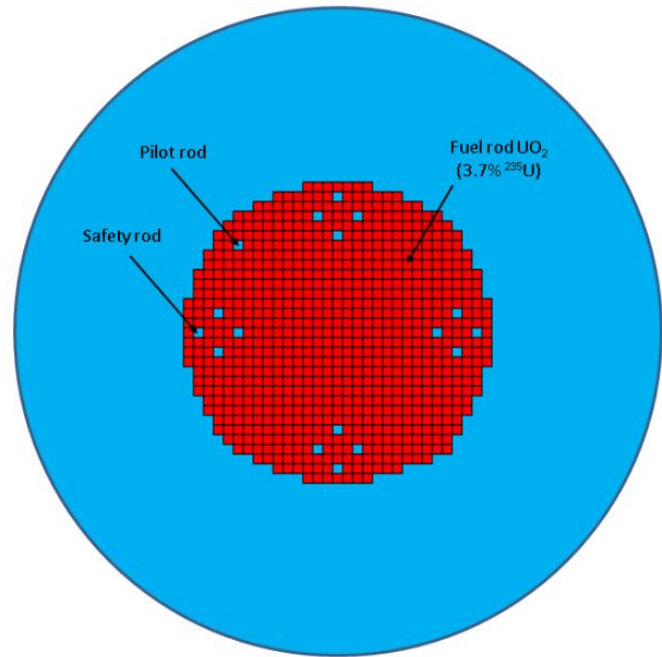


Fig. 2.1 Radial cross section of MISTRAL-1 core from EOLE reactor.

Table 1.1. Differences in reactivity  $\Delta\rho = C - E$  (pcm) obtained with the thermal scattering laws of JEFF-3.1.1, CAB model and with the free gas approximation for the MISTRAL-1 configuration. The statistical uncertainty due to the Monte Carlo calculations is 2 pcm. The magnitude of the experimental uncertainties ranges 200 pcm.

<b>Moderator</b>	<b><math>\Delta\rho = C - E</math> (pcm)</b>
<sup>1</sup> H in H <sub>2</sub> O of JEFF-3.1.1	192
<sup>1</sup> H in H <sub>2</sub> O of CAB model	283
<sup>1</sup> H as free gas	962

### *1.3 Objectives*

The first key point in the present study is to analyze the behavior of the two models and study the feasibility of producing thermal neutron scattering data calculated by means of molecular dynamics.

The second issue is to evaluate and quantify the uncertainties of the two models. None of the existing nuclear data libraries provides the uncertainties for the thermal scattering data of light water. A correct estimation of the uncertainties on the nuclear data, in general, enables determining the safety margins of a critical system.

### *1.4 Report description*

The chapter 2 is dedicated to explain the thermal neutron scattering theory which sets the background for the present report. It also presents the evaluation methodology of the scattering function, which is done with the LEAPR module of the processing code NJOY.

In the chapter 3, the models IKE and CAB will also be presented. The behavior of the models is characterized microscopically, studying the frequency spectrum of hydrogen in light water, the double differential and total cross sections.

The chapter 4 describes the neutron time-of-flight experiment carried out at Laue-Langevin Institute (Grenoble, France), where it was measured the double differential cross section of light water at cold reactor operating conditions. A Monte Carlo simulation was done to evaluate the agreement of the thermal scattering models with the new experimental data.

In the chapter 5, the thermal scattering laws of light water are compared macroscopically in integral calculations. It is evaluated their impact on an integral experiment at cold reactor operating conditions. The MISTRAL experimental program performed at EOLE reactor (France) was selected as benchmark.

Chapter 6 covers the methodology for evaluating and quantifying the uncertainties due to the thermal neutron scattering with light water. Firstly, the framework regarding the uncertainty treatment is explained and secondly, the approach for producing covariances is presented.

Finally, propagation of the uncertainties due to the thermal scattering data are presented in chapter 7. Covariance matrices of the thermal scattering function and the scattering cross section of hydrogen in light water were produced. The impact of the uncertainty of the calculated reactivity in the MISTRAL benchmark was studied as well.

# Chapter 2

## Thermal neutron scattering

The present chapter is devoted to the theory of neutron scattering. Firstly and taking as a reference bibliography [6], the basic notions of neutron scattering are presented. Later on, it is explained how the thermal scattering function is evaluated using the LEAPR module of NJOY processing code [7].

### 2.1 Introduction to thermal neutron scattering theory

In the low neutron energy range, typically below 5 eV, neutron scattering is affected by the atomic bonding of the scattering molecule in the moderator. Compared to a free nucleus, this changes the reaction cross section and, thus, the energy and angular distribution of the secondary neutrons.

Neutron scattering is classified as elastic and inelastic scattering. While the former is important, the latter has direct link to the reactor applications because neutrons need to slow down to increase the fission probability of the fissile isotopes. Both elastic and inelastic scattering can be coherent or incoherent. In coherent scattering, the interference phenomena between the waves reflected by close nuclei affect the scattering target. However, in the particular case of light water the scattering process can be treated as pure incoherent as it will be seen further in the chapter.

The H<sub>2</sub>O total microscopic cross section of thermal neutrons is given by:

$$\sigma_t^{H_2O}(E) = 2\sigma_t^H(E) + \sigma_t^O(E), \quad (1)$$

where  $\sigma_t^O$  is the total cross section of <sup>16</sup>O and  $\sigma_t^H$  is the total cross section of <sup>1</sup>H. The latter is given by

$$\sigma_t^H(E) = \sigma_\gamma(E) + \sigma_n(E). \quad (2)$$

In the thermal energy range, the capture cross section  $\sigma_\gamma(E)$  can be approximated as:

$$\sigma_\gamma(E) = \sigma_{\gamma 0} \sqrt{\frac{E_0}{E}}, \quad (3)$$

where  $\sigma_{\gamma 0}$  is the capture cross section measured at the thermal neutron energy  $E_0 = 25.3$  meV.

Figure 2.1 compares the scattering cross section at T = 0 K and 294 K with the capture cross section of hydrogen as given in the nuclear data library JEFF-3.1.1. For a given temperature the cross section is broadened using the processing code NJOY [R. E. MacFarlane et al., *The NJOY Data Processing System, Version 2012, Los Alamos National Laboratory (2012)*].

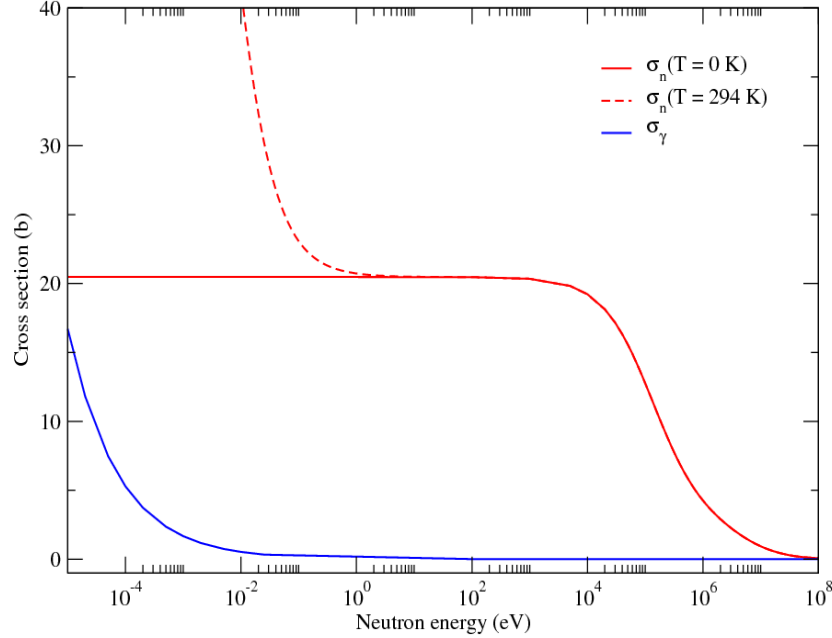


Fig. 2.1 Hydrogen scattering and capture cross sections as a function of the neutron energy from JEFF-3.1.1 library.

In the case of hydrogen bonded to the water molecule, the inelastic scattering cross section  $\sigma_n$  is related to the double differential cross section as:

$$\sigma_n(E) = \iint \frac{d^2\sigma_n}{d\Omega dE'} dE' d\Omega. \quad (4)$$

For simplicity, the subscript  $n$  in the scattering cross section  $\sigma_n$  will be omitted from now on.

The double differential cross section expresses the probability that an income neutron flux of energy  $E$  and direction  $\Omega$  will be scattered by a target at a secondary energy  $E'$  and direction  $\Omega'$  [6]:

$$\frac{d^2\sigma}{d\Omega dE'} = \frac{1}{4\pi k_B T} \sqrt{\frac{E'}{E}} e^{-\frac{\beta}{2}} (\sigma_{coh} S(\alpha, \beta) + \sigma_{inc} S_s(\alpha, \beta)), \quad (5)$$

where  $\sigma_{coh}$  and  $\sigma_{inc}$  are respectively the coherent and incoherent scattering cross sections,  $k_B$  is the Boltzmann constant and  $T$  is the temperature of the material.

The  $S(\alpha, \beta)$  function is the thermal scattering function, which is given by:

$$S(\alpha, \beta) = S_s(\alpha, \beta) + S_d(\alpha, \beta), \quad (6)$$

where  $S_s(\alpha, \beta)$  is the self-scattering function that accounts for non-interference or incoherent effects, and  $S_d(\alpha, \beta)$  is the distinct-scattering function that accounts for interference or coherent effects.

The scattering law is a function of the dimensionless momentum transfer  $\alpha$  and energy transfer  $\beta$ :

$$\alpha = \frac{E' + E - 2\sqrt{E'E}\mu}{Ak_B T}, \quad (7)$$

$$\beta = \frac{E' - E}{k_B T} = \frac{\hbar\omega}{k_B T}, \quad (8)$$

where  $\mu$  is the cosine of the scattering angle in the laboratory system and  $A$  is the ratio between the mass of the scattering target  $M$  and the neutron mass  $m$ . The energy transfer  $E' - E$  is sometimes denoted as the product between the reduced Planck's constant  $\hbar$  and the excitation frequency  $\omega$ .

In the literature, the scattering function might be expressed as a function of other variables rather than the dimensionless momentum and energy transfer  $\alpha, \beta$ . If  $\bar{q}$  is the neutron wave vector change, then the scattering law can be expressed as:

$$S(\bar{q}, \omega) = S(\alpha, \beta) \frac{e^{\frac{\hbar\omega}{2k_B T}}}{k_B T}. \quad (9)$$

The module of the wave vector change  $\bar{q}$  is related to the dimensionless momentum transfer  $\alpha$  as:

$$q^2 = |\bar{k} - \bar{k}'|^2 = \frac{2m}{\hbar^2} (E' + E - 2\mu\sqrt{EE'}). \quad (10)$$

From eq. (7) we have then:

$$q^2 = \frac{2Mk_B T}{\hbar^2} \alpha. \quad (11)$$

Expressing the scattering function as  $S(\bar{q}, \omega)$  can be especially useful when performing experimental measurements, as one obtains direct information of the transferred energy and angle of the scattered neutrons. In practice, the  $\alpha$  and  $\beta$  variables are used for the evaluation of the scattering function with the LEAPR module as it will be seen later.

The next sections will be devoted to explain how to calculate the coherent and the incoherent cross sections and the self and distinct scattering functions using the formalism introduced by L. Van Hove in 1954 [9]. Next, the subject will be focused on light water, and to the way the scattering function is obtained using the processing code NJOY.

## 2.2 The coherent and incoherent cross sections

It can be shown [6] that at low neutron energy, the cross section in scattering of neutrons with a single fixed nucleus is given by:

$$\sigma_n = 4\pi b^2. \quad (12)$$

The parameter  $b$  is known as the scattering length. It depends on the target nucleus and the spin state of the nucleus-neutron system. If the nucleus has a spin  $I$ , the combined system can have a spin  $I \pm$

1/2 (the neutron spin is 1/2). Each spin state has its own value of  $b$ . There will be then two possible values of the scattering length for that particular nucleus. The exceptions are nuclei with spin zero, where the scattering will be purely coherent as it will be demonstrated further on this chapter.

Considering a scattering system of a single element where the scattering length varies from one nucleus to another, then the average value of  $b$  for the whole system is:

$$\bar{b} = \sum_i f_i b_i. \quad (13)$$

The relative frequencies  $f_i$  denote the probability of a system to have a scattering length  $b_i$ . If  $b^+$  is the scattering length given by the spin of the system neutron-nucleus  $I + 1/2$  and  $b^-$  the one given by the spin  $I - 1/2$ , then the number of states associated with each spin will be respectively:

$$2\left(I + \frac{1}{2}\right) = 2I + 2. \quad (14)$$

$$2\left(I - \frac{1}{2}\right) = 2I - 1. \quad (15)$$

If the neutrons are unpolarized and the nuclear spins are randomly orientated (no correlation between the scattering lengths of different nuclei), then each spin is equiprobable. Eq. (13) turns into:

$$\bar{b} = f^+ b^+ + f^- b^- = \frac{2I + 2}{2I + 2 + 2I} b^+ + \frac{2I}{2I + 2 + 2I} b^- = \frac{I + 1}{2I + 1} b^+ + \frac{I}{2I + 1} b^-. \quad (16)$$

A generalization can be made assuming that there are different isotopes in the scattering system. Then the frequencies  $f^+$  and  $f^-$  are multiplied by the relative abundance of the isotope  $\zeta_i$ :

$$\bar{b} = \sum_i \zeta_i \left( \frac{I_i + 1}{2I_i + 1} b_i^+ + \frac{I_i}{2I_i + 1} b_i^- \right). \quad (17)$$

The microscopic coherent and incoherent cross sections are defined as:

$$\sigma_{coh} = 4\pi(\bar{b})^2, \quad (18)$$

$$\sigma_{inc} = 4\pi \left[ \overline{b^2} - (\bar{b})^2 \right], \quad (19)$$

where the average value of the square of the scattering length is:

$$\overline{b^2} = \sum_i f_i b_i^2. \quad (20)$$

Considering that the potential interaction between the neutron and the system is given by the "Fermi Pseudo potential", which essentially is a delta function in space, and following the notation in [6], the double differential cross section can be expressed as the sum of the coherent and the incoherent double differential cross sections:

$$\frac{d^2\sigma}{d\Omega dE'} = \left( \frac{d^2\sigma}{d\Omega dE'} \right)_{coh} + \left( \frac{d^2\sigma}{d\Omega dE'} \right)_{inc}, \quad (21)$$

$$\frac{d^2\sigma}{d\Omega dE'} = \frac{k'(\bar{b})^2}{k} \frac{1}{2\pi\hbar} \sum_{j'j'; j' \neq j} \int \langle j', j \rangle e^{-i\omega t} dt + \frac{k' \bar{b}^2}{k} \frac{1}{2\pi\hbar} \sum_j \int \langle j, j \rangle e^{-i\omega t} dt, \quad (22)$$

where the internal product  $\langle j', j \rangle$  is defined as:

$$\langle j', j \rangle = \langle \exp(-i\bar{q} \cdot \bar{R}_{j'}(0)) \exp(i\bar{q} \cdot \bar{R}_j(t)) \rangle, \quad (23)$$

where  $\bar{k}$  and  $\bar{k}'$  are the incident and final neutron wave vectors,  $\bar{R}_j (j = 1, \dots, N)$  the position vector of the  $j^{\text{th}}$  nucleus in the scattering system of  $N$  nuclei.

Multiplying and dividing eq. (22) by the factor  $4\pi$  we can express explicitly the double differential cross section as a function of  $\sigma_{coh}$  and  $\sigma_{inc}$ :

$$\left( \frac{d^2\sigma}{d\Omega dE'} \right)_{coh} = \sigma_{coh} \frac{1}{4\pi} \frac{k'}{k} \frac{1}{2\pi\hbar} \sum_{j'j} \int \langle \exp(-i\bar{q} \cdot \bar{R}_{j'}(0)) \exp(i\bar{q} \cdot \bar{R}_j(t)) \rangle e^{-i\omega t} dt. \quad (24)$$

$$\left( \frac{d^2\sigma}{d\Omega dE'} \right)_{inc} = \sigma_{inc} \frac{1}{4\pi} \frac{k'}{k} \frac{1}{2\pi\hbar} \sum_j \int \langle \exp(-i\bar{q} \cdot \bar{R}_j(0)) \exp(i\bar{q} \cdot \bar{R}_j(t)) \rangle e^{-i\omega t} dt. \quad (25)$$

It can be seen from eq. (22) that the coherent scattering depends on the correlation between the positions of the same nuclei at different times, and on the correlation between the positions of different nuclei at different times. The incoherent scattering depends only on the correlation between the positions of the same nuclei at different times. This is the reason why the coherent component arises interference effects.

### 2.3 The coherent and incoherent scattering functions

Following the mathematical formulation of the scattering introduced by Van Hove in 1954 [9], we define firstly the intermediate scattering function  $I(\bar{q}, t)$  as:

$$I(\bar{q}, t) = \sum_{j'j} \langle \exp(-i\bar{q} \cdot \bar{R}_{j'}(0)) \exp(i\bar{q} \cdot \bar{R}_j(t)) \rangle. \quad (26)$$

Secondly, we define the time dependent pair correlation function  $G(\bar{r}, t)$  by:

$$G(\bar{r}, t) = \frac{1}{(2\pi)^3} \int I(\bar{q}, t) \cdot e^{-i\bar{q} \cdot \bar{r}} d\bar{q}. \quad (27)$$

And finally, the scattering function of the system is defined as the Fourier transform in time of the intermediate scattering function:

$$S(\bar{q}, \omega) = \frac{1}{2\pi\hbar} \int I(\bar{q}, t). e^{-i\omega t} dt. \quad (28)$$

Arranging the expressions, we derive the scattering function as the Fourier transform in space and time of the time dependent pair correlation function  $G(\bar{r}, t)$ :

$$S(\bar{q}, \omega) = \frac{1}{2\pi\hbar} \int \int G(\bar{r}, t). e^{i(\bar{q}\cdot\bar{r}-\omega t)} dt d\bar{r}. \quad (29)$$

Replacing in eq. (24) and rearranging terms, we can find an elegant expression for the coherent double differential cross section as a function of the scattering law:

$$\left( \frac{d^2\sigma}{d\Omega dE'} \right)_{coh} = \frac{\sigma_{coh}}{4\pi} \frac{k'}{k} S(\bar{q}, \omega). \quad (30)$$

In a similar way, we define the self intermediate scattering function as:

$$I_s(\bar{q}, t) = \sum_j \langle \exp(-i\bar{q} \cdot \bar{R}_j(0)) \exp(i\bar{q} \cdot \bar{R}_j(t)) \rangle. \quad (31)$$

And we define the incoherent scattering function of the system as:

$$S_s(\bar{q}, \omega) = \frac{1}{2\pi\hbar} \int \int G_s(\bar{r}, t). e^{i(\bar{q}\cdot\bar{r}-\omega t)} dt d\bar{r}, \quad (32)$$

where the function  $G_s(\bar{r}, t)$  is the self time dependent pair correlation function, given by:

$$G_s(\bar{r}, t) = \frac{1}{(2\pi)^3} \int I_s(\bar{q}, t). e^{-i\bar{q}\cdot\bar{r}} d\bar{q}. \quad (33)$$

Replacing eq. (32) in (25), we obtain the expression for the double differential incoherent scattering cross section:

$$\left( \frac{d^2\sigma}{d\Omega dE'} \right)_{inc} = \frac{\sigma_{inc}}{4\pi} \frac{k'}{k} S_{inc}(\bar{q}, \omega). \quad (34)$$

Thus, the total double differential scattering cross section is the sum of eq. (30) and (34):

$$\frac{d^2\sigma}{d\Omega dE'} = \frac{1}{4\pi} \frac{k'}{k} [\sigma_{coh} S(\bar{q}, \omega) + \sigma_{inc} S_s(\bar{q}, \omega)]. \quad (35)$$

Using the equivalent expression relating  $S(\bar{q}, \omega)$  and  $S(\alpha, \beta)$ , given by eq. (9), and the definition of the module of the neutron wave vector  $k = \sqrt{2mE}/\hbar$ , we arrive to the double differential cross section in terms of  $\alpha, \beta$  presented at the beginning of this chapter:

$$\frac{d^2\sigma}{d\Omega dE'} = \frac{1}{4\pi k_B T} \sqrt{\frac{E'}{E}} e^{-\frac{\beta}{2}} (\sigma_{coh} S(\alpha, \beta) + \sigma_{inc} S_s(\alpha, \beta)). \quad (36)$$

The double differential cross section is essentially given by the product of the microscopic cross section  $\sigma_{coh}$  or  $\sigma_{inc}$  and the scattering function  $S$ . The microscopic cross section depends on the interaction between the neutron and the nuclei in the scattering system (the scattering length is dependent of the spin of the system neutron-isotope). The scattering function is only a property of the scattering system. It depends only of the relative positions and motion of the particles, given by the interaction forces between them and the temperature of the system.

In the next section it will be seen how the scattering function of light water is evaluated through some approximations in order to obtain the double differential scattering cross section.

## 2.4 The approximations of scattering in light water

In practice, the scattering law  $S(\alpha, \beta)$  is generated with the LEAPR module of NJOY Nuclear Data Processing System [7]. This code computes the scattering function in the incoherent and the Gaussian approximations.

### 2.4.1 The incoherent approximation

The incoherent approximation might be physically supported due to the fact that the molecules conforming liquids (like light water) are subjected to a constant thermal agitation that depends of the medium temperature. This yields that the interatomic distances do not remain constant like in an ordered crystalline solid. Under this effect, the contribution of the coherent interference may be neglected over the incoherent component.

According to reference [8], the incoherent approximation is also numerically sustained because the incoherent scattering cross section is much more larger than the coherent counterpart. Under this assumption, the double differential cross section turns into:

$$\frac{d^2\sigma}{d\Omega dE'} \cong \frac{\sigma_{coh} + \sigma_{inc}}{4\pi k_B T} \sqrt{\frac{E'}{E}} S_s(\alpha, \beta). \quad (37)$$

### 2.4.2 The Gaussian approximation

In short time dynamics, the particles in the liquid behave like free nuclei and they approximate to a perfect gas. From the scattering theory of neutrons with a single nucleus of mass  $M$ , it can be demonstrated that the self pair correlation function  $G_s(\vec{r}, t)$  adopts a Gaussian form [6]:

$$G_s(\vec{r}, t) = \frac{1}{[2\pi\sigma^2(t)]^{3/2}} e^{\frac{-r^2}{2\lambda^2(t)}}, \quad (38)$$

where the time dependent function  $\lambda^2$  is given by:

$$\lambda^2(t) = \frac{t^2}{M\beta}. \quad (39)$$

Applying the inverse relation of the Fourier transform to eq. (33), and replacing eq. (40), we obtain the expression for the self-intermediate scattering function:

$$I_s(\bar{q}, t) = \int G_s(\bar{r}, t) e^{i\bar{q}\cdot\bar{r}} d\bar{r} = e^{\frac{-q^2 \lambda^2(t)}{2}}. \quad (40)$$

No assumption of the time dependence of  $\lambda^2$  was needed for the integration. In general:

$$\lambda^2(t) = \frac{\gamma(t)}{M\beta}. \quad (41)$$

Changing the variable to the dimensionless momentum transfer  $\alpha$  in eq. (42):

$$I_s(\alpha, t) = e^{-\alpha\gamma(t)}. \quad (42)$$

The function  $\gamma(t)$  is called the width function. It is related to the frequency spectrum  $\rho(\beta)$  of the target by:

$$\gamma(t) = \int_0^\infty \rho(\beta) \frac{[1 - e^{-i\beta t}] e^{-\beta/2}}{2\beta \sinh(\beta/2)} d\beta. \quad (43)$$

The  $\rho(\beta)$  is a probability density function, normalized such that:

$$\int_0^\infty \rho(\beta) d\beta = 1 \quad (44)$$

The frequency spectrum  $\rho(\beta)$  is the key parameter that characterizes the dynamics of the scattering target. It gives information about the excitations states of the material, containing a complete description of the intermolecular and the intramolecular vibration modes. In LEAPR module, it serves as input to calculate the scattering function.

The principle of detail balance applies for systems in thermal equilibrium and gives a relation between the down-scattering ( $\beta < 0$ ) and the up-scattering ( $\beta > 0$ ):

$$S(\alpha, \beta) = e^{-\beta} S(\alpha, -\beta) \quad (45)$$

## 2.5 The evaluation of the scattering law with the LEAPR module of NJOY

The total or generalized frequency spectrum  $\rho(\beta)$  of the scattering target is introduced in the LEAPR module as a decomposition of three possibilities:

$$\rho(\beta) = \sum_{i=1}^J \omega_i \delta(\beta_i) + \omega_t \rho_t(\beta) + \omega_c \rho_c(\beta). \quad (46)$$

The discrete oscillators are represented by  $\delta(\beta_i)$  and describe the intramolecular modes of vibration, where  $\beta_i$  is the energy and  $\omega_j$  the associated weight. The continuous frequency distribution  $\rho_c(\beta)$  models the intermolecular modes. The weight corresponding to this partial spectrum is  $\omega_c$ . Finally,  $\rho_t$  accounts for the translation of the molecule.

As an illustrative example, Figure 2.2 shows the frequency spectrum of  $^1\text{H}$  in  $\text{H}_2\text{O}$  at 294 K of the JEFF-3.1.1 nuclear data library [4]. The solid-type or continuous spectrum is seen for the lower vibration energies, while the internal modes of the water molecule are described by the two discrete energies. The first oscillator accounts for the bending mode and the second the stretching modes (symmetric and asymmetric).

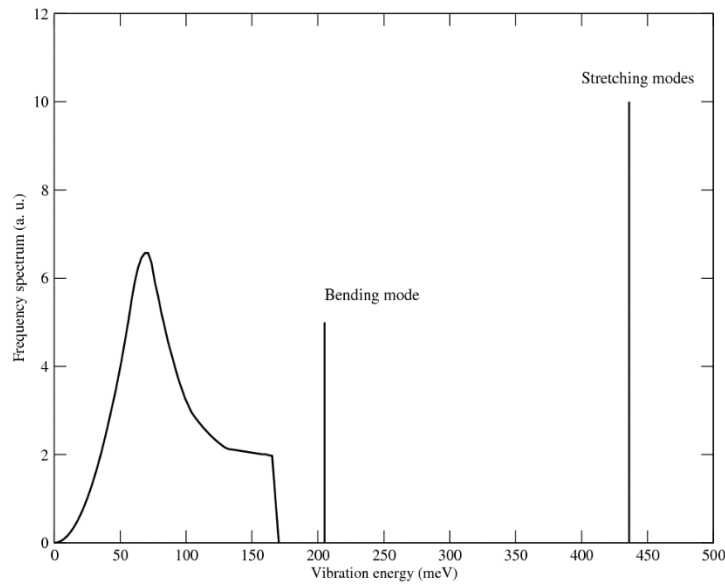


Fig. 2.2 Continuous frequency spectra and intramolecular vibration modes of  $^1\text{H}$   $\text{H}_2\text{O}$  at 294 K for JEFF-3.1.1 nuclear data library.

In the following subsections it will be analyzed how to calculate the scattering law due to each contribution of the partial spectra.

### 2.5.1 The phonon expansion

For the continuous frequency spectra we do an expansion in series of the time-dependent part of the exponential of eq. (45):

$$e^{-\gamma_s(t)} = e^{-\alpha\lambda_s} \sum_{n=0}^{\infty} \frac{1}{n!} \left[ \alpha \int_{-\infty}^{\infty} \frac{\rho(\beta)}{2\beta \sinh(\beta/2)} e^{-\beta/2} e^{-i\beta t} d\beta \right]^n, \quad (47)$$

where  $\lambda_s$  is the Debye-Waller factor, given by:

$$\lambda_s = \int_{-\infty}^{\infty} \frac{\rho(\beta)}{2\beta \sinh(\beta/2)} e^{-\beta/2} d\beta. \quad (48)$$

So the scattering function for the solid-type spectrum:

$$S_c(\alpha, \beta) = e^{-\alpha\lambda_s} \sum_{n=0}^{\infty} \frac{1}{n!} \alpha^n x \frac{1}{2\pi} \int_{-\infty}^{\infty} e^{i\beta t} \left[ \int_{-\infty}^{\infty} \frac{\rho(\beta')}{2\beta' \sinh(\beta'/2)} e^{-\beta'/2} e^{-i\beta' t} d\beta' \right]^n dt. \quad (49)$$

Renaming the whole second factor of eq. (51) as  $\lambda_s^n T_n(\beta)$ :

$$S_c(\alpha, \beta) = e^{-\alpha\lambda_s} \sum_{n=0}^{\infty} \frac{1}{n!} [\alpha\lambda_s]^n T_n(\beta) = e^{-\alpha\lambda_s} [T_0(\beta) + \alpha\lambda_s T_1(\beta) + \alpha^2 \lambda_s^2 T_2(\beta)] \quad (50)$$

$$T_0(\beta) = \frac{1}{2\pi} \int_{-\infty}^{\infty} e^{i\beta t} dt = \delta(\beta) \quad (51)$$

$$T_1(\beta) = \int_{-\infty}^{\infty} \frac{\rho(\beta')}{2\beta' \sinh(\beta'/2)} e^{-\beta'/2} \left[ \frac{1}{2\pi} \int_{-\infty}^{\infty} e^{i(\beta-\beta')t} dt \right] d\beta' = \frac{\rho(\beta)}{2\beta \sinh(\beta/2)} e^{-\beta/2} \frac{1}{\lambda_s} \quad (52)$$

In general the functions  $T_n(\beta)$  are obtained recursively as:

$$T_n(\beta) = \int_{-\infty}^{\infty} T_1(\beta') T_{n-1}(\beta - \beta') d\beta', \quad (53)$$

where the number of phonons exchanged  $n$  is given as input in LEAPR. Typically,  $n = 200$  is fair enough to converge the series.

As the function for  $n = 0$  is a delta function, this term is computed separately doing the convolution with the translational component, as we will see later. This term is called the zero-phonon term.

## 2.5.2 Molecular translations

In LEAPR the translation of the water molecules is modeled by a free gas law or by a diffusion model.

### 2.5.2.1 The free gas model

The first possibility is to model the translational part as a free gas distribution. Replacing eq. (42) in eq. (28) and performing a Fourier transform in time, we have an analytic expression for the translational scattering law:

$$S_t(\bar{q}, \omega) = \left( \frac{\beta}{4\pi E_r} \right)^{1/2} \exp\left( -\frac{\beta}{4E_r} [\hbar^2 \omega^2 - 2\hbar\omega E_r] \right), \quad (54)$$

where  $E_r$  is the recoil energy, given by:

$$E_r = \frac{\hbar^2 q^2}{2M}. \quad (55)$$

Changing variable in eq. (56) yields:

$$S_t(\alpha, \beta) = \frac{1}{\sqrt{4\pi\omega_t\alpha}} \exp\left[ -\frac{(\omega_t + \beta)^2}{4\omega_t\alpha} \right]; (\beta < 0) \quad (56)$$

The eq. (58) is valid for the down-scattering regime ( $\beta > 0$ ). The principle of detailed balance applies for  $\beta > 0$ .

The combined scattering laws corresponding to the solid-type spectra  $S_c(\alpha, \beta)$  and the translational mode  $S_t(\alpha, \beta)$  are obtained by doing the following convolution:

$$S_{c,t}(\alpha, \beta) = S_t(\alpha, \beta) e^{-\alpha\lambda_s} + \int_{-\infty}^{\infty} S_t(\alpha, \beta') S_s(\alpha, \beta - \beta') d\beta'. \quad (57)$$

As stated in the previous subsection, the zero-phonon term of the phonon expansion is convoluted with the translational mode, accounted in the first term of eq. (50).

### 2.5.2.2 The Egelstaff and Schofield diffusion model

Egelstaff and Schofield developed a diffusion model called “effective width model” [10]. The analytic expression for the frequency spectrum is:

$$\rho_t(\beta) = \omega_t \frac{4c}{\pi\beta} \sqrt{c^2 + 1/4} \sinh(\beta/2) K_1\left(\beta\sqrt{c^2 + 1/4}\right), \quad (58)$$

where  $K_1$  is the modified Bessel function of second kind,  $\omega_t$  is the translational weight and  $c$  is the dimensionless diffusion constant. Both are provided as inputs in LEAPR. The parameter  $c$  links the translational weight and the molecular diffusion coefficient  $D$ :

$$c = \frac{M_H D}{\omega_t \hbar}. \quad (59)$$

Under this spectrum, the analytic form of the translational part of the scattering law is:

$$S_t(\alpha, \beta) = \frac{2c\omega_t\alpha}{\pi} \exp[2c^2\omega_t\alpha - \beta/2] \frac{\sqrt{c+1/4}}{\sqrt{\beta^2 + 4c^2\omega_t^2\alpha^2}} K_1\left(\sqrt{c+1/4}\sqrt{\beta^2 + 4c^2\omega_t^2\alpha^2}\right). \quad (60)$$

### 2.5.3 The intramolecular vibration modes

The oscillators will model the internal vibration modes present in a polyatomic molecule. Their distribution is a delta function in an energy  $\beta$ . If the sub-index  $i$  describes each discrete oscillator, then the corresponding scattering law is given by:

$$S_i(\alpha, \beta) = e^{-\alpha\lambda_i} \sum_{n=-\infty}^{\infty} \left[ \delta(\beta - n\beta_i) I_n\left(\frac{\alpha\omega_i}{\beta_i \sinh(\beta_i/2)}\right) e^{-n\beta_i/2} \right], \quad (61)$$

$$\text{where } \lambda_i = \omega_i \frac{\coth(\beta_i/2)}{\beta_i}$$

If there is only one discrete oscillator, then the convolution with the scattering laws of the rotational and translational modes is done in the following way:

$$S(\alpha, \beta) = \int_{-\infty}^{\infty} S_1(\alpha, \beta') S_{c,t}(\alpha, \beta - \beta') d\beta', \quad (62)$$

where  $S_1$  is obtained with eq. (63) and  $S_{c,t}$  comes from eq. (59).

If there are two internal modes, then:

$$S(\alpha, \beta) = \int_{-\infty}^{\infty} S_2(\alpha, \beta') S_{s,t,1}(\alpha, \beta - \beta') d\beta', \quad (63)$$

where  $S_2$  is again obtained with eq. (63) but  $S_{s,t,1}$  comes from the convolution done with eq. (64).

### 2.5.4 The Short Collision Time approximation

In order to avoid numerical problems in eq. (52) as the parameters  $\alpha$  and  $\beta$  increase, the module LEAPR calculates the scattering law in the free gas approximation, where the thermodynamic temperature is corrected by an effective temperature that depends of the frequency spectrum and the vibration modes present as well.

The scattering law is given by:

$$S(\alpha, \beta) = \frac{1}{\sqrt{4\pi\omega_c\alpha\frac{T_{eff}}{T}}} \exp\left[-\frac{(\omega_c\alpha + \beta)^2}{4\omega_c\alpha\frac{T_{eff}}{T}}\right]; (\beta < 0) \quad (64)$$

The counterpart scattering function for  $\beta > 0$  is obtained using the detailed balance principle.

In the general case where all vibration modes are present, the effective temperature is obtained as:

$$T_{eff} = \omega_t T + \omega_c T_{eff}^c + \sum_{i=1}^n \omega_i \frac{\beta_i}{2} \coth\left(\frac{\beta_i}{2}\right) T, \quad (65)$$

where  $\omega_i$  and  $\beta_i$  correspond to the weight and energy of each oscillator of the intramolecular mode, and  $T_{eff}^c$  is the effective temperature corresponding to the rotational mode, which depends on the frequency spectrum as:

$$T_{eff}^s = T \frac{\int_{-\infty}^{\infty} \beta^2 P_s(\beta) e^{-\beta} d\beta}{2}. \quad (66)$$

In the particular case where the molecule doesn't have internal modes, the effective temperature is calculated as a simple weighted average between the thermodynamic and solid-type frequency spectrum effective temperature:

$$T_{eff} = \omega_t T + \omega_s T_{eff}^s. \quad (67)$$

## *2.6 Preliminary conclusions*

In this chapter it was explained how the neutron scattering cross section of light water is obtained. It was seen that it depends directly on the thermal scattering law, which is evaluated by means of the LEAPR module of the NJOY code. This code computes the  $S(\alpha, \beta)$  function in the incoherent and the Gaussian approximations. The frequency spectrum is introduced as input, as a combination of three partial spectra (continuous frequency distribution, discrete oscillators and a free gas model or diffusion model for the diffusive motion of water molecules).

In the next chapter, we will analyze the model of the light water thermal scattering law used in the nuclear data libraries ENDF/B-VII.1 and JEFF-3.1.1, called IKE model, which is based on experimental measurements of the frequency spectrum. We will also introduce a recently developed model based on molecular dynamic simulations, namely CAB model. A comparison from a microscopic point of view will be carried out to analyze their behavior in terms of the scattering physics.

## Chapter 3

# Thermal neutron scattering models for light water

It was seen in chapter 2 that the double differential scattering cross section depends on the thermal scattering function  $S(\alpha, \beta)$ . This function is calculated with the LEAPR module of NJOY code introducing as input the frequency spectrum  $\rho(\beta)$ .

In this chapter we will present two frequency spectra of hydrogen in light water ( $^1\text{H}$  in  $\text{H}_2\text{O}$ ). One gives origin to the thermal scattering law in the nuclear data libraries ENDF/B-VII.1 [2] and JEFF-3.1.1 [3], namely IKE model. The second one is based on molecular dynamic simulations, namely CAB model.

The frequency spectrum of a material is a probability density function which describes the number of states available to be occupied in a certain energy interval. It is a dynamic property of the material structure which defines the excitation states. Especially in solid-state physics, the frequency spectrum is referred also as the phonon density of states (PDOS), where the energy exchange in scattering is traduced as the creation or annihilation of phonons.

### 3.1 IKE model

The IKE model (Institute for Nuclear Technology and Energy Systems in German) for light water was developed by J. Keinert and M. Mattes in 1984 [11]. The frequency spectrum of  $^1\text{H}$  in  $\text{H}_2\text{O}$  was obtained from the so-called Haywood-II model by Koppel [12]. This spectrum derives from the experimental measurements of the double differential cross section at 294 K and 550 K performed in the late sixties by Haywood and Page [13] and [14].

In the phenomenological model, the portion of the frequency spectrum due to the hindered translations was removed and the corresponding area was assigned to free translations of the water molecule. Figure 3.1 shows a comparison between the frequency spectra measured by Haywood and the modification done by Koppel at 294 K. To avoid numerical difficulties, it was introduced a  $\hbar\omega^2$  behavior at the origin (like a Debye spectrum behavior) and the spectrum was cut-off at 165 meV and renormalized to unity [15].

In 2005 the frequency spectrum was adapted to be processed with the LEAPR module of NJOY code and the results were incorporated in the nuclear data library JEFF-3.1.1 [4].

The rotational mode is described by a solid-type frequency distribution (Figure 3.2). The two temperatures, 294 K and 550 K, represent the minimum and maximum thermodynamic temperatures where water works as a moderator in a nuclear reactor. Between these two temperatures, the spectrum is obtained by linear interpolation. As seen in the plot, the rotational band broadens due to the temperature increase but the librational band for both cases is found at around 70 meV. No downshift in energy effect is detected, however some authors claim that the spectrum softens because

of the relaxation of the hydrogen bonds originated by the increase of the thermal agitation [16] and [17].

The translation mode is defined by a free gas law with a temperature dependent mass to account the molecular clustering effect. At room temperature, the water molecules tend to regroup with two or even four cluster of molecules. At higher temperatures, is more likely that the molecules stay alone.

Finally, the intramolecular modes are modeled with two discrete oscillators. One bending mode at 205 meV of energy transfer and one stretching mode (symmetric and asymmetric) at 436 meV.

Table 3.1 resumes the IKE model parameters of the LEAPR module at room temperature and the weights corresponding to each vibration mode.

In the case of the nuclear data library ENDF/B-VII.1 the model was slightly modified on the energy scale of the rotational spectrum in order to improve the agreement with experimental measurements of the total cross section in the energy region between 10 meV and 100 meV [7]. A comparison between the solid-type frequency spectra of  $^1\text{H}$  in  $\text{H}_2\text{O}$  for ENDF/B-VII.1 and JEFF-3.1.1 is shown in Figure 3.3. The peak of the librational band is found at around 60 meV.

Table 3.1. IKE (JEFF-3.1.1) and CAB model parameters introduced in the LEAPR module for  $^1\text{H}$  in  $\text{H}_2\text{O}$  at 294K.

LEAPR module parameter	JEFF-3.1.1 (IKE model)	CAB model
Translational weight $\omega_t$	0.021739	0.007918
Continuous spectrum weight $\omega_c$	0.489131	0.522080
Bending mode energy (meV) $E_1$	205.0	205.0
Bending mode weight $\omega_1$	0.163043	0.156667
Stretching modes energy (meV) $E_2$	436.0	415.0
Stretching mode weight $\omega_2$	0.326087	0.313335
Diffusion constant $c$	0	3.969
Free scattering cross section (b) $\sigma_b^H$	20.478	20.478

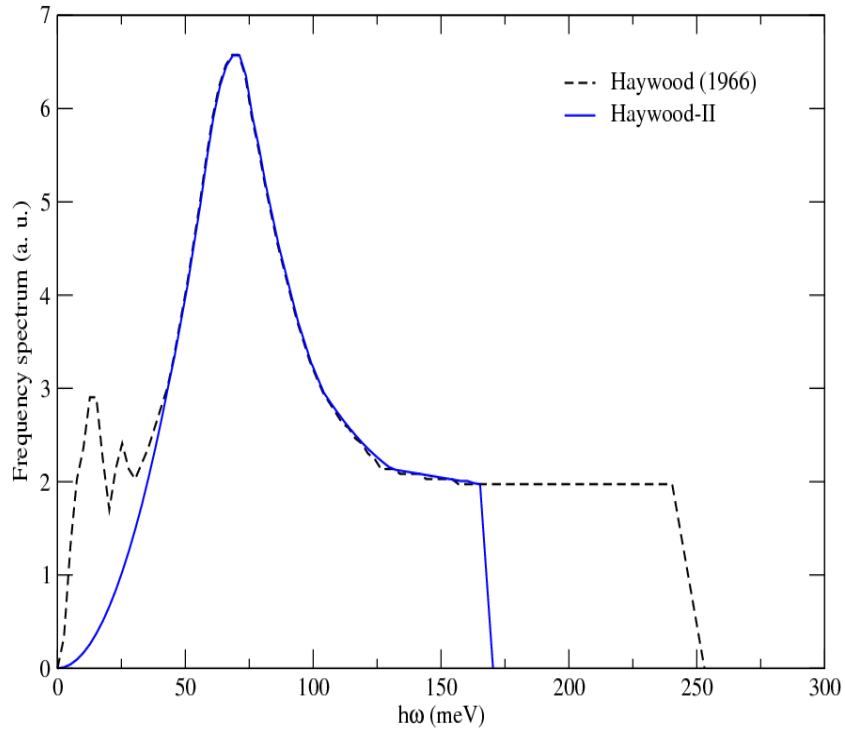


Fig. 3.1 Frequency spectra of  $^1\text{H}$  in  $\text{H}_2\text{O}$  at 294 K measured by Haywood and modified by Koppel.

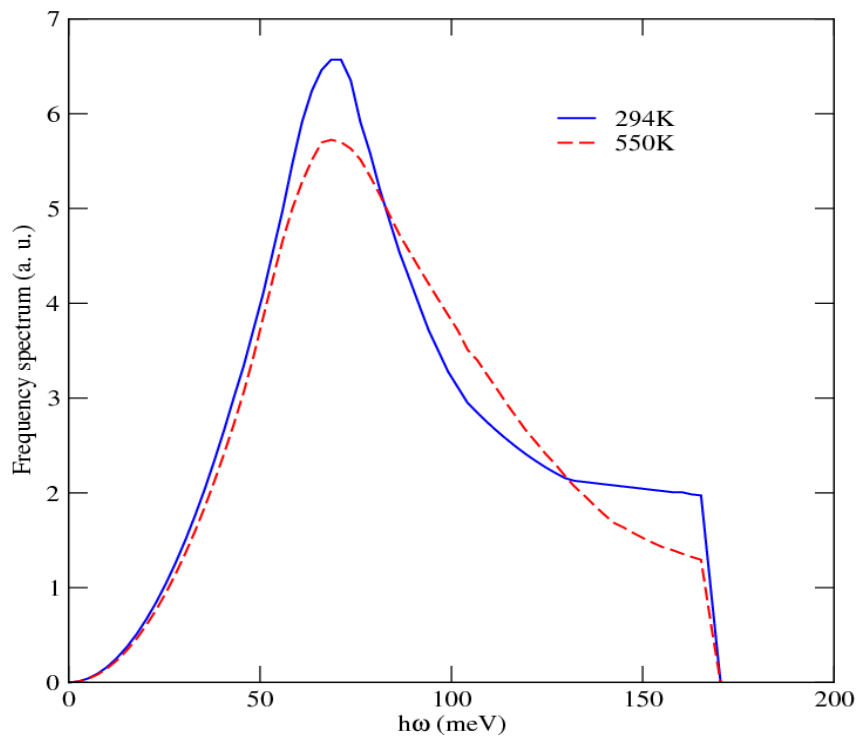


Fig. 3.2 Continuous frequency spectra of  $^1\text{H}$  in  $\text{H}_2\text{O}$  at 294 K and 550 K as a function of the vibration energy used in IKE model (ENDF/B-VII.1 and JEFF-3.1.1 nuclear data libraries).

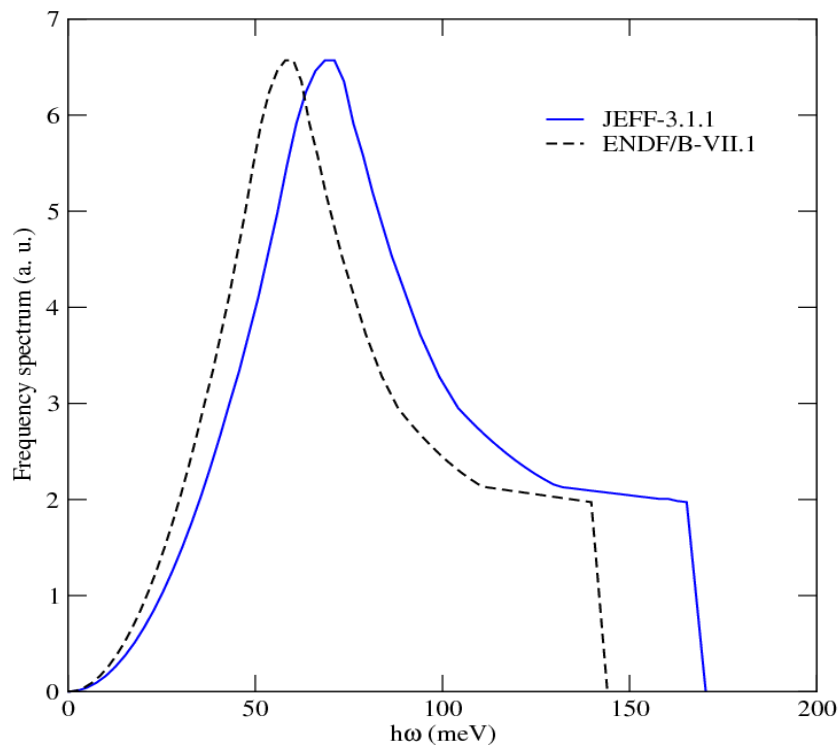


Fig. 3.3 Continuous component of the frequency spectrum of  $^1\text{H}$  in  $\text{H}_2\text{O}$  at 294 K of the nuclear data libraries ENDF/B-VII.1 and JEFF-3.1.1

## 3.2 Molecular dynamic simulations

### 3.2.1 State of the art in molecular dynamic simulations for reactor applications

It was seen that the model to generate the scattering law of light water in JEFF-3.1.1 is based on experimental measurements done in the sixties. Nowadays, there are available solid and reliable tools to calculate the frequency spectra as a function of the temperature based on the molecular dynamic simulations.

The scattering function is only a property of the scattering system, thus, it depends only on the relative positions and motion of the particles, given by the interaction forces between them. These forces are originated by the potentials present in the interactions between the molecules. We will understand how the molecular dynamic successfully computes the frequency spectrum simulating the behavior of the ensemble of the molecules in the system.

Many research groups have studied the scattering physics of light water. A Japanese group from Kyoto University obtained a frequency spectrum of  $^1\text{H}$  in  $\text{H}_2\text{O}$  using molecular dynamic simulations [18]. Then the scattering function is calculated as the Fourier transform in time of the intermediate scattering function (see section 2.3 of chapter 2). At *Institut Laue-Langevin* (ILL) in Grenoble, France, efforts were done to produce a merged experimental and calculated scattering law for light water [19]. The dynamical range of the measured scattering law was completed with molecular dynamic simulations.

Similar to the research carried out in Japan, the calculated scattering function was obtained by a Fourier transform. Finally, a group in Argentina at the Bariloche Atomic Center applied the same technique but the frequency spectrum was adapted to be processed with the LEAPR module of NJOY [5], something equivalent to what J. Keinert and M. Mattes have done in 2005.

The present work will follow the model created by Marquez Damian et al. in Argentina, named CAB model (Centro Atomico Bariloche in Spanish). In this frame, an international collaboration was started in order to receive the expertise to reproduce the calculation sequence, starting from molecular dynamic calculations to the final thermal scattering library in ENDF-6 format. We would like to thank Ignacio Marquez Damian for all the valuable support provided throughout all this work.

### 3.2.2 Introduction to molecular dynamic simulations

The need for creating such a calculation tool was especially motivated by studying areas like chemistry and biology. In general, this technique enables to compute macroscopic physical properties under a detailed knowledge on an atomic scale, modeling liquids or compounds.

Supposing a number  $n$  of non-relativistic particles, the molecular dynamic simulation codes require as input the position of each atom in the system  $\bar{r}$ , the velocities  $\bar{v}$  and the potential interaction as a function of the atoms positions  $V = V(r_1, r_2, \dots, r_n)$ .

The potential functions are divided into non-bonded and bonded. The non-bonded arise from intermolecular interactions, while the bonded give birth to intramolecular forces.

The forces exerted on a certain atom of the system are calculated as the negative derivate of the potential function with respect to the atom position:

$$\bar{F}_i = -\frac{\partial V}{\partial \bar{r}_i} (i = 1, \dots, n). \quad (1)$$

The second law of motion of Newton is simulated numerically to obtain the new positions and velocities as a function of time:

$$\frac{\bar{F}_i}{m_i} = \frac{\partial^2 \bar{r}_i}{\partial t^2}, \quad (2)$$

$$\frac{\partial \bar{r}_i}{\partial t} = \bar{v}_i. \quad (3)$$

The file containing all the positions and velocities for every time step represents the trajectory of the system. By averaging over an equilibrium trajectory, the macroscopic properties can be derived. Figure 3.4 shows an example of a simulation with the code GROMACS with 512 H<sub>2</sub>O molecules for a given simulation time.

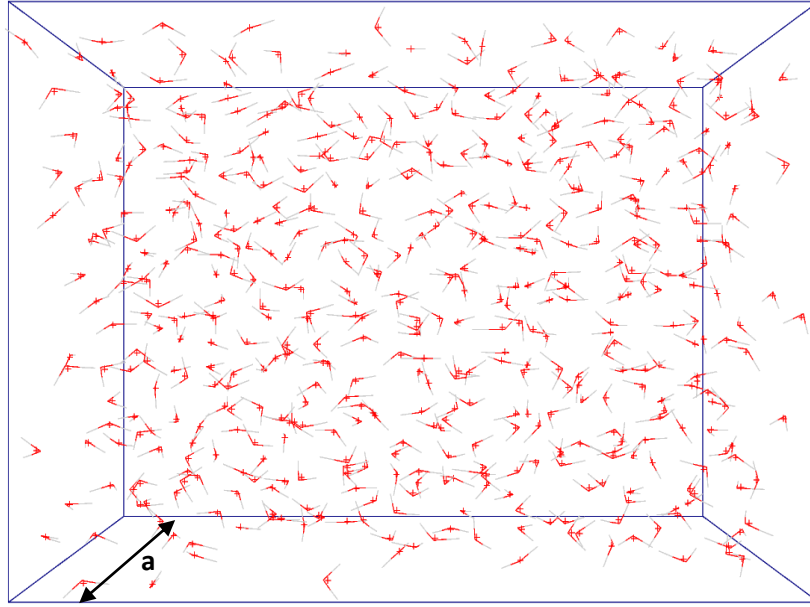


Fig. 3.4 Simulation of 512 H<sub>2</sub>O molecules with GROMACS code in a cubic box of side  $a = 2.48$  nm

In the case of study, we are interested in obtaining the frequency spectrum of the simulated material. The key to relate the frequency spectrum with the trajectory file of the system is the Velocity Autocorrelation function.

### 3.2.3 The velocity autocorrelation function (VACF)

Considering the motion of atoms in a liquid where each particle has a defined position and velocity at a certain time, we define the velocity autocorrelation function as [6]:

$$VACF(t) = \langle \bar{v}(t_0) \cdot \bar{v}(t_0 + t) \rangle, \quad (4)$$

where the brackets indicate the scalar product of the velocity  $\bar{v}(t_0)$  of an atom at a time  $t_0$  with the velocity  $\bar{v}(t_0 + t)$  of the same atom at a time  $t_0 + t$ .

It can be demonstrated [6] that the Fourier transform of the velocity autocorrelation function is the frequency spectrum of the material:

$$\rho(\omega) = \frac{M\beta}{3\pi} \int_{-\infty}^{\infty} \langle \bar{v}(t_0) \cdot \bar{v}(t_0 + t) \rangle e^{-i\omega t} dt, \quad (5)$$

where  $M$  is the scattering target mass.

### 3.3 The CAB model

The CAB model [5] was obtained using the molecular dynamic simulation code GROMACS (Groningen Machine for Chemical Simulations) [20]. The water potential implemented in the code was the TIP4P/2005f [21].

#### 3.3.1 The water potential of the CAB model

The TIP4P/2005f is a flexible water potential that models the water molecule with internal vibration modes and intermolecular interactions. It has four positions corresponding to the two hydrogen atoms, one oxygen and one so-called M-site. The M-site corresponds to the dummy atom, which has no mass and takes the negative charge of the oxygen to balance electrically the molecule. It is located over the angle bisector formed by the two hydrogens and the oxygen.

The intermolecular interactions are represented by a Lennard-Jones potential  $V_{LJ}$  between the oxygens, and the Coulomb potential  $V_C$  :

$$V_{LJ}(r_{ij}) = 4\epsilon_0 \left[ \left( \frac{\sigma_0}{|r_i - r_j|} \right)^{12} - \left( \frac{\sigma_0}{|r_i - r_j|} \right)^6 \right], \quad (6)$$

$$V_C(r_{ij}) = k \frac{q_i q_j}{r_{ij}}, \quad (7)$$

where  $\epsilon_0$  is the depth of the potential well,  $\sigma_0$  the distance where the potential is zero,  $k$  is the Coulomb's constant,  $q_i$  is the electrical charge of the particle and  $r_{ij}$  is the distance between two atoms.

The intramolecular interactions are characterized by a Morse potential  $V_M$  to account the stretching of the hydrogen-oxygen bond and a harmonic angle potential  $V_{HOH}$  for the bending mode:

$$V_M(r_{ij}) = D_{OH} \left[ 1 - e^{-\beta_{OH}(r_{ij} - d_{OH})} \right], \quad (8)$$

$$V_{HOH}(\theta_{ij}) = \frac{1}{2} k_\theta (\theta_{ij} - \theta_0)^2, \quad (9)$$

where  $D_{OH}$  is the depth of the potential well,  $\beta_{OH}$  is the steepness of the well,  $d_{OH}$  is the equilibrium distance between the oxygen and the hydrogen,  $k_\theta$  strength constant and  $\theta_0$  is the equilibrium angle between the hydrogens and the oxygen.

Table 3.2 lists the TIP4P/2005f water potential parameters and their nominal values for CAB model.

The water potential allows calculating the forces exerted over the atoms and thus its positions and velocities. All the information is saved in the trajectory file used by the code GROMACS to calculate the VACF as a function of time. Figure 3.5 shows the VACF for hydrogen and oxygen in light water, H(H<sub>2</sub>O) and O(OH<sub>2</sub>O) respectively, at 293.6 K. It points out the high correlation between the hydrogen atoms at

the first stages of the simulation. After the system has reached a stationary state, given by the thermodynamic conditions, the fluctuations decay on time and the information of previous time steps of the atoms is lost. Instead, the oxygen atoms are weakly correlated, probably due to the fact that the internal modes are driven by the H atoms and in this case the relaxation time is longer than the relaxation time of the oxygens to reach the equilibrium.

### 3.3.2 The frequency spectrum of the CAB model

The Fourier transform in time of the VACF gives the generalized frequency spectrum for each isotope. The frequency spectrum of H<sub>2</sub>O is obtained doing an average between the spectra of H(H<sub>2</sub>O) and O(H<sub>2</sub>O) weighted by the bound scattering cross sections of each isotope:

$$\rho_{H_2O} = \frac{2\sigma_H\rho_{H(H_2O)} + \sigma_O\rho_{O(H_2O)}}{2\sigma_H + \sigma_O}. \quad (10)$$

For the particular case of light water, the bound scattering cross section of <sup>16</sup>O is negligible compared with the <sup>1</sup>H, so the shape of the spectrum of H<sub>2</sub>O is fairly well represented by the spectrum of H(H<sub>2</sub>O). Figure 3.6 shows the generalized frequency spectra of H(H<sub>2</sub>O) and O(H<sub>2</sub>O) and H<sub>2</sub>O at 294 K.

I. Marquez Damian et al. have done an extensive work in validating the spectrum with available experimental data [22].

The calculated translational motion peak is found at around 6 meV for H(H<sub>2</sub>O) and O(H<sub>2</sub>O). The librational band caused by the molecular rotations is centered at approximately 60 meV. Finally, the two sharp structures at around 205 meV and 415 meV describe the internal vibration modes of the water molecule (bending and stretching respectively).

There is a very strong contribution of the O(H<sub>2</sub>O) spectrum for low energy transfer, where the diffusive processes are very important. This might be related due to the fact that the <sup>16</sup>O mass is much more significant than <sup>1</sup>H and the major role it carries out in the effective mass of the molecular clusters. The number of occupied states in the probability density of O(H<sub>2</sub>O) is insignificant with respect to H(H<sub>2</sub>O) in the intramolecular interactions. The internal modes are driven by the hydrogen atoms.

This frequency spectrum contains all the vibration modes present in the water molecule. In the next section we will see how the generalized frequency spectrum was implemented in the LEAPR module, decomposing it in a continuous frequency spectrum, two discrete oscillators for the intramolecular modes and a translational component (eq. 48 of chapter 2):

$$\rho(\beta) = \sum_{i=1}^J \omega_i \delta(\beta_i) + \omega_t \rho_t(\beta) + \omega_c \rho_c(\beta).$$

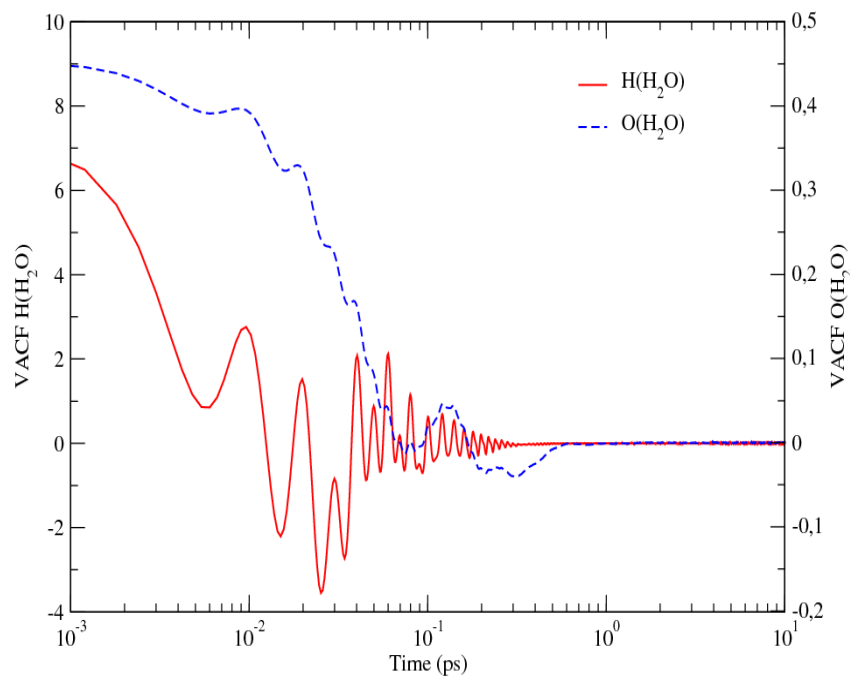


Fig. 3.5 VACF of H(H<sub>2</sub>O) (continuous red line) and O(H<sub>2</sub>O) (dash blue line) at 294 K generated with the molecular dynamic simulations code GROMACS and the water potential TIP4P/2005f.

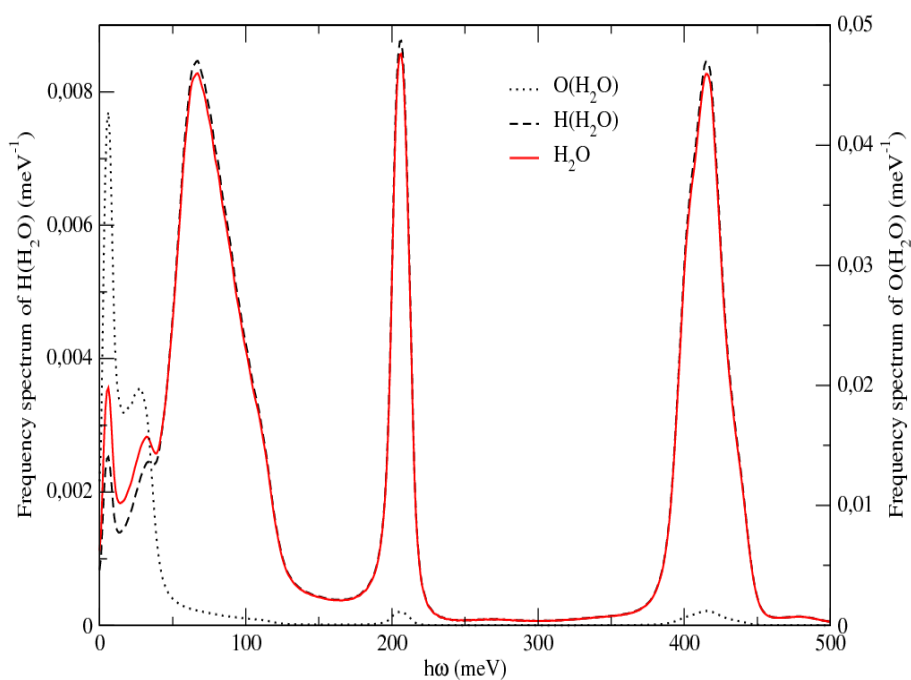
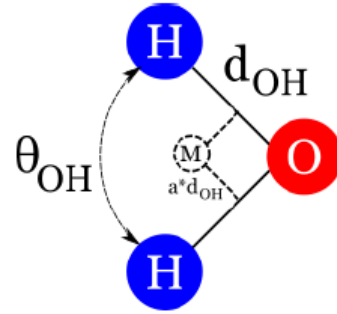


Fig. 3.6 Generalized frequency spectrum of H(H<sub>2</sub>O) (left scale), O(H<sub>2</sub>O) (right scale) and H<sub>2</sub>O (left scale) at 294 K

Table 3.2. Parameters of the TIP4P/2005f water potential.

TIP4P/2005f potential parameter	
$\epsilon_0$ (KJ/mol)	0.7749
$\sigma_O$ (nm)	3.1644
$q_H$ (e <sup>-</sup> )	0.5564
$q_M$ (e <sup>-</sup> )	-1.1128
$D_{OH}$ (KJ/mol)	432.581
$\beta_{OH}$ (1/nm)	22.87
$d_{OH}$ (nm)	0.09419
$k_\theta$ (KJ/mol/rad <sup>2</sup> )	367.81
$\theta_{OH}$ (°)	107.4
$d_{OM}$ (nm)	0.15555



### 3.3.3 Implementation in the LEAPR module

As discussed before, the CAB model is intended to follow the working line of the IKE model in order to process the frequency spectrum with LEAPR. Therefore, the solid-type spectrum, the translational mode and the discrete oscillators were detached from the generalized frequency spectrum calculated with GROMACS.

In the CAB model the translational mode is modeled with the Egelstaff-Schofield diffusion model (see section 2.5.2 of chapter 2).

Considering a cut-off energy transfer of 158 meV in the generalized frequency spectrum [5], the translational spectrum  $\rho_t$  was subtracted to obtain the continuous spectrum  $\rho_c$ . Figure 3.7 shows the low energy detail of the generalized, the continuous and the diffusive spectrum. The subtraction is done such that  $\rho_c(0) = 0$

The dimensionless diffusion coefficient  $c$  in Egelstaff-Schofield model (eq. 60 of chapter 2) is obtained as:

$$c = \frac{M_H D}{\omega_t \hbar}, \quad (11)$$

where  $M_H$  is the hydrogen mass,  $D$  is the molecular diffusion coefficient,  $\omega_t$  is the translational weight and  $\hbar$  is the reduced Plank constant. The translational weight is calculated as:

$$\omega_t = \frac{M_H}{M_{diff}}, \quad (12)$$

where  $M_{diff}$  is the diffusion mass.

In CAB model the parameters  $M_{diff}$  and  $D$  were obtained from experimental data [5]. Table 3.3 lists the value of the parameters at 294 K.

Table 3.3. Water diffusion mass  $M_{diff}$  and molecular diffusion coefficient  $D$  used in the CAB model at 294 K.

Parameter	
$M_{diff}$ [a.m.u.]	126.2
$D$ [nm <sup>2</sup> ps <sup>-1</sup> ]	0.002025

The weights of the internal modes of the molecule are obtained integrating the generalized frequency spectrum over the cut-off energy. A discrete oscillator at 205 meV represents the bending mode and an oscillator at 415 meV models the symmetric and asymmetric stretching.

Table 3.1 resumes the LEAPR module parameters of CAB model at 294 K and the weights corresponding to each vibration mode. It is also shown the parameters of the IKE model.

The continuous spectra of <sup>1</sup>H in H<sub>2</sub>O of CAB model and JEFF-3.1.1 nuclear data library are shown in Figure 3.8. Both models present equivalent internal vibration modes. The stretching mode of JEFF-3.1.1 slightly higher. The librational band in both cases is found at 0.06 eV. The translational mode is not seen in the plot.

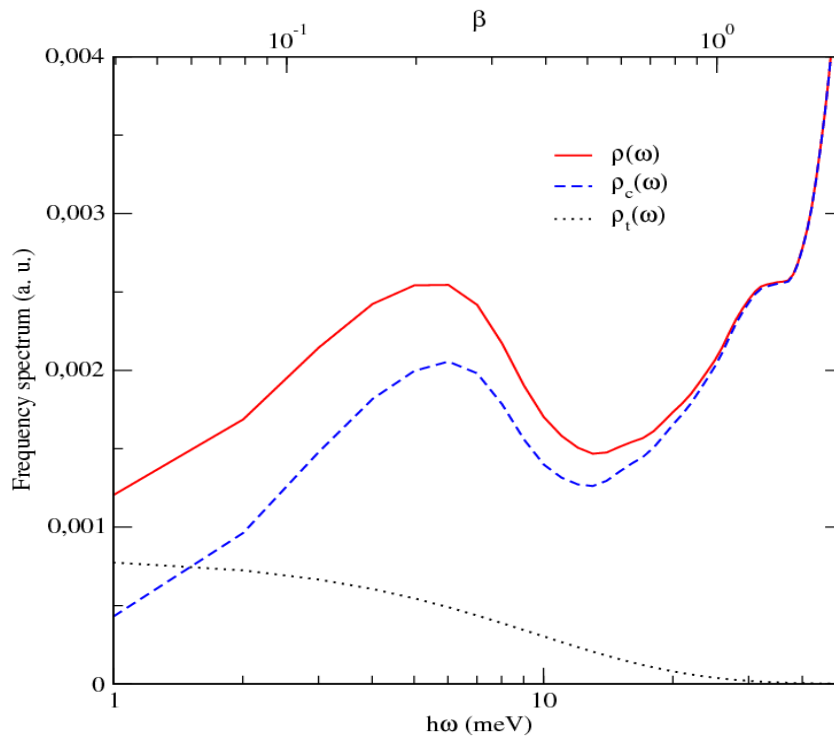


Fig. 3.7 Low energy detail of the generalized frequency (continuous line), continuous (dash line) and translational spectrum (dotted line) from Egelstaff-Schofield model of <sup>1</sup>H H<sub>2</sub>O at 294 K.

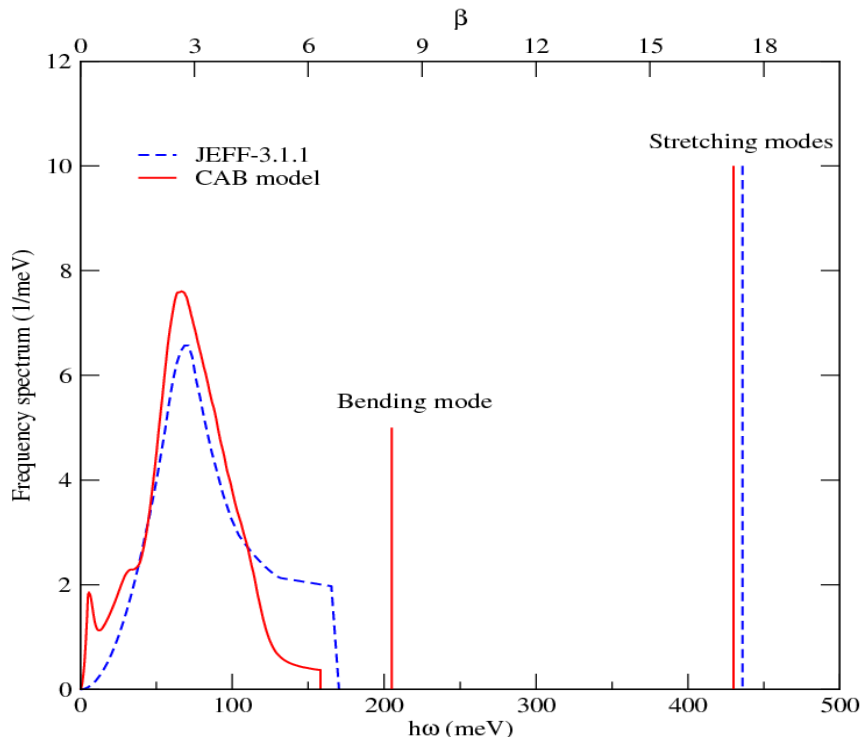


Fig. 3.8 CAB model (continuous red line) and JEFF-3.1.1 (dash blue line) continuous frequency spectra and intramolecular vibration modes of  $^1\text{H H}_2\text{O}$  at 294 K as a function of the excitation energy (lower scale) and dimensionless energy transfer (upper scale).

### 3.4 Comparison between JEFF-3.1.1 and CAB model

#### 3.4.1 The scattering function $S(\alpha, \beta)$

The LEARP module processes the frequency spectrum and convolutes the scattering function of each vibration mode. The output is the  $S(\alpha, \beta)$  matrix that extends to an energy transfer  $\beta$  and a momentum transfer  $\alpha$  given by the user.

Figure 3.9 shows the  $S(\alpha, \beta)$  curves for different  $\beta$  values as a function of  $\alpha$  for the CAB model and JEFF-3.1.1 library, at 294 K. The parametrization was done for energy transfers lower than approximately 126 meV ( $\beta < 5.0$ ), corresponding to a representative cut-off energy for the continuous frequency spectra shown in Fig. 3.8.

The impact of the different shapes of the frequency spectra of CAB model and JEFF-3.1.1 is clearly seen for  $\beta = 0.5$  (approximately 13 meV). The use of a diffusion model in the case of CAB model instead of a free gas model is mainly responsible for such different shapes in the  $S(\alpha, \beta)$  function for  $\beta < 0.05$  (energy transfer corresponding to 1.3 meV).

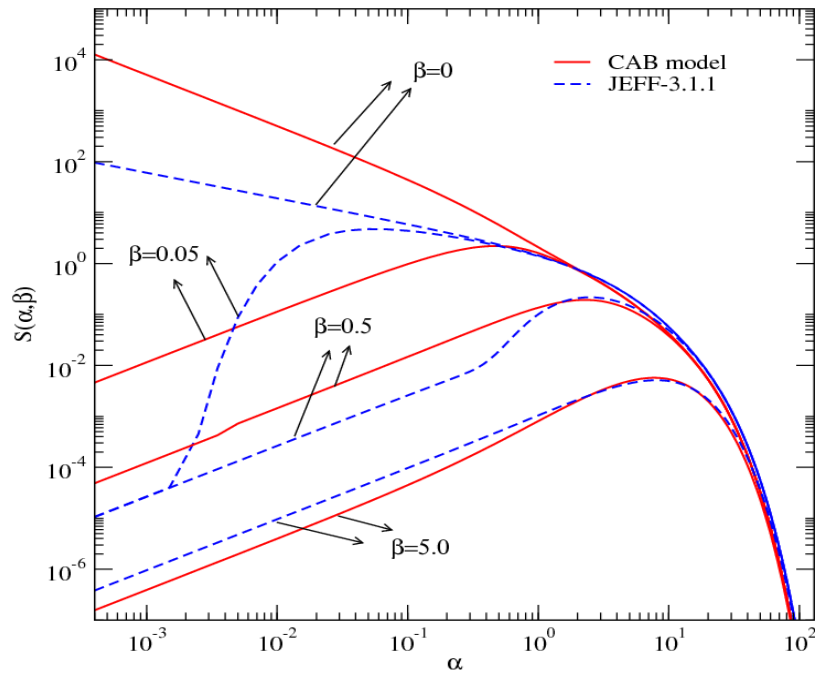


Fig. 3.9  $S(\alpha,\beta)$  as a function of the momentum transfer for CAB model and JEFF-3.1.1 nuclear data library at 294 K.

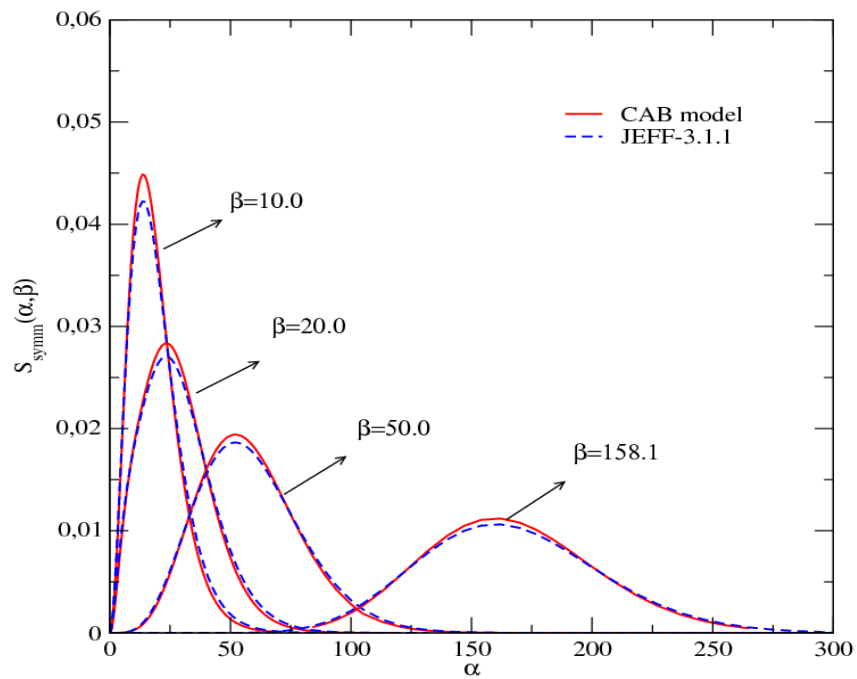


Fig. 3.10 Symmetric  $S(\alpha,\beta)$  as a function of the momentum transfer for CAB model and JEFF-3.1.1 nuclear data library at 294 K.

For higher energy transfers, it is more convenient to visualize the scattering function  $S(\alpha, \beta)$  in the so-called symmetric counterpart:

$$S_{sym}(\alpha, \beta) = S(\alpha, \beta)e^{\beta/2}. \quad (13)$$

The comparison of the symmetric scattering function between CAB model and JEFF-3.1.1 is presented in Figure 3.10 at 294 K. The differences found for higher energy transfers are not significant (<5%) as compared to the low  $\beta$  values. At this energy range, the impact of the neutron scattering with  $^1\text{H}$  bound to the water molecule becomes less significant due to the increase of the thermal agitation of the atoms.

### 3.4.2 The double differential cross section

The double differential cross section is calculated with the scattering function  $S(\alpha, \beta)$ . In order to compare the validity of the two models at low and high energy transfers, we chose two sets of experimental measurements of light water double differential cross sections.

The comparison aims at giving a qualitative point of view as we do not have access to detailed information about the experimental conditions. A quantitative comparison will be carried out with the experimental measures done in the frame of this thesis and will be presented in the next chapter.

The first set was taken from measurements done by Novikov et al. for an incident neutron energy of  $E = 8$  meV (cold neutron energy), a scattering angle  $\theta = 37^\circ$  and  $T = 294$  K [23]. Figure 3.11 compares these data and the calculated double differential cross section as a function of the transfer energy  $\hbar\omega$  with the CAB model and JEFF-3.1.1. The calculated cross sections were normalized and broadened with an energy resolution of 7%. There is a clear difference in the width of the quasi-elastic peak of both models. The replacement of the free gas model by a diffusion model in CAB, allows to better describe the very low energy exchanges physics, reflected directly in the quasi-elastic peak of the double differential cross section. Such a cold incident neutron energy exposes the weakness of the thermal scattering of JEFF-3.1.1.

The second data comes from a series of experiments done by Bischoff et al. at the Rensselaer Polytechnic Institute for an incident energy of  $E = 231$  meV, a scattering angle  $\theta = 25^\circ$  and  $T = 294$  K [24]. In Figure 3.12, displays a comparison of the double differential cross section measured by Bischoff and the theoretical calculation obtained with CAB model and JEFF-3.1.1. As the incident energy of the neutrons is much bigger than the average energy of the water sample (approximately 25 meV), the thermalization will occur especially in the down-scattering regime. This is why there is more information in the negative energy transfers. The calculated cross sections were normalized to the same constant and broadened with an energy resolution of 5%. In overall, the trends of both models are similar; no important discrepancies are seen between CAB model and JEFF-3.1.1. The elastic peak is fairly well reproduced by both models. The structure at  $\hbar\omega = 60$  meV, where the librational band of the continuous frequency spectrum is found, is captured by JEFF-3.1.1 and CAB model. The feature close to 200 meV accounts the bending mode of the water molecule, not seen by the experimental data due to technological limitations.

For comparison, it was calculated the double differential cross section with the Free Gas Model for  $^1\text{H}$  and  $^{16}\text{O}$ . The distribution presents no elastic peak due to absence of a structure factor describing the

chemical bonds of the water molecule. This results in a more equiprobable emission in energy of the scattered neutron.

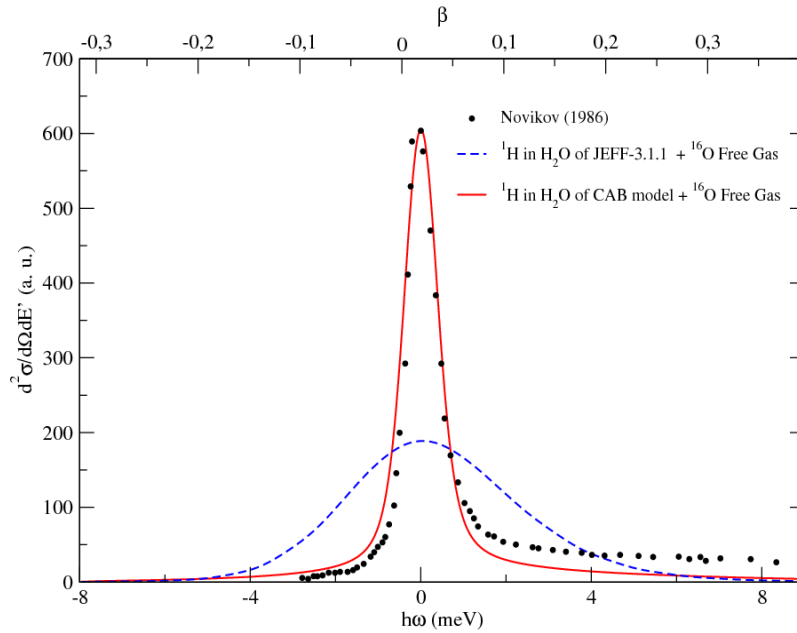


Fig. 3.11 Double differential inelastic scattering cross section for light water calculated with CAB model and JEFF-3.1.1 compared with data measured by Novikov (1986), for  $E_0 = 8$  meV,  $\theta = 37^\circ$  and  $T = 294$  K. The energy resolution is 7%

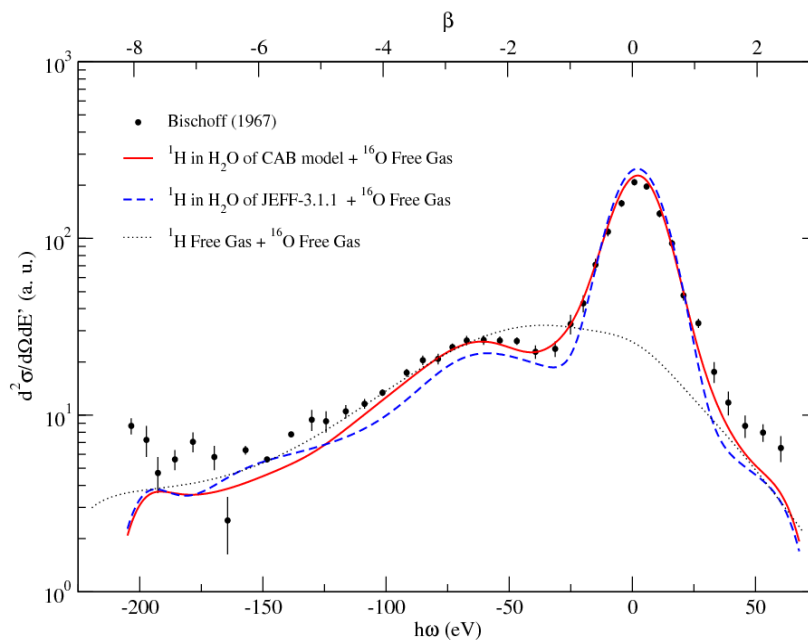


Fig. 3.12 Double differential inelastic scattering cross section for light water calculated with CAB model and JEFF-3.1.1 compared with data measured by Bischoff (1967), for  $E_0 = 231$  meV,  $\theta = 25^\circ$  and  $T = 294$  K. The energy resolution is 5%

### 3.4.3 The $^1\text{H}$ in $\text{H}_2\text{O}$ scattering cross section

The scattering cross section of  $^1\text{H}$  in  $\text{H}_2\text{O}$  is obtained integrating the double differential scattering cross section over the secondary energy  $E'$  and the scattering angle  $\theta$ :

$$\sigma_n(E) = \int_0^{2\pi} d\varphi \int_0^\pi \sin\theta d\theta \int_0^\infty \frac{\sigma_b}{4\pi kT} \sqrt{\frac{E'}{E}} e^{-\frac{\beta}{2}} S_s(\alpha, \beta) dE'. \quad (14)$$

A comparison between the scattering cross sections of  $^1\text{H}$  in  $\text{H}_2\text{O}$  at 294 K calculated with CAB model and JEFF-3.1.1 is shown in Figure 3.13 (upper plot). The ratio between JEFF-3.1.1 and CAB model is shown on the bottom plot. Above approximately 7 meV, the scattering cross section calculated with JEFF-3.1.1 overestimates the CAB model results, reaching a maximum ratio of 1.05 (5% difference) at the thermal neutron energy (25.3 meV). The discrepancy vanishes as both models tend to the free gas approximation. Between 0.3 meV and 7 meV (cold neutron range), the trend is inverted, and the cross section of the CAB model is bigger than JEFF-3.1.1. A maximum ratio of 0.94 is found at 1.5 meV. Finally, below 0.3 meV the differences are very significant and attain a ratio of 1.62 at  $10^{-5}$  eV. The use of a free gas model to account the molecular translations in JEFF-3.1.1 and a diffusion model in CAB may explain the origin of such disagreement.

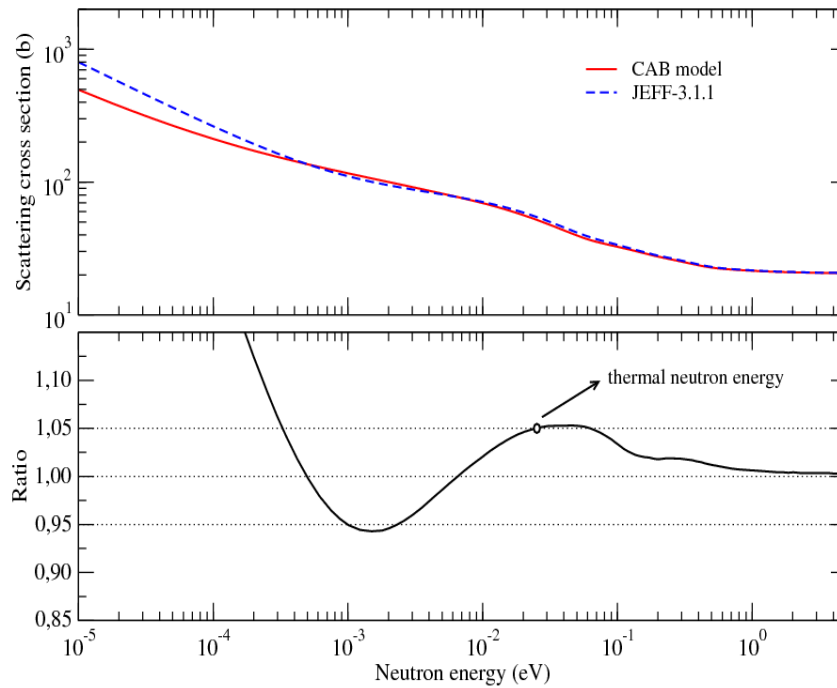


Fig. 3.13  $^1\text{H}$  in  $\text{H}_2\text{O}$  scattering cross section calculated with CAB model and JEFF-3.1.1 at 294 K (upper plot). The ratio between JEFF-3.1.1 and CAB model is in the bottom plot.

### 3.4.4 The H<sub>2</sub>O total cross section

Following the notation described in the beginning of chapter 2, the total cross section of H<sub>2</sub>O is calculated as:

$$\sigma_t^{H_2O} = 2\sigma_t^H + \sigma_t^O, \quad (15)$$

where the scattering cross section of <sup>16</sup>O is calculated in the free gas approximation.

A comparison between the total cross section at 294 K calculated with CAB model and JEFF-3.1.1, together with experimental data [25, 26, 27, 28] is shown in Figure 3.14. The cross section calculated with the Free Gas Model is also included in the plot. The CAB model shows a good agreement with the experimental data all over the energy range, while JEFF-3.1.1 fails to reproduce the data at the cold range.

Regarding the H<sub>2</sub>O total cross section calculated with the Free Gas Model, the shape demonstrates the incorrect description of this model for light water. For an energy of approximately 1 eV, where the chemical binding of hydrogen and oxygen becomes negligible due to the important thermal agitation of the nuclei, the free gas cross section converges to the cross section of H<sub>2</sub>O.

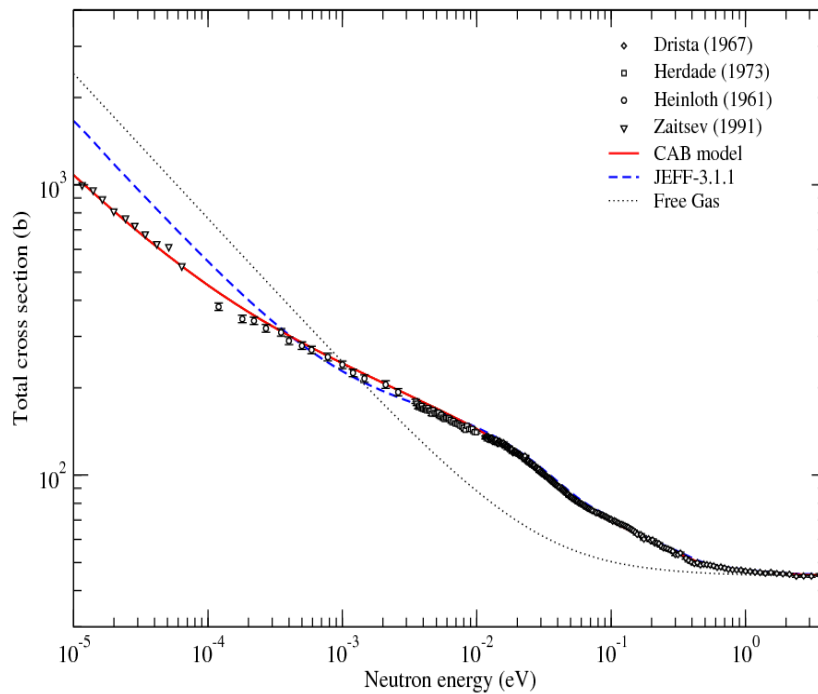


Fig. 3.14 Total H<sub>2</sub>O cross section calculated with CAB model and JEFF-3.1.1 at 294 K.

### 3.5 Impact of the $^{16}\text{O}$ in $\text{H}_2\text{O}$ thermal scattering law in the microscopic data

In the previous sections, the  $S(\alpha, \beta)$  of  $^1\text{H}$  in  $\text{H}_2\text{O}$  and the approximation of  $^{16}\text{O}$  as a free gas was used to calculate the microscopic cross sections with the CAB model. In this section, the impact on using the  $S(\alpha, \beta)$  of  $^1\text{H}$  in  $\text{H}_2\text{O}$  and of  $^{16}\text{O}$  in  $\text{H}_2\text{O}$  will be studied.

In the case of having a structure factor for the secondary scatterer, the double differential scattering cross section is computed as follows for light water:

$$\frac{d^2\sigma}{d\Omega dE'} = \frac{\sigma_b^H}{4\pi k_B T} \sqrt{\frac{E'}{E}} e^{-\frac{\beta}{2}} \left[ S_H(\alpha_H, \beta) + \frac{\sigma_b^O}{\sigma_b^H} S_O(\alpha_O, \beta) \right], \quad (16)$$

where  $\sigma_b^H$  is the bound scattering cross section of  $^1\text{H}$ ,  $\sigma_b^O$  is the bound scattering cross section of  $^{16}\text{O}$ ,  $S_H$  is the scattering function of  $^1\text{H}$  in  $\text{H}_2\text{O}$  and  $S_O$  is the scattering function of  $^{16}\text{O}$  in  $\text{H}_2\text{O}$ .

#### 3.5.1 The double differential cross section

Figure 3.15 shows the double differential cross section for an incident energy of 231 meV and a scattering angle of  $25^\circ$ , calculated with  $^1\text{H}$  in  $\text{H}_2\text{O}$  of CAB model and  $^{16}\text{O}$  in the free gas approximation compared with  $^1\text{H}$  in  $\text{H}_2\text{O}$  and  $^{16}\text{O}$  in  $\text{H}_2\text{O}$  of CAB model. Slight differences are seen at the energy transfers where it is found the quasi-elastic peak of the distribution. In this energy range, the contribution of the frequency spectrum of  $\text{O}(\text{H}_2\text{O})$  to the total  $\text{H}_2\text{O}$  spectrum is the highest, attenuating above 40 meV approximately. This is reflected in the double differential cross section of  $^{16}\text{O}$  in  $\text{H}_2\text{O}$ , where the distribution decays rapidly for this excitation energy. Nevertheless, the ratio between both cross section remains lower than 1.05

#### 3.5.2 The scattering cross section of $^{16}\text{O}$ in $\text{H}_2\text{O}$

Figure 3.16 shows a comparison between the scattering cross section calculated with CAB model,  $^{16}\text{O}$  in  $\text{H}_2\text{O}$ , and the  $^{16}\text{O}$  in the free gas approximation of JEFF-3.1.1 nuclear data library. Important discrepancies are detected at energies below 10 meV. Above this energy the  $^{16}\text{O}$  bound to the light water tends to the free gas approximation. The ratio found at the thermal neutron energy is below 1.015 (1.5% difference).

Taking into account this results and the fact that the thermalization of neutrons is mostly carried out by the  $^1\text{H}$  isotope (due to its much bigger scattering cross section), no major impact is expected in a neutron transport calculation. This will be confirmed in the next chapters.

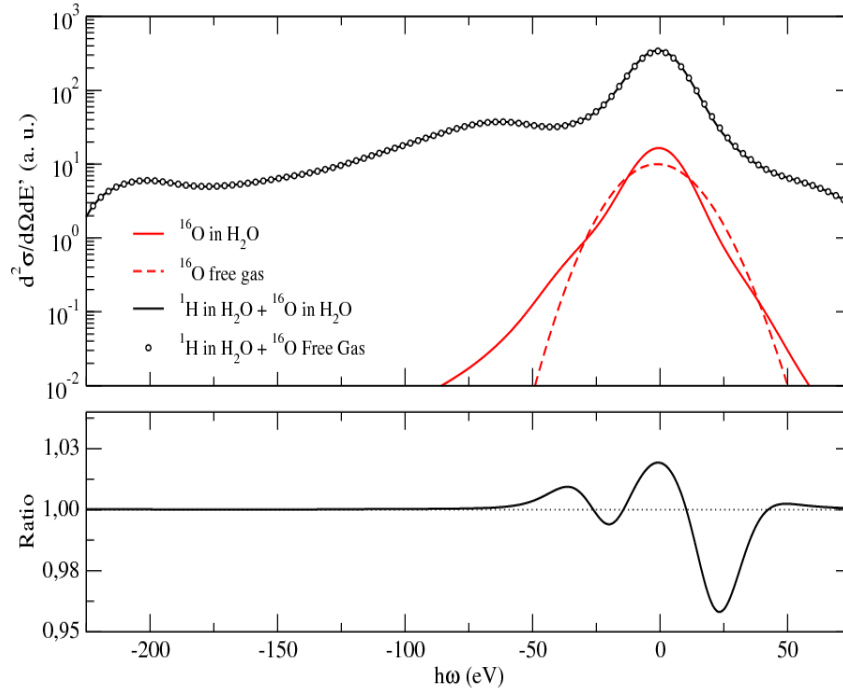


Fig. 3.15 Double differential scattering cross section calculated with  $^1\text{H}$  in  $\text{H}_2\text{O}$  of CAB model and  $^{16}\text{O}$  in the free gas approximation compared with  $^1\text{H}$  in  $\text{H}_2\text{O}$  and  $^{16}\text{O}$  in  $\text{H}_2\text{O}$  of CAB model, for  $E_0 = 231$  meV,  $\theta = 25^\circ$  and  $T = 294$  K.

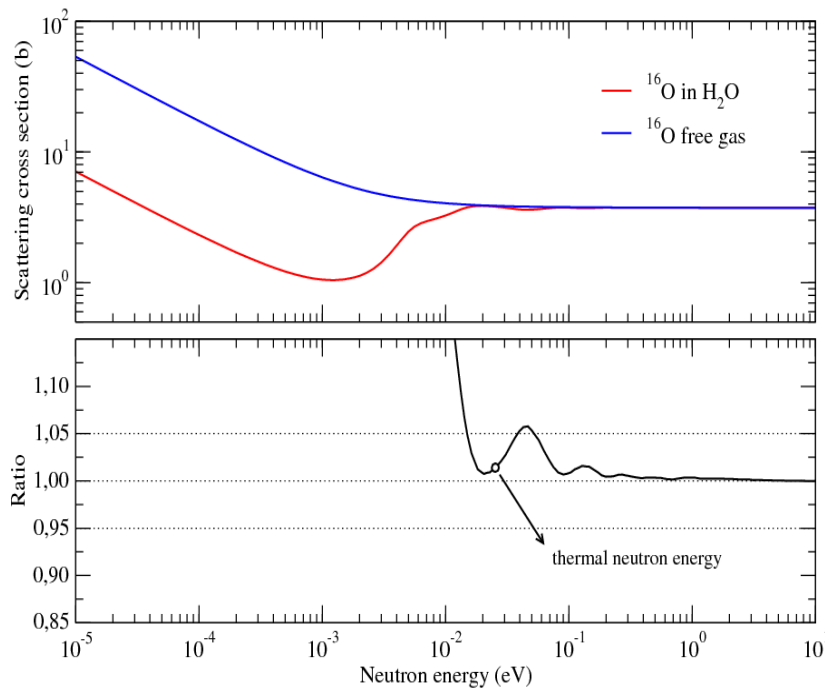


Fig. 3.16 Scattering cross sections of  $^{16}\text{O}$  in  $\text{H}_2\text{O}$  calculated with CAB model and  $^{16}\text{O}$  calculated in the free gas approximation of JEFF-3.1.1 at 294 K (upper plot). The ratio between JEFF-3.1.1 and CAB model is in the bottom plot.

### *3.6 Preliminary conclusions*

This chapter was dedicated to present the models CAB and JEFF-3.1.1 that provide a thermal scattering function for H<sub>2</sub>O. Both models were compared from a microscopic point of view: the frequency spectrum, the scattering kernel, the double differential cross section and the integrated cross section.

Firstly, the results illustrate the differences of the models at low energy transfers, where the CAB model incorporated a diffusion model to describe the low energy dynamics of scattering. Secondly, it was shown the feasibility to produce a frequency spectrum of light water by means of molecular dynamic simulations and obtain reliable microscopic calculations, validated with experimental data.

As regards the impact of the <sup>16</sup>O isotope on the light water thermal scattering, it was seen that the free gas approximation works good in terms of the calculation of the microscopic data. The negligible contribution of O(H<sub>2</sub>O) should be confirmed in an integral benchmark calculation as well.

The following chapter describes the measurements of the distribution in energy and angle of light water performed at the Institut Laue-Langevin (ILL). The experiment was carried out for cold incident neutron energies, where the impact of the thermal scattering is very important and where the CAB model and JEFF-3.1.1 reveal discrepancies.

# Chapter 4

## Light water double differential cross section measurements at 300 K and 350 K

A collaboration started in 2014 in the framework of the NAUSICAA project [29], aimed at improving the accuracy of the neutron cross section libraries for reactor physics applications. In this frame, and pointing to extend the available data needed to validate the thermal scattering models, experimental measures of the double differential cross section were done at the Insitut Laue-Langevin (ILL) at Grenoble, France.

The intensity of the scattered neutrons measured by the detectors is proportional to the double differential cross section. Two time-of-flight (ToF) spectrometers were used, namely IN4c and IN6. The neutrons in the experiments are produced by an open pool-type reactor of 58.3 MW and moderated and cooled by heavy water. As heavy water has a very low neutron absorption cross section, compared to the scattering cross section, a higher neutron flux than regular light water reactors of this type can be achieved ( $10^{15}$  n.cm<sup>-2</sup>.s<sup>-1</sup>) [30].

### 4.1 ToF Spectrometers

The neutrons produced in the reactor are conducted through guide tubes for the different scientific applications. For our experiment, we have used the spectrometers IN4c and IN6.

The neutron time-of-flight technique consists of measuring the time traveled by the neutrons  $t_n$  within a know flight path distance  $L_n$ , from their generation till their detection. Afterwards, the time is converted to energy using the following relation for non-relativistic neutrons:

$$E_n = \frac{1}{2} m_n \left( \frac{L_n}{t_n} \right)^2 = \left( 72.298 \frac{L_n}{T_n} \right)^2, \quad (1)$$

where the flight distance is measured in m, the flight time in  $\mu$ s and the neutron energy in eV.

#### 4.1.1 IN4c Spectrometer

The IN4c is a ToF (Figure 4.1) spectrometer used for the study of excitation in condensed matter [31]. The neutrons coming from the reactor go through two background choppers that partially monochromatise the beam, eliminating fast neutrons and gamma rays. The crystal monochromator selects the energy from the neutron spectrum for carrying out the experiment. Afterwards, a fermi chopper sends the pulse to the water sample. A fission chamber monitor is placed between the fermi chopper and the sample to normalize the measured signal to the total number of counts. Then a radial collimator is used to reduce the undesired scattering from the sample environment (cryostat and other

materials). A layer of gadolinium in the walls absorbs the spurious neutrons. The neutrons travel 2 m (flight distance) in a vacuum box to avoid parasitic scattering, where they are detected by a bank of  $^3\text{He}$  detectors.

In the present work, the selected neutron wavelength was 2.4 Å, corresponding to an incident energy of 14 meV. At this regime, the spectrometer is able to measure energy transfers of approximately 170 meV. The detectors cover scattering angles ranging from  $14^\circ$  to  $120^\circ$ .

#### 4.1.2 IN6 Spectrometer

The IN6 instrument (Figure 4.2) is a time focusing time-of-flight spectrometer designed for quasielastic and inelastic scattering [31]. The beam in the guide tube is extracted by an assembly of three monochromators and then focused to the sample. In order to avoid the second order reflections due to the multiple monochromators a Beryllium filter is placed before the fermi chopper. A helium-filled box is used between the  $^3\text{He}$  detectors and the sample is used to minimize the background. For this spectrometer the flight distance is 2.48 m. The gain in this instrument is that the intensity of the signal is increased by a factor of three (number of monochromators).

For this experiment a neutron wavelength of 5.1 Å (3 meV) was selected. Under this conditions, the capabilities of this instrument permit to measure energy transfers of 200 meV. The detectors cover scattering angles of  $10^\circ$  to  $115^\circ$ .

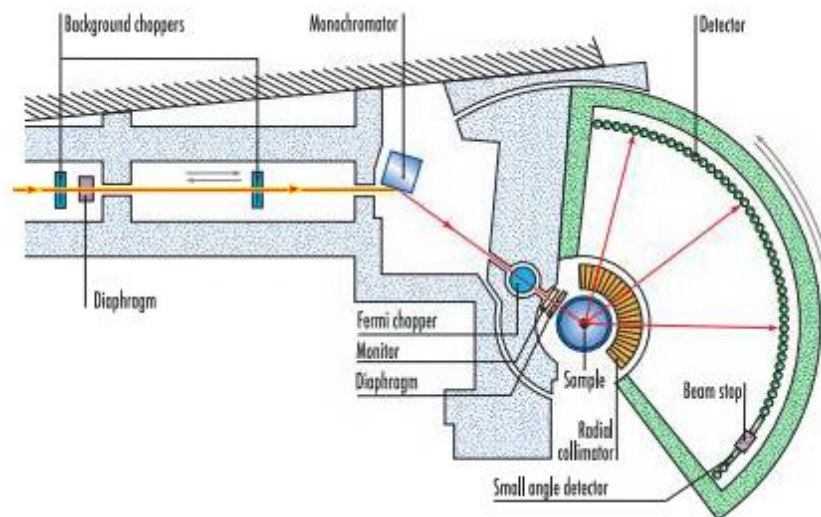


Fig. 4.1 The IN4c time-of-flight spectrometer.

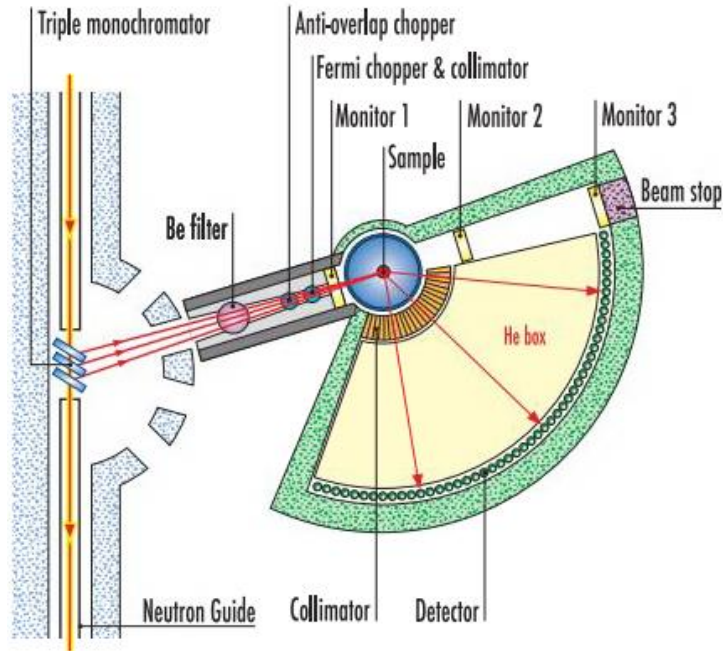


Fig. 4.2 The IN6 time-of-flight spectrometer.

#### 4.2 Experimental set-up conditions

The sample used in both spectrometers was light water and the sample holder was made of a copper-beryllium alloy. A pressure cell was designed specifically for the experience to emulate and withstand a nuclear reactor pressure vessel operation condition. The temperature of the water was controlled using a cryofurnace. The geometry and the dimensions of the sample holder are shown in Figure 4.3.

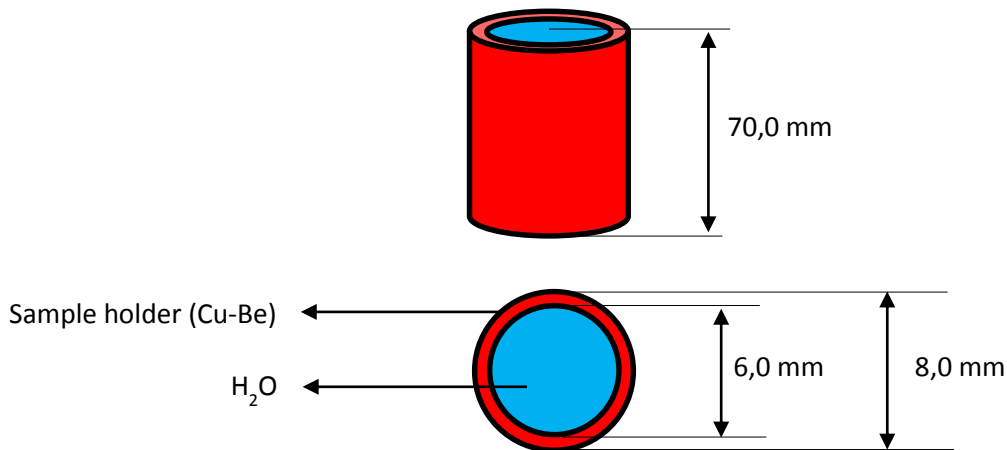


Fig. 4.3 Characteristics of the Cu-Be sample holder.

The measured thermodynamic states are listed in Table 4.1 and shown in Figure 4.4 in a pressure-temperature water phase diagram. In order to improve the statistics, the measurements which were

performed at the same temperature but at a different pressure were merged. The acquired data is only sensitive to the temperature [32].

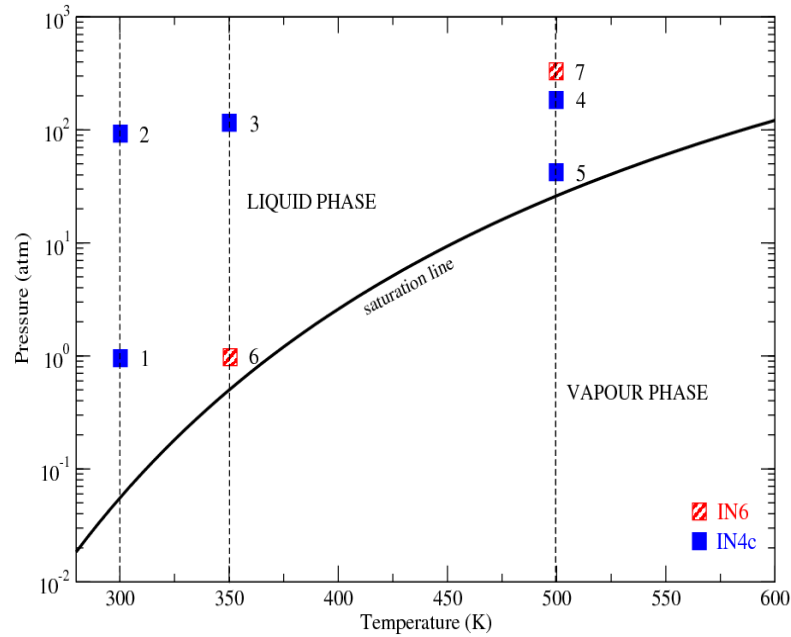


Fig. 4.4 Water pressure – temperature diagram showing the thermodynamic states measured for IN4c (blue full squares) and IN6 (red squares) spectrometers.

Table 4.1. Measured thermodynamic experimental conditions of water for the spectrometers IN4c ( $E_0 = 14.2$  meV) and IN6 ( $E_0 = 3$  meV) and the acquisition time in hours.

IN4c - E = 14 meV				IN6 - E = 3 meV			
State	T (K)	P (bar)	Time (h)	State	T (K)	P (bar)	Time (h)
1	300	1	2.5	6	350	1	4.0
2	300	94	2.0	7	500	340	4.5
3	350	115	2.0				
4	500	185	10.5				
5	500	42	3.0				

Special attention was given to avoid attaining the saturation state of water and have a coexistence of two phases. In order to dissipate the transients between two consecutive measures due to changes in the temperature and the pressure, it was waited an appropriate stabilization time.

Additional measurements of the sample holder without water were done to quantify the background level. Table 4.2 summarizes the temperatures and acquisition times for all the empty cell measures. At this stage of the experiment, we encounter stability difficulties with the regulation temperature of the cryofurnace that did not allow to have exactly the same temperatures for the water measurements. The final temperatures presented in the table are a result of an average weighted with the acquisition time. In the present work, only the results at room pressure (300 K and 350 K) will be presented.

Table 4.2. Temperature and acquisition time measured at IN4c and IN6 spectrometers for the empty cell.

IN4c - E = 14 meV		IN6 - E = 3 meV	
T (K)	Time (h)	T (K)	Time (h)
340	6.5	410	2.5
523	8.0	500	14.5

### 4.3 Analysis of the resolution function of the spectrometers

The time of flight of a neutron has a time distribution in time (equivalently in distance) called the resolution function. The effect of the resolution function in a spectrometer is to broaden the cross section and attenuate its intensity. It is the result of a combination of the 3 main factors: the time distribution of the initial neutron burst coming from the fermi chopper to the sample, the component linked to the multiple scattering of the He<sup>3</sup> detectors and the contribution of the angle of the detector with respect to the H<sub>2</sub>O sample.

To account for the resolution function of the installation, measurements of vanadium were carried out that serve as reference. The energy resolution for each spectrometer is determined from the elastic peak of the vanadium. This material behaves as a pure incoherent elastic scatterer (no energy loss) at energies below the neutron thermal energy [33]. The scattering function can be calculated simply with the zero-phonon term of the phonon expansion (chapter 2, section 2.5.1). This means that essentially the vanadium (as opposed to water) has no structure factor and it also serves as a calibration run for the rest of the measures [34].

Figure 4.5 shows the intensity of the vanadium measurements as a function of the energy transfer for two scattering angles (IN4c spectrometer). The vanadium at 14° presents a distribution with a tail for positive energy transfers. This feature is detected up to a scattering angle of approximately 21°. And afterwards it vanishes. For 120°, the distribution is very close to a Gaussian. The Gaussian fit to these distributions gives an energy resolution of 0.274 meV (half-width at half-maximum or HWHM) for  $\theta = 14^\circ$  and 0.294 meV for  $\theta = 120^\circ$ .

In the case of IN6 spectrometer, the vanadium data for  $\theta = 11^\circ$  and  $115^\circ$  are presented in Figure 4.6. The Gaussian fit of the distributions gives an energy resolution of 37.97  $\mu\text{eV}$  and 40.76  $\mu\text{eV}$  (HWHM) for  $11^\circ$  and  $115^\circ$  respectively.

A more detailed analysis of the HWHM of the resolution function as a function of the scattering angle is shown in Figure 4.7.

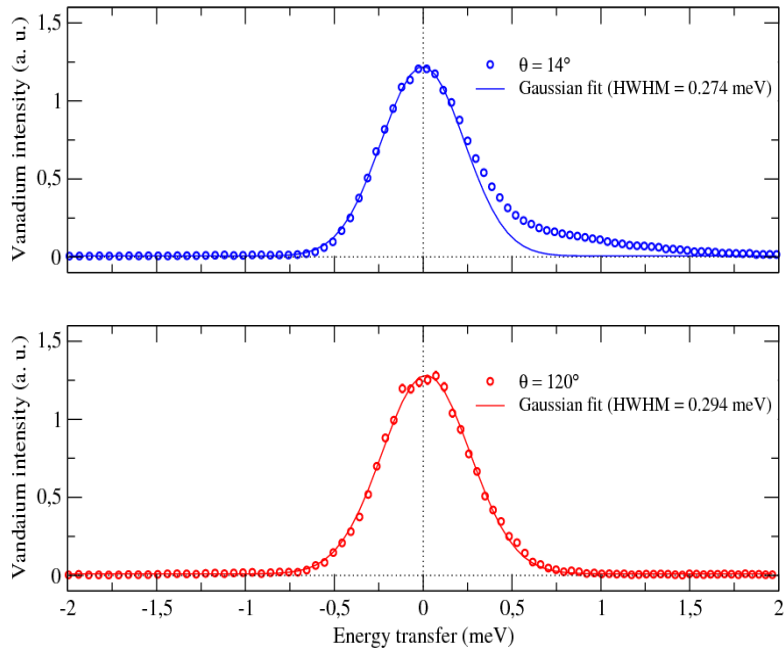


Fig. 4.5 Vanadium intensity measured at IN4c spectrometer for  $\theta = 14^\circ$  (upper plot) and  $\theta = 120^\circ$  (lower plot).

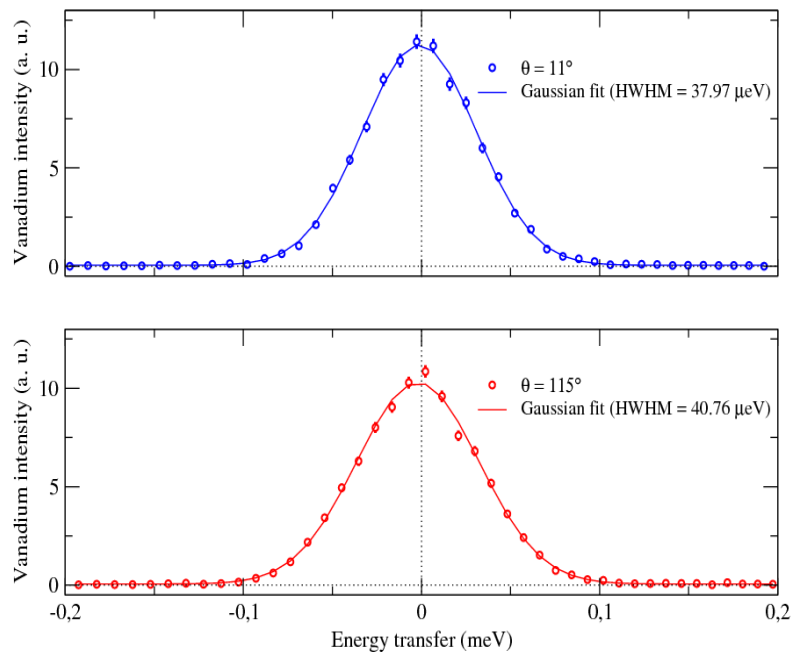


Fig. 4.6 Vanadium intensity measured at IN6 spectrometer for  $\theta = 11^\circ$  (upper plot) and  $\theta = 115^\circ$  (lower plot).

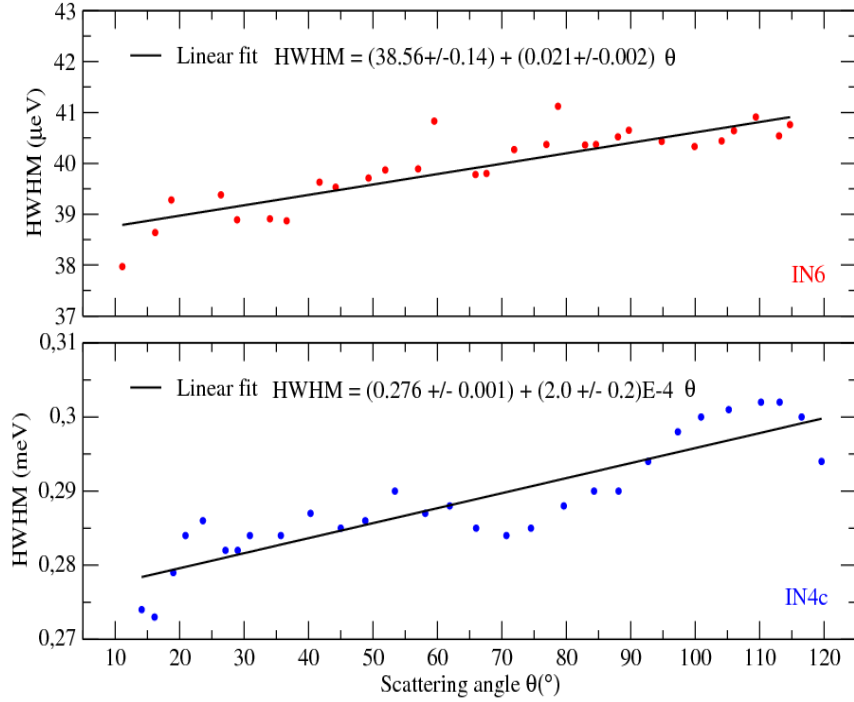


Fig. 4.7 Half-width at half-maximum of the vanadium elastic peak as a function of the scattering angle  $\theta$ .

The trend indicates that the elastic peak of the vanadium becomes broader with the scattering angle. Nevertheless the effect is slight, so the angular emission of the scattered neutrons has a negligible contribution to the resolution function of both instruments, IN4c and IN6. A linear fit gives the following equation:

$$HWHM(IN4c) = (0.276 \pm 0.001) + (2.0 \pm 0.2)E^{-4}\theta [meV]. \quad (2)$$

$$HWHM(IN6) = (38.56 \pm 0.14) + (0.021 \pm 0.002)\theta [\mu eV]. \quad (3)$$

It was decided to use the experimental measures of the vanadium for the data analysis because some of the distributions at low scattering angle present deviations from a Gaussian-type distributions.

## 4.4 Data post-processing

The data reduction was done with the processing software LAMP (Large Array Manipulation Program) [35]. It incorporates a graphic interface which enables the user to see the preliminary results step by step in the reduction process.

### 4.4.1 Data reduction routine

The standard processing routine carried out for all the measurements (IN4c and IN6 spectrometers) includes the following steps:

1. Normalization to monitor counts.
2. Dead time correction due to the physical characteristics of the detectors itself and the acquisition system.
3. Elimination of the spurious detectors.
4. Detector energy-dependent efficiency correction.
5. Calibration to the vanadium reference.
6. Conversion of the ToF spectra in time to energy
7. Background subtraction.

For the present work, no multiple scattering corrections were done. We expect a large contribution because the characteristic size of the sample (6 mm) is of the order or magnitude of the neutron mean free path at the measured incident energies: approximately 2 mm for 14 meV at 300 K (IN4c) and 1.5 mm for 3 meV (IN6).

After the reduction of the raw data, a distribution of the intensity as a function of the scattering angle  $\theta$  and the energy transfer  $\hbar\omega$  is obtained. An example of the processed water signal without the subtraction of the background, compared with the processed empty cell is shown in Figure 4.8 for IN4c at 300 K. The signals were normalized to the monitor counts and to the vanadium elastic peak. For a scattering angle close to  $60^\circ$  there are strong diffraction Bragg peaks of the copper, originated by the empty cell. It was decided then to use only the experimental data for scattering angles lower than  $60^\circ$ . This limitation was not detected for the case of IN6, where the intensity remains approximately constant as a function of the scattering angle (Figure 4.9).

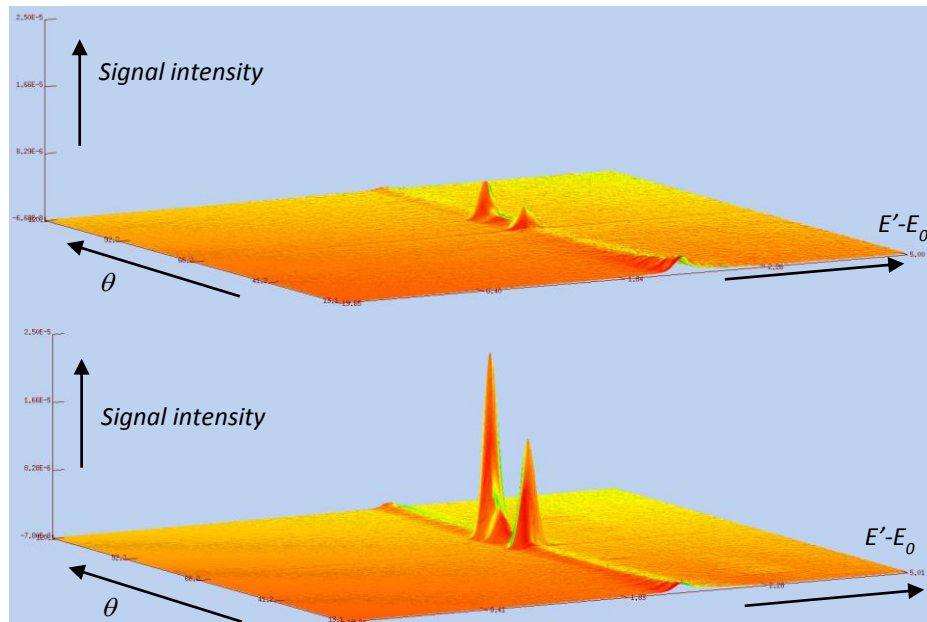


Fig. 4.8 Intensity of the water signal and empty cell as a function of  $\theta$  and  $E'-E_0$  (upper plot) and intensity of the empty cell measure (lower plot) for IN4c at 300 K.

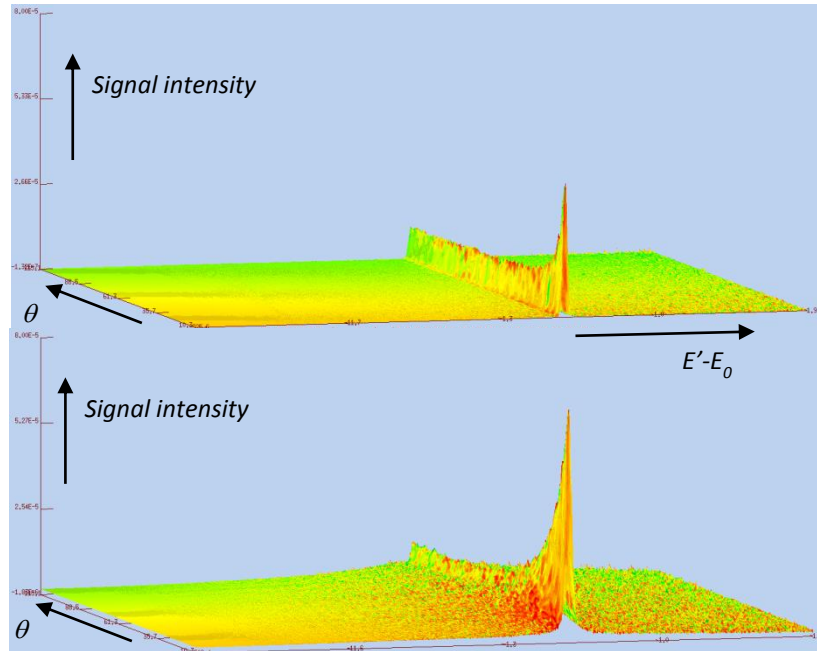


Fig. 4.9 Intensity of the water signal and empty cell as a function of  $\theta$  and  $E'-E_0$  (upper plot) and intensity of the empty cell measure (lower plot) for IN6 at 350 K.

#### 4.4.2 Background subtraction

The subtraction of the contribution of the sample holder is not straightforward. A transmission coefficient  $t$  was applied to the sample holder in order to take into account its scattering component to the final signal:

$$H_2O = (H_2O + dummy) - t * (dummy), \quad (4)$$

where the  $H_2O + dummy$  represent the raw water measure and  $H_2O$  the processed water signal.

In practice, the coefficient is determined empirically by performing a simulation with the Monte Carlo code TRIPOLI4 of the experiments done at IN4c and IN6 (see section 4.6). The study of the distributions reveals that the transmission coefficient is dependent on the scattering angle as well. Qualitatively, a high coefficient should be used for low  $\theta$ , while a small contribution of the background should be subtracted at higher scattering angles.

Figure 4.10 shows the intensity as a function of the secondary energy of the “H<sub>2</sub>O+sample holder” and “sample holder” signals for  $\theta = 15^\circ$  measured in IN4c spectrometer at 300 K. The Monte Carlo calculation determined that the experimental data and the simulation are compatible with a transmission coefficient  $t = 0.8$  (named as Water 0.8 in the plot).

As it was detailed in tables 4.1 and 2.4, there is an offset in temperature of about 40 K between the acquisitions of the “H<sub>2</sub>O+sample holder” and the “sample holder”. This originates another source of systematic uncertainty because the thermal agitation of the target nuclei is not the same for both cases. Due to the Doppler broadening, the width of the quasi-elastic peak of the dummy measure should be wider than in the “H<sub>2</sub>O+sample holder” distribution, making the subtraction incorrect in theory. In a deeper uncertainty analysis of the measures this aspect needs to be taken into account.

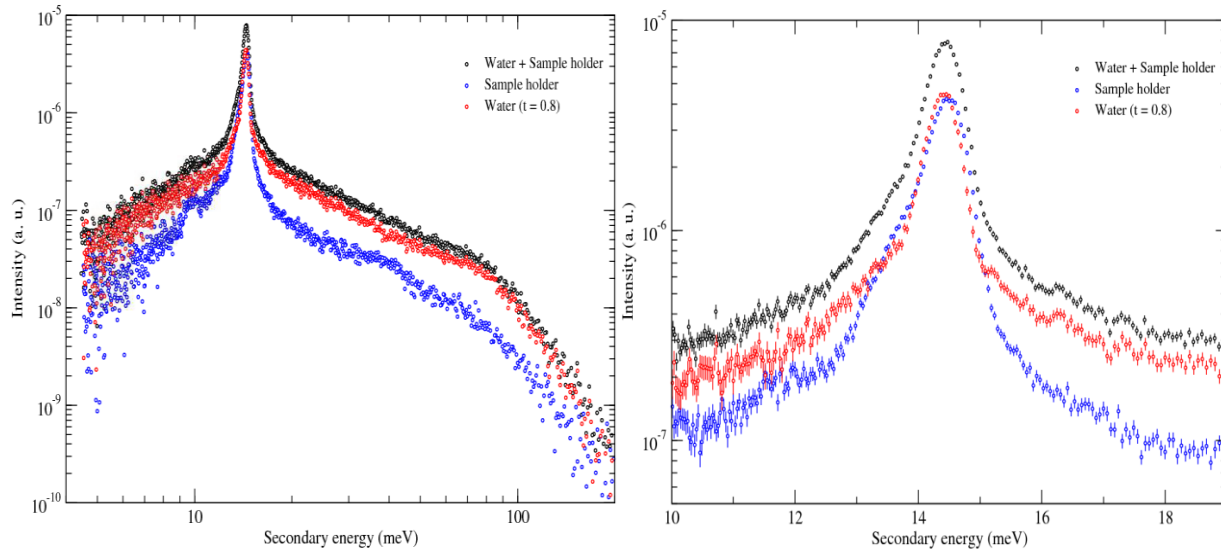


Fig. 4.10 Intensity of the “H<sub>2</sub>O+sample holder” and “sample holder” as a function of  $E'-E_0$  for  $\theta = 15^\circ$  measured in IN4c spectrometer at 300 K (left plot). Detail of the quasi-elastic peaks (right plot).

Figure 4.11 shows the intensity as a function of the secondary energy of the “H<sub>2</sub>O+sample holder” and “sample holder” signals for  $\theta = 15^\circ$  measured in IN6 spectrometer at 350 K. The Monte Carlo calculation determined that the experimental data and the simulation are compatible with a transmission coefficient  $t = 1.0$  (named as Water 1.0 in the plot).

The detail of the quasi-elastic peaks shows a not negligible energy shift of the “H<sub>2</sub>O+sample holder” and “sample holder” signals. The amount of such shift is approximately 0.017 meV, which corresponds to a shift in time of 8.6  $\mu$ s. The origin of this phenomenon might be explained due to the offset in temperature (like in IN4c spectrometer) of 60 K between both measures. Because the dummy measure was done at higher temperature, the up-scattering rate should be more important than in the water case. This is translated in a slightly harder spectrum than water, so in overall the scattered neutrons will be more energetic and they will be detected “faster”.

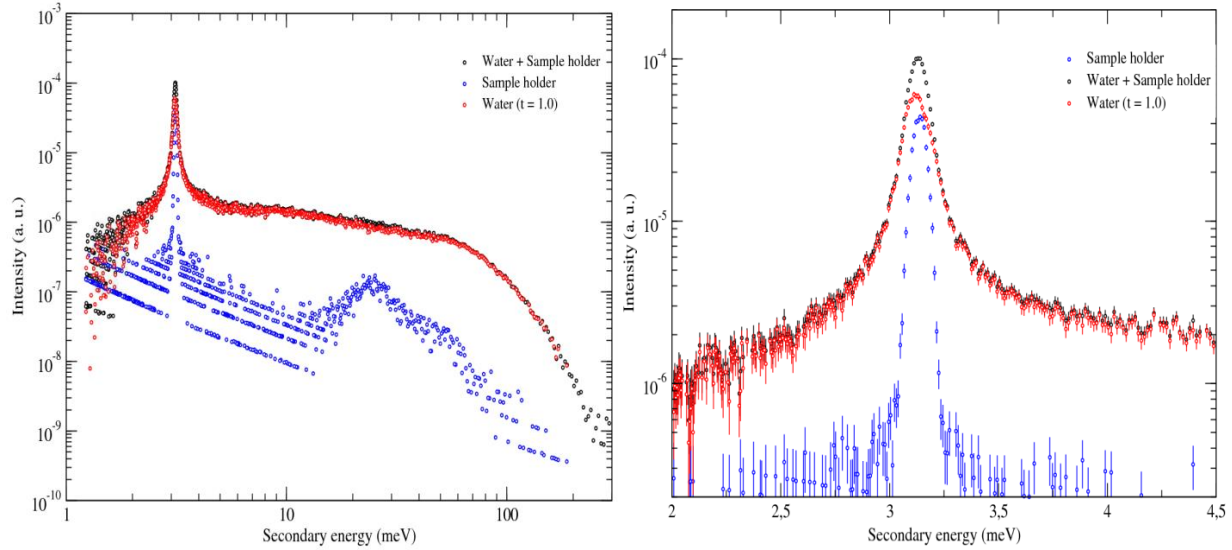


Fig. 4.11 Intensity of the “H<sub>2</sub>O+sample holder” and “sample holder” as a function of  $E'-E_0$  for  $\theta = 15^\circ$  measured in IN6 spectrometer at 350 K (left plot). Detail of the quasi-elastic peaks (right plot).

## 4.5 Results and discussions

### 4.5.1 IN4c Spectrometer

The double differential scattering cross section as a function of the secondary energy  $E'$  is shown in Figure 4.12, for two scattering angles:  $15^\circ$  and  $45^\circ$ , at 300 K. For the sake of clarity, the distribution for  $15^\circ$  was rescaled. For  $\theta = 45^\circ$  it was deduced from the Monte Carlo calculations a transmission coefficient of  $t = 0.3$ .

We selected an incident neutron energy in the experiment (14 meV) lower than the average energy of the thermal agitation of the water molecules at the measured temperature (approximately 26 meV at 300 K). In the distribution, this is translated in having better statistical uncertainties in the up-scattering regime, rather than in the down-scattering.

The right-hand plot shows close details of the quasi-elastic peak of the distributions. For  $\theta = 15^\circ$ , it can be seen the asymmetry of the peak already highlighted in the analysis of the vanadium measures, while for  $45^\circ$ , the tail effect is not present. There is an attenuation of the quasi-elastic peak as the scattering angle increases.

### 4.5.2 IN6 Spectrometer

The double differential scattering cross section as a function of the secondary energy  $E'$  is shown in Figure 4.13, for two scattering angles:  $15^\circ$  and  $45^\circ$ . Again, for the sake of clarity, the distribution for  $15^\circ$  was rescaled. It is worth highlighting the resolution in energy achieved with IN6, compared with IN4c. For  $\theta = 45^\circ$  it was deduced a transmission coefficient of  $t = 0.4$ .

The statistical uncertainties remain lower than the experimental points in the plot. The down-scattering contribution is very poor because almost all the emitted neutrons gain energy when scattering with the water target. There is one order of magnitude of difference between the selected incident neutron energy (3 meV) and the average energy of the thermal agitation of water at the measured temperature (30 meV at 350 K).

Examining carefully the quasi-elastic peak of the double differential cross sections, we note the symmetrical shape in both cases. The distributions in IN6 are very close to a Gaussian distributions.

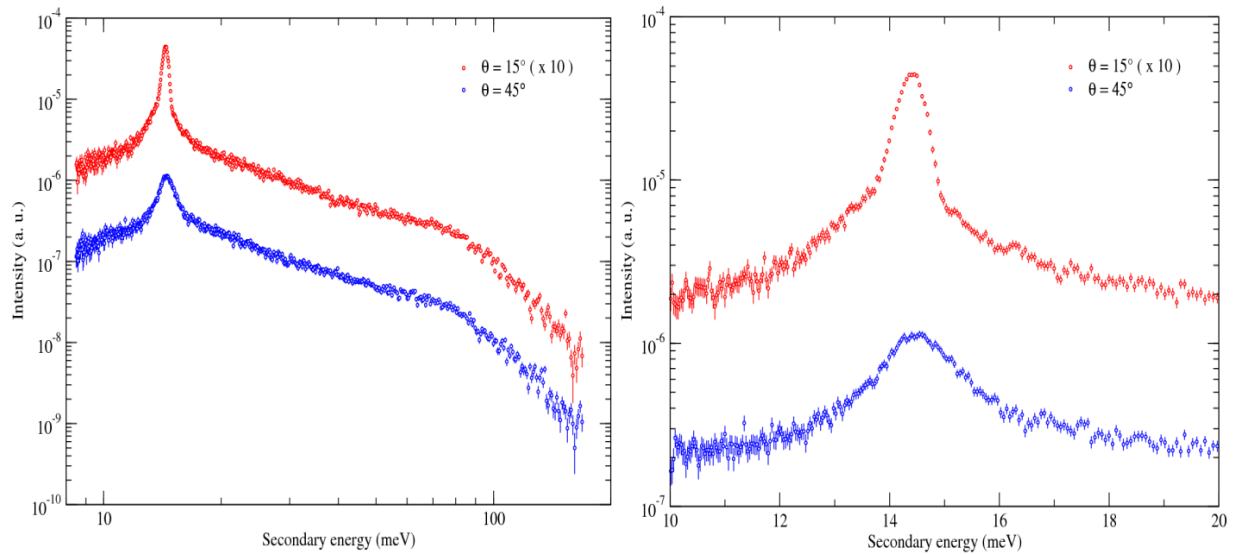


Fig. 4.12 Water double differential scattering cross section at  $E_0 = 14$  meV and  $\theta = 15^\circ$  and  $45^\circ$ , measured in IN4c spectrometer at 300 K. Detail of the quasi-elastic peaks (right plot).

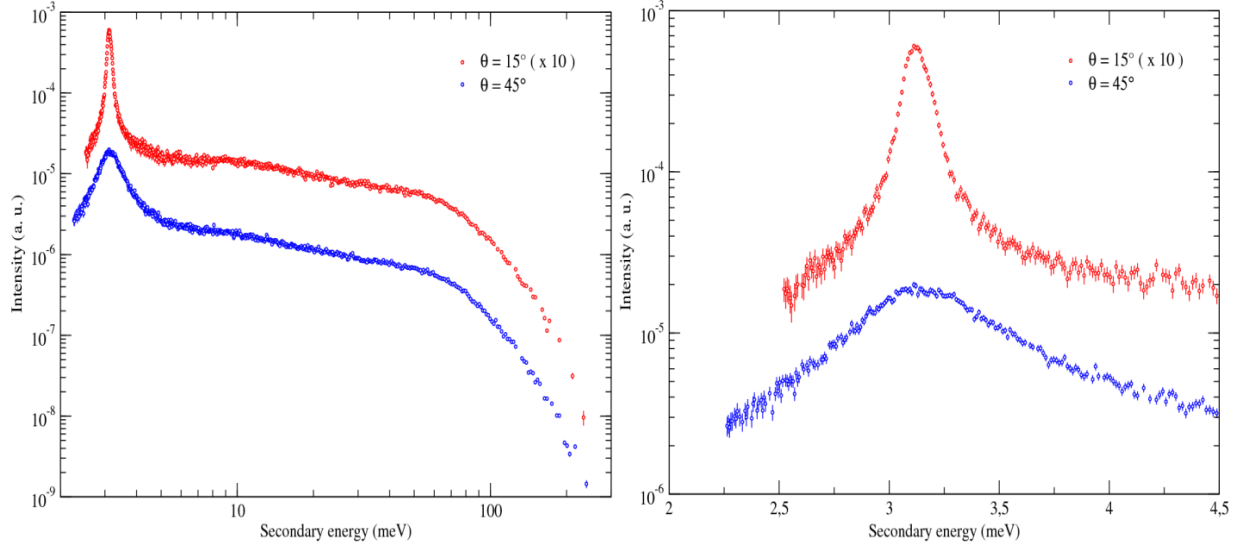


Fig. 4.13 Water double differential scattering cross section at  $E_0 = 3$  meV and  $\theta = 15^\circ$  and  $45^\circ$ , measured in IN6 spectrometer at 350 K. Detail of the quasi-elastic peaks (right plot).

## 4.6 Monte Carlo simulation

The processed experimental data was used to validate the theoretical models that describe the neutron thermal scattering in water in the JEFF-3.1.1 library and that of the CAB model.

### 4.6.1 Simplified ToF experiment model in TRIPOLI4

Comparisons were done by means of the Monte Carlo code TRIPOLI4 [36]. A simple model was created to reproduce the ToF experiment like thr IN4c and IN6 (Figure 4.14).

The dimensions of the water sample (diameter  $\phi_s$  and height  $h_s$ ), the detectors (diameter  $\phi_d$  and height  $h_d$ ) and the flight path distance  $L$  were respected.

Two effects were not taken into account in the model but are intrinsically encompassed by the resolution function (vanadium peak). The first is the time distribution of the neutron burst from the Fermi chopper. The second is the multiple scattering of the neutrons in the  $^3\text{He}$  detectors.

The calculations were done replacing alternatively the evaluation of  $^1\text{H}$  in  $\text{H}_2\text{O}$  of JEFF-3.1.1 nuclear data library, CAB model and  $^1\text{H}$  in the free gas approximation.

In order to compare directly the calculations with the experimental data, it was done a broadening of the calculated cross sections, convoluting them with the resolution function of each spectrometer. The vanadium measurements were used in this task. The convolution is done in the following way:

$$\sigma_R(E, \theta) = \int_{E_{min}}^{E_{max}} V(E, E^*, \theta) \sigma(E^*, \theta) dE^*, \quad (5)$$

where the function  $V$  represents the experimental vanadium function and  $\sigma$  and  $\sigma_R$  are the broadened and unbroadened double differential cross sections, respectively.

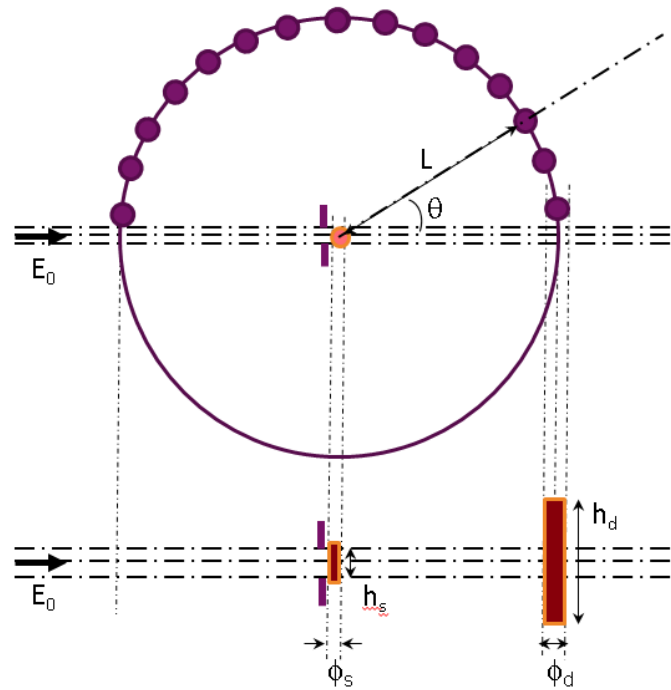


Fig. 4.14 Simplified ToF model implemented in the TRIPOLI4 code.  $E_0$  designates the incident neutron energy,  $\theta$  the scattering angle,  $L$  the flight path distance and  $E'$  the secondary energy.

Figure 4.15 compares the calculated broadened and unbroadened double differential cross sections at  $E_0 = 14$  meV (IN4c),  $\theta = 15^\circ$  and  $T = 300$  K. The continuous line represents the convolution of the TRIPOLI4 calculation with the experimental vanadium measure. The intensity of the quasi-elastic peak is attenuated while its width is broadened. It can be seen the tail effect typical of the resolution function of IN4c spectrometer, below  $21^\circ$ .

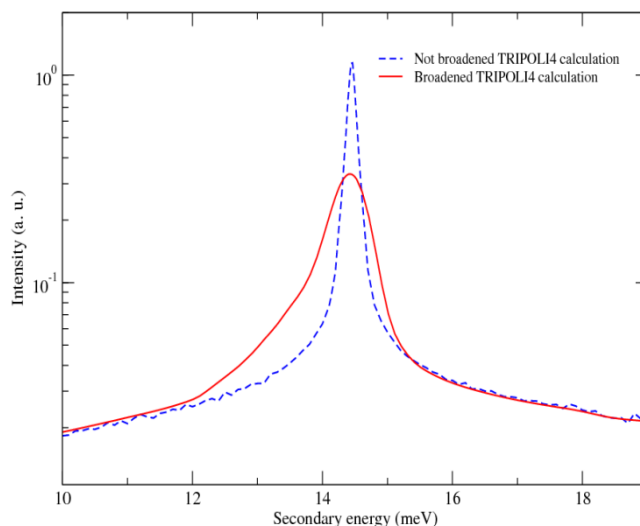


Fig. 4.15 Comparison between the unbroadened (dashed curve) and broadened (continuous curve) double differential cross sections calculated with the Monte Carlo code TRIPOLI4 for  $E_0 = 14$  meV,  $\theta = 15^\circ$  and 300 K. The convolution was done with the experimental vanadium measures.

#### 4.6.2 Results for IN4c spectrometer

The comparison of the experimental data for  $E_0 = 14$  meV,  $\theta = 15^\circ$  and  $T = 300$  K with JEFF-3.1.1, CAB model and the Free Gas model is shown in Figure 4.16.

The free gas model is not appropriate to describe the quasi-elastic peak of the distribution. Up to approximately 80 meV, there is a poor agreement with the inelastic up-scattering component. This is because the free gas model lacks of a frequency spectrum describing the excitation states of  $H^1$  in  $H_2O$ .

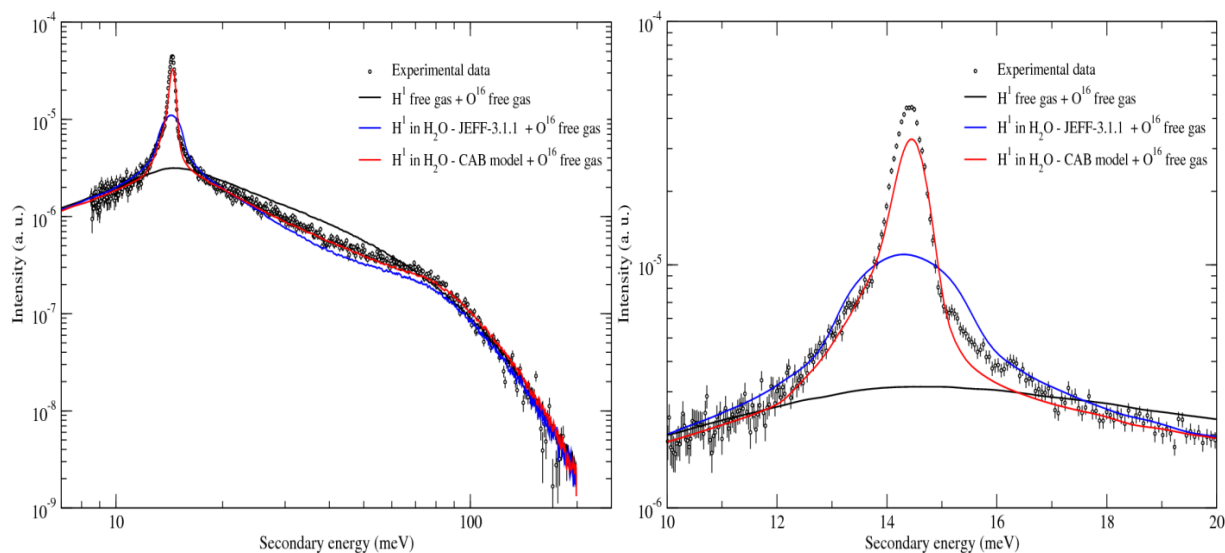


Fig. 4.16 Double differential scattering cross section at  $E_0 = 14$  meV,  $\theta = 15^\circ$  and 300 K calculated with JEFF-3.1.1, CAB model and Free gas model compared with the experimental data

The result of accounting the chemical bindings of the hydrogens with the oxygen is illustrated in the case of JEFF-3.1.1. The continuous component of the frequency spectrum of  $^1\text{H}$  in  $\text{H}_2\text{O}$  improves the agreement with the data in the 20 meV to 80 meV energy range, where this vibration mode dominates the neutron-water molecule interaction. However, this model is not sufficient to reproduce the quasi-elastic peak. At very low energy transfers, diffusive processes of the water molecules become important. JEFF-3.1.1 adopted a free gas model to describe the translation mode of the frequency spectrum. These results confirm the weakness of JEFF-3.1.1

In the case of the CAB model, the overall agreement with the measurements is satisfactory. A close look to the elastic peak shows the outcome of replacing the free gas model by the Egelstaff-Schofield diffusion model in CAB. Nevertheless the whole shape is not completely fulfilled. The origin of such big discrepancies is not well understood.

#### 4.6.3 Results for IN6 spectrometer

The comparison of the experimental data for  $E_0 = 3$  meV,  $\theta = 15^\circ$  and  $T = 350$  K with JEFF-3.1.1 and CAB model is shown in Figure 4.17.

Such cold incident neutron energy provides a good ground for testing the thermal scattering libraries. The JEFF-3.1.1 nuclear data library presents, in general, a poor agreement. This model fails to reproduce the low energy dynamics of scattering.

The energy where the experimental data describes the inelastic scattering is fairly well represented by the CAB model. However, as seen for IN4c results, there are still discrepancies between the measurements and the calculations in the quasi-elastic peak.

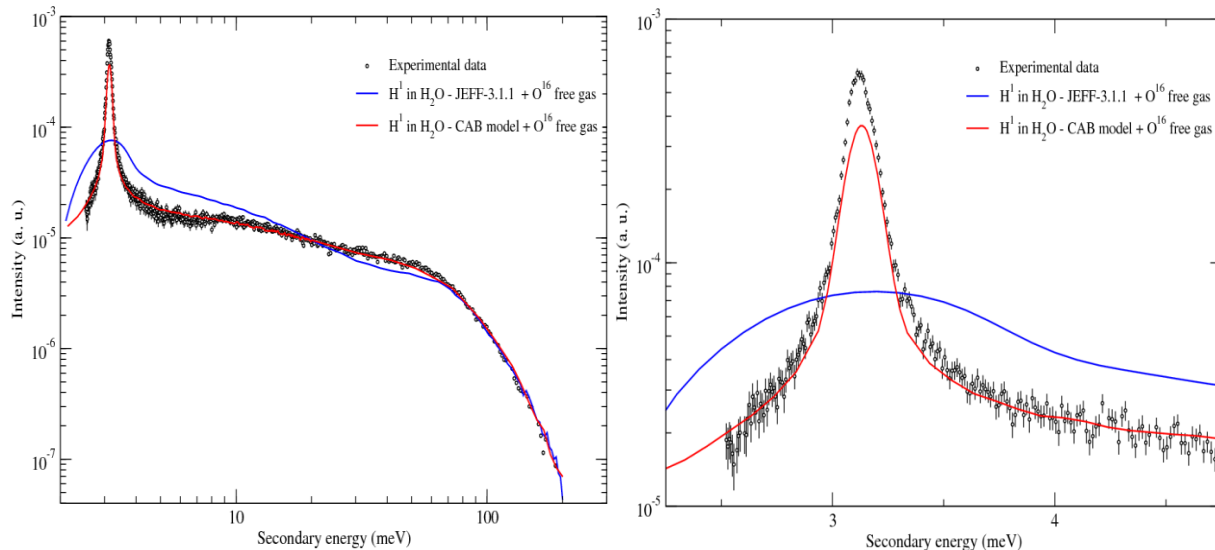


Fig. 4.17 Double differential scattering cross section at  $E_0 = 3$  meV,  $\theta = 15^\circ$  and 350 K calculated with JEFF-3.1.1 and CAB model compared with the experimental data

## 4.6.4 Discussion on the origin of the differences between calculations and experimental data

### 4.6.4.1 Experimental problems

It might be possible that the resolution function of the IN4c spectrometer is not correctly taken into account in the vanadium measurements. Figure 4.18 shows a comparison between two options of convolution of the calculated double differential cross sections for  $E_0 = 14$  meV (IN4c),  $\theta = 15^\circ$  and  $T = 300$  K. The continuous line represents the convolution with the vanadium, while the dashed line is the convolution with a Gaussian function (1.44% of resolution). This latter broadening option accounts better for the quasi-elastic peak but it worsens the description of the tail feature, correctly accomplished with the vanadium broadening.

Regarding the IN6 results, the problem of having measurements of the water sample and the empty cell at different temperatures was already pointed out. As the background was measured at a higher temperature, the width of the distribution is broader and attenuated. The subtraction with the water measurements is then underestimated, because the intensity of the peak of the sample holder should be larger at the same temperature.

This might have introduced a systematic source of uncertainty throughout all the scattering angles. The analysis of the double differential cross section at  $\theta = 45^\circ$  confirms the trend perceived for  $\theta = 15^\circ$  (Figure 4.19). The calculation done with the CAB model still underestimates the intensity of the quasi-elastic peak.

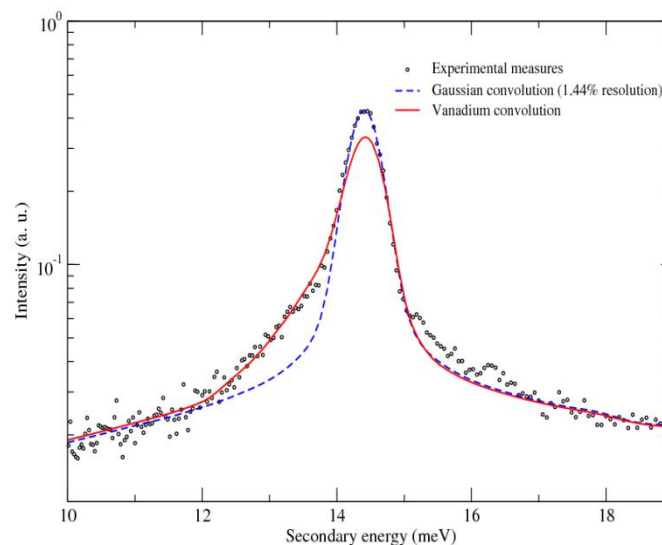


Fig. 4.18 Comparison of two convolution options for  $E_0 = 14$  meV (IN4c),  $\theta = 15^\circ$  and  $T = 300$  K. The dashed line was obtained convoluting the double differential cross section with a Gaussian function of 1.44% of resolution. The continuous line was obtained convoluting with the vanadium measures.

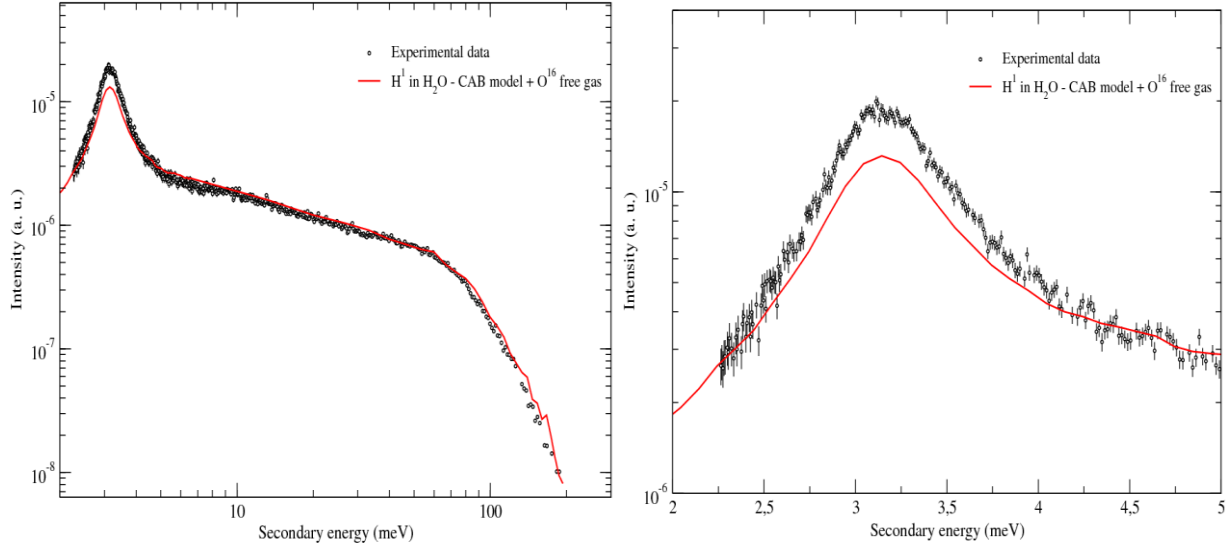


Fig. 4.19 Double differential scattering cross section at  $E_0 = 3$  meV,  $\theta = 45^\circ$  and 350 K calculated with CAB model compared with the experimental data

#### 4.6.4.2 Theoretical problems

In the work done by Y. Abe et al. [37], it was identified an inconsistency of the calculated double differential cross section with the experimental data in the quasi-elastic peak.

The origin of such problem was attributed to the Gaussian approximation assumption in the self intermediate scattering function (Fourier transform in space of the Van-Hoove space-time self correlation function), which is suitable for scattering with free gas atoms but presents difficulties when the hydrogen bonds between the water molecules are strong. In this latter case, the diffusion of the water molecules cannot be explained with the simple diffusion model but with the so-called *jump-diffusion* model. The molecules diffuse in a step-like movement caused by the formation of a network with the neighbor molecules.

This non-classical behavior becomes particularly relevant below the cold neutron energy range where the quasi-elastic neutron scattering is dominant. Abe et al. have applied a *quantum correction* to the scattering function to account for the latter effect. Figure 4.20 [37] shows the scattering function  $S(\vec{q}, \omega)$  for a neutron wave vector change of  $\vec{q} = 1.6 \text{ \AA}^{-1}$  at 294 K (left hand plot). The calculation using the quantum correction, named as GAAQC, presents a narrower and more intense quasi-elastic peak than the scattering law obtained with the Gaussian approximation. The calculation of the double differential cross section using both scattering laws is illustrated in the right hand plot, compared with experimental data measured at  $E_0 = 3$  meV,  $\theta = 71^\circ$  and 294 K. The higher quasi-elastic peak is achieved using the quantum correction. The agreement with the data is better than with the Gaussian approximation.

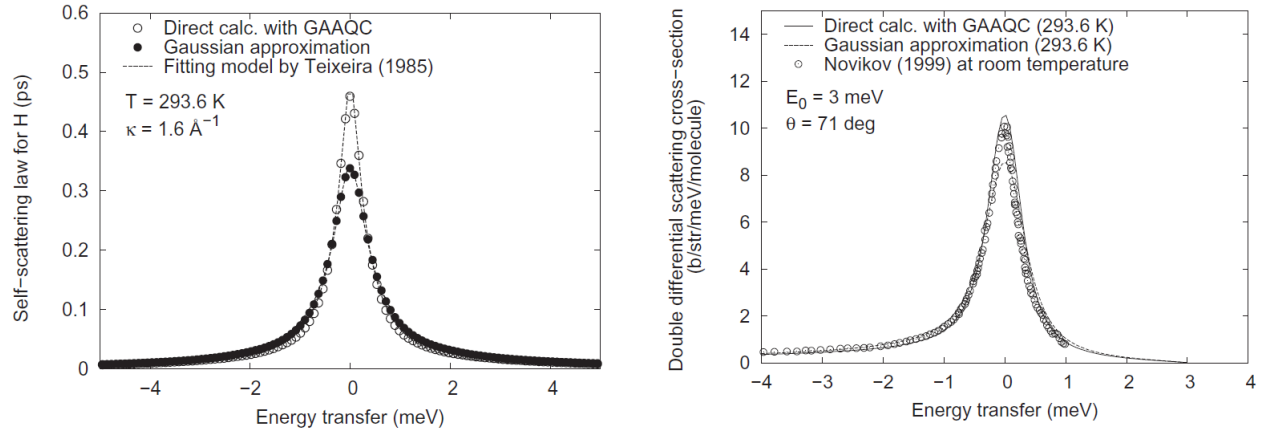


Fig. 4.20  $S(\bar{q}, \omega)$  for  $\bar{q} = 1.6 \text{ \AA}^{-1}$  at 294 K (left hand plot) obtained using the quantum correction (GAAQC) and the Gaussian approximation. In the right hand plot it was calculated the double differential cross section for  $E_0 = 3 \text{ meV}$ ,  $\theta = 71^\circ$  and 294 K using both approaches. The figures were taken from the reference [37].

#### 4.6.4.3 Problems induced by using the LEAPR module of NJOY

In the LEARP module of NJOY the generalized frequency of  $^1\text{H}$  in  $\text{H}_2\text{O}$  is decomposed in three partial spectra: a translational mode, a rotational mode and discrete oscillators. Each component has a weight that accounts the individual contribution to the total spectrum.

When analyzing the quasi-elastic peak of the double differential cross section, the translational vibration mode is dominant over the other scattering processes. The weight of the translational vibration mode,  $\omega_t$ , has a direct relation to the shape of the peak.

The physical meaning of the parameter  $\omega_t$  is related with the effective mass of the molecular clusters conformed by the water molecules. A low translational weight indicates a high effective mass.

The translational weight of the frequency spectrum of JEFF-3.1.1 is larger than in the CAB model and the intensity of the quasi-elastic peak calculated with JEFF-3.1.1 is lower than in the CAB model. The trend suggests that a lower translational weight than the used in the CAB model would be able to increase the amplitude of the peak.

The fitting algorithm of the CONRAD code [38] could be used to obtain a best-estimate value for  $\omega_t$  in order to improve the agreement with the experimental data. This latter study was not done in the frame of this thesis.

## *4.7 Preliminary conclusions*

The experimental measurements of the double differential scattering cross section of water serve as an important basis of validation of the theoretical models of thermal scattering. Particularly, at the incident neutron energies selected in the spectrometers IN4c and IN6 (thermal and cold energies respectively), the impact of the chemical binding of water is important, so it represents a real test for JEFF-3.1.1 and CAB model.

Firstly, the results have shown that using the  $^1\text{H}$  as a free gas model is not correct for thermal scattering. Secondly, they have revealed the weaknesses of JEFF-3.1.1 at 14 meV, while at 3 meV it was demonstrated its failure. Lastly, it was confirmed the improvement of the CAB model over JEFF-3.1.1 in the low energy dynamics of scattering, and especially for low energy transfers.

There were discrepancies identified between the experimental data and the calculations performed with the CAB model in the shape of the quasi-elastic peak. It was identified the different sources of such discrepancies. We encountered experimental problems coming from the background measurements and the resolution function of IN4c for low scattering angles. Having analyzed the work of Y. Abe et al., a possible hypothesis is that the Gaussian approximation in the intermediate scattering function is an incorrect assumption when studying the cold neutron energy dynamics.

Having done a deep analysis of the thermal scattering models from a microscopic point of view, the next chapter will deal the issue from a macroscopic one. Taking as reference the integral experiment Mistral performed at the EOLE reactor (Cadarache, France), the models will be compared performing integral calculations.

## Chapter 5

# Impact of the thermal scattering law of H in H<sub>2</sub>O on the isothermal temperature reactivity temperature coefficient in MISTRAL experiments

As the main interest in the present work addresses to the reactor applications, this chapter will discuss from a macroscopic point of view the results of a benchmark comparing the studied thermal scattering libraries, CAB model and JEFF-3.1.1. The selected integral experiment is MSITRAL, which was carried out in the EOLE reactor at CEA Cadarache (France). The configurations of the MISTRAL program are representative of a pressurized water reactor (PWR) but the measurements were done at cold reactor operating conditions. Such benchmark will allow quantifying the impact of the frequency spectra of <sup>1</sup>H in H<sub>2</sub>O originated by CAB model and JEFF-3.1.1 library.

The results presented in this chapter have already been published in the reference [39]. It was studied as well the impact on the modification in the continuous frequency spectrum introduced in the ENDF/B-VII.1 nuclear data library (Chapter3, section 3.1).

### *5.1 The MISTRAL experimental program*

The MISTRAL (MOX Investigation of Systems which are technically Relevant of Advanced Light water reactors) experimental program was created in the late nineties with the objective of evaluating the feasibility of charging 100% of MOX fuel in the light water reactors. It was carried out in the EOLE experimental facility at CEA Cadarache. Three different configurations were tested (MISTRAL -1, MISTRAL -2, MISTRAL -3), modifying fuel type (UOX or MOX), number of fuel pins and moderation ratio [40 and 41].

The neutronic parameters measured at cold reactor conditions were: the critical mass, geometric buckling, spectral indices, conversion factor, isothermal temperature coefficient, single absorber worth, soluble boron worth and effective delayed neutron fraction. The present work focuses on the isothermal reactivity temperature coefficient (RTC), which is a parameter involved directly in the reactor safety issues.

The MISTRAL-1 core is a homogenous UO<sub>2</sub> configuration that serves as reference for the MISTRAL program. The cylindrical core consists of a regular lattice using 750 standard PWR fuel pins (3.7% enriched in <sup>235</sup>U) in a square pitch of 1.32 cm with 16 clusters dedicated to safety rods. The moderation ratio set to 1.7 is representative of a light water reactor moderation lattice (Figure 5.1).

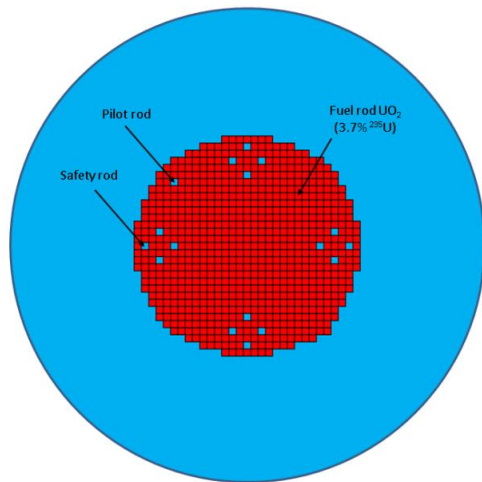


Fig. 5.1 Radial cross section of MISTRAL-1 core.

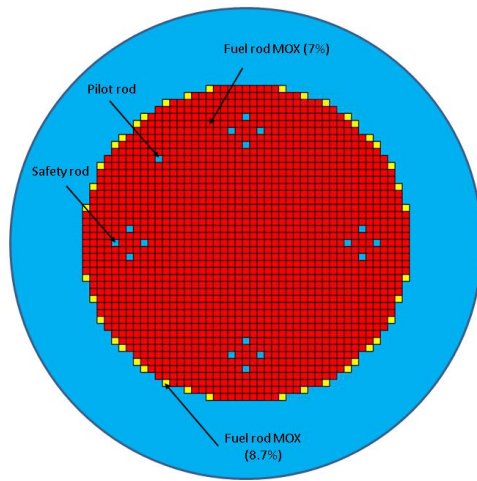


Fig. 5.2 Radial cross section of MISTRAL-2 core. The configuration corresponds to 20°C.

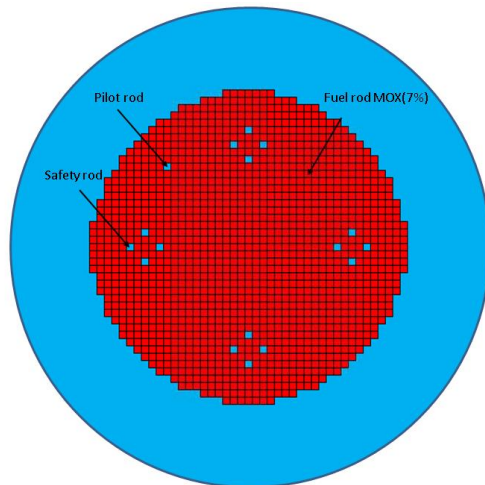


Fig. 5.3 Radial cross section of MISTRAL-3 core.

The MISTRAL-2 core is a homogenous MOX configuration with 1572 MOX fuel pins (7% enriched in Am-PuO<sub>2</sub>). Figure 5.2 shows the configuration corresponding to 20 °C.

The MISTRAL-3 core is a homogenous 100% MOX configuration with 1388 fuel pins (7% enriched in Am-PuO<sub>2</sub>) (Figure 5.3). The main differences with respect to MISTRAL-2 are the moderation ratio, close to 2.1 and the square pitch which was set to 1.39 cm. The aim of this configuration was to measure the fundamental neutronic parameters in a slightly over-moderated lattice (softer neutron spectrum than MISTRAL-2).

The main features of the MISTRAL-1, MISTRAL-2 and MISTRAL-3 configurations are summarized in Table 5.1.

The excess reactivity was measured as a function of the temperature from 10 °C to 80 °C (from 6 °C in MISTRAL-1) with a fine temperature step of 5 °C. In the MISTRAL-1 and MISTRAL-3 configurations, the concentration of soluble boron in the moderator was adjusted in order to compensate the reactivity loss due to the temperature increase. In the case of MISTRAL-2, the criticality was achieved by adjusting the critical size of the core. MOX fuel pins enriched to 8.7% in Am-PuO<sub>2</sub> were strategically added to the periphery of the core. The radial cross section of the MISTRAL-2 configuration for each temperature step is included in the appendix A.

Table 5.1. Summary of the main characteristics of the three MISTRAL configurations.

	<b>MISTRAL-1</b>	<b>MISTRAL-2</b>	<b>MISTRAL-3</b>
<b>Fuel composition</b>	UO <sub>2</sub>	UO <sub>2</sub> /Am-PuO <sub>2</sub>	UO <sub>2</sub> /Am-PuO <sub>2</sub>
<b>Number of fuel pins</b>	750	1572	1388
<b>Lattice pitch (cm)</b>	1.32	1.32	1.39
<b>Moderator</b>	H <sub>2</sub> O + H <sub>3</sub> BO <sub>3</sub>	H <sub>2</sub> O	H <sub>2</sub> O + H <sub>3</sub> BO <sub>3</sub>
<b>Moderation ratio</b>	1.7	1.7	2.1

## 5.2 Interpretation of the MISTRAL experiments using the Monte-Carlo code TRIPOLI4

As stated at the beginning of the chapter, the present work addresses to characterizing the isothermal reactivity temperature coefficient  $\alpha_{iso}(T)$ . It represents the change in the reactivity due to a change in temperature, and is determined from the excess reactivity  $\rho(T)$  measured at the given temperatures  $T$ .

In practice, the experimental results allow estimating  $\Delta\alpha_{iso}(T)$  which represents the calculation error on the reactivity temperature coefficient. The latter is given by the derivative of the reactivity

difference  $\Delta\rho(T)$  with respect to the temperature. If  $\rho_C(T)$  and  $\rho_E(T)$  are the calculated and measured reactivities respectively, then:

$$\Delta\alpha_{iso}(T) = \frac{\partial\Delta\rho(T)}{\partial T} = \frac{\partial}{\partial T}[\rho_C(T) - \rho_E(T)]. \quad (1)$$

### 5.2.1 Processing of the TSL with TRIPOLI4 code

The Monte-Carlo code TRIPOLI4 [36] was used for the interpretation of the MISTRAL experiments. For this purpose, the thermal scattering files of  $^1\text{H}$  in  $\text{H}_2\text{O}$  were generated for each temperature step in a format compatible with the official nuclear data library of TRIPOLI4 based on JEFF-3.1.1.

The processing of the TSL data files was performed with the NJOY code (version 99, update 364) [42]. Two modules of NJOY are specifically dedicated to this treatment: the LEAPR and THERMR modules.

The LEAPR module calculates the  $S(\alpha,\beta)$  matrix. A modification, provided by J. I. Marquez Damian, was introduced in LEAPR in order to process the inputs for larger energy and momentum transfer grids, which were used in the CAB model.

The THERMR module calculates the double differential scattering cross section. The original version was modified as well to create the libraries compatible with the TRIPOLI4 code libraries. The impact of using a different version of THERMR was not investigated.

Figure 5.4 shows the flowchart representing the processing scheme applied to the TSL files of JEFF-3.1.1 and that generated with the CAB model. For all the nuclides, it was used the JEFF-3.1.1 nuclear data library in the neutron transport calculations, with the exception of  $^1\text{H}$  in  $\text{H}_2\text{O}$  which was alternately replaced by the evaluation file of the CAB model. In order to facilitate the generation of the files for all the temperatures in an automated process, the CADTOOL package was used [43].

### 5.2.2 Considerations about the crystal lattice effect on the fuel

The crystal bindings of U in  $\text{UO}_2$  lattices inside the fuel are not negligible. This produces strong solid state-effects in the Doppler broadening of the  $^{238}\text{U}$  neutron capture resonances. The impact of this effect is especially important at cold reactor conditions. As the temperature increases it attenuates due to the increase of the thermal agitation of the nuclei, for which the crystal bindings become negligible.

Since currently reactor calculation codes are not prepared for Doppler calculations with such effect, the Free Gas approximation is used with an effective temperature [44]. This effective temperature preserves the  $^{238}\text{U}$  total capture rate for thermal reactors up to 1000 K.

If  $T$  is the thermodynamic fuel temperature, then the effective temperature is calculated as follows:

$$T_{eff} = T \left( 1 + \frac{8.6}{T} + \frac{3100}{T^2} \right). \quad (2)$$

This correction was applied in the calculations with TRIPOLI4 code, for the oxide fuel lattices and for the mixed oxide lattices as well.

Figure 5.5 shows the correction to be applied to the fuel temperature from cold to hot reactor conditions. The MISTRAL operating conditions (from 10 °C to 80 °C) present strong crystal lattice effects, while at a temperature close to the normal operation of a PWR (approximately 310 °C) the nuclei behave approximately as free gas.

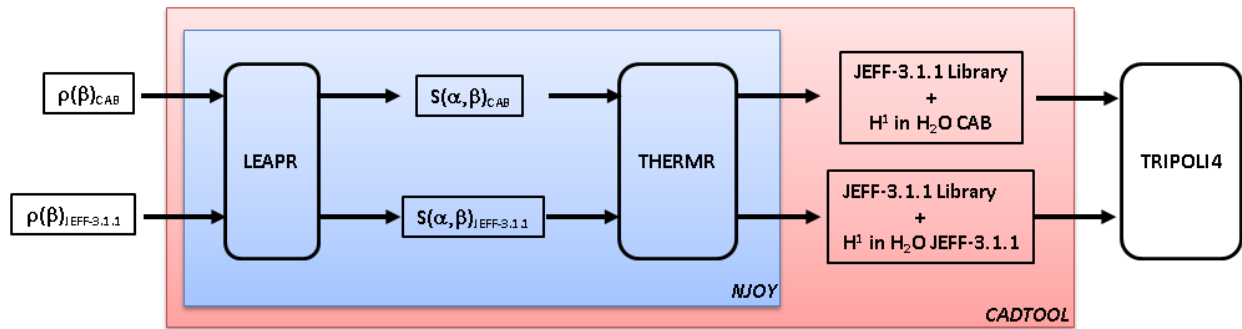


Fig. 5.4 Flowchart of the calculation scheme used to produce the thermal scattering libraries for TRIPOLI4.

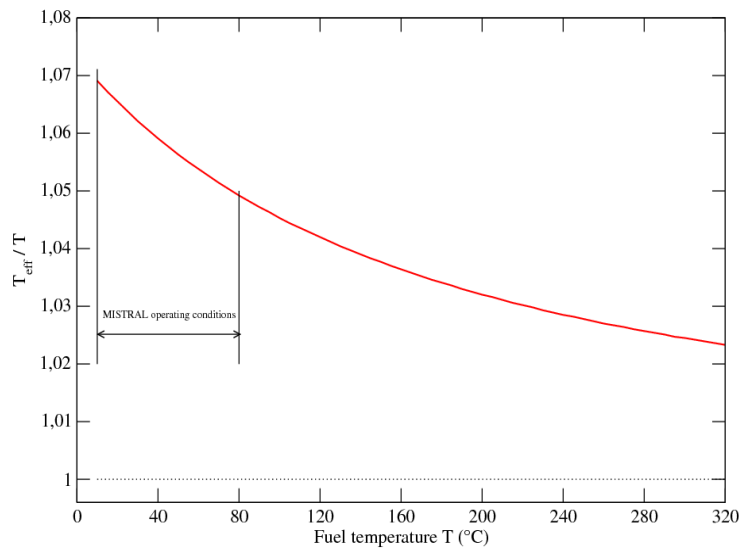


Fig. 5.5 Effective temperature correction to the temperature for taking into account the crystal lattice effects in the fuel matrix (eq. 2)

### 5.2.3 Material thermal expansion effects

The temperature increase produces a thermal expansion of all the core materials that conform the MISTRAL experiments, including water. Even though the temperature change is relatively small (from 10 °C to 80 °C) compared to a pressurized water reactor (from 20 °C to 310 °C), materials such as the aluminum, the water and the fuel itself will have an impact in our calculations.

The water density decreases with the temperature. This effect tends to decrease the reactivity as there is less amount of moderator for the neutrons to slow down to thermal energies and produce new fissions.

The lattice pitch will increase with the temperature (due to the expansion of the aluminum grid) modifying the moderation ratio. Consequently, the contribution of the resonance absorption will decrease and the resonance escape probability will increase. This effect gives a positive contribution to the reactivity.

The aluminum overclad in MISTRAL is used to simulate the water expansion effects. It will have an opposite effect to the lattice pitch expansion because its objective is to remove moderator, compensating the increase in the moderation ratio.

The UOX and MOX oxides have a lower linear thermal expansion coefficient than aluminum. They are characterized by a volume change close to 0.4% between 10 °C and 80 °C, which has a slight impact on the resonance absorption.

The expansion of the aluminum materials and the fuel was taken into account assuming that the expansion is isotropic and independent of the temperature. If  $L_0$  is the characteristic dimension at 20 °C and  $\Delta T$  the temperature change, then the dimension at each temperature is given by:

$$L = L_0(1 + \alpha\Delta T), \quad (3)$$

where  $\alpha$  is the linear expansion coefficient, whose value for aluminum is  $2.47E-5$  1/K and for UO<sub>2</sub>/PuO<sub>2</sub>-UO<sub>2</sub> is  $1.1E-5$  1/K [45].

Such a correction was applied in a previous interpretation of the MISTRAL-1 experiment [46] with the deterministic code APOLLO2 [47]. In the present work, it was decided to use a similar strategy in order to have a comparison reference of the MISTRAL-1 calculations. For MISTRAL-2 and MISTRAL-3, the calculated reactivity will include the thermal dilatation effects and no correction will be needed.

The reactivity correction due to the thermal expansion of the materials in MISTRAL-1 was calculated for four temperatures: 6 °C, 20 °C, 40 °C and 80 °C. Figure 5.6 shows the difference in the calculated reactivities  $\Delta\rho_{corr}$  taking as a reference the reactivity at 20 °C. The linear fit of the thermal expansion corrections in pcm gives the following equation:

$$\Delta\rho_{corr}(T) = (0.9 \pm 0.1)T + (-21.1 \pm 2.4). \quad (4)$$

According to eq. (2), this conduces to a correction in the isothermal reactivity temperature coefficient of  $\Delta\alpha_{corr} = 0.9 \pm 0.1$  pcm/°C

The present result is twice as large as the correction found in previous interpretations performed with the APOLLO2 code. Unfortunately, no obvious explanations were found for understanding the differences.

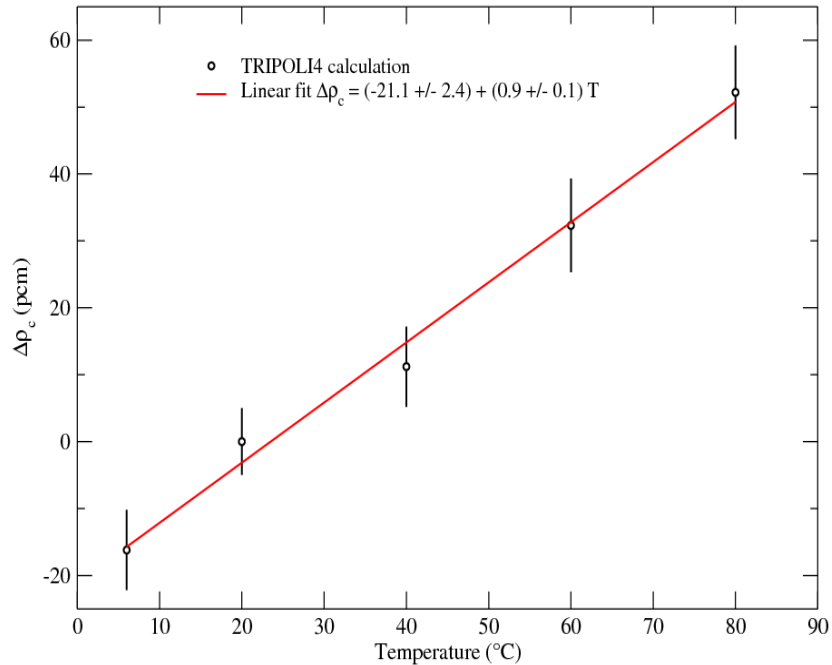


Fig. 5.6 Reactivity corrections as a function of the temperature due to the thermal expansion of the MISTRAL-1 core. The reference corresponds to reactivity at 20 °C. The solid line represents the linear fit.

#### 5.2.4 Validation of the calculation scheme

The calculation scheme to obtain the thermal scattering laws was validated against the official library of TRIPOLI4 code. It was compared the calculated effective multiplication factor ( $k_{eff}$ ) of MISTRAL-1 configuration at 20 °C of the official library and our NJOY treatment.

The two NJOY modules were tested separately. The THERMR module was applied to the  $S(\alpha,\beta)$  matrix of JEFF-3.1.1 and compared with the official TRIPOLI4 library. The thermal energy cut-off is set to 4.95 eV. The LEAPR module was tested using the input file of  $^1\text{H}$  in  $\text{H}_2\text{O}$  reported in [4].

The results are listed in Table 5.2. The differences between the  $k_{eff}$  values calculated with the TSL coming from our processing scheme and the official library TRIPOLI4 are negligible. The good agreement shows that our processing scheme can be used for the interpretation of the MISTRAL experiments.

Table 5.2. Excess of reactivity calculated with the TRIPOLI4 code for the MISTRAL-1 configuration at 20 °C.  $\Delta$  is the impact relative to the reference case of the official T4 library. The statistical uncertainty of calculations is 4 pcm.

Thermal Scattering Law of H1 in H2O	C - E (pcm)	$\Delta$ (pcm)
Official T4 library based on JEFF-3.1.1	196 $\pm$ 4	-
<sup>1</sup> H in H <sub>2</sub> O generated with THERMR module	187 $\pm$ 4	-9 $\pm$ 6
<sup>1</sup> H in H <sub>2</sub> O generated with LEAPR+THERMR modules	186 $\pm$ 4	-10 $\pm$ 6

## 5.2.5 Energy treatment for thermal scattering libraries in TRIPOLI4

### 5.2.5.1 Thermal energy cut-off

The THERMR module provides the thermal scattering data up to a thermal energy cut-off defined by the user. For our calculations this energy was set to 4.95 eV.

For higher energies, TRIPOLI4 code uses the so-called Sampling of the Velocity of the Target nucleus (SVT) to take into account the thermal agitation of the collided nuclei. The code assumes that the nuclei are at thermal equilibrium with a Maxwell-Boltzmann velocity distribution. This model is adopted up to a threshold energy set by default to  $E_{\max} = 400K_B T$ , where  $K_B$  is the Boltzmann constant and  $T$  the moderator temperature. If the temperature is 294 K, then the SVT model is used from 4.95 eV up to 10.13 eV.

Beyond the threshold energy, the neutron energy is in general larger than the average moderator energy, so the nucleus can be considered at rest as seen from the incoming neutron energy. In this case, the standard two-body kinematics can be applied for the elastic collisions, which results in the so-called Asymptotic elastic scattering Kernel (AK).

Aiming at evaluating the impact of the different treatments of <sup>1</sup>H in H<sub>2</sub>O in TRIPOLI4 as a function of the energy, a simple test was performed with the MISTRAL-1 configuration at 20 °C. It was calculated the reactivity for the three cases, shown in Figure 5.7. In all tests, thermal scattering data of <sup>1</sup>H in H<sub>2</sub>O was used up to 4.95 eV. In test 1, the SVT model was used up to 10.13 eV and the AK approximation beyond this energy. In test 2, the SVT model was used to treat the <sup>1</sup>H as a free gas. Finally in test 3, the SVT model was replaced with the AK approximation. The results are listed in Table 5.3.

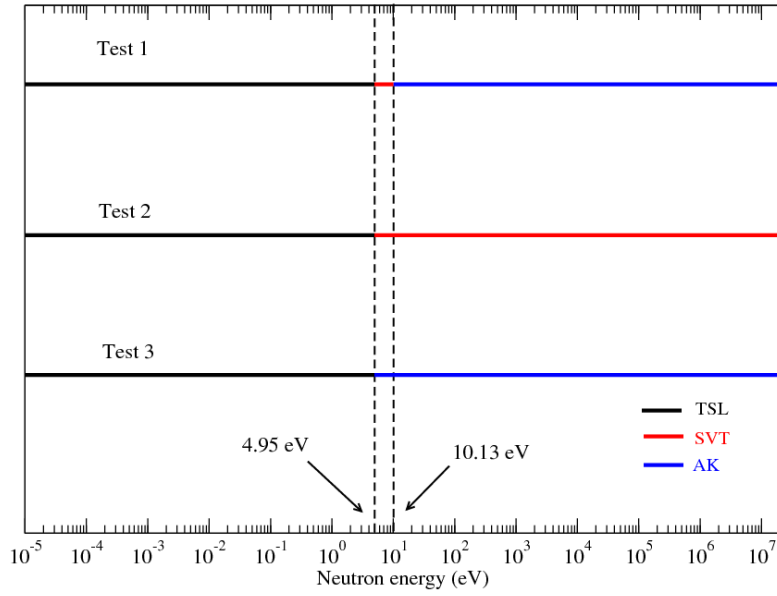


Fig. 5.7 Energy ranges for the tests performed over MISTRAL-1 configuration at 20 °C.

Table 5.3. Excess of reactivity calculated with the TRIPOLI4 code for the MISTRAL-1 configuration at 20 °C for three cases. The statistical uncertainty of the calculations is 3 pcm.

Case	C - E (pcm)	$\Delta$ (pcm)
1	192 ± 3	-
2	193 ± 3	1 ± 4
3	217 ± 3	25 ± 4

Neglecting the thermal agitation of the target nuclei in the transition zone between thermal scattering and free gas (4.95 eV) produces an increase of the reactivity of 25 pcm. However, there is no impact on the calculated keff on sampling the velocity and direction of the  $^1\text{H}$  atoms throughout all the neutron energy range. The energy treatment for the thermal scattering of case 1 represents the most adequate for our calculations. It is least expensive in terms of computational cost (no sampling of the velocities and directions of the target nuclei beyond 400 K<sub>B</sub>T) without having impact on the calculated reactivity.

#### 5.2.5.2 Study of the discontinuity of the $^1\text{H}$ scattering cross section

As it was seen before, the scattering cross section of  $^1\text{H}$  through all the energy domain of interest in reactor calculations ( $10^{-5}$  eV to 20 MeV) is reconstructed with two models. The thermal scattering data is used to calculate the cross section of  $^1\text{H}$  in  $\text{H}_2\text{O}$  up to the thermal energy cut-off of 4.95 eV. Beyond this energy, the free gas model is used to calculate the cross section of  $^1\text{H}$ .

At the energy where the switch between the models is produced, there is a discontinuity in the cross section. Figure 5.8 compares the scattering cross sections of  $^1\text{H}$  in  $\text{H}_2\text{O}$  (continuous line) and  $^1\text{H}$  in the

free gas approximation (dotted line) at 294 K. A detailed analysis around 4.95 eV (right plot) allows visualizing the mismatch of the cross sections due to the shift of the thermal scattering model to the free gas model.

The problem originates because the evaluation  $^1\text{H}$  in the free gas approximation is used at the thermodynamic temperature and not at an effective temperature calculated taking into account the frequency spectrum of  $^1\text{H}$  in  $\text{H}_2\text{O}$  (eq. 67 of chapter 2). When the  $^1\text{H}$  cross section is broadened at an effective temperature of 1250 K (dashed line in the plot) it becomes compatible with the  $^1\text{H}$  in  $\text{H}_2\text{O}$  cross section.

Nevertheless, the discontinuity of the scattering cross sections is not significant and we do not expect an impact on our calculations for the MISTRAL benchmarks. In the present work it was used the thermodynamic temperature of  $^1\text{H}$  for all the calculations.

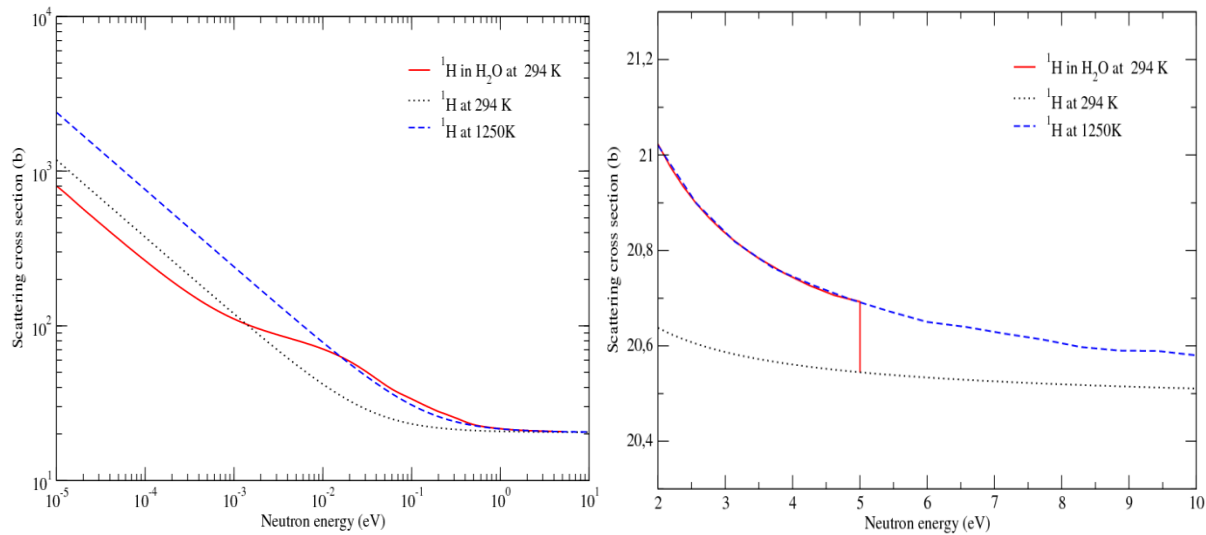


Fig. 5.8  $^1\text{H}$  scattering cross sections bound to  $\text{H}_2\text{O}$  at 294 and in the free gas approximation at 294 K and 1250 K from JEFF-3.1.1 library.

### 5.2.6 Interpolation of the LEAPR model parameters of JEFF-3.1.1

In the JEFF-3.1.1 library, the thermal scattering law is tabulated over a broad temperature mesh. Only three temperatures (20 °C, 50 °C and 100 °C) are reported to map the temperature range of the MISTRAL programs from 6 °C to 80 °C. Such a broad temperature mesh is not adequate for a precise estimation of the isothermal reactivity temperature coefficient at room temperature.

New  $S(\alpha,\beta)$  matrices were generated up to 80 °C with a fine temperature step of 5 °C by interpolating linearly the model parameters and the frequency spectra of IKE model [4]. Results are shown in Figure 5.9 and Figure 5.10, respectively.

Figure 5.11 compares the total cross-sections of  $^1\text{H}$  in  $\text{H}_2\text{O}$  from the JEFF-3.1.1 library to the total cross sections calculated with a fine temperature mesh. High sensitivities to the temperature are observed for cold neutrons ( $E < 25.3$  meV).

Final results were verified by comparing the total cross section reconstructed from our interpolation procedure to the JEFF-3.1.1 total cross-section evaluated at 20 °C and 50 °C. In both cases, the differences remain negligible over the neutron energy range of interest. They reach a maximum of 1.5 barns at 0.01 meV, corresponding to a calculation error of 0.15%.

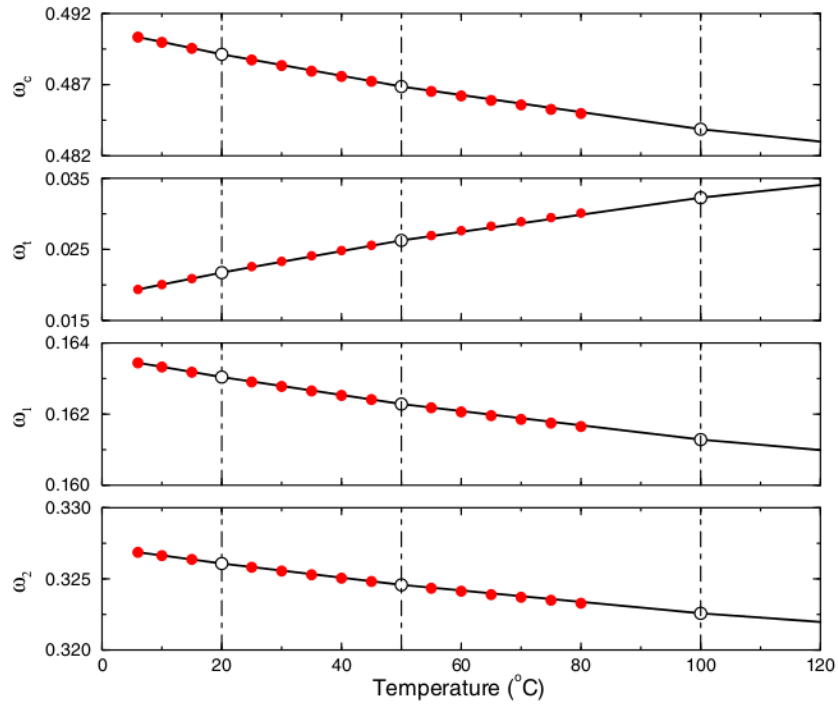


Fig. 5.9 Interpolation of the model parameters established by Mattes and Keinert between 6 °C and 80 °C.

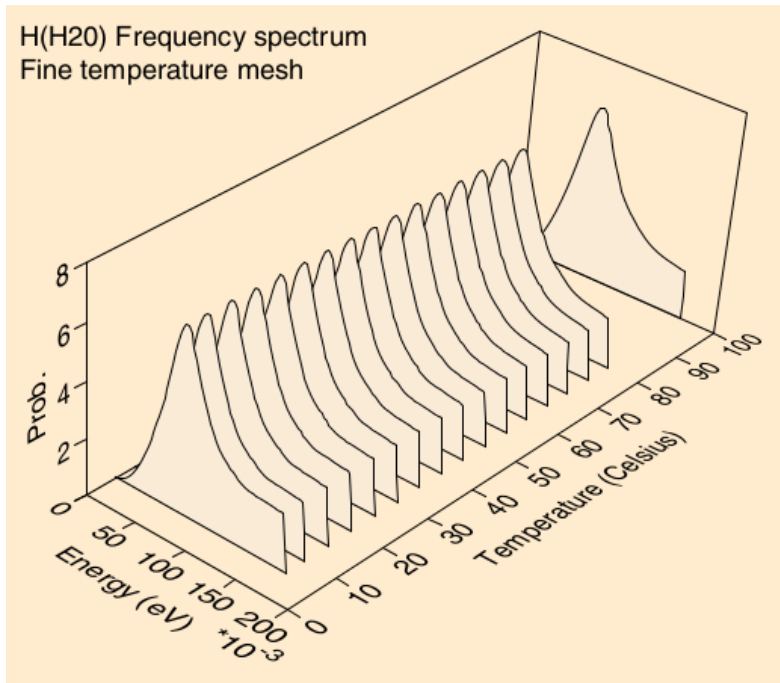


Fig. 5.10 Continuous frequency spectra for  $^1\text{H}$  in  $\text{H}_2\text{O}$  interpolated over a fine temperature mesh.

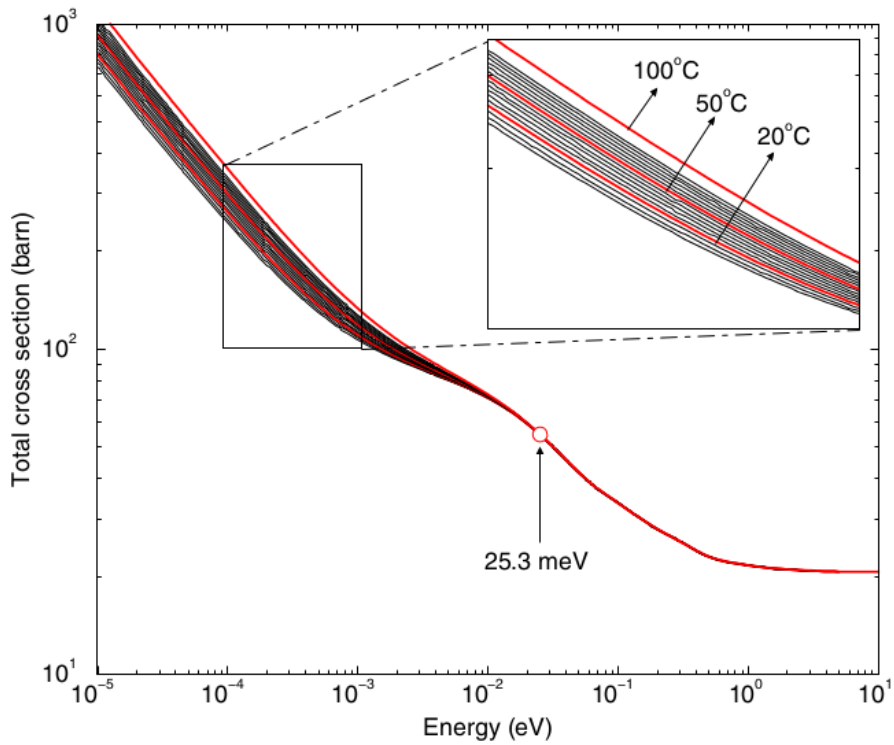


Fig. 5.11 Total cross section of  $^1\text{H}$  in  $\text{H}_2\text{O}$  calculated with the broad temperature mesh of the JEFF-3.1.1 library (20 °C, 50 °C and 100 °C) and interpolated over a fine temperature mesh (from 6 °C to 80 °C).

### *5.3 Reactivity excess as a function of the temperature in the MISTRAL experiments*

The interpretation of the three MISTRAL configurations was performed with the JEFF-3.1.1 library. As shown in the flowchart of Figure 5.4, it was only replaced the thermal scattering laws of  $^1\text{H}$  in  $\text{H}_2\text{O}$  by those calculated with our processing scheme.

Results reported in Table 5.4 represent the differences in reactivity  $\Delta\rho(T)$ , where  $\Delta$  indicates the deviation from the experimental values. In the case of MISTRAL-1, the results do not take into account the correction due to thermal expansion effects.

Contributions of the experimental uncertainties and those coming from the Monte Carlo calculations are taken into account separately. For each configuration the statistical uncertainty due to the Monte Carlo calculations is close to 2 pcm. The experimental uncertainties account for uncertainties that mainly come from the kinetic parameters, the measurements of the doubling time and of the boron concentration. The final experimental uncertainty ranges from 12 pcm to 25 pcm. In the present work, the contribution of the kinetic parameters to the final uncertainty is small because we have used delayed neutron fraction values ( $\beta_{\text{eff}}$ ) which have been measured during the MISTRAL-1 and MISTRAL-2 programs. Results reported in reference [48] are  $788 \pm 12$  pcm for MISTRAL-1 (UOX core) and  $370 \pm 6$  pcm for MISTRAL-2 (MOX core). Technological uncertainties are not included. For the EOLE facility, the magnitude of such uncertainties is close to 200 pcm.

Table 5.4. Differences in reactivity  $\Delta\rho = C - E$  (pcm) obtained with the thermal scattering laws of JEFF-3.1.1 and CAB model for the MISTRAL-1, MISTRAL-2 and MISTRAL-3 configurations. In MISTRAL-1, the reactivity differences do not include the correction due to thermal expansion effects. The statistical uncertainty due to the Monte Carlo calculations is 2 pcm.

T (°C)	MISTRAL-1 (UOX)		MISTRAL-2 (MOX)		MISTRAL-3 (MOX)	
	JEFF-3.1.1	CAB model	JEFF-3.1.1	CAB model	JEFF-3.1.1	CAB model
6	206	295	-	-	-	-
10	206	293	746	916	707	835
15	-	-	732	900	-	-
20	192	283	732	900	657	788
25	-	-	727	903	-	-
30	193	282	725	904	687	826
40	198	291	730	897	672	815
45	-	-	712	897	-	-
50	-	-	705	889	-	-
60	161	264	697	878	627	772
65	148	257	708	894	-	-
70	128	240	690	872	614	768
75	127	232	686	860	-	-
80	124	234	688	869	621	779

The top plot of Figure 5.12 shows the  $\Delta\rho(T)$  values obtained for the MISTRAL-1 experiment as a function of the temperature. Using the JEFF-3.1.1 library, we observe a slight overestimation of the core reactivity (+192 pcm at 20 °C). Compared to JEFF-3.1.1, the thermal scattering law of CAB model increases the calculated reactivity by approximately +100 pcm on average.

The middle and bottom plots of Figure 5.12 show the  $\Delta\rho(T)$  values obtained for the MISTRAL-2 and MISTRAL-3 experiments. Using the JEFF-3.1.1 library, the MISTRAL-2 core reactivity is overestimated by +732 pcm at 20 °C. As for MISTRAL-1, the calculated reactivity increases when the thermal scattering laws of CAB model is used. For MISTRAL-2, the mean difference is approximately +180 pcm. A similar trend is obtained for MISTRAL-3 (+140 pcm).

The continuous lines represent the polynomial fitting for each configuration, according to the following equation:

$$\Delta\rho(T) = a_0 + \sum_{i=1}^n a_i T^i + \Delta\rho_{corr}(T), \quad (5)$$

where the coefficients  $a_i$  are free parameters and  $\Delta\rho_{corr}$  is the correction due to thermal expansion effects ( $\Delta\rho_{corr} = 0$  in MISTRAL-2 and MISTRAL-3 configurations).

The fitting algorithm of the CONRAD code [38] was used. It was not found a correlation between the degree  $n$  of the polynomial and the different physical phenomena present in the experiences (spectral shifts and water expansion). The degree of the polynomial was chosen after doing a Chi-squared analysis up to a third order. The polynomial coefficients for the three MISTRAL configurations are listed in Table 5.5. The reported uncertainties derived only from the Monte Carlo calculation are statistical uncertainties. In order to have a global trend for the MOX cores, MISTRAL-2 and MISTRAL-3, it was done a simultaneous analysis of  $\Delta\rho(T)$  for these two configurations. The calculations were performed by introducing a free normalization factor which does not change the shape of  $\Delta\rho$  as a function of the temperature.

The reactivity correction due to the thermal expansion effects on the MISTRAL-1 configuration is shown in Figure 5.13. The contribution to be done at each temperature step was obtained using eq. (4). The fit (dashed lines) was done in the same way as described before. The polynomial coefficients are summarized in Table 5.6. Likewise the MISTRAL-2 and MISTRAL-3 cores, after the thermal expansion corrections are applied to MISTRAL-1, the best-fit is a linear fit

Table 5.5. Polynomial coefficients  $a_i$  provided by the CONRAD code after the least-square adjustment of the  $\Delta\rho$  values reported in Table 5.4 with eq. (5). A quadratic polynomial fit was done for MISTRAL-1, while a linear fit was proposed for MISTRAL-2 and MISTRAL-3.

Configuration	<sup>1</sup> H in H <sub>2</sub> O TSL model	Polynomial coefficients		
		$a_0$	$a_1$	$a_2$
MISTRAL-1	JEFF-3.1.1	203.2 ± 1.1	0.236 ± 0.023	-0.0164 ± 0.0004
	CAB model	291.2 ± 1.1	0.250 ± 0.023	-0.0128 ± 0.0004
MISTRAL-2	JEFF-3.1.1	758.4 ± 1.1	-0.978 ± 0.188	-
	CAB model	924.0 ± 1.1	-0.722 ± 0.188	-
MISTRAL-3	JEFF-3.1.1	698.2 ± 1.5	-0.978 ± 0.188	-
	CAB model	829.6 ± 1.5	-0.722 ± 0.188	-

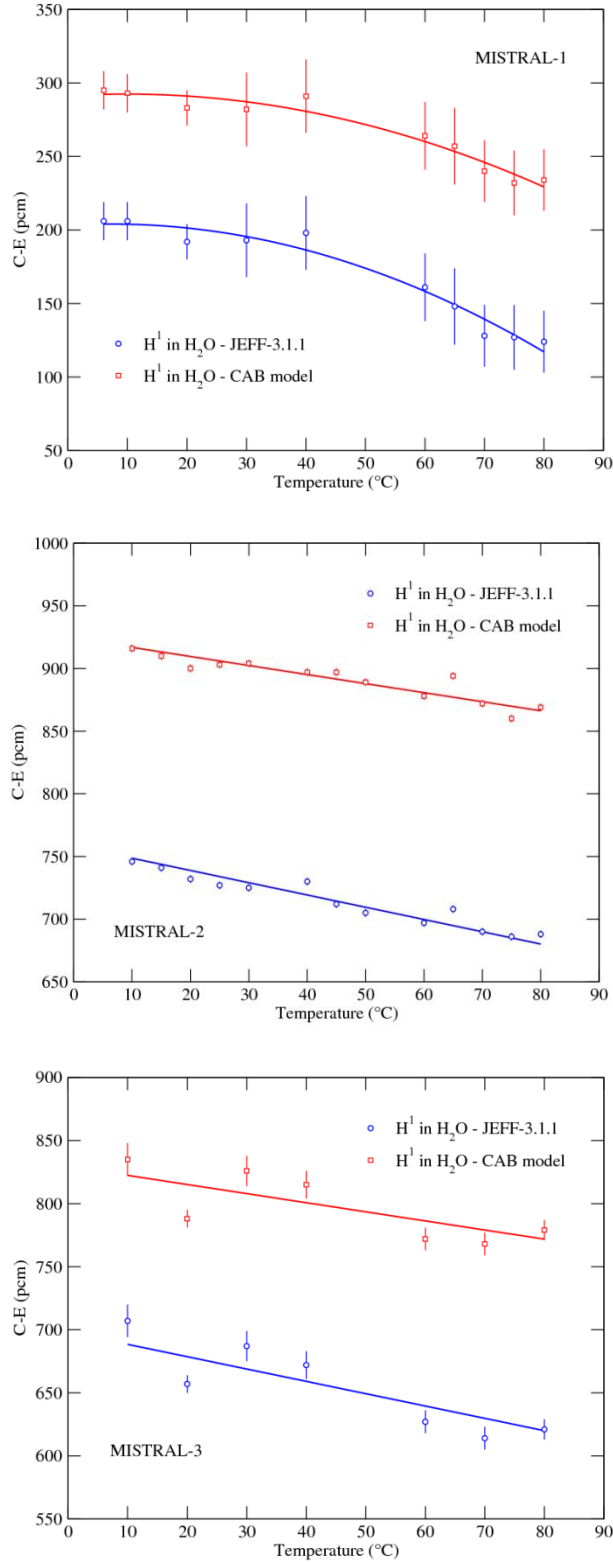


Fig. 5.12 Differences in reactivity  $\Delta\rho(T)$  obtained with the thermal scattering laws of JEFF-3.1.1 and CAB model for the MISTRAL-1, MISTRAL-2 and MISTRAL-3 configurations. The solid lines represent the best fit curves calculated with the CONRAD code.

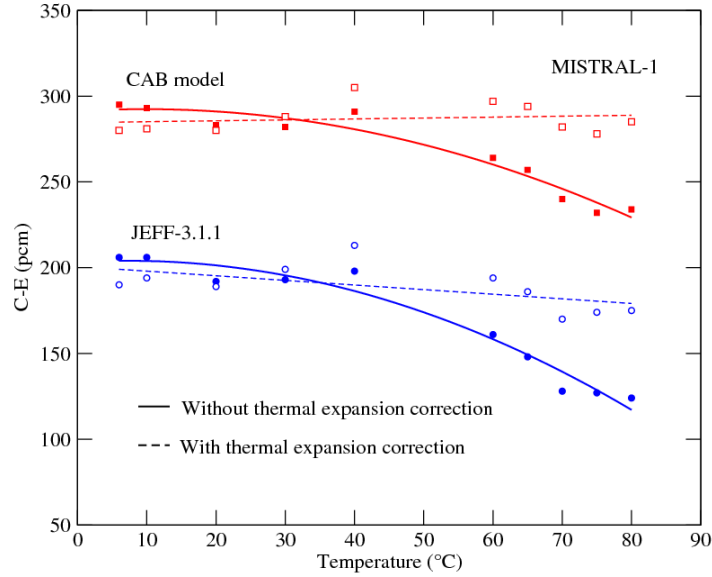


Fig. 5.13 Differences in reactivity  $\Delta\rho(T)$  obtained with the thermal scattering laws of JEFF-3.1.1 and CAB model for the MISTRAL-1 with (empty points) and without (filled points) the thermal expansion effects.

Table 5.6. Comparison of the polynomial coefficients  $a_i$  provided by the CONRAD code after the least-square adjustment of the  $\Delta\rho$  values calculated for MISTRAL-1 with and without the thermal expansion effects corrections. A linear fit is obtained when the reactivity corrections are taken into account.

MISTRAL-1	$^1\text{H}$ in $\text{H}_2\text{O}$ TSL model	Polynomial coefficients		
		$a_0$	$a_1$	$a_2$
Without thermal expansion corrections	JEFF-3.1.1	$203.2 \pm 1.1$	$0.236 \pm 0.023$	$-0.0164 \pm 0.0004$
	CAB model	$291.2 \pm 1.1$	$0.250 \pm 0.023$	$-0.0128 \pm 0.0004$
With thermal expansion corrections	JEFF-3.1.1	$200.7 \pm 12.9$	$-0.269 \pm 0.134$	-
	CAB model	$284.5 \pm 8.9$	$0.054 \pm 0.112$	-

#### 5.4 Analysis and discussions of the reactivity excess in the MISTRAL experiments

The increase of the calculated reactivity of CAB model over JEFF-3.1.1 in the MISTRAL experiments can be explained by analyzing the reaction rates of the relevant isotopes that interact with the neutrons:  $^1\text{H}$  (moderator) and  $^{235}\text{U}$ ,  $^{239}\text{Pu}$  and  $^{241}\text{Pu}$  (fissile isotopes).

#### 5.4.1 Analysis of the $^1\text{H}$ reaction rates

The increase of the calculated reactivity of the CAB model over JEFF-3.1.1 in the MISTRAL experiments can be explained analyzing the  $^1\text{H}$  in  $\text{H}_2\text{O}$  scattering cross sections. Figure 5.14 shows the  $\text{H}_2\text{O}$  cross sections of JEFF-3.1.1 and CAB model at 294 K together with the neutron spectrum of MISTRAL-2 core at the same temperature. In the energy range where it is found the peak of the thermal flux, the cross section of JEFF-3.1.1 is larger than CAB model. This might lead to a higher down-scattering rate of neutrons, increasing then the probability that the thermal neutrons will be absorbed in water instead of being scattered back to the fuel and produce new fissions. The final result is that with the CAB model evaluation, fewer neutrons will be absorbed, producing more fissions and consequently an increase in the keff value.

In MISTRAL-2 and MISTRAL-3 cores, larger differences are detected because MOX fuel calculations are more sensitive to the thermal scattering laws of hydrogen in light water. This might be due to the fact that  $^{239}\text{Pu}$  and  $^{241}\text{Pu}$  have strong fission resonances close to 0.29 eV and 0.27 eV respectively.. This trend was also seen by [49], where it was noticed that plutonium benchmarks have a higher sensitivity to  $^1\text{H}$  in  $\text{H}_2\text{O}$  thermal scattering data than uranium benchmarks from the International Safety Benchmark Evaluation Project (ICSBEP).

In order to confirm this hypothesis, it was calculated the absorption  $\tau_a$  and the scattering  $\tau_n$  reaction rates of  $^1\text{H}$  in  $\text{H}_2\text{O}$  in MISTRAL-1, MISTRAL-2 and MISTRAL-3 configurations at 20 °C. Two energy ranges of interest were calculated:  $10^{-5}$  eV to 7 meV (cold neutrons) and 7meV to 4.95 eV (thermal neutrons). The ratio of the absorption and scattering reaction rates between the JEFF-3.1.1 and CAB model are listed in Table 5.7.

It is seen that from 7 meV to 4.95 eV the absorption and the scattering reaction rates calculated with the TSL of JEFF-3.1.1 are larger than those obtained with CAB model. From  $10^{-5}$  eV to 7 meV, the trend is inversed. This behavior is perceived for the three configurations. This has a correlation with  $^1\text{H}$  in  $\text{H}_2\text{O}$  scattering cross section. Below approximately 7 meV, the cross section obtained with CAB model is larger than JEFF-3.1.1. Above 7meV the cross section of JEFF-3.1.1 overestimates CAB model, reaching a difference of about 5% at the thermal neutron energy. This difference is compatible with the ratio calculation of the scattering reaction rate between the two models: +4.64%, +4.72% and +4.42% for MISTRAL-1, MISTRAL-2 and MISTRAL-3 respectively.

In MISTRAL-2 core, the ratio of the absorption reaction rate from 7 meV to 4.95 eV is almost twice as MISTRAL-1 and MISTRAL-3. This is due to the presence of soluble bore in the moderator. While in MISTRAL-2 the neutron thermal captures in the moderator are caused by water, in the other configurations the neutrons will be more likely absorbed by the  $^{10}\text{B}$  isotope due to its very high thermal absorption cross section. Thus, the hydrogen absorption reaction rate will decrease.

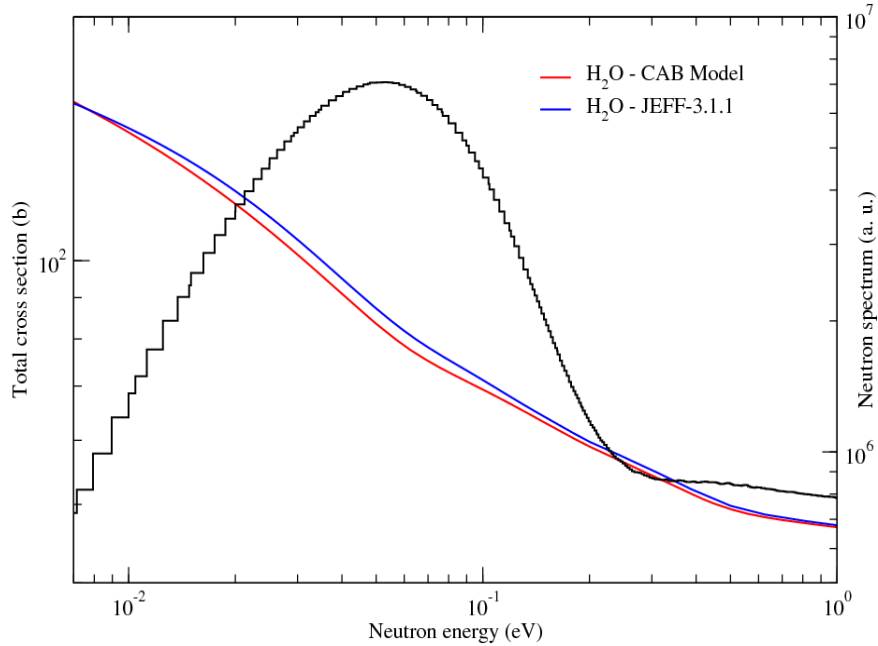


Fig. 5.14 H<sub>2</sub>O cross section calculated with CAB model and JEFF-3.1.1 at 293.6 K, together with the MISTRAL-2 neutron spectrum at the same temperature.

Table 5.7. Ratio of JEFF-3.1.1 to CAB model of the absorption and scattering <sup>1</sup>H in H<sub>2</sub>O reaction rates at 20°C calculated in the MISTRAL experiments.

Energy range	MISTRAL-1 (UOX)		MISTRAL-2 (MOX)		MISTRAL-3 (MOX)	
	absorption	scattering	absorption	scattering	absorption	scattering
10 <sup>-5</sup> eV to 7 meV	-1.31	-3.46	-0.58	-2.76	-1.21	-3.37
7 meV to 4.95 eV	+0.26	+4.64	+0.40	+4.72	+0.18	+4.42

#### 5.4.2 Analysis of the fissile isotopes <sup>235</sup>U, <sup>239</sup>Pu and <sup>241</sup>Pu

If the neutrons are not captured by the <sup>1</sup>H isotope, then they have a chance to be absorbed by the fuel, and produce new fissions if the absorption is carried out by the <sup>235</sup>U, <sup>239</sup>Pu or the <sup>241</sup>Pu.

In order to compare the interaction of the neutrons with the fissile isotopes between JEFF-3.1.1 and CAB model, the ratios of the capture to fission reaction rates for an energy range 10<sup>-5</sup> eV to 7 meV and 7 meV to 4.95 eV were calculated. The ratios of JEFF-3.1.1 to CAB are summarized in Table 5.8 for MISTRAL-1 and MISTRAL-2 configurations.

At the cold neutron energy range (10<sup>-5</sup> eV to 7 meV) the differences between JEFF-3.1.1 and CAB model are negligible and do not explain the origin of the reactivity difference. However, at the thermal energy range (7 meV to 4.95 eV), there are sizable discrepancies for the two configurations (UOX and MOX).

The difference between the capture to fission ratio of the  $^{235}\text{U}$  calculated with the JEFF-3.1.1 thermal scattering law is about 30 pcm larger than the CAB model calculation (MISTRAL-1). In the CAB model there are more fissions, which is translated to a reactivity increase of 100 pcm.

In the case of the MISTRAL-2 core (MOX), the proportion of  $^{235}\text{U}$  in the fuel is lower than in MISTRAL-1 because the main fissile isotope is the  $^{239}\text{Pu}$ . Although the difference between JEFF-3.1.1 and CAB for the  $^{235}\text{U}$  is almost 4 times as MISTRAL-1, the impact on the final reactivity increase is reduced. The reactivity increase of 180 pcm in MISTRAL-2 due to CAB model is mainly driven by the  $^{239}\text{Pu}$ . The thermal scattering of JEFF-3.1.1 increases the capture to fission rate of this isotope approximately 510 pcm more than with CAB model.

Table 5.8. Ratio of JEF-3.1.1 to CAB model of the capture to fission ratio of the three main fissile isotopes at 20 °C calculated in the MISTRAL-1 and MISTRAL-2 experiments. The ratios are measured in pcm.

Energy range	Isotope	MISTRAL-1 (UOX)	MISTRAL-2 (MOX)
10 <sup>-5</sup> eV to 7 meV	$^{235}\text{U}$	+0.08	-0.41
	$^{239}\text{Pu}$	-	-0.99
	$^{241}\text{Pu}$	-	-2.19
7 meV to 4.95 eV	$^{235}\text{U}$	+29.49	+110.31
	$^{239}\text{Pu}$	-	+508.89
	$^{241}\text{Pu}$	-	+14.17

## 5.5 Calculation errors on the isothermal reactivity temperature coefficient for the MISTRAL experiments

Replacing eq. (5) into eq. (1), we obtain the following expression for the calculation error on the reactivity temperature coefficient:

$$\Delta\alpha_{iso}(T) = \sum_{i=1}^n i a_i T^{i-1} + \Delta\alpha_{corr}, \quad (6)$$

where  $\Delta\alpha_{corr}$  is a correction factor introduced to account for the thermal expansion of the materials. For MISTRAL-1,  $\Delta\alpha_{corr} = 0.9 \pm 0.1$  pcm/°C, while for MISTRAL-2 and MISTRAL-3 configurations  $\Delta\alpha_{corr} = 0$  (section 5.2.3).

### 5.5.1 Previous works

Previous interpretations [50, 51] were performed with the deterministic code APOLLO2 [47] by using the evaluated nuclear data libraries JEF-2.2 and JEFF-3.1.1. Results are summarized in Table 5.9.

According to conclusions reported in reference [51], the  $\Delta\alpha_{iso}(T)$  is mainly sensitive to the spectral shift of thermal neutrons in the low temperature range ( $T < 40$  °C). The contribution of the water density effects becomes sizeable when the temperature increases. In addition, the contribution of the thermal spectrum effects to the calculation errors is strongly dependent on the shape of the  $^{235}\text{U}$  and  $^{239}\text{Pu}$  neutron cross sections in the thermal region.

Table 5.9. Summary of the calculation errors  $\Delta\alpha_{iso}(T)$  for the MISTRAL experiments obtained with the deterministic code APOLLO2 in association with the JEF-2.2 and JEFF-3.1.1 nuclear data libraries.

Configuration	Temperature range [°C]	$\Delta\alpha_{iso}(T)$ [pcm/°C]	
		JEF-2.2	JEFF-3.1.1
<b>MISTRAL-1 (UOX)</b>	10 to 40	-0.0 ± 0.3	+0.9 ± 0.4
	40 to 80	-0.1 ± 0.4	+0.1 ± 0.4
	10 to 80	-0.0 ± 0.3	+0.4 ± 0.3
<b>MISTRAL-2 (MOX)</b>	10 to 40	-2.0 ± 0.2	-0.5 ± 0.4
	40 to 80	-1.0 ± 0.3	-1.1 ± 0.4
	10 to 80	-1.5 ± 0.2	-0.9 ± 0.3
<b>MISTRAL-3 (MOX)</b>	10 to 40	-2.3 ± 0.3	-0.4 ± 0.5
	40 to 80	-0.8 ± 0.3	-1.4 ± 0.5
	10 to 80	-1.6 ± 0.3	-1.0 ± 0.4

The main physical trends observed in the MISTRAL-1 configuration between 6 °C and 80 °C for UOX lattices are confirmed by a sensitivity analysis performed on the critical assembly of the Kyoto University between 27 °C and 57 °C [52]. The reported results mainly emphasize the importance of the thermal scattering cross section of hydrogen bound to H<sub>2</sub>O. Such a contribution to the calculation errors  $\Delta\alpha_{iso}(T)$  was not reported in the previous interpretations of the MISTRAL programs.

### 5.5.2 Present results with TRIPOLI4

The calculation errors on the reactivity temperature coefficient are summarized in Table 5.10. The results were averaged over three broad temperature intervals in an equivalent way as in reference [51] in order to point out the physical phenomena dominant in each temperature range.

The present work provides the first interpretation of the calculation errors of the reactivity temperature coefficient with the Monte Carlo code TRIPOLI4. Previous calculations were performed with the deterministic code APOLLO2.

For the UOX configuration (MISTRAL-1), we observe differences of about 0.8 pcm/°C between the APOLLO2 and TRIPOLI4 results. The origin of such a systematic bias is hard to explain, especially since a

better agreement is achieved for the MOX configurations (MISTRAL-2 and MISTRAL-3). Previous studies [53] on the reactivity temperature coefficient showed that the approximations used in a deterministic code like APOLLO2 (discretization of the Boltzmann equation variables, leakage model, etc.) cannot explain the present discrepancy with an exact Monte Carlo calculation. However, results averaged over the whole temperature range (10 °C to 80 °C) remain consistent with those reported in reference [51] and still confirm that the calculation errors are lower (UOX core) or nearly equal (MOX core) to the target accuracy of 1 pcm/°C:

$$\Delta\alpha_{iso} (\text{UOX}) = -0.36 \pm 0.3 \text{ pcm/}^\circ\text{C (JEFF-3.1.1)}$$

$$\Delta\alpha_{iso} (\text{MOX}) = -0.98 \pm 0.4 \text{ pcm/}^\circ\text{C (JEFF-3.1.1)}$$

For the UOX configuration, an improvement is achieved above 40 °C with the thermal scattering law of CAB model. As shown in Figure 5.15, this improvement reaches +0.6 pcm/°C at 80 °C. As a result, the calculation error on the reactivity temperature coefficient over the broad temperature range (10 °C to 80 °C) is close to zero:

$$\Delta\alpha_{iso} (\text{UOX}) = -0.02 \pm 0.3 \text{ pcm/}^\circ\text{C (CAB model)}$$

For the MOX cores, the CAB model for <sup>1</sup>H in H<sub>2</sub>O also leads to an improvement of the calculation error on the reactivity temperature coefficient. Over the temperature range of interest, it was obtained:

$$\Delta\alpha_{iso} (\text{MOX}) = -0.72 \pm 0.4 \text{ pcm/}^\circ\text{C (CAB model)}$$

Table 5.10. Summary of the calculation errors  $\Delta\alpha_{iso}$  (in pcm/°C) for the MISTRAL experiments obtained with the Monte Carlo code TRIPOLI4. The present results are compared with those obtained with the deterministic code APOLLO2 [51]. The experimental uncertainties are also given in pcm/°C. The contribution of the statistical uncertainties due to the Monte Carlo calculations is negligible ( $\pm 0.02$  pcm/°C).

Configuration	Temperature range [°C]	Exp. unc.	$\Delta\alpha_{iso}(T)$ [pcm/°C]		
			JEFF-3.1.1 (APOLLO2)	JEFF-3.1.1 (TRIPOLI4)	CAB model (TRIPOLI4)
MISTRAL-1 (UOX)	10 to 40	$\pm 0.40$	+0.90	+0.29	+0.49
	40 to 80	$\pm 0.40$	+0.10	-0.86	-0.41
	10 to 80	$\pm 0.30$	+0.40	-0.36	-0.02
MISTRAL-2 (MOX)	10 to 80	$\pm 0.30$	-0.90	-0.98	-0.72
MISTRAL-3 (MOX)	10 to 80	$\pm 0.40$	-1.00	-0.98	-0.72

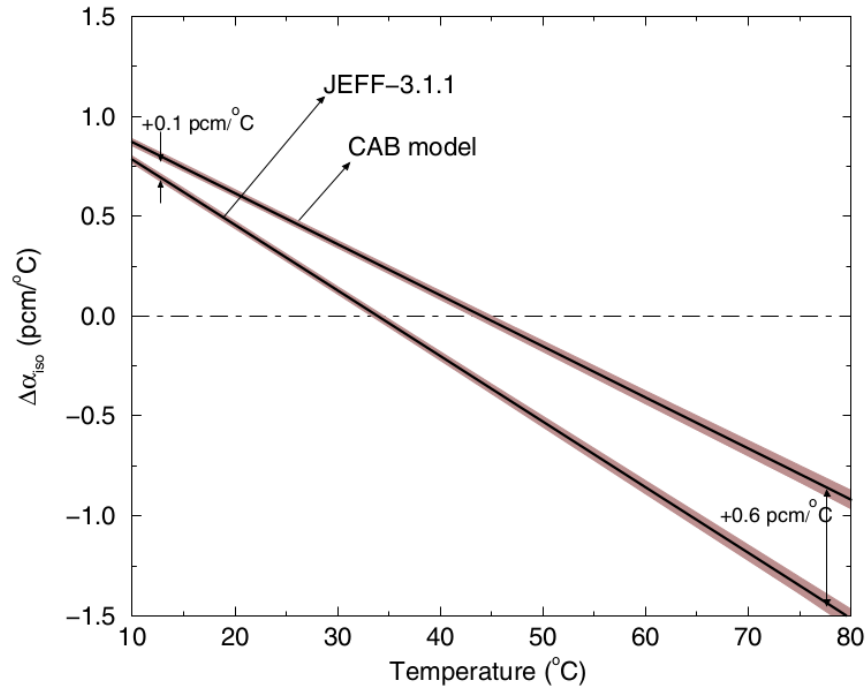


Fig. 5.15 Calculation errors on the reactivity temperature coefficient as a function of the temperature for the MISTRAL-1 experiment. The uncertainty bands accounts for the statistical uncertainty of the Monte Carlo calculations

In order to demonstrate the compatibility of the results when taking into account the thermal expansions effects in MISTRAL-1 to the reactivity difference  $\Delta\rho$ , eq. (6) was applied to the polynomial fit obtained in Table 5.6 (in this case  $\Delta\alpha_{corr} = 0$  for MISTRAL-1 as well). Table 5.11 compares the calculation error on the reactivity temperature coefficient (10 °C to 80 °C) when the thermal expansion corrections are done to the reactivity difference and to reactivity temperature coefficient. The discrepancy between both cases is negligible for JEFF-3.1.1 and for CAB model as well.

Table 5.11. Comparison of the calculation errors  $\Delta\alpha_{iso}$  (in pcm/°C) for the MISTRAL-1 experiment applying the thermal expansion corrections to the reactivity difference  $\Delta\rho$  and to the reactivity temperature coefficient difference  $\Delta\alpha_{iso}$ .

MISTRAL-1	$\Delta\alpha_{iso}(T)$ [pcm/°C]	
	JEFF-3.1.1	CAB model
Thermal expansion corrections to $\Delta\alpha_{iso}$	-0.36	-0.02
Thermal expansion corrections to $\Delta\rho$	-0.27	+0.05

## 5.6 Impact of new evaluations on the MISTRAL benchmark

Two isotope evaluations were corrected in the JEFF-3.1.1 nuclear data library during the development of the present studies. An impact analysis was carried out in the MISTRAL experiments to investigate the influence of the  $^{241}\text{Am}$  (JEFF-3.2) and the  $^{16}\text{O}$  (JEFF-3.3) on the presented results.

### 5.6.1 $^{241}\text{Am}$ (JEFF-3.2)

A remarkable result is the sizeable overestimation of the experimental reactivity by the calculations in MOX lattices (MISTRAL-2 and MISTRAL-3). In MISTRAL-2 it reaches 900 pcm at 20 °C when the thermal scattering law calculated with the CAB model is used. Such an integral trend could be attributed to the americium cross-sections.

New experimental works seem to indicate that the thermal capture cross section and the capture resonance integral of  $^{241}\text{Am}$  could be underestimated in JEFF-3.1.1 by 15% and 20%, respectively [54]. A new  $^{241}\text{Am}$  evaluation was included in the JEFF-3.2 library for improving the calculations of the keff values [55]. Figure 5.16 shows a comparison between the neutron capture cross sections of the  $^{241}\text{Am}$  of JEFF-3.1.1 and JEFF-3.2 nuclear data libraries. The ratio between the cross sections illustrates the increase by 15% of the thermal capture in JEFF-3.2. The thermal neutron spectrum of MISTRAL-2 calculated at 20 °C and 80 °C are also included to highlight the sensitivity of such a change in the cross section.

The excess reactivity was recalculated for MISTRAL-2 and MISTRAL-3 at 20 °C using the new evaluation of the  $^{241}\text{Am}$  of JEFF-3.2 and the two thermal scattering models of  $^1\text{H}$  in  $\text{H}_2\text{O}$  (JEFF-3.1.1 and CAB model). To account the effects with the temperature, the cases for 80 °C were also computed. The differences in reactivity  $\Delta\rho = C - E$  (pcm) are summarized in Table 5.12.

The increase of the thermal capture cross section of the  $^{241}\text{Am}$  decreases the calculated reactivity in  $565 \pm 4$  pcm for MISTRAL-2 at 20 °C when using the TSL of JEFF-3.1.1. Both thermal scattering models of light water give the same trend. At 80 °C it is found the same reactivity decrease. For MISTRAL-3 equivalent tendencies were achieved. A calculated reactivity decrease of  $592 \pm 4$  pcm was found for JEFF-3.1.1 and  $598 \pm 4$  pcm for the CAB model.

Regarding the influence of the change in the  $^{241}\text{Am}$  capture cross section in the thermalization process, no impact is detected using the evaluation of JEFF-3.2 or JEFF-3.1.1. The reactivity difference of MISTRAL-2 at 20 °C between  $^1\text{H}$  in  $\text{H}_2\text{O}$  of CAB model and JEFF-3.1.1, using the  $^{241}\text{Am}$  of JEFF-3.1.1 is  $168 \pm 4$  pcm. The new  $^{241}\text{Am}$  evaluation of JEFF-3.2 gives a reactivity difference of  $166 \pm 4$  pcm at the same temperature. The case at 80 °C confirms this behavior. The discrepancies between the thermal scattering models is  $181 \pm 4$  pcm and  $182 \pm 4$  pcm, for the  $^{241}\text{Am}$  of JEFF-3.1.1 and JEFF-3.2, respectively. Thus, the reactivity difference between the two thermal scattering models remains unchanged.

Finally, the increase of the thermal capture cross section of the  $^{241}\text{Am}$  in JEFF-3.2 library does not have an impact on the reactivity temperature coefficient. It was seen before that the same reactivity

decrease for MISTRAL-2 and MISTRAL-3 was achieved for 20 °C and 80 °C, so the change in the evaluation of this isotope is not sensitive to the reactivity temperature coefficient.

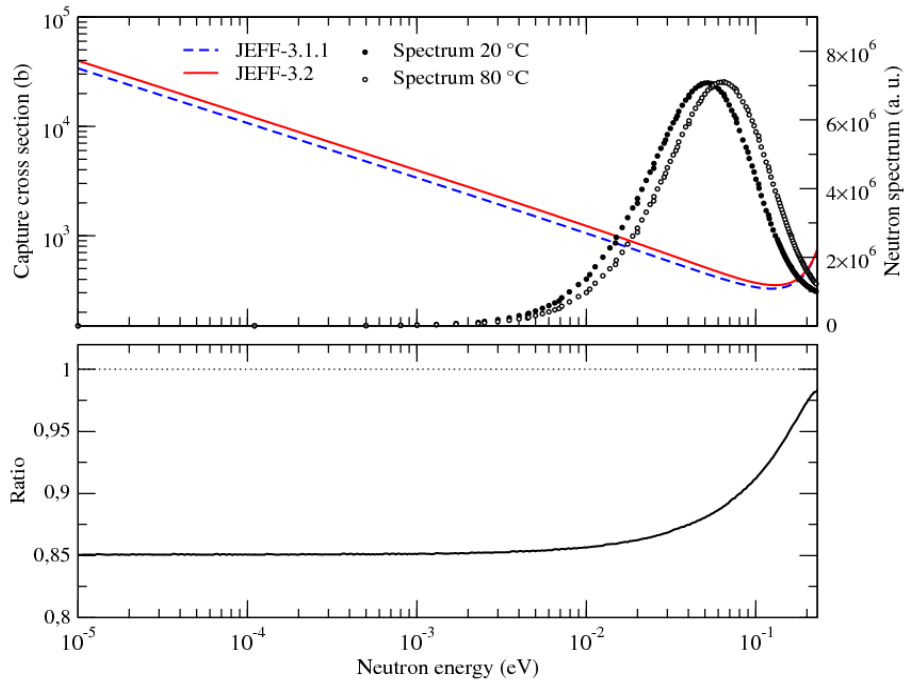


Fig. 5.16 Comparison between the  $^{241}\text{Am}$  capture cross sections as a function of the energy of JEFF-3.1.1 and JEFF-3.2 libraries at 294 K, together with the MISTRAL-2 neutron spectrum at 20 °C and 80 °C.

Table 5.12. Differences in reactivity  $\Delta\rho = C - E$  (pcm) obtained with the thermal scattering laws of JEFF-3.1.1 and CAB model and the  $^{241}\text{Am}$  evaluations of JEFF-3.1.1 and JEFF-3.2 libraries for the MISTRAL-2 and MISTRAL-3 configurations at 20 °C and 80 °C. The statistical uncertainty due to the Monte Carlo calculations is 3 pcm.

T (°C)	$^{241}\text{Am}$	MISTRAL-2 (MOX)		MISTRAL-3 (MOX)	
		$^1\text{H}$ in $\text{H}_2\text{O}$		$^1\text{H}$ in $\text{H}_2\text{O}$	
		JEFF-3.1.1	CAB model	JEFF-3.1.1	CAB model
20	JEFF-3.1.1	732	900	657	788
	JEFF-3.2	167	333	65	190
80	JEFF-3.1.1	688	869	621	779
	JEFF-3.2	122	304	35	187

### 5.6.2 $^{16}\text{O}$ (JEFF-3.3 T3)

The  $^{16}\text{O}$  presents a  $(n,\alpha)$  reaction at an energy threshold of about 2.354 MeV (Figure 5.17). Large differences up to 30% between the measured and the evaluated data  $^{16}\text{O}$   $(n,\alpha)$  cross section were identified. This issue motivated the re-evaluation of this isotope in the frame of the Collaborative International Evaluated Library Organization, named CIELO project [56]. L. Leal et al. [57] identified that the  $^3\text{He}$  production in JEFF-3.1.1 was underestimated when compared with the experimental data of Bair and Hass [58]. A new evaluation was proposed in the recent JEFF-3.3 T3 nuclear data library where the cross section was renormalized to be compatible with the data.

The  $^3\text{He}$  production has important consequences in a critical system. As the neutrons are produced after fission at an energy close to the reaction threshold, an increase of the cross section will reduce the amount of neutrons that will slow down to produce new fissions. The trend, thus, is to lower the reactivity.

The reactivity excess was recalculated for MISTRAL-1, MISTRAL-2 and MISTRAL-3 at 20 °C and 80 °C using the new evaluation of the  $^{16}\text{O}$  of JEFF-3.3 and the two thermal scattering models of  $^1\text{H}$  in  $\text{H}_2\text{O}$  (JEFF-3.1.1 and CAB model). The differences in reactivity  $\Delta\rho = C - E$  (pcm) are summarized in Table 5.13.

The increase of the  $^3\text{He}$  production reaction cross section of the  $^{16}\text{O}$  decreases the calculated reactivity in  $191 \pm 4$  pcm for MISTRAL-1 at 20 °C when using the TSL of JEFF-3.1.1. The same trend is found for CAB model,  $189 \pm 4$  pcm. For the MOX configurations the impact is slightly less significative than for the UOX configuration. In the case of MISTRAL-2, the reactivity decreases  $124 \pm 4$  pcm and  $122 \pm 4$  pcm with the JEFF-3.1.1 and CAB model respectively. Finally for MISTRAL-3, similar trends are achieved. The calculated reactivity decreases  $128 \pm 4$  pcm if the thermal scattering model of JEFF-3.1.1 is used, and  $133 \pm 4$  pcm with the CAB model.

It was found a reactivity decrease at 80 °C equivalent for the MISTRAL-1, MISTRAL-2 and MISTRAL-3 configurations. The new evaluation for the  $^{16}\text{O}$  of JEFF-3.3 does not have an impact on the reactivity temperature coefficient.

The difference in reactivity between JEFF-3.1.1 and CAB model using the  $^{16}\text{O}$  of JEFF-3.3 exhibits no change with respect to the  $^{16}\text{O}$  of JEFF-3.1.1. The change in the  $(n,\alpha)$  reaction of this isotope is not sensitive to thermal neutron scattering.

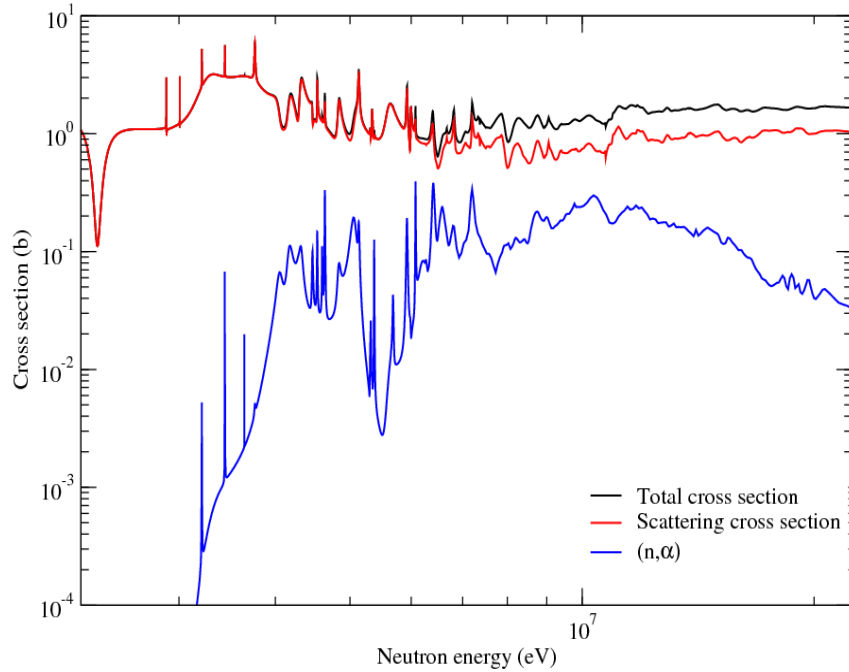


Fig. 5.17 Comparison between the  $^{16}\text{O}$  total, scattering and  $(n,\alpha)$  cross sections as a function of the energy of JEFF-3.1.1 at 294 K.

Table 5.13. Differences in reactivity  $\Delta\rho = C - E$  (pcm) obtained with the thermal scattering laws of JEFF-3.1.1 and the CAB model and the  $^{16}\text{O}$  evaluations of JEFF-3.1.1 and JEFF-3.3 libraries for the MISTRAL-1, MISTRAL-2 and MISTRAL-3 configurations at 20 °C and 80 °C. The statistical uncertainty due to the Monte Carlo calculations is 3 pcm.

T (°C)	$^{16}\text{O}$	MISTRAL-1 (UOX)		MISTRAL-2 (MOX)		MISTRAL-3 (MOX)	
		$^1\text{H}$ in $\text{H}_2\text{O}$		$^1\text{H}$ in $\text{H}_2\text{O}$		$^1\text{H}$ in $\text{H}_2\text{O}$	
		JEFF-3.1.1	CAB model	JEFF-3.1.1	CAB model	JEFF-3.1.1	CAB model
20	JEFF-3.1.1	192	283	732	900	657	788
	JEFF-3.3	1	94	608	778	529	654
80	JEFF-3.1.1	124	234	688	869	621	779
	JEFF-3.3	-60	51	568	746	495	653

## 5.7 Impact of the $^{16}\text{O}$ in $\text{H}_2\text{O}$ thermal scattering law in the MISTRAL experiment

In order to evaluate the impact of treating the  $^{16}\text{O}$  isotope as a free gas or bound to  $\text{H}_2\text{O}$ , it was calculated the reactivity at 20 °C for MISTRAL-1 using the  $^{16}\text{O}$  in  $\text{H}_2\text{O}$  obtained with the CAB model. Table 5.14 compares the reactivity excess  $\Delta\rho$  of  $^{16}\text{O}$  in the free gas approximation and bound to the water molecule. The discrepancy between both cases is negligible.

In chapter 3 it was seen that the scattering cross section of  $^{16}\text{O}$  in  $\text{H}_2\text{O}$  presents important disagreements with the free gas approximation below 10 meV. The thermal reactors are not sensitive to the cold neutron energy range, so the impact of using  $^{16}\text{O}$  in  $\text{H}_2\text{O}$  in the MISTRAL-1 calculation is unimportant.

Table 5.14. Excess reactivity calculated with the TRIPOLI4 code for MISTRAL-1 at 20 °C for oxygen bound to light water molecule and as a free gas. The statistical uncertainty of the calculations is 3 pcm.

Moderator	$\Delta\rho$ (pcm)
$^1\text{H}$ in $\text{H}_2\text{O}$ + $^{16}\text{O}$ free gas	$283 \pm 12$
$^1\text{H}$ in $\text{H}_2\text{O}$ + $^{16}\text{O}$ in $\text{H}_2\text{O}$	$271 \pm 12$

## 5.8 Preliminary conclusions

The physics of thermal scattering were analyzed from a microscopic point of view in chapters 3 and 4, studying specifically the light water. This chapter aimed at characterizing the behavior of the thermal scattering laws of JEFF-3.1.1 nuclear data library and of CAB model in a neutron transport calculation. A benchmark calculation allows to examine global trends which involve other important isotopes in reactor physics like  $^{16}\text{O}$ ,  $^{235}\text{U}$ ,  $^{239}\text{Pu}$ .

The interpretation of the reactivity temperature coefficient of the MISTRAL experiments was done using the Monte-Carlo code TRIPOLI4. The results confirmed the previous work performed with the deterministic code APOLLO2 and provided new integral trends in relation with the thermal scattering law of hydrogen bound to light water.

The comparison of the excess of reactivity calculated with the thermal scattering laws of JEFF-3.1.1 library and CAB model shows the impact of the different shapes of the scattering cross section in the thermal energies in the neutron transport. The decrease in the scattering cross section of  $^1\text{H}$  in  $\text{H}_2\text{O}$  of CAB model leads to an increase of the calculated reactivity of +100 pcm on average for MISTRAL-1 (UOX lattice) and +180 pcm on average for MISTRAL-2 configuration (MOX fuel). The reaction rates calculated for MISTRAL-1, MISTRAL-2 and MISTRAL-3 might explain these trends, as the thermal captures of  $^1\text{H}$  of JEFF-3.1.1 are larger than CAB model in the same energy range of interest. The neutrons that were not absorbed in water will produce new fissions with the  $^{235}\text{U}$  isotope. The effect is even more sensitive for MOX cores because the  $^{239}\text{Pu}$  and  $^{241}\text{Pu}$  have fission resonances close to 0.29 and 0.27 eV.

In the whole temperature range of interest for this work [10 °C - 80 °C], the calculation error on RTC for a standard UOX lattice is close to 0.4 pcm/°C when the JEFF-3.1.1 library is used. Such a bias vanishes and becomes closer to zero ( $\Delta\alpha_{iso} = 0.02$  pcm/°C) when the thermal scattering law is replaced by the one generated with the CAB model. This result indicates that the spectral components of the error in the RTC as well as the water expansion effects are well described. For MOX fuel configurations, the calculation error on RTC is of the order of 1.0 pcm/°C by using the JEFF-3.1.1 library. Our Monte-Carlo calculations show a slight reduction of the bias with the thermal scattering laws coming from the CAB model. The calculation error on RTC becomes close to 0.7 pcm/°C. Such an improvement (+0.3 pcm/°C) is of the same order of magnitude as the uncertainty of the  $^{239}\text{Pu}$  thermal cross section shapes.

Results obtained with the CAB model aim at demonstrating the interest of using Molecular Dynamic simulations for producing reliable thermal scattering laws of hydrogen bound in light water. In cold operating conditions at atmospheric pressure, Molecular Dynamic simulations seem to provide better  $S(\alpha,\beta)$  tables at temperatures where the change of water phase becomes relevant.

# Chapter 6

## Thermal scattering function uncertainties

In the previous chapters it was seen how the microscopic (double differential cross section, total cross section) and macroscopic quantities (keff, reactivity temperature coefficient) are calculated from the evaluation of the thermal scattering function. No information was given regarding the uncertainties of the TSL models and the propagation to other quantities of interest.

The uncertainty quantification of the neutronic parameters is fundamental for the correct prediction of a critical system behavior determining as well the safety operation margins. The main uncertainty source in a neutronic calculation comes from the nuclear data uncertainties. This is the reason why the uncertainty quantification of the evaluated nuclear data is an important issue for the evaluators. The evaluators report the uncertainties in terms of the variance-covariance matrices. The variance is the measure of the dispersion of certain variables with respect to the mean value (or nominal value). The covariance is the measure of the joint variability of two variables.

Till the date, there are no covariance matrices reported for the light water thermal scattering function for any nuclear data library. Its generation is not straightforward because of the very large amount of data needed to be stored, representing a major concern in terms of the format.

The beginning of this chapter will deal with an overview of the uncertainty quantification, necessary for the following sections. Then it will be presented the methodology used for producing the variance-covariance matrices for the thermal scattering models of JEFF-3.1.1 library and CAB model at T = 294 K.

### *6.1 Introduction to uncertainty quantification*

#### *6.1.1 Classification of the uncertainties*

It is worth defining the nature of the uncertainties that arise in an experiment. There are many ways for their classification but following the reference [59], the uncertainties can be categorized in random and systematic.

The random (or statistical) errors are related to the counting process done in a measurement. If the measurements are independent, then they obey a statistical law, which tends to a Poisson distribution for a large number of counts. The systematic uncertainties correspond to the unavoidable deviations from the true value that cannot be minimized by the repetition of the experiment. They introduce a bias in the measurement and correlations between the data.

#### *6.1.2 Uncertainties propagation*

If we consider a variable  $z$  which is derived from the measurements of two quantities  $x_1$  and  $x_2$ , each one with uncertainties  $\sigma_{x_1}$  and  $\sigma_{x_2}$  respectively, then the uncertainty in  $z$  is calculated as [59]:

$$\sigma_z^2 = \left( \frac{\partial z}{\partial x_1} \sigma_{x_1} \right)^2 + \left( \frac{\partial z}{\partial x_2} \sigma_{x_2} \right)^2 + 2 \frac{\partial z}{\partial x_1} \frac{\partial z}{\partial x_2} \sigma_{x_1 x_2}, \quad (1)$$

where the standard deviation  $\sigma_{x_1}$  (likewise for  $\sigma_{x_2}$ ) is:

$$\sigma_{x_1} = \sqrt{\frac{1}{N} \sum_{i=1}^N (x_{1i} - \bar{x}_1)^2}, \quad (2)$$

where  $N$  is the number of measurements done in the experiment and  $\bar{x}_1$  the average value of all the  $x_{1i}$  measurements.

The third term in eq. (1) is originated by the fact that  $x_1$  and  $x_2$  might, in general, be correlated, and  $\sigma_{x_1 x_2}$  is called the covariance, which is defined as:

$$\sigma_{x_1 x_2} = \frac{1}{N} \sum_{i=1}^N (x_{1i} - \bar{x}_1)(x_{2i} - \bar{x}_2). \quad (3)$$

Particularly, if the quantities  $x_1$  and  $x_2$  are independent, then the covariance term is zero. The uncertainty for the variable  $z$  turns to:

$$\sigma_z = \sqrt{\left( \frac{\partial z}{\partial x_1} \sigma_{x_1} \right)^2 + \left( \frac{\partial z}{\partial x_2} \sigma_{x_2} \right)^2}. \quad (4)$$

A generalization can be done if now  $z$  is the *output* vector of dimension “ $k$ ”,  $\bar{z} = \bar{z}(\bar{x})$ , where each  $z_i = z_i(\bar{x})$ . If the *input* parameter vector  $\bar{x}$  has a dimension “ $n$ ”, then it can be demonstrated that eq. (1) turns to the matrix form:

$$\begin{pmatrix} \sigma_{z_1}^2 & \dots & \sigma_{z_1 z_k} \\ \vdots & \ddots & \vdots \\ \sigma_{z_k z_1} & \dots & \sigma_{z_k}^2 \end{pmatrix} = \begin{pmatrix} \frac{\partial z_1}{\partial x_1} & \dots & \frac{\partial z_1}{\partial x_n} \\ \vdots & \ddots & \vdots \\ \frac{\partial z_k}{\partial x_1} & \dots & \frac{\partial z_k}{\partial x_n} \end{pmatrix} \begin{pmatrix} \sigma_{x_1}^2 & \sigma_{x_1 x_2} & \dots & \sigma_{x_1 x_n} \\ \sigma_{x_2 x_1} & \sigma_{x_2}^2 & \dots & \sigma_{x_2 x_n} \\ \vdots & \vdots & \ddots & \vdots \\ \sigma_{x_n x_1} & \sigma_{x_n x_2} & \dots & \sigma_{x_n}^2 \end{pmatrix} \begin{pmatrix} \frac{\partial z_1}{\partial x_1} & \dots & \frac{\partial z_k}{\partial x_1} \\ \vdots & \ddots & \vdots \\ \frac{\partial z_1}{\partial x_n} & \dots & \frac{\partial z_k}{\partial x_n} \end{pmatrix}. \quad (5)$$

The standard deviation of any output variable  $z_i$  and the covariance between two any output variables  $z_i, z_j$  are then calculated respectively as:

$$\sigma_{z_i} = \sqrt{\sum_{l=1}^n \sum_{m=1}^n \frac{\partial z_i}{\partial x_l} \frac{\partial z_i}{\partial x_m} \sigma_{x_l x_m}}, \quad (6)$$

$$\sigma_{z_i z_j} = \sum_{l=1}^n \sum_{m=1}^n \frac{\partial z_i}{\partial x_l} \frac{\partial z_j}{\partial x_m} \sigma_{x_l x_m}. \quad (7)$$

The derivative terms  $\frac{\partial z}{\partial x}$  represent the change in the output variable when there is a perturbation in an input variable. Physically they quantify how sensitive is a variable to an input parameter.

If  $M_x$  and  $\Sigma$  are the variance-covariance matrix between the input parameters  $\bar{x}$  and the output parameters  $\bar{y}$  respectively, then the eq. (5) can be represented more synthetically in the so-called “sandwich formula” form:

$$\Sigma = SM_xS^T. \quad (8)$$

This approach consists then of calculating the derivative matrix  $S$  in order to perform the uncertainties propagation. However, a constraint appears if the output variable is subjected to strong nonlinear effects. In this case, other methods like the Total Monte Carlo (TMC) uncertainty propagation [60] might be an option. The disadvantage is the large number of calculations demanded which are expensive computationally, representing a limitation for the applications to nuclear data uncertainty propagation.

An analytic uncertainty propagation approach was done in the present work. Till now, nothing was said regarding the covariance matrix of the input parameters  $M_x$ . In general, the correlation between the parameters is not straightforwardly obtained. The nuclear data evaluators rely on the probability theory and on the experimental data to produce a best-estimate set of these parameters. In the next section it will be explained how the Bayes theorem and an analytic method, like the Generalized Least Square Method (GLSM), are used to upgrade the knowledge of the parameters with the experimental data.

## 6.2 The generalized least squared method

Using the Bayes’ theorem [61], it can be settled that the *posterior* information of a quantity is proportional to the *prior* one and a likelihood function which yields the probability to obtain an experimental data set  $\bar{y}$  for a given model parameters  $\bar{x}$ :

$$\text{posterior } p(\bar{x}/\bar{y}, U) \propto \text{prior } p(\bar{x}, U) \cdot \text{likelihood } p(\bar{y}/\bar{x}, U). \quad (9)$$

The eq. (9) points out that the posterior probability distribution  $p(\bar{x}/\bar{y}, U)$  on the model parameters  $\bar{x}$  can be obtained with a certain prior distribution *prior*  $p(\bar{x}, U)$  and a likelihood function  $p(\bar{y}/\bar{x}, U)$  that expresses the probability to obtain the observed data, given the prior parameters values.

In order to have an analytic resolution, we need a probability distribution for the prior and the likelihood distributions. It can be demonstrated [62] that a Gaussian form distribution in both maximizes the information entropy from the theorem of maximum entropy. The posterior probability distribution yields then:

$$p(\bar{x}/\bar{y}) \propto \exp \left[ -\frac{1}{2} (\bar{x} - \bar{x}_{prior})^T M_{\bar{x}_{prior}}^{-1} (\bar{x} - \bar{x}_{prior}) - \frac{1}{2} (\bar{y} - \bar{t})^T M_{\bar{y}}^{-1} (\bar{y} - \bar{t}) \right], \quad (10)$$

where the  $M_{\bar{x}_{prior}}$  is the prior parameters covariance matrix,  $M_{\bar{y}}$  is the experimental covariance matrix and  $\bar{t} = \bar{t}(\bar{x})$  is the theoretical model.

The problem of finding the best estimates parameters vector  $\bar{x}$  from a prior knowledge is reduced to minimizing a cost function [63]:

$$\chi^2 = [(\bar{x} - \bar{x}_{prior})^T M_{\bar{x}_{prior}}^{-1} (\bar{x} - \bar{x}_{prior}) + (\bar{y} - \bar{t})^T M_{\bar{y}}^{-1} (\bar{y} - \bar{t})] = \min \quad (11)$$

This procedure is the Generalized Least Squared Method (GLSM). The solution to eq. (11) is found iteratively by the Newton-Raphson method. The posterior parameter vector at the iteration “ $i$ ” and the model parameter covariance matrix are calculated respectively as:

$$\bar{x}^i = \bar{x}^{i-1} M_{\bar{x}}^i (G_{\bar{x}}^{i-1})^T (M_{\bar{y}})^{-1} (\bar{y} - \bar{t}^{i-1}), \quad (12)$$

$$(M_{\bar{x}}^i)^{-1} = (M_{\bar{x}}^{i-1})^{-1} (G_{\bar{x}}^{i-1})^T (M_{\bar{y}})^{-1} G_{\bar{x}}^{i-1}, \quad (13)$$

where the matrix  $G_{\bar{x}}$  is the derivative matrix of the theoretical model with respect to the parameters:

$$G_{\bar{x}} = \begin{pmatrix} \frac{\partial t_1}{\partial x_1} & \dots & \frac{\partial t_1}{\partial x_n} \\ \vdots & \ddots & \vdots \\ \frac{\partial t_k}{\partial x_1} & \dots & \frac{\partial t_k}{\partial x_n} \end{pmatrix}. \quad (14)$$

This GLS fitting algorithm was used to find the covariance matrix of the thermal scattering model with the CONRAD code (Code for Nuclear Reaction Analysis and Data Assimilation) [38].

### 6.3 The systematic uncertainties

A key point in the nuclear data uncertainty evaluating process is the evaluation of the uncertainties of systematic origin. They are responsible for introducing strong correlations between experimental data.

Examples of the experimental parameters that affect significantly the data are: the normalization, the background, the experimental resolution, the sample composition and the temperature. These parameters, called “nuisance” parameters, correspond to the aspect of physical realities whose properties are not of particular interest as such but are fundamental for assessing reliable model parameters [64].

In this frame, it was implemented in the CONRAD code [38], an analytic marginalization technique for taking into account the nuisance parameters [65].

If  $\bar{\theta} = (\theta_1, \theta_2, \dots, \theta_m)$  is the nuisance parameter vector with a covariance matrix  $M_{\bar{\theta}}$ , it can be demonstrated that the posterior covariance matrix after the marginalization  $M_{\bar{x}}^{marg}$  is obtained as [66]:

$$M_{\bar{x}}^{marg} = M_{\bar{x}} + (G_{\bar{x}}^T G_{\bar{x}})^{-1} G_{\bar{x}}^T G_{\bar{\theta}} M_{\bar{\theta}} G_{\bar{\theta}}^T G_{\bar{x}} (G_{\bar{x}}^T G_{\bar{x}})^{-1}, \quad (15)$$

where the matrix  $G_{\bar{\theta}}$  is the derivative matrix of the theoretical model with respect to the nuisance parameters vector:

$$G_{\bar{\theta}} = \begin{pmatrix} \frac{\partial t_1}{\partial \theta_1} & \cdots & \frac{\partial t_1}{\partial \theta_m} \\ \vdots & \ddots & \vdots \\ \frac{\partial t_k}{\partial \theta_1} & \cdots & \frac{\partial t_k}{\partial \theta_m} \end{pmatrix}. \quad (16)$$

The full covariance matrix  $\Sigma$  between the *extended* model parameter vector  $\bar{\delta} = \begin{pmatrix} \bar{x} \\ \bar{\theta} \end{pmatrix}$  is expressed as:

$$\Sigma = \begin{pmatrix} M_{\bar{x}}^{marg} & M_{\bar{x},\bar{\theta}} \\ M_{\bar{\theta},\bar{x}} & M_{\bar{\theta}} \end{pmatrix}. \quad (17)$$

The cross-covariance terms between  $\bar{x}$  and  $\bar{\theta}$  are calculated by introducing the ‘‘variance penalty’’ terms [67]. The variance penalty is a measure of the contribution of the uncertainty of the nuisance variables to the variance of the calculated quantity  $\bar{t}$ . This work was implemented in the CONRAD code and effectively applied for calculating the covariances of the fast neutron capture cross sections of Xe isotopes [66]. The cross-covariance term is:

$$M_{\bar{x},\bar{\theta}} = -(G_{\bar{x}}^T G_{\bar{x}})^{-1} G_{\bar{x}}^T G_{\bar{\theta}} M_{\bar{\theta}}. \quad (18)$$

Throughout these sections it was explored briefly the theory behind the covariance matrix evaluation methodology, which will be necessary for producing a covariance matrix of the thermal scattering function  $S(\alpha, \beta)$ . It was presented the GLS method to find the best-estimate model parameters and the associated covariance matrix. This fitting algorithm was implemented in the data assimilation code CONRAD. For the treatment of the systematic uncertainties that arise from the nuisance parameters, it was developed the marginalization technique (eq. 15) and implemented as well in the CONRAD code.

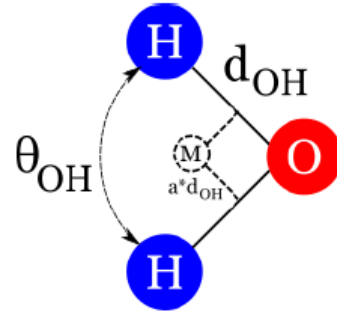
## 6.4 Covariance matrix of the thermal scattering law of the CAB model

### 6.4.1 Parameters of the CAB model

The generation of a  $S(\alpha, \beta)$  covariance matrix requires the determination of the covariance matrix of the parameters involved in the CAB model [5]. The frequency spectrum  $\rho(\beta)$  of the CAB model is produced by means of the molecular dynamics simulation code GROMACS [20]. This code needs as input the water potential that describes the intermolecular and intramolecular interactions between an ensemble of water molecules. The CAB model uses the TIP4P/2005f potential [21]. The description of each parameter of the potential, listed in Table 6.1, was done in section 3.3.1 of chapter 3.

Table 6.1. Parameters of the TIP4P/2005f water potential.

TIP4P/2005f potential parameter	
$\epsilon_O$ (KJ/mol)	0.7749
$\sigma_O$ (nm)	3.1644
$q_H$ (e <sup>-</sup> )	0.5564
$q_M$ (e <sup>-</sup> )	-1.1128
$D_{OH}$ (KJ/mol)	432.581
$\beta_{OH}$ (1/nm)	22.87
$d_{OH}$ (nm)	0.09419
$k_\theta$ (KJ/mol/rad <sup>2</sup> )	367.81
$\theta_{OH}$ (°)	107.4
$d_{OM}$ (nm)	0.15555



The analysis does not include the parameter  $q_M$  (dummy atom charge), because its nominal value is redundant to the hydrogen charge  $q_H$ . Following the notation introduced in this chapter, the model parameter vector  $\bar{x}$  is in this context:

$$\bar{x} = (\epsilon_O, \sigma_O, q_H, D_{OH}, \beta_{OH}, d_{OH}, k_\theta, \theta_{OH}, d_{OM}). \quad (19)$$

The aim of the present work is not to produce a new set of best-estimate water potential parameters. That task was already accomplished in [21], where it was done a parameterization of the parameters with thermophysical properties of water. The objective is to generate the variances and the covariances between the parameters (retroactive analysis).

#### 6.4.2 Experimental data for the fit in the GLSM

In eq. (12), an appropriate set of experimental data  $\bar{y}$  is required by the generalized least squared method to find iteratively the variance-covariance matrix  $M_{\bar{x}}$ .

The experimental data of the light water total cross section at 294 K found in EXFOR database, shown in Figure 6.1, were used [25, 26, 27, 28]. The reaction cross section are important microscopic quantities that serve as input in reactor calculation codes to obtain global parameters such as the keff value, the neutron spectrum, etc.

It was used in the fitting procedure, in addition, the measurements of the light water average cosine of the scattering angle  $\bar{\mu}$  at 294 K done by J. Beyster et al. (Figure 6.2) [68]. From the average cosine of the scattering angle we derive other important parameters like the neutron diffusion coefficient which is used in the diffusion equation to calculate the neutron flux.

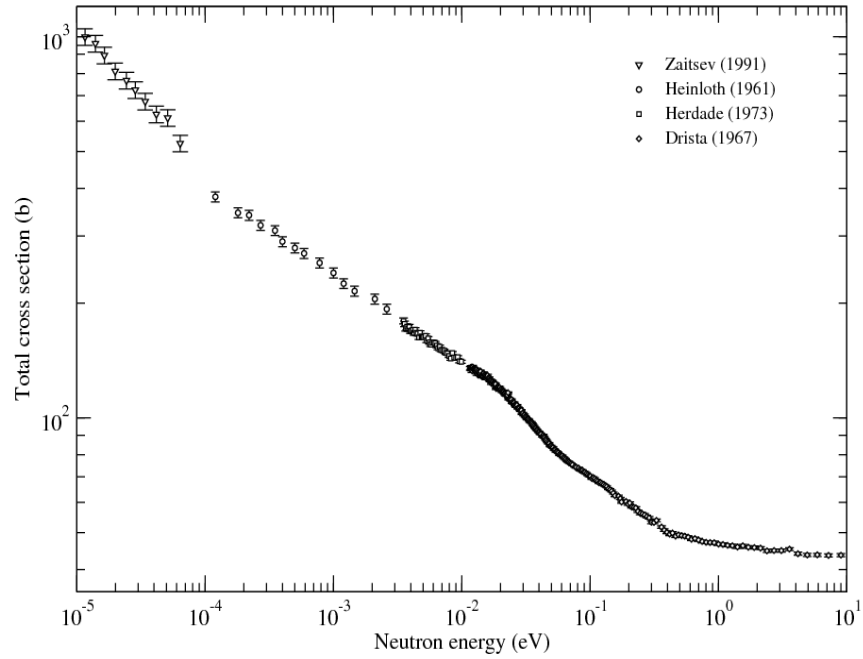


Fig. 6.1 Total cross section measurements at 294 K used in the fitting procedure of the GLSM.

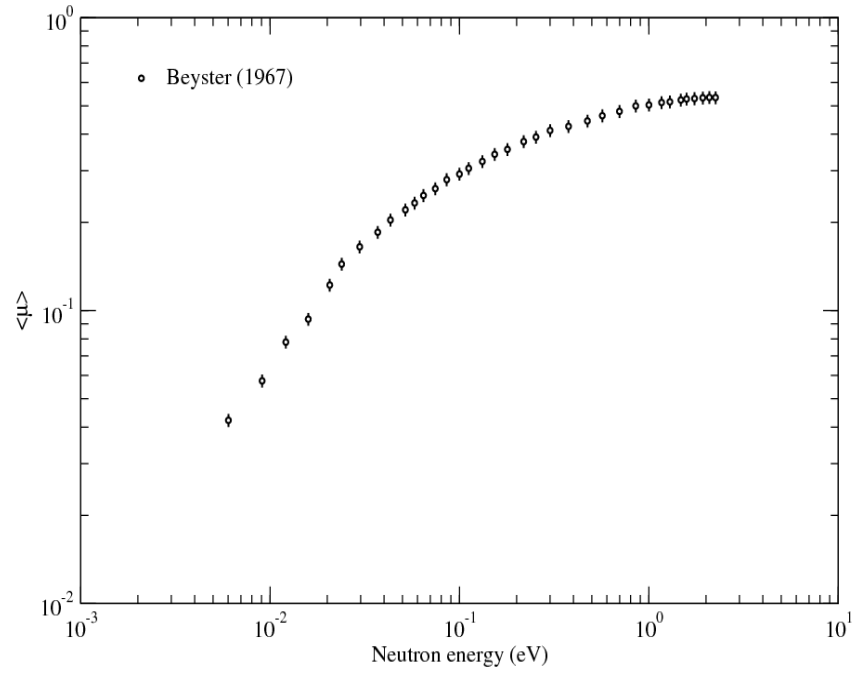


Fig. 6.2 Average cosine of the scattering angle measurements at 294 K used in the fitting procedure of the GLSM.

### 6.4.3 The nuisance parameters

#### 6.4.3.1 Experimental parameters

The total cross section data was converted to transmission data in order to perform the analysis of the experimental parameters involved in the experiments. The transmission coefficient  $C(E)$  and the total cross section  $\sigma_{tot}(E)$  are related by the following equation:

$$C(E) = \exp[-n\sigma_{tot}(E)], \quad (20)$$

where  $n$  is the sample areal density in  $\text{barn}^{-1}$ .

Figure 6.3 shows the transmission coefficient as a function of the neutron energy measured by [26, 27, 28] with the theoretical transmission calculated with the CAB model at 294 K. The data measured by Zaitsev et al. [25] was not possible to convert to transmission because the sample thickness used in the experiment was not published.

The cross section uncertainties, reported in the literature, combine the statistical errors and the areal density errors. As the latter one is a systematic source of uncertainty its contribution was subtracted to be marginalized, while the statistical uncertainties were included in the fitting procedure.

In addition, the experimental normalization factor  $N$  and the background correction  $B$  need to be added in the study. The eq. (20) turns into:

$$C(E) = N \cdot \exp[-n\sigma_{tot}(E)] + B. \quad (21)$$

The average cosine of the scattering angle  $\bar{\mu}$  is calculated with the double differential scattering cross section  $\frac{d^2\sigma}{d\Omega dE'}$  provided by the THERMR module of NJOY code, with the following equation:

$$\bar{\mu} = \int_0^\pi \cos \theta \left[ \int_0^\infty \frac{d^2\sigma}{d\Omega dE'} dE' \right] d\theta. \quad (22)$$

Finally, the temperature of the water sample presents an uncertainty which depends on the quality of the regulation system. No information is available in the references. At 294 K it was adopted an uncertainty of  $\pm 5$  K.

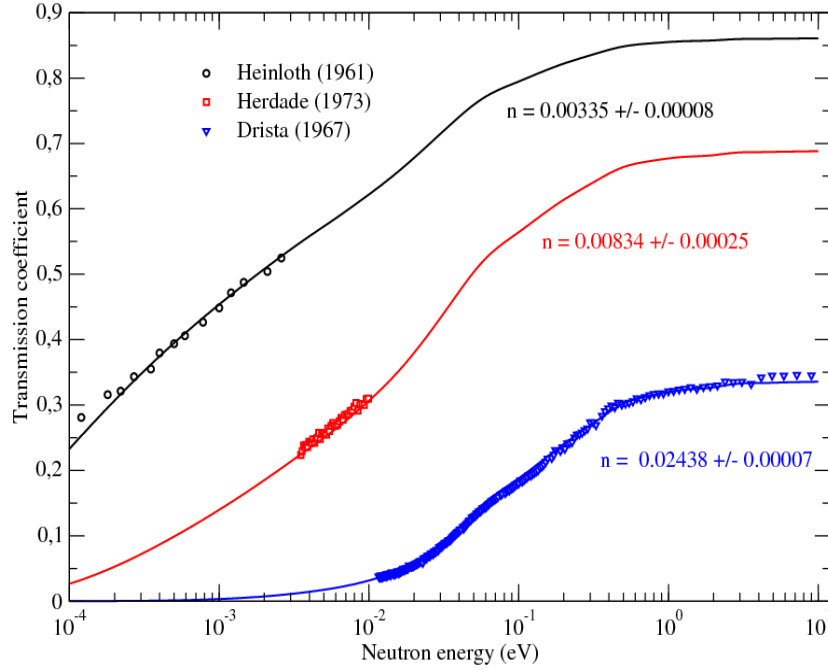


Fig. 6.3 Transmission data of [26, 27, 28] measured at 294 K.

#### 6.4.3.2 Fixed model parameters

In the LEAPR module there are two additional parameters which in the CAB model derive from experimental data: the weight of the translation mode  $\omega_t$  of the generalized frequency spectrum (chapter 3, section 3.3.3) and the free atom cross section of  $^1\text{H}$ .

From the measures of the water diffusion mass  $M_{diff}$  done by Novikov et al. [69], the parameter  $\omega_t$  is introduced in LEAPR as a fixed model parameter. A relative uncertainty on  $\omega_t$  of 10% is assumed because no information was published:

$$\omega_t = 0.007918 \pm 0.0007918. \quad (23)$$

Regarding the free atom cross section, the relative uncertainty of  $\pm 0.2\%$  recommended by the Neutron Standard Working Group of IAEA [A. D. Carlson et al., Nucl. Data Sheets 110, 3215 (2009)] was used:

$$\sigma_b^H = 20.478 \pm 0.041 \text{ b}. \quad (24)$$

Under these conditions, the nuisance parameter vector is:

$$\bar{\theta} = (n, N, B, T, \omega_T, \sigma_b^H). \quad (25)$$

Table 6.2 summarizes the nuisance parameters with the respective uncertainties adopted for each experimental data set.

Table 6.2. Nuisance parameters for the experimental measures used in the retroactive analysis.

Parameter	Zaitsev	Heinloth	Herdade	Drista	Beyster
<b>n [at/b]</b>	-	0.00335 ± 0.00008	0.00834 ± 0.00025	0.02438 ± 0.00007	-
<b>N</b>	1.0 ± 0.045	1.0 ± 0.01	1.0 ± 0.01	1.0 ± 0.01	1.0 ± 0.05
<b>B</b>	-	± 0.001	± 0.001	± 0.001	± 0.005

#### 6.4.4 The derivative matrices $G_{\bar{x}}$ and $G_{\bar{\theta}}$

The last ingredients for the GLS method and the marginalization procedure are the derivative matrices  $G_{\bar{x}}$  and  $G_{\bar{\theta}}$  to be used in eqs. (13), (15) and (18). In the context explained in the last three sections, the derivative matrices of the theoretical model with respect to the model parameters vector and with respect to the nuisance parameters vector for the CAB model are respectively:

$$G_{\bar{x}} = \begin{pmatrix} \frac{\partial t_1}{\partial \epsilon_0} & \frac{\partial t_1}{\partial \sigma_0} & \frac{\partial t_1}{\partial q_H} & \frac{\partial t_1}{\partial D_{OH}} & \frac{\partial t_1}{\partial \beta_{OH}} & \frac{\partial t_1}{\partial d_{OH}} & \frac{\partial t_1}{\partial k_\theta} & \frac{\partial t_1}{\partial \theta_{OH}} & \frac{\partial t_1}{\partial d_{OM}} \\ \vdots & & & & \vdots & & & & \vdots \\ \frac{\partial t_k}{\partial \epsilon_0} & \frac{\partial t_k}{\partial \sigma_0} & \frac{\partial t_k}{\partial q_H} & \frac{\partial t_k}{\partial D_{OH}} & \frac{\partial t_k}{\partial \beta_{OH}} & \frac{\partial t_k}{\partial d_{OH}} & \frac{\partial t_k}{\partial k_\theta} & \frac{\partial t_k}{\partial \theta_{OH}} & \frac{\partial t_k}{\partial d_{OM}} \end{pmatrix}, \quad (26)$$

$$G_{\bar{\theta}} = \begin{pmatrix} \frac{\partial t_1}{\partial A} & \frac{\partial t_1}{\partial N} & \frac{\partial t_1}{\partial B} & \frac{\partial t_1}{\partial T} & \frac{\partial t_1}{\partial \omega_T} & \frac{\partial t_1}{\partial \sigma_b^H} \\ \vdots & & & \vdots & & \vdots \\ \frac{\partial t_k}{\partial A} & \frac{\partial t_k}{\partial N} & \frac{\partial t_k}{\partial B} & \frac{\partial t_k}{\partial T} & \frac{\partial t_k}{\partial \omega_T} & \frac{\partial t_k}{\partial \sigma_b^H} \end{pmatrix}. \quad (27)$$

Generically, the derivate of a quantity  $t$  with respect to a parameter  $p$  is approximated as:

$$\frac{\partial t}{\partial p} \approx \frac{t_{nom} - t_{pert}}{p_{nom} - p_{pert}}, \quad (28)$$

where the subscripts "nom" and "pert" represent the nominal and the perturbed value.

To calculate each of the derivatives in eq. (25), a perturbation of +1% was done to the parameters of the water potential. For each perturbation the GROMACS code was run, obtaining a set of 9 perturbed frequency spectra of  $^1\text{H}$  in  $\text{H}_2\text{O}$ . The frequency spectra were introduced as input in the LEAPR module to compute the perturbed  $S(\alpha, \beta)$ . Finally, the total cross section was obtained with the THERMR module.

The latter were converted to transmission data with the eq. (20) and to average cosine of the scattering angle with the eq. (22).

In eq. (26), the derivatives of the theory with respect to  $T$ ,  $\omega_T$ , and  $\sigma_b^H$  were obtained perturbing these parameters in the LEAPR module. Regarding the derivatives with respect to the areal density  $n$ , the normalization  $N$  and the background  $B$ , they were calculated directly with the CONRAD code.

The perturbation calculations allow also to calculate the sensitivity coefficients of any microscopic quantity to the water potential parameters. This study permits to identify which are the parameters most sensitive that govern the behavior of the quantity. The sensitivity coefficient is:

$$S_p = \frac{\partial t/t_{nom}}{\partial p/p_{nom}}. \quad (29)$$

### 6.4.5 Results

It was done a two-step calculation process with the CONRAD code. Firstly, the fitting procedure provides the covariance matrix of the CAB model parameters  $M_x$  and secondly, these results are used in the marginalization technique.

#### 6.4.5.1 Results after the fitting procedure

As an initial guess in eq. (12) it was assumed that the model parameters are fully uncorrelated and have a relative uncertainty of 1%. The results before (prior) and after (posterior) the fit are detailed in Table 6.3. After the fit, very low and unrealistic uncertainties are attained (below 1%). A posterior correlation matrix is obtained as well, with weak correlations between the parameters. These results demonstrate the need for the use of the marginalization technique.

Table 6.3. Prior and posterior relative uncertainties and correlation matrix of the parameters of the TIP4P/2005f water potential.

Paramter	Value	Before the fit								Results after the fit												
		Relative prior uncertainty	Prior correlation matrix								Relative posterior uncertainty	Posterior correlation matrix										
$\sigma_o$ [nm]	0.31644	1.0%	100	0	0	0	0	0	0	0	0	0	0.6%	100	-17	25	63	-31	-14	19	-25	19
$\epsilon_o$ [KJ.mol <sup>-1</sup> ]	0.77491	1.0%		100	0	0	0	0	0	0	0	0	0.8%		100	-33	-3	-10	-16	1	-26	-15
$q_H$ [e]	0.5564	1.0%			100	0	0	0	0	0	0	0	0.7%			100	-51	-18	-13	12	-25	15
$d_{OH}$ [nm]	0.09419	1.0%				100	0	0	0	0	0	0	0.7%				100	5	-14	-16	-5	5
$D_{OH}$ [KJ.mol <sup>-1</sup> ]	432.58	1.0%					100	0	0	0	0	0	0.8%					100	-31	15	-22	-2
$\beta_{OH}$ [nm <sup>-1</sup> ]	22.87	1.0%						100	0	0	0	0	0.7%						100	-7	-24	4
$\theta_o$ [°]	107.4	1.0%							100	0	0	0	0.9%							100	-4	-9
$k_g$ [KJ.mol <sup>-1</sup> rad <sup>-2</sup> ]	367.81	1.0%								100	0	0	0.8%								100	-10
$a$ [nm]	0.13288	1.0%									100	0	0.7%									100

### 6.4.5.2 Results after the marginalization technique

Figure 6.4 shows the four blocks of the full correlation matrix of the extended parameter vector  $\bar{\delta}$ .

The upper right and lower left blocks correspond to the cross-covariance matrix between the models parameters and the nuisance parameters  $M_{\bar{x},\bar{\theta}}$ . In overall, we see that the water potential parameters and the experimental parameters are weakly correlated. In principle, no direct relation stands for  $\bar{x}$  and  $\bar{\theta}$ . The lower right section of the matrix defines the correlation matrix between the nuisance parameters  $M_{\bar{\theta}}$ .

The block in the upper left part corresponds to the correlation matrix between the model parameters after the marginalization  $M_{\bar{x}}^{marg}$ . In this second calculation step with the CONRAD code, strong correlations between the model parameters are produced after the marginalization of the nuisance parameters. Table 6.4 summarizes the relative uncertainties of the CAB model parameters and the correlation matrix corresponding to this block. Comparing the results after the fit and after the marginalization it can be seen that in the latter case more realistic uncertainties are achieved. The uncertainties oscillate between 2% and 6%, excepts the parameter  $\epsilon_0$  which corresponds to the depth of the potential well of the Lennard-Jones potential between the oxygens.

100	-77	93	69	33	-18	-64	83	-14	1	0	15	0	15	1	-4	-2	-14	-5	72	59	13	-5	-8
-77	100	-71	-98	-85	53	97	-54	-32	-4	0	-4	2	-5	0	2	1	-6	-2	-99	-10	3	-1	-2
93	-71	100	59	28	-2	-60	81	-18	14	0	5	4	5	-1	1	-1	-9	-3	65	68	15	7	0
69	-98	59	100	89	-63	-96	44	38	2	0	6	-1	6	0	-3	-1	7	3	99	-5	-3	-4	-1
33	-85	28	89	100	-63	-88	6	57	0	0	-5	-9	-9	-1	2	1	16	6	88	-38	-9	6	8
-18	53	-2	-63	-63	100	51	-11	-28	-24	0	-22	4	-23	-5	8	3	-6	-3	-55	51	11	39	27
-64	97	-60	-96	-88	51	100	-45	-49	2	0	4	-3	-3	1	1	0	-21	-8	-96	0	1	-3	-4
83	-54	81	44	6	-11	-45	100	-14	13	0	10	0	38	2	-15	-4	9	4	44	72	11	-13	-9
-14	-32	-18	38	57	-28	-49	-14	100	-33	0	-26	3	7	-1	-5	-1	64	25	33	-38	-19	4	10
1	-4	14	2	0	-24	2	13	-33	100	0	0	0	0	0	0	0	0	0	0	0	0	0	0
0	0	0	0	0	0	0	0	0	0	100	0	0	0	0	0	0	0	0	0	0	0	0	0
15	-4	5	6	-5	-22	4	10	-26	0	0	100	0	0	0	0	0	0	0	0	0	0	0	0
0	2	4	-1	-9	4	-3	0	3	0	0	0	100	0	0	0	0	0	0	0	0	0	0	0
15	-5	5	6	-9	-23	-3	38	7	0	0	0	0	100	0	0	0	0	0	0	0	0	0	0
1	0	-1	0	-1	-5	1	2	-1	0	0	0	0	0	100	0	0	0	0	0	0	0	0	0
-4	2	1	-3	2	8	1	-15	-5	0	0	0	0	0	0	100	0	0	0	0	0	0	0	0
-2	1	-1	-1	1	3	0	-4	-1	0	0	0	0	0	0	0	100	0	0	0	0	0	0	0
-14	-6	-9	7	16	-6	-21	9	64	0	0	0	0	0	0	0	0	100	0	0	0	0	0	0
-5	-2	-3	3	6	-3	-8	4	25	0	0	0	0	0	0	0	0	0	100	0	0	0	0	0
72	-99	65	99	88	-55	-96	44	33	0	0	0	0	0	0	0	0	0	0	100	0	0	0	0
59	-10	68	-5	-38	51	0	72	-38	0	0	0	0	0	0	0	0	0	0	0	100	0	0	0
13	3	15	-3	-9	11	1	11	-19	0	0	0	0	0	0	0	0	0	0	0	0	100	0	0
-5	-1	7	-4	6	39	-3	-13	4	0	0	0	0	0	0	0	0	0	0	0	0	0	100	0
-8	-2	0	-1	8	27	-4	-9	10	0	0	0	0	0	0	0	0	0	0	0	0	0	0	100

Fig. 6.4 Full correlation matrix between the model and the experimental parameters after marginalization.

Table 6.4. Relative uncertainties and correlation matrix of the parameters of the TIP4P/2005f water potential after the marginalization.

Parameter	Value	Relative posterior uncertainty	Posterior correlation matrix
$\sigma_O$ [nm]	0.31644	2.3%	100 -77 93 69 33 -18 -64 83 -14
$\varepsilon_O$ [KJ/mol]	0.77491	14.6%	100 -71 -98 -85 53 97 -54 -32
$q_H$ [e]	0.5564	3.2%	100 59 28 -2 -60 81 -18
$d_{OH}$ [nm]	0.09419	6.3%	100 89 -63 -96 44 38
$D_{OH}$ [KJ/mol]	432.58	6.2%	100 -63 -88 6 57
$b_{OH}$ [1/nm]	22.87	4.2%	100 51 -11 -28
$\theta_b$ [°]	107.4	6.4%	100 -45 -49
$k_\theta$ [KJ/mol/rad <sup>2</sup> ]	367.81	3.8%	100 -14
$a$ [nm]	0.13288	2.7%	100

### 6.5 Covariance matrix of the thermal scattering law of JEFF-3.1.1

An equivalent methodology was adopted to create the covariance matrix for the thermal scattering law of the JEFF-3.1.1 nuclear data library. The details of the calculation can be found in the publication [70]. Here, the main results are summarized.

#### 6.5.1 Parameters of the TSL

In chapter 3 it was seen that the model parameters of the light water thermal scattering function of JEFF-3.1.1 correspond to the LEAPR module parameters, established by M. Matter and J. Keinert [4]. Figure 6.5 illustrates the parameters that describe the frequency spectrum of <sup>1</sup>H in H<sub>2</sub>O at 294 K and Table 6.5 gives a list of their values.

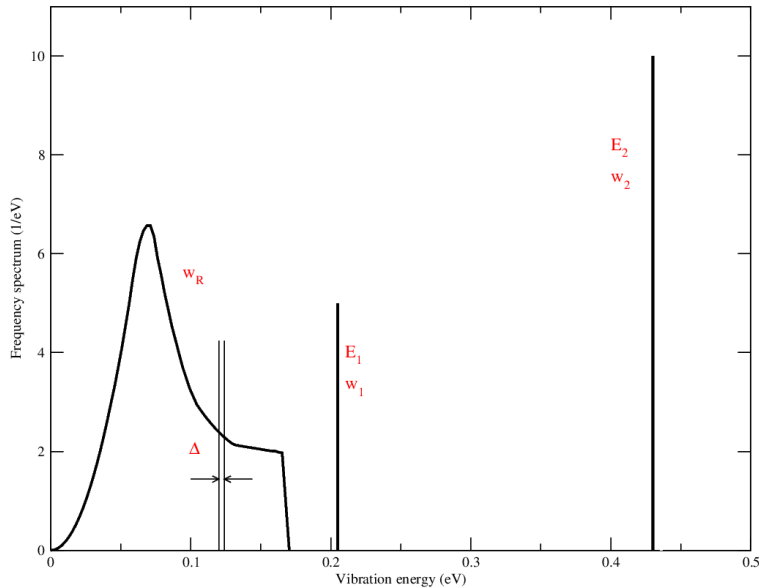


Fig. 6.5 Continuous distribution and discrete oscillators used in JEFF-3.1.1 at 294 K.

Table 6.5. JEFF-3.1.1 model parameters introduced in the LEAPR module for  $^1\text{H}$  in  $\text{H}_2\text{O}$  at 294K.

LEAPR module parameters		JEFF-3.1.1
Translational weight	$w_t$	0.0217
Continuous spectrum weight	$w_c$	0.4891
Bending mode energy (meV)	$E_1$	205.0
Bending mode weight	$w_1$	0.1630
Stretching modes energy (meV)	$E_2$	436.0
Stretching mode weight	$w_2$	0.3261
Diffusion constant	$c$	0.0
Energy interval (meV)	$\delta$	2.542
Free scattering cross section (b)	$\sigma_b^H$	20.478

The way the generalized frequency spectrum is divided in LEAPR (a translational mode, a rotational mode and discrete oscillators) imposes the constraint:

$$w_t + w_c + w_1 + w_2 = 1. \quad (30)$$

Taking into account the link between the weights of each vibration mode, two factor were introduced in eq. (29), such that:

$$Fw_t + G(w_c + w_1 + w_2) = 1, \quad (31)$$

where  $F$  is a normalizing multiplicative factor and  $G$  is consequently obtained as:

$$G = \frac{1 - Fw_t}{w_c + w_1 + w_2}. \quad (32)$$

The shape of the continuous component of the frequency spectrum is driven by the parameter  $\delta$ . It was applied a scaling factor  $\Delta$  to the vibration energy grid  $e$  used to reconstruct the frequency spectrum:

$$e = \Delta \cdot \delta \quad (33)$$

The study of the energy interval of the continuous frequency spectrum allows to evaluate the impact of this parameter on the total cross section, and particularly on the thermal cross section. Figure 6.6 shows the impact of  $\Delta$  on the calculated total cross section of  $\text{H}_2\text{O}$  of JEFF-3.1.1 at 294 K. A 10% variation of this parameter implies an increase of 2% of the thermal cross section.

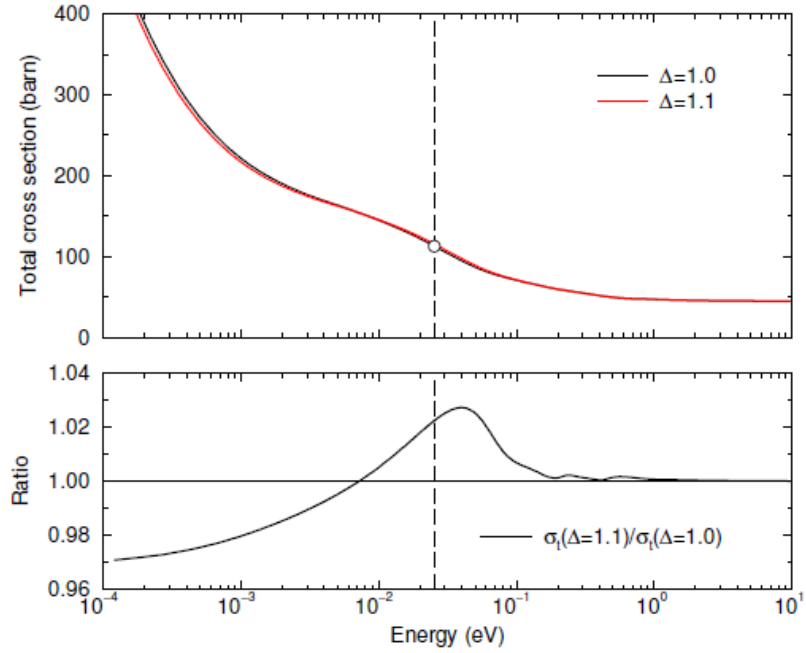


Fig. 6.6 Effect on the H<sub>2</sub>O total cross section of the scaling factor applied to the vibration energy grid used to reconstruct the frequency distribution at 294 K.

Under these conditions, the parameters  $F$  and  $\Delta$  are the model parameters vector

$$\bar{x} = (F, \Delta) \tag{34}$$

### 6.5.2 Experimental data for the fitting in the GLSM

The total cross section measurements from the EXFOR database were used in the fitting procedure. As it was done for the CAB model analysis, the data was transformed to transmission using a generic areal density  $n = 0.017 \text{ barn}^{-1}$  for all the data sets. Figure 6.7 shows the total cross section data at 294 K from the EXFOR database compared with the total cross section from JEFF-3.1.1 (upper plot) and the data converted to transmission.

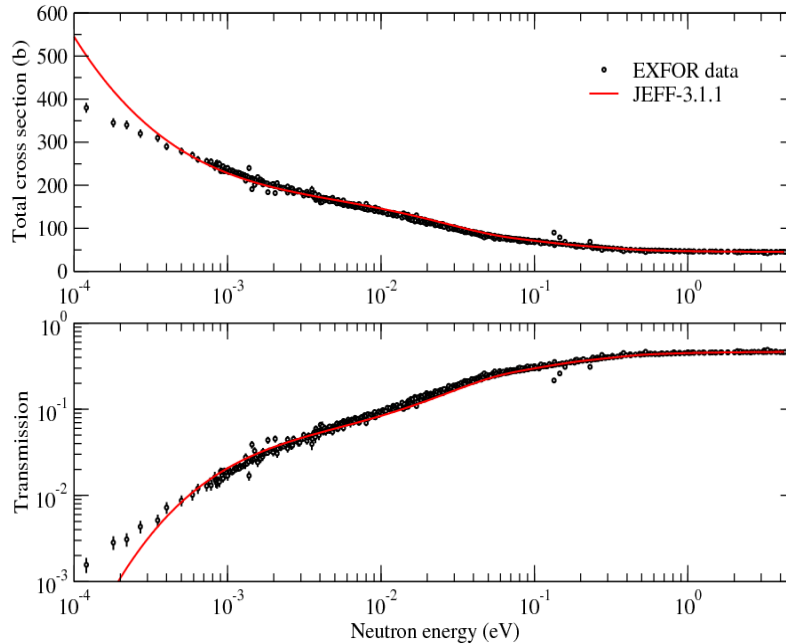


Fig. 6.7 H<sub>2</sub>O total cross section measurements at 294 K from the EXFOR database compared to the cross section of JEFF-3.1.1 (upper plot) and the transmission data converted using a generic areal density of 0.017 barn<sup>-1</sup>.

### 6.5.3 The nuisance parameters

#### 6.5.3.1 Experimental parameters

In the case of JEFF-3.1.1 no background correction was taken into account. As it will be seen in the next section, the dimensionless diffusion constant  $c$  should encompass such a contribution.

For most of the H<sub>2</sub>O total cross sections reported in the EXFOR database, the uncertainty on the normalization factor  $N$  is poorly documented. Owing to the accuracy of the transmission measurements achieved over the last ten years in the existing time-of-flight facilities, a 1% uncertainty was considered in the calculations.

Finally, the uncertainty on the temperature  $T$  was considered as well. At 294 K, it was used an uncertainty of 2 K.

#### 6.5.3.2 The diffusion constant $c$

As it can be seen in Fig. 6.7, the cross section calculated with the LEAPR module parameters established by M. Mattes et al. nearly follows the experimental trend in a large energy range of interest for light water reactor applications. Below 1 meV, the calculations fail to correctly reproduce the experimental values. When the model calculations deviate significantly from the measurements, Leeb et al. have proposed to account for Model Defects in covariance matrices [71].

The proposed strategy consists of adding extra covariance terms to produce large uncertainties that cannot be explained by the model parameters. In the case of the TSL model of JEFF-3.1.1, the origin of the Model Defects observed in the cold neutron energy range is directly related to the choice of the diffusion constant  $c = 0$ .

Figure 6.8 shows the impact of the diffusion constant on a theoretical transmission calculated with  $n = 0.017 \text{ barn}^{-1}$ . The diffusion constant  $c = 4$  corresponding to the new LEAPR parameterization established by Marquez Damian et al. [5]. The diffusion constant acts as a background term that mainly affects the low energy range (mainly below 1 meV) of the theoretical transmission.

The contribution of the diffusion constant will be treated separately, as this parameter is related to a Model Defect.

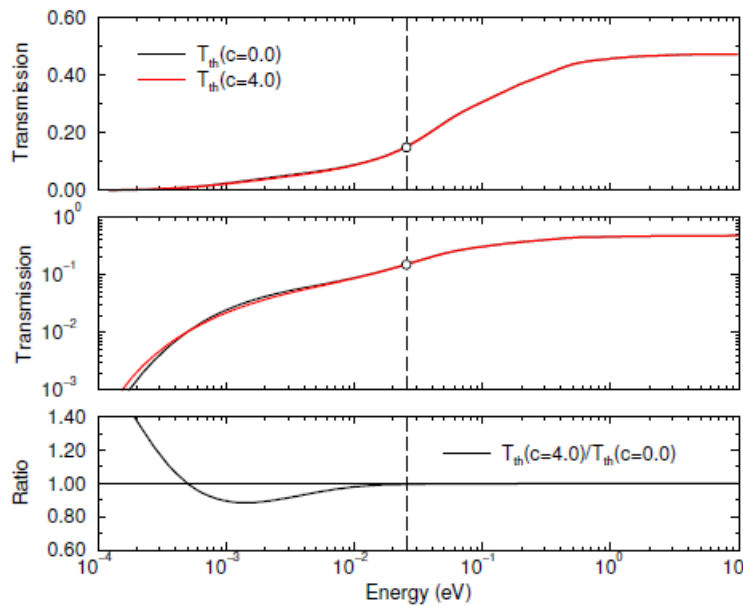


Fig. 6.8 Modifications of the low energy part of a given theoretical transmission of a thick water sample according to the diffusion constant  $c$ .

### 6.5.3.3 Fixed model parameters

The bending and the stretching internal modes of the water molecule are represented in JEFF-3.1.1 with two discrete oscillators at  $E_1 = 205 \text{ meV}$  and  $E_2 = 436 \text{ meV}$ . The calculation done by molecular dynamics in CAB model show a good agreement with the bending mode, and an energy shift of about 22 meV for the stretching mode (Figure 6.9). The water potential introduced in the simulations was optimized with the vibration energies measured by Lappi et al. [72].

The discrete representation of the bending and stretching modes does not take into account the spread around the mean value. The calculated Full Width at Half Maximum (FHHM) are 14 meV and 33 meV respectively, providing uncertainties on the position of the two oscillators close to 6 meV and 14 meV.

The uncertainty on  $E_1$  is deduced then from the width of the bending mode, while the uncertainty on  $E_2$  the width and the energy shift of 22 meV:

$$E_1 = 205 \pm 6 \text{ meV}, \quad (35)$$

$$E_2 = 436 \pm 36 \text{ meV}. \quad (36)$$

In regard to the free atom cross section of  $^1\text{H}$ , it was taken the same approach as for the CAB model analysis:

$$\sigma_b^H = 20.478 \pm 0.041 \text{ b}. \quad (37)$$

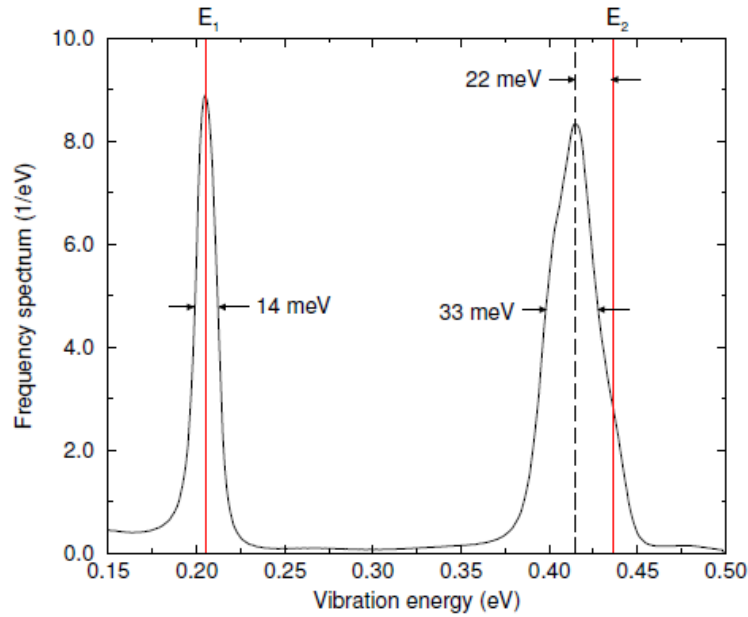


Fig. 6.9 Bending and stretching modes calculated at 294 K with the molecular dynamic code GROMACS and parameters used in reference [5]. The mean energies of the two modes (205.2 meV and 415.5 meV) are compared with the energies of the first and second oscillators introduced in JEFF-3.1.1 (205.0 meV and 436.0 meV).

Under these conditions, the nuisance parameter vector is:

$$\bar{\theta} = (N, T, E_1, E_2, \sigma_b^H). \quad (38)$$

#### 6.5.4 The derivative matrices $G_{\bar{x}}$ and $G_{\bar{\theta}}$

The derivative matrices of the theoretical model with respect to the model parameters vector and with respect to the nuisance parameters vector for JEF-3.1.1 are respectively:

$$G_{\bar{x}} = \begin{pmatrix} \frac{\partial t_1}{\partial \Delta} & \frac{\partial t_1}{\partial F} \\ \frac{\partial t_k}{\partial \Delta} & \frac{\partial t_k}{\partial F} \end{pmatrix}, \quad (39)$$

$$G_{\bar{\theta}} = \begin{pmatrix} \frac{\partial t_1}{\partial N} & \frac{\partial t_1}{\partial T} & \frac{\partial t_1}{\partial E_1} & \frac{\partial t_1}{\partial E_2} & \frac{\partial t_1}{\partial \sigma_b^H} \\ \vdots & & \vdots & & \vdots \\ \frac{\partial t_k}{\partial N} & \frac{\partial t_k}{\partial T} & \frac{\partial t_k}{\partial E_1} & \frac{\partial t_k}{\partial E_2} & \frac{\partial t_k}{\partial \sigma_b^H} \end{pmatrix}. \quad (40)$$

As it was done for the CAB model, a perturbation of +1% was done to the LEAPR module parameters to calculate each derivate with eq. (27).

### 6.5.5 Results

A two-step calculation process with the CONRAD code was done. The covariance matrix  $M_{\bar{x}}$  between the model parameters is obtained after the fitting procedure, while in the second step the marginalization technique includes the contributions due to other sources of uncertainties.

#### 6.5.5.1 Results after the fitting procedure

At the beginning of the fitting procedure, it was assumed that the parameters are poorly known and independent, making the prior covariance matrix diagonal with uninformative prior variances. The relative prior uncertainties for  $\Delta$  and  $F$  were set to 10%. At the end of the fitting procedure, the central values are unchanged, but the obtained uncertainties are rather low:

$$\Delta = 1.000 \pm 0.005 \text{ (0.5\%)}, \quad (41)$$

$$F = 1.000 \pm 0.013 \text{ (1.3\%)}. \quad (42)$$

#### 6.5.5.2 Results after the marginalization technique

When the contributions of the nuisance parameters vector uncertainties is taken into account, the uncertainties on the observable parameters increase significantly:

$$\Delta = 1.000 \pm 0.24 \text{ (24.0\%)}, \quad (43)$$

$$F = 1.000 \pm 0.186 \text{ (18.6\%)}. \quad (44)$$

In order to generate uncertainties on the total cross section around the thermal energy consistent with the bias detected with the EXFOR experimental data (5% to 6%), a constraint in the form of an additional normalization term was introduced in the calculations.

In the LEAPR module, the choice of the value of the diffusion constant  $c$  implies switching the model that will describe the translational vibration mode of the frequency spectrum. If  $c = 0$  (JEFF-3.1.1) it means that the free gas law will be used, while a constant different to zero will use the Egelstaff-Schofield model for diffusion. As a consequence,  $c$  is a parameter that can be easily used to account for Model Defects in the covariance matrix.

The value of the diffusion constant depends on the phonon spectrum introduced in the calculations. In the case of CAB model, a value of  $c \approx 4$  was obtained. For JEFF-3.1.1, lower amplitude of variation was

established by trial and error. It was found that the optimal interval of variation for the diffusion constant is close to  $\pm 1.5$

The relative uncertainties and the correlation matrix between the LEAPR module parameters of JEFF-3.1.1 is reported in Table 6.6.

Table 6.6. Relative uncertainties and correlation matrix of the LEAPR parameters of JEFF-3.1.1 after the marginalization.

Parameter	Value	Relative posterior uncertainty	Posterior correlation matrix
$\Delta$ [meV]	1.0	<b>24.1%</b>	<b>100</b>
$\sigma_H$ [b]	20.478	<b>0.2%</b>	<b>-1 100</b>
F	1.000	<b>18.6%</b>	<b>15 14 100</b>
$E_1$ (meV)	205.0	<b>2.9%</b>	<b>-1 0 6 100</b>
$E_2$ (meV)	436.0	<b>8.3%</b>	<b>2 0 46 0 100</b>
c	0.0	<b><math>\pm 1.5</math></b>	<b>0 0 0 0 0 100</b>

## 6.6 Preliminary conclusions

In this chapter it was presented the methodology for producing the covariance matrix between the CAB model parameters and the LEAPR module parameters of JEFF-3.1.1 was presented. It was described the generalized least square method, which iteratively finds the posterior covariance matrix between the model parameters and the marginalization technique, which allows introducing long range correlations incorporating the nuisance parameters in the analysis. Both methods were implemented in the data assimilation code CONRAD.

After the marginalization, large uncertainties on the CAB model parameters were obtained. Such  $1\sigma$  uncertainties must be interpreted with caution. If the real value of the parameter is within the calculated uncertainties, the forces between the atoms originated by the potentials would be severely modified. These perturbations would introduce changes at the level of the water composition.

The approach taken in the present work was to obtain uncertainties for all the parameters retroactively with the total cross section and the average cosine of the scattering angle measurements. In order to achieve more realistic uncertainties, it would be necessary to include in the fitting procedure only those parameters which show a high sensitivity to the chosen experimental data. As it was done for the free atom cross section  $\sigma_b^H$  and the weight of the translational vibration mode  $\omega_t$ , the other parameters should be treated as fixed model parameters whose uncertainties could deduced from experimental measures of the thermophysical properties of water.

As regards the results of JEFF-3.1.1, large uncertainties for the parameter that describes the translation mode weight and the scaling factor on the frequency spectrum were obtained as well. The uncertainty on this latter is approximately 24%. As it was seen throughout the chapter, this parameter governs the shape of the continuous frequency spectrum, and such a large uncertainty accounts the fact that it is not correctly considered. At the beginning of chapter 3, it was explained that in the nuclear data library ENDF/B-VII.1, the energy scale of the frequency spectrum was modified to improve the agreement with the thermal cross section measurements.

In the following chapter, the uncertainties of JEFF-3.1.1 and CAB model will be propagated to obtain covariances on microscopic data (thermal scattering law  $S(\alpha, \beta)$ , scattering cross section of  $^1\text{H}$  in  $\text{H}_2\text{O}$ ) and on integral calculations (keff, reactivity temperature coefficient).

# Chapter 7

## Thermal scattering uncertainties propagation

In the previous chapter the covariance matrices between the parameters of the CAB model and the JEFF-3.1.1 library were obtained. The following step is to perform the uncertainty propagation to the quantities of interest for the nuclear reactors applications. The main goal of this study is to evaluate the impact of the nuclear data uncertainties on the final outcomes such as the effective multiplication factor  $k_{eff}$ .

In general two methods are used to propagate the nuclear data uncertainties. The first has already been presented in the last chapter and is based on direct perturbations of the model parameters to estimate the sensitivity coefficients. We recall that the main drawback of this method is the assumption of linearity when the sensitivities are calculated. When the problem presents strong non-linear effects, the Monte Carlo uncertainty propagation is another option. The most important disadvantage is the very high number of calculations needed.

By doing a direct perturbation of the parameters of the thermal scattering models (CAB and JEFF-3.1.1), an uncertainty propagation was done to the thermal scattering function  $S(\alpha, \beta)$ , to scattering cross section of  $^1\text{H}$  in  $\text{H}_2\text{O}$  and to the integral calculations of the MISTRAL experiments.

Finally, the results will be compared with a second uncertainty propagation option, namely the Iterated Fission Probability (IFP) method [73], recently implemented in the Monte Carlo code TRIPOLI4. Due to its simplicity, the IFP methodology represents a pragmatic approach to quantify the uncertainties coming from the thermal elastic scattering cross section.

### 7.1 Introduction

In general, the so-called “sandwich formula”, already presented in chapter 6, is used to propagate analytically the uncertainties of a given set of input parameters  $x$  to a generic output quantity  $z$ . The variance of  $z$  is calculated as follows:

$$\text{Var}(z) = S\Sigma S^T, \quad (1)$$

where  $\Sigma$  is the covariance matrix between the input parameters and  $S$  is the derivative matrix of  $z$  to the parameters.

In the last chapter the covariance matrix  $\Sigma$  for the CAB model (table 6.3 of chapter 6) and for the JEFF-3.1.1 library (table 6.6 of chapter 6) were obtained with the CONRAD code.

## 7.2 Uncertainties propagation to the $S(\alpha, \beta)$ function of CAB model

In general, the thermal scattering matrix contains a very large number of values. For the CAB model, the number of points is around 70000 and for JEFF-3.1.1 is close to 47000. Such a large amount of data makes difficult the treatment and storage of their covariance matrices.

It was decided to do a multigroup treatment, averaging in 37 momentum transfer  $\alpha$  intervals for CAB and JEFF-3.1.1. The average scattering function in the  $ij$  interval,  $\bar{S}_{ij}(\alpha_{ij}, \beta_0)$ , for a given energy transfer  $\beta_0$  is obtained as:

$$\bar{S}_{ij}(\alpha_{ij}, \beta_0) = \frac{\int_{\alpha_i}^{\alpha_j} S(\alpha, \beta_0) d\alpha}{\int_{\alpha_i}^{\alpha_j} d\alpha}. \quad (2)$$

As an illustrative example, Figure 7.1 shows the symmetric form of  $S(\alpha, \beta_0)$  and the multigroup  $\bar{S}(\alpha, \beta_0)$  as a function of the momentum transfer for  $\beta_0 = 1.0$  calculated with the CAB model at 294 K. The corresponding energy exchange is approximately 25.3 meV.

### 7.2.1 Sensitivities of the $S(\alpha, \beta)$ function to the CAB model parameters

A perturbation of +1% was done to the water potential parameters of the CAB model to calculate the sensitivity vectors. Figure 7.2 shows the sensitivity profiles in %/% to the  $S(\alpha, \beta)$  as a function of  $\alpha$  for  $\beta_0 = 1.0$ . For the sake of clarity in the plot, it was included the profiles which correspond to the most sensitive parameters to the scattering function.

The scattering function is very sensitive to the distance  $\sigma_O$ , where the Lennard-Jones potential (intermolecular potential) is zero, to the electrical charge  $q_H$  of the hydrogen site of the Coulomb potential (intermolecular potential) and to the equilibrium distance  $d_{OH}$  between the hydrogen and oxygen in the Morse potential (potential controlling the internal modes).

The sensitivity of the  $S(\alpha, \beta)$  to  $\sigma_O$  indicates that a positive perturbation will increase the scattering function. Physically, it happens that the Lennard-Jones potential becomes repulsive, so the water molecules tend to separate themselves, attenuating the molecular clustering effect. At a cold neutron energy range (<0.01 eV), a decrease of the effective mass of the molecule ensemble will have a positive effect on the scattering cross section of  $^1\text{H}$  in  $\text{H}_2\text{O}$ .

The trend followed by  $q_H$  and  $d_{OH}$  is nearly similar and opposed to  $\sigma_O$ . We expect, thus, a decrease of the scattering cross section for the cold energy range when these parameters are perturbed.

### 7.2.2 Covariance matrix of the $S(\alpha, \beta)$ function to the CAB model parameters

The relative uncertainties of the  $S(\alpha, \beta)$  function are directly linked to the shape of the sensitivities. Figure 7.3 shows the relative uncertainties and the covariance matrix of the multigroup scattering function for two energy transfers,  $\beta = 1.0$  and  $\beta = 10.0$ . The results were obtained with the uncertainties of the CAB model parameters listed in table 6.4 of chapter 6. In both cases the relative

uncertainties on the  $S(\alpha, \beta)$  function oscillate between 10% in the peak of the distribution and approximately 30% in the wings, where the function approaches to zero.

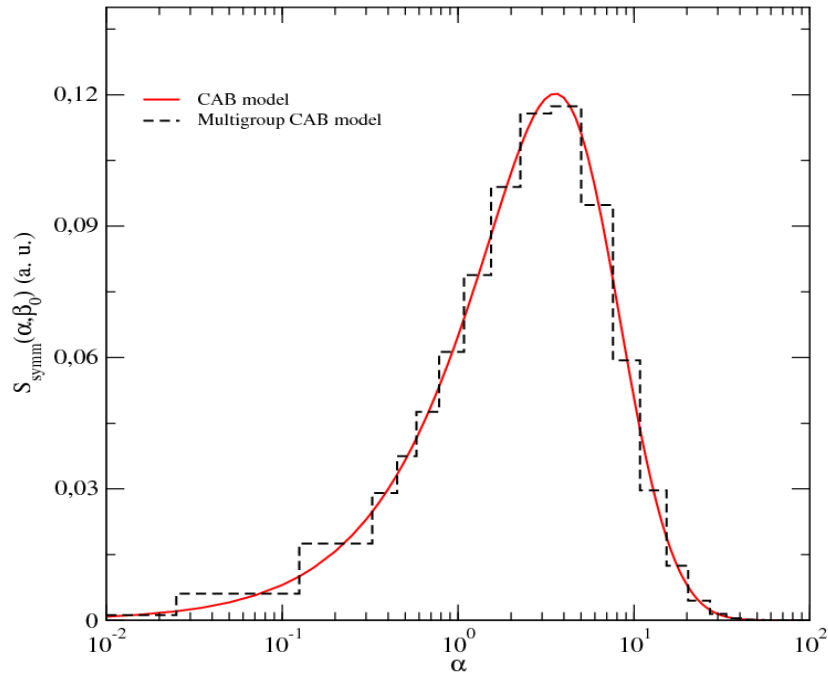


Fig. 7.1  $S(\alpha, \beta_0)$  and the multigroup  $\bar{S}(\alpha, \beta_0)$  as a function of the momentum transfer for  $\beta_0 = 1.0$  calculated with the CAB model at 294 K.

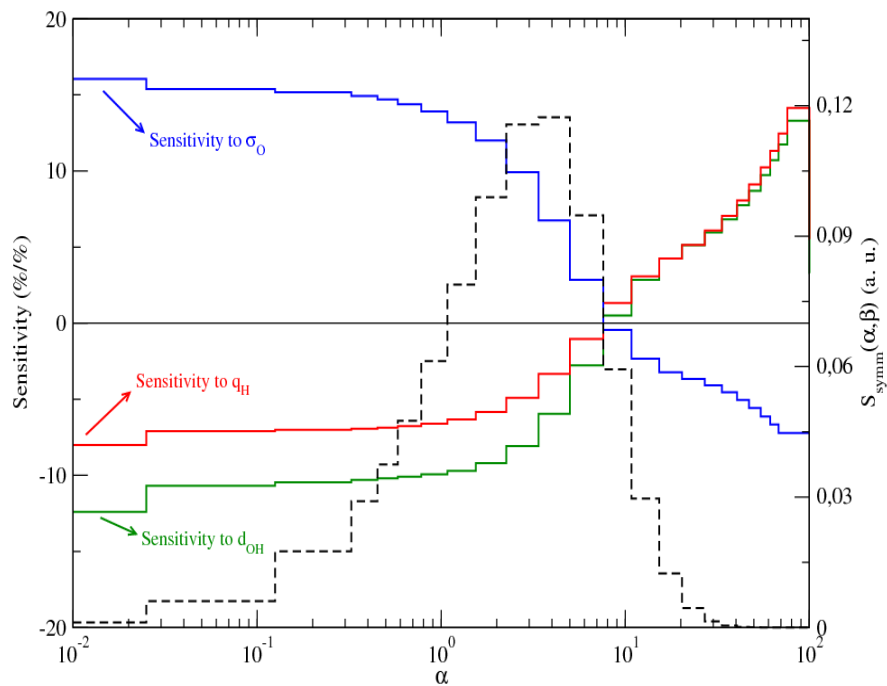


Fig. 7.2 Sensitivities of the  $\bar{S}(\alpha, \beta_0)$  function (dashed line) to the CAB model parameters as a function of the momentum transfer for  $\beta_0 = 1.0$  calculated with the CAB model at 294 K.

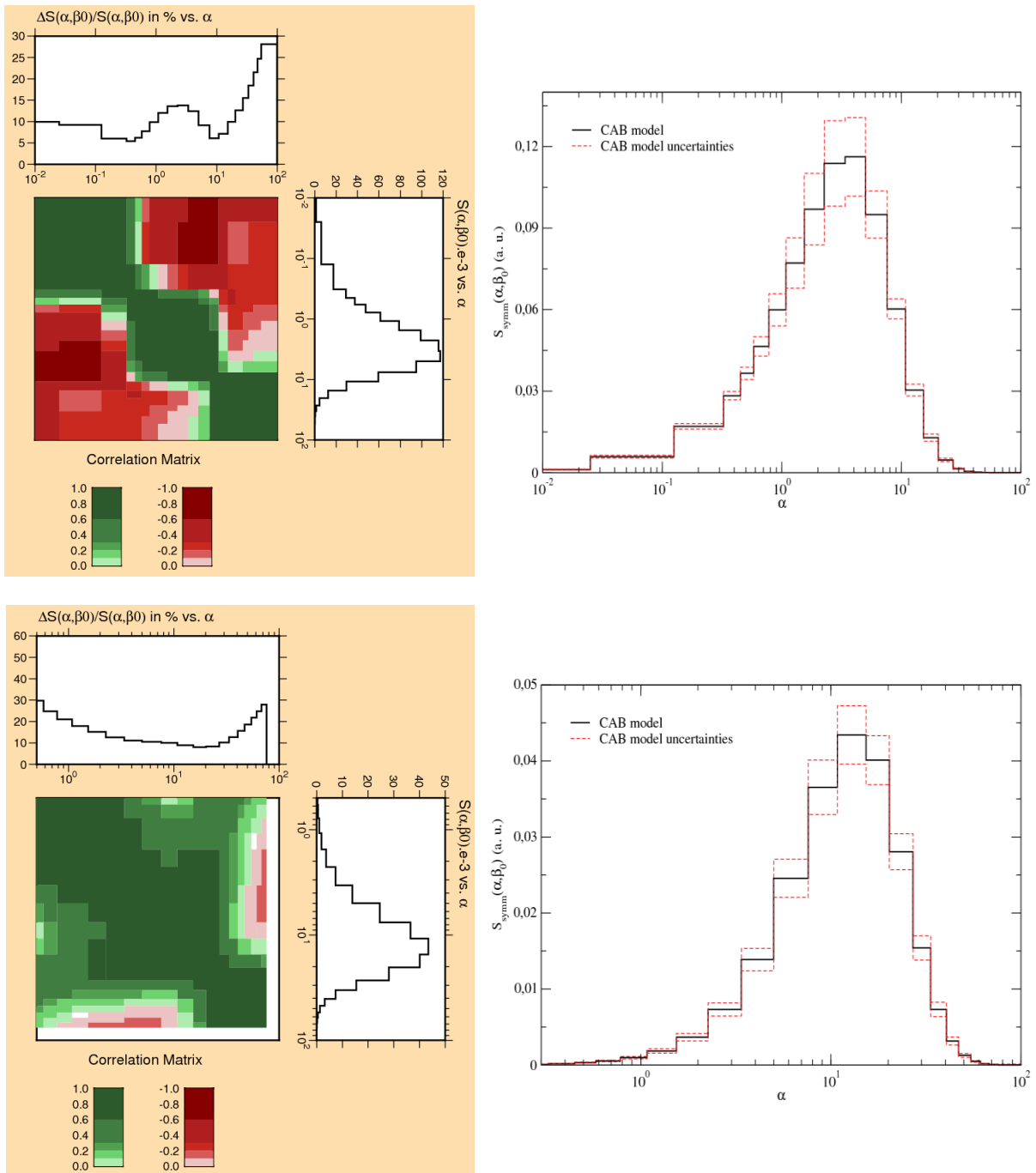


Fig. 7.3 Relative uncertainties and correlation matrix of the  $\bar{S}(\alpha, \beta_0)$  function for  $\beta_0 = 1.0$  (upper plot) and  $\beta_0 = 10.0$  (bottom plot) calculated with the CAB model at 294 K.

## 7.3 Uncertainties propagation to the $^1\text{H}$ in $\text{H}_2\text{O}$ scattering cross section of CAB model

### 7.3.1 Sensitivities of the $S(\alpha, \beta)$ function to the CAB model parameters

Figure 7.4 shows the sensitivity of the  $^1\text{H}$  in  $\text{H}_2\text{O}$  scattering cross section at 294 K to the TIP4P/2005f water potential parameters. For the sake of clarity it was only included in the plot the most sensitive parameters, which are the same as the  $S(\alpha, \beta)$  function: the distance where the Lennard-Jones potential in zero  $\sigma_{\text{O}}$ , the equilibrium distance between the hydrogen and the oxygen in the Morse potential  $d_{\text{OH}}$  and the electrical charge of the particle  $q_{\text{H}}$ .

The scattering cross section shows a high sensitivity to these parameters below 1 meV, accounting the importance of the chemical binding between the hydrogen and the oxygen in the cold neutron energy range. At 6 meV all the sensitivities converge to zero. Further investigations are needed to explain this behavior. Above 0.1 eV, the scattering cross section presents a negligible dependence to the parameters as the free gas model drives the cross section at this energy range. We expect that the uncertainties on the scattering cross section presents equivalent trends, large uncertainties for the cold neutron energy range and small uncertainties where the sensitivities are nearly zero.

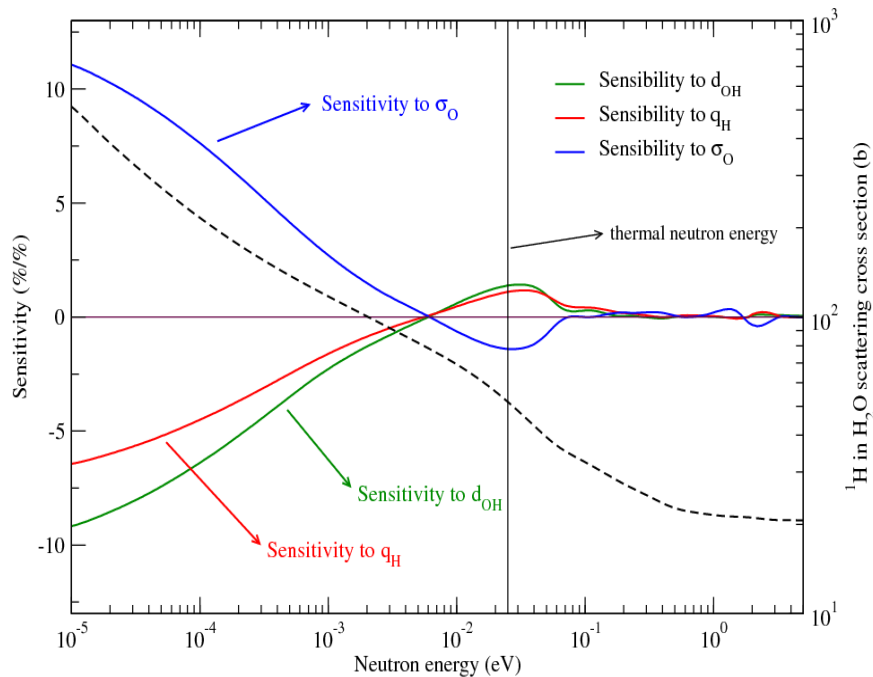


Fig. 7.4 Sensitivity of the  $^1\text{H}$  in  $\text{H}_2\text{O}$  scattering cross section at 294 K to the TIP4P/2005f water potential parameters. The dashed line represents the scattering cross section of  $^1\text{H}$  in  $\text{H}_2\text{O}$ .

### 7.3.2 Covariance matrix of the $^1\text{H}$ in $\text{H}_2\text{O}$ scattering cross section of CAB model

It was done an uncertainty propagation of the CAB model parameters to the scattering cross section of  $^1\text{H}$  in  $\text{H}_2\text{O}$  at 294 K. The results obtained after the fitting procedure and after the marginalization of the nuisance parameters are analyzed to point out the remarkable difference in both cases.

Figure 7.5 shows the relative uncertainties and the correlation matrix after the fitting step (left hand plot) and after the marginalization step (right hand plot). The small uncertainties of the CAB model parameters obtained after the fit (close to 1%) provide underestimated uncertainties on the scattering cross section of  $^1\text{H}$  in  $\text{H}_2\text{O}$ .

When the experimental parameters are marginalized, long range correlations are produced between the CAB model parameters, which yields in more realistic uncertainties on the scattering cross section. At the thermal neutron energy (0.0253 eV), the relative uncertainty reaches approximately 3.3%. Beyond 1 eV, the uncertainty, mainly driven by the relative uncertainty of the hydrogen free atom cross section, is close to 0.9%. The unusual structures seen at this energy range might be originated by the transition to the short collision time approximation model to calculate the thermal scattering data.

## 7.4 Uncertainties propagation to the average cosine of the scattering angle of CAB model

### 7.4.1 Sensitivities of the $\bar{\mu}$ to the CAB model parameters

Figure 7.6 shows the sensitivities coefficients of the average cosine of the scattering angle to the CAB model parameters at 294 K. Similar trends are obtained compared to the scattering function and the scattering cross section. The most sensitive parameters are:  $\sigma_O$ ,  $q_H$  and  $d_{OH}$ .

The calculated sensitivities can be described in two different energy ranges. Up to approximately 0.3 eV, the covalent bonds between the hydrogens and the oxygen are strong, so the incident neutron sees that the mass of the scattering target is very close to the water molecule mass. The sensitivities to the parameters of the water potential will be important, and thus large uncertainties are expected. Beyond 0.3 eV, the energy of the neutron is large enough to consider that the scattering target is represented by the hydrogen, which is the main scatterer of the water molecule. This transition is quantified by the average cosine of the scattering angle which is a measure of the deviation of the isotropic scattering. As seen in the plot, the sensitivities are unimportant.

At 2 eV, some unusual fluctuations on the sensitivities are detected which may be attributed to the short collision time approximation switch of the LEAPR module.

### 7.4.2 Covariance matrix of the $\bar{\mu}$ for the CAB model

Figure 7.7 shows the relative uncertainties and the correlation matrix at 294 K of the average cosine of the scattering angle after the marginalization.

As stated in the sensitivities analysis, large uncertainties are obtained for the cold neutron energy range, reaching close to 30% at 5 meV. At the thermal energy, the relative uncertainty ranges approximately 12%. The right hand plot of Fig. 7.7 shows the calculated  $\bar{\mu}$  and the uncertainty bands compared with the experimental measures from Beyster [68] used in the retroactive analysis. It can be seen that such large uncertainty bands overlap the data for all the energy range.

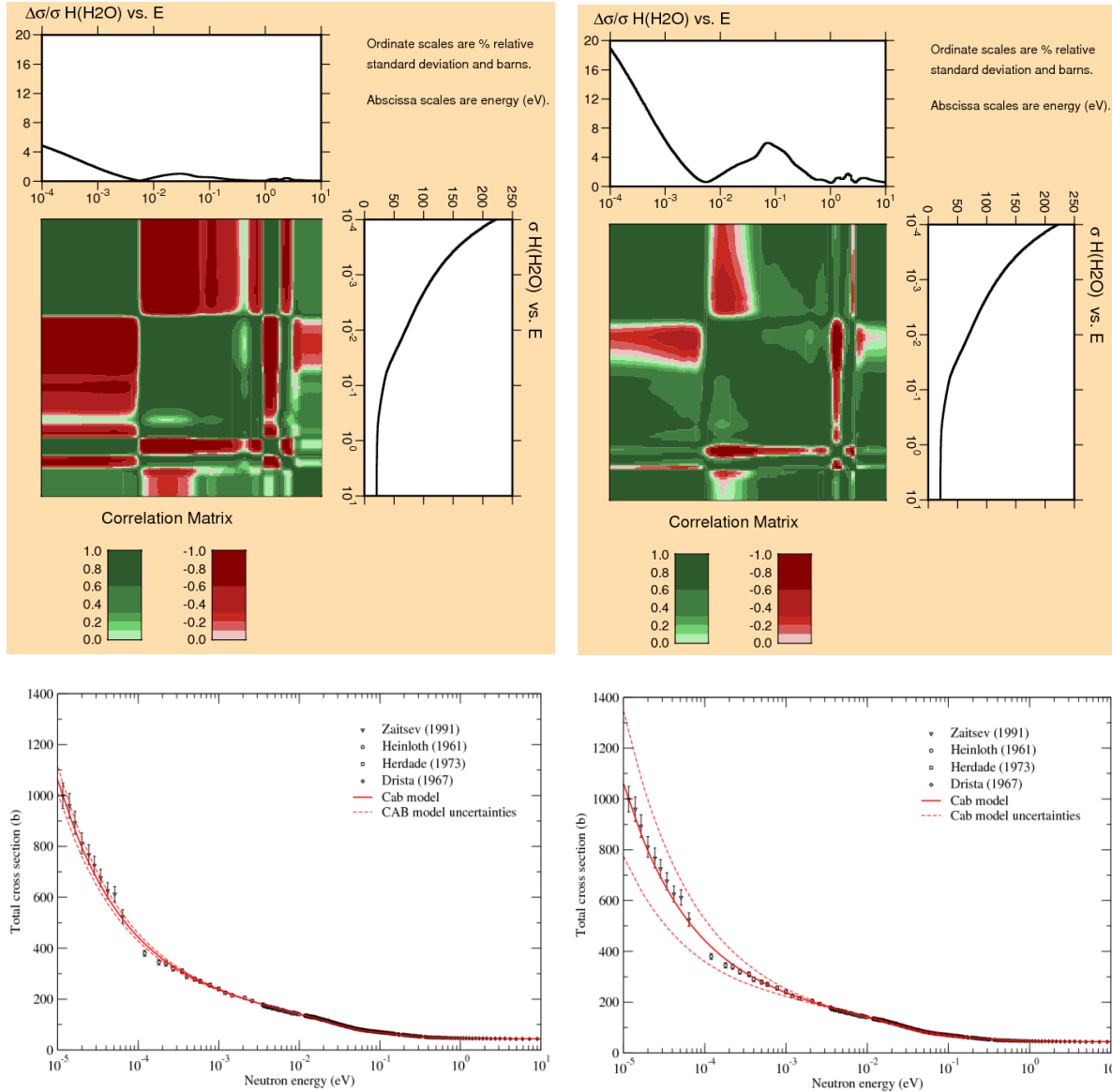


Fig. 7.5 Relative uncertainties and correlation matrix of the  $^1\text{H}$  in  $\text{H}_2\text{O}$  scattering cross section calculated with the CAB model at 294 K. The left hand plot shows the results after the fitting procedure and the right hand plot the results after the marginalization. For both cases the calculated cross section and the uncertainty bands are plotted with the experimental data used in the retroactive analysis.

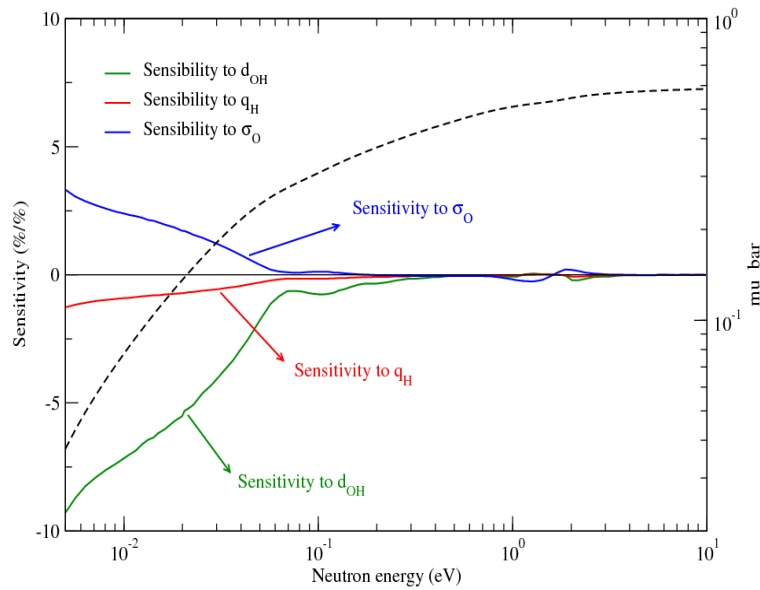


Fig. 7.6 Sensitivity of the  $\bar{\mu}$  to the TIP4P/2005f water potential parameters. The dashed line represents the calculation done with CAB model at 294 K.

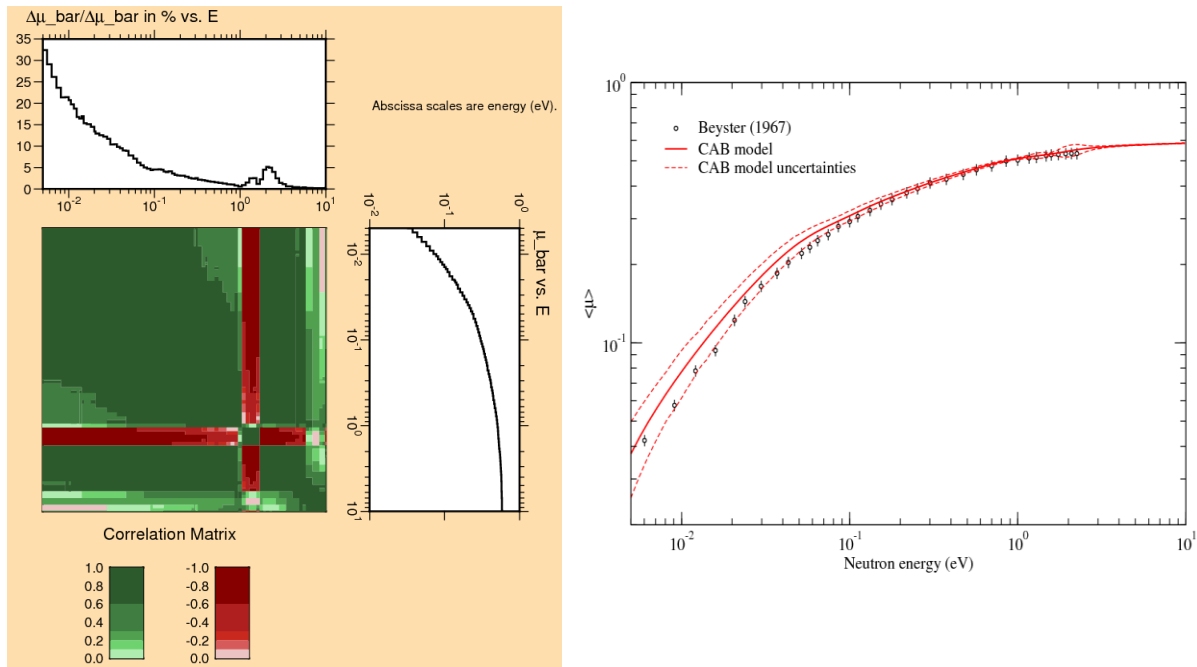


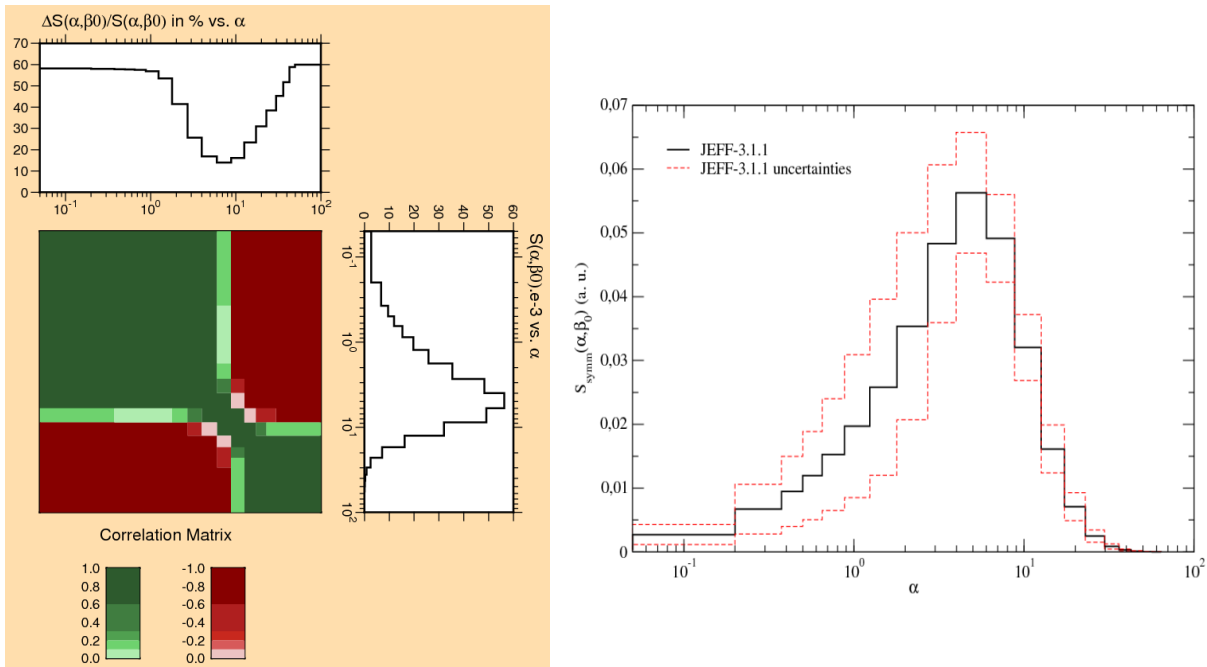
Fig. 7.7 Relative uncertainties and correlation matrix of average cosine of the scattering angle  $\bar{\mu}$  calculated with the CAB model at 294 K. The right plot represents the calculated  $\bar{\mu}$  and the uncertainty bands compared with the experimental data used in the retroactive analysis.

## 7.5 Uncertainties propagation to the $S(\alpha, \beta)$ function of JEFF-3.1.1 library

Figure 7.8 shows the relative uncertainties and the covariance matrix of the multigroup scattering function of JEFF-3.1.1 library for two energy transfers,  $\beta = 1.0$  and  $\beta = 10.0$  at 294 K. The results were obtained with the uncertainties of the LEAPR module parameters listed in table 6.6 of chapter 6.

For an energy transfer of  $\beta = 1.0$  (25.3 meV), where the rotational vibration mode is dominant, the uncertainty in the peak of the distribution is similar to the calculation done with the CAB model (close to 10%). However, the large uncertainties in the wings account the effect derived by the large relative uncertainty on the scaling factor  $\Delta$  (24%) of the frequency spectrum of  $^1\text{H}$  in  $\text{H}_2\text{O}$ .

For  $\beta = 10.0$  (253 meV), the calculated uncertainties in the  $S(\alpha, \beta)$  function are equivalent to those obtained with the CAB model.



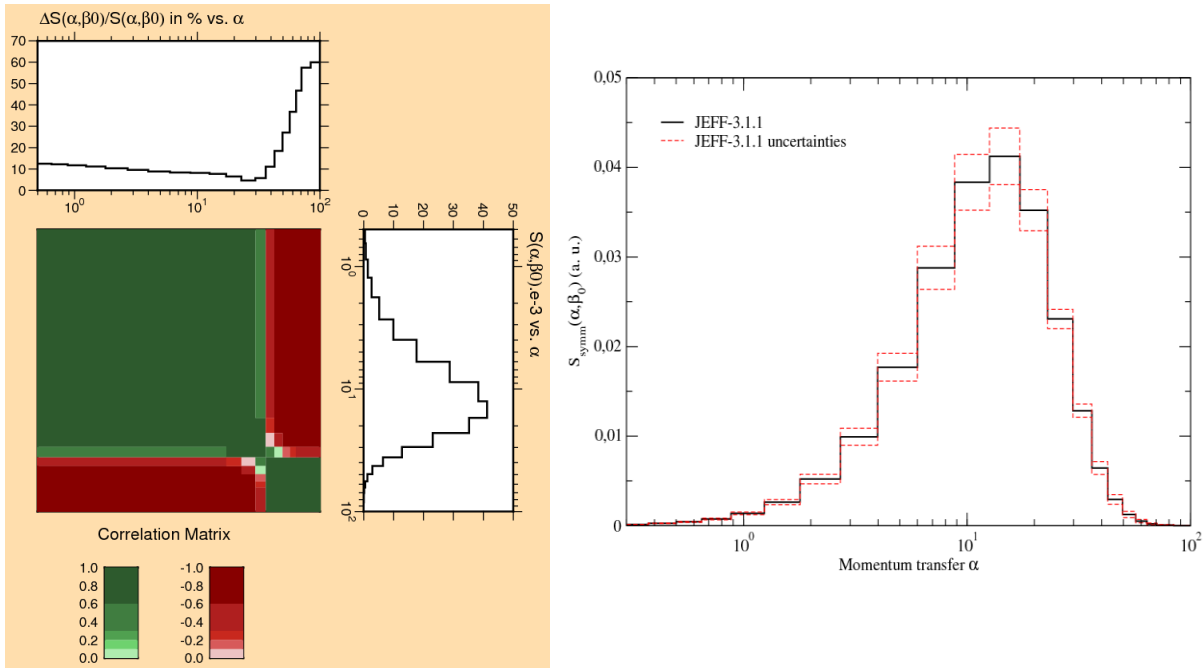


Fig. 7.8 Relative uncertainties and correlation matrix of the  $\bar{S}(\alpha, \beta_0)$  function for  $\beta_0 = 1.0$  (upper plot) and  $\beta_0 = 10.0$  (lower plot) calculated with the JEFF-3.1.1 library at 294 K.

### 7.6 Uncertainties propagation to the $^1\text{H}$ in $\text{H}_2\text{O}$ scattering cross section of JEFF-3.1.1 library

Figure 7.9 shows the relative uncertainties and the correlation matrix of the scattering cross section of  $^1\text{H}$  in  $\text{H}_2\text{O}$  at 294 K.

The uncertainty at  $10^{-4}$  eV is consistent with the results obtained with the CAB model. However, the constraint introduced in the thermal neutron energy in the retroactive analysis yields an uncertainty at this energy that reaches approximately 5.0%

The relative uncertainty of the scattering cross section at the thermal energy is larger than the CAB model (3.3%). Figure 7.10 compares the total cross sections around the thermal energy calculated with the CAB model and with JEFF-3.1.1 at 294 K. The fact that the cross section of the CAB model agrees better with the experimental data than JEFF-3.1.1 is reflected in a larger calculated uncertainty for this latter.

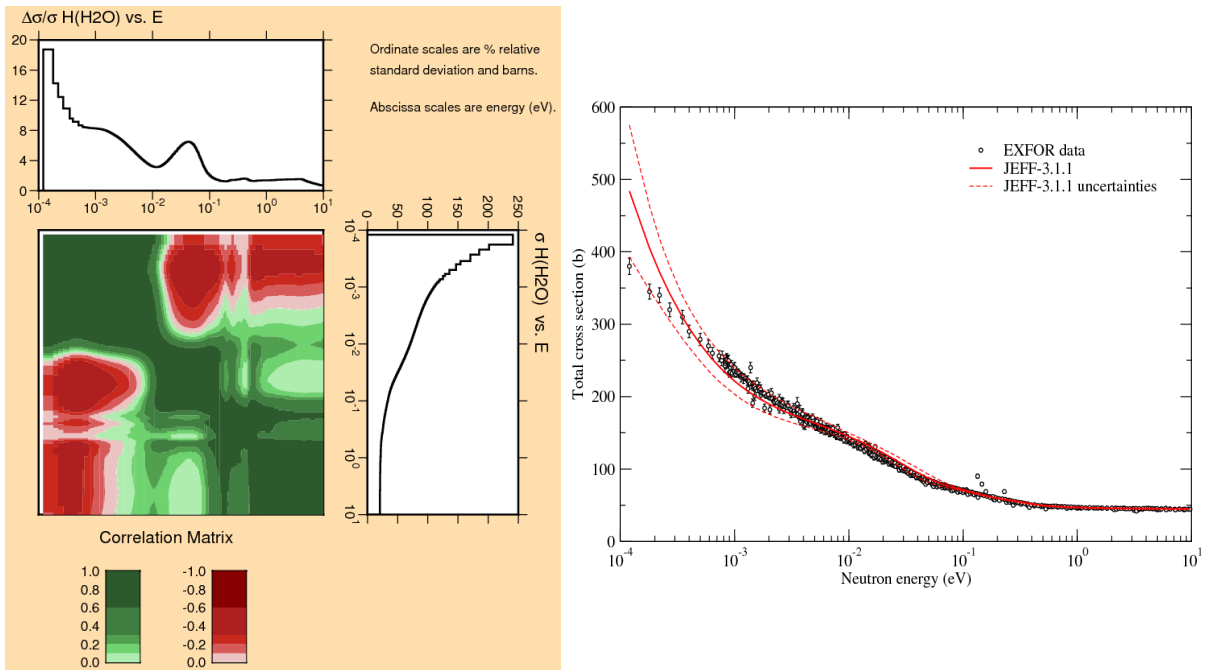


Fig. 7.9 Relative uncertainties and correlation matrix of the  $^1\text{H}$  in  $\text{H}_2\text{O}$  scattering cross section calculated with the JEFF-3.1.1 library at 294 K after the marginalization.

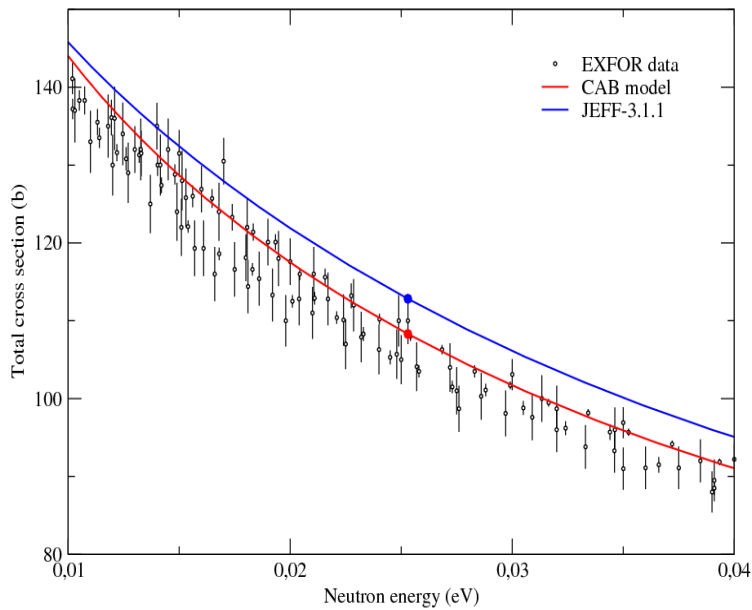


Fig. 7.10 Comparison of the total cross section calculated with the CAB model and the JEFF-3.1.1 library at 294 K around the thermal neutron energy.

## 7.7 Uncertainties propagation of the CAB model to the MISTRAL experiments

In chapter 5, the reactivity difference as a function of the temperature was calculated for the MISTRAL experiments with the thermal scattering law of the CAB model and JEFF-3.1.1 library. The reported uncertainties combined the statistical component due to the convergence of the Monte Carlo code TRIPOLI4 and the experimental uncertainties coming from the kinetic parameters, the boron concentration and the doubling time measurements. The uncertainties owing to the nuclear data were not taken into account.

The covariance matrix of the thermal scattering function allows to quantify the contribution of the uncertainty of the calculated reactivity due to the  $^1\text{H}$  in  $\text{H}_2\text{O}$ . The reactivity of the MISTRAL-1 and MISTRAL-2 configurations at 20 °C and 80 °C were calculated for each +1% perturbation of the model parameters. Table 7.1 reports the difference in reactivity  $\Delta\rho$  for each configuration as well as the associated uncertainties.

The covariance matrices for both models were calculated at  $T = 20$  °C. The direct propagation of the uncertainties to the calculated reactivities at 80 °C was done with the same covariance matrices. This could be the reason why the obtained uncertainties at this latter temperature are larger than at room temperature.

There is a factor two between the uncertainty on the CAB model evaluation and that of the JEFF-3.1.1 library for the MISTRAL-1 at room temperature. Using the CAB model, the uncertainty of  $^1\text{H}$  in  $\text{H}_2\text{O}$  is improved over the JEFF-3.1.1 library. The larger uncertainties at 20 °C and at 80 °C obtained for the MOX calculation confirms the sensitivity of the thermal scattering data to these fuels.

Table 7.1. Differences in reactivity  $\Delta\rho = C - E$  (pcm) obtained with the thermal scattering laws of JEFF-3.1.1 and CAB model for the MISTRAL-1 and MISTRAL-2 configurations. In MISTRAL-1, the reactivity differences include the correction due to thermal expansion effects. The reported uncertainties on each case are due to the CAB model parameters and to the LEAPR module parameters, in the case of JEFF-3.1.1, which were propagated with the CONRAD code. The combined statistical uncertainty due to the Monte Carlo calculations is 25 pcm for the CAB model and 18 pcm for JEFF-3.1.1.

Configuration	T (°C)	JEFF-3.1.1	CAB model
MISTRAL-1 (UOX)	20	192 ± 125	283 ± 71
	80	176 ± 137	286 ± 155
MISTRAL-2 (MOX)	20	-	900 ± 110
	80	-	869 ± 203

## 7.8 Uncertainties propagation using the Iterated Fission Probability method of the Monte Carlo code TRIPOLI4

So far, the results presented were obtained using the direct perturbation method of the nuclear data uncertainties, which relies on performing small perturbations around a reference value in order to obtain the sensitivity profiles. To calculate the uncertainty of the keff value, it was needed to perform one calculation per perturbed parameter. This makes difficult to employ the methodology at a large scale for practical applications.

In this section, the results will be compared with the Iterated Fission Probability (IFP) principle, recently implemented in the Monte Carlo code TRIPOLI4 [73]. This method applies the exact perturbation theory to evaluate the sensitivities, without any previous assumption like in the direct perturbation.

The comparison of the propagation techniques was done for a simple test case: the PST-001.1 benchmark of the International Criticality Safety Benchmark Evaluation Project (ICSBEP) [74]. Only the thermal scattering law of the JEFF-3.1.1 nuclear data library was considered in the study.

### 7.8.1 Uncertainty on the calculated reactivity due to the direct propagation of the LEAPR parameters of JEFF-3.1.1

It was done a direct perturbation of the LEAPR module parameters of +1%. The sensitivities of the keff value to the parameters were then obtained. Using the covariance matrix reported in table 6.6 of chapter 6, it was done the uncertainties propagation. The calculated reactivity and the uncertainty of the PST-001.1 benchmark obtained by the direct perturbation of the LEAPR module parameters are:

$$\rho = 140 \pm 245 \text{ pcm}$$

### 7.8.2 Uncertainty on the calculated reactivity using the IFP method

Aiming to study the convergence of the sensitivities of the keff value to the  $S(\alpha, \beta)$  calculated with IFP method of TRIPOLI4, two different approaches were considered.

The first case considers the  $S(\alpha, \beta)$  averaged in 27 groups over the momentum transfer  $\alpha$  (see section 7.2). The size of the resultant covariance matrix will have 6993\*6993 values. In the second case, it was done an average in the momentum transfer over only one group. The size of the new covariance matrix will be then 259\*259. Such a coarser grid will have a higher number of collisions scored by TRIPOLI4 than the first case, which represents having better statistics. For a given energy transfer  $\beta_i$ , the scattering function is calculated as:

$$\bar{S}_i(\beta_i) = \frac{\int_{\alpha_{min}}^{\alpha_{max}} S(\alpha, \beta_i) d\alpha}{\alpha_{max} - \alpha_{min}}. \quad (3)$$

Figure 7.11 shows the sensitivity profiles of the keff value to the multigroup  $\bar{S}(\alpha_0, \beta)$  for  $\alpha_0 = 0.5$  (left hand plot) and to the  $\bar{S}(\beta)$  (right hand plot) as a function of the energy transfer  $\Delta E$  calculated at 294 K.

The large uncertainties indicate that the convergence achieved in both cases is not enough to ensure reliable sensitivities values. In order to have better statistics, the number of collisions in the energy range of interest for the thermal scattering data should be larger, which was not possible because of the computing power limitations.

Nevertheless, there is a trend perceived in both approaches. The  $k_{eff}$  value presents high sensitivities to the scattering function for the lower energy transfers. Beyond an energy exchange of approximately 200 meV, no events were registered by the Monte Carlo code. This demonstrates as well the high sensitivity of the  $k_{eff}$  to the continuous frequency spectrum of  $^1\text{H}$  in  $\text{H}_2\text{O}$  which is present at the low energy exchanges.

The uncertainty on the calculated reactivity of the PST-001.1 benchmark was evaluated for the sensitivity case where the scattering function was averaged in one momentum transfer group. The results are summarized in Table 7.2. The relative uncertainties and the correlation matrix of  $\bar{S}(\beta)$  for one momentum transfer group are shown in Figure 7.12.

Finally, it was evaluated the impact on the calculated uncertainty utilizing the sensitivity profiles of the  $k_{eff}$  value to the scattering cross section of  $^1\text{H}$  in  $\text{H}_2\text{O}$  was evaluated. The covariance matrix of the  $^1\text{H}$  in  $\text{H}_2\text{O}$  at 294 K was obtained by direct perturbation of the LEAPR parameters. The results were already presented in section 7.6. The calculated uncertainty of this propagation option is reported in table 7.2.

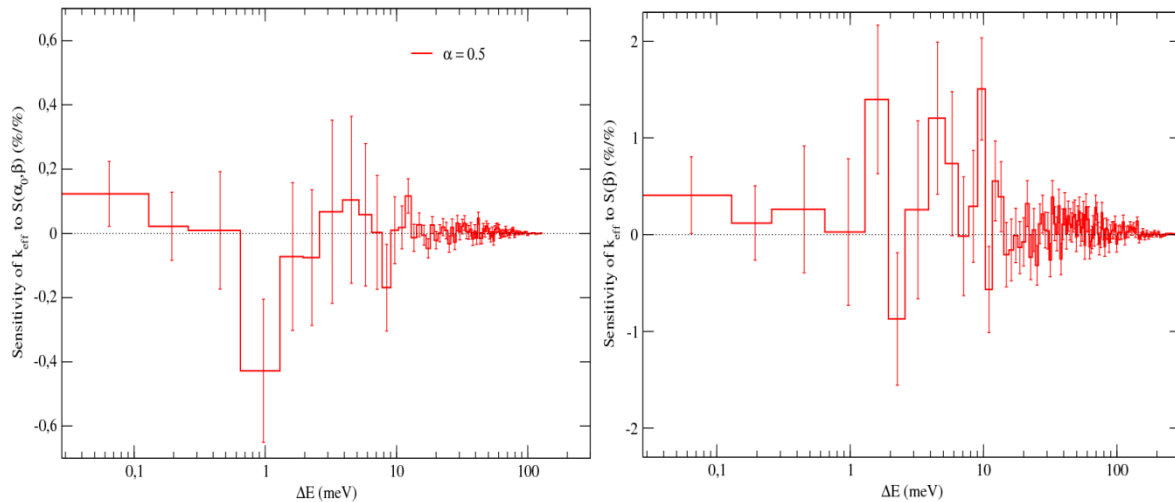


Fig. 7.11 Sensitivity profiles of the  $k_{eff}$  value to the multigroup  $\bar{S}(\alpha_0, \beta)$  for  $\alpha_0 = 0.5$  (left hand plot) and to the  $\bar{S}(\beta)$  (right hand plot) calculated at 294 K.

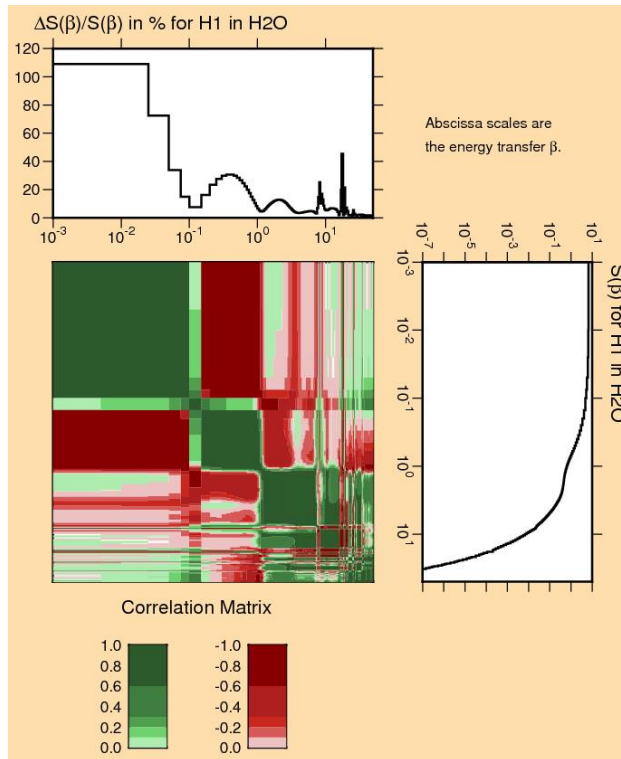


Fig. 7.12 Relative uncertainties and correlation matrix of the scattering function  $\bar{S}(\beta)$  averaged in one momentum transfer group at 294 K.

Table 7.2. Comparison of the calculated uncertainty on the keff value of the PST-001.1 benchmark using different uncertainty propagation methods. The reference case corresponds to the direct perturbation of the LEAPR parameters.

Uncertainty propagation method	$\Delta\rho$ (pcm)
Direct perturbation of the LEAPR parameters	$\pm 245$
IFP method with the $\bar{S}(\beta)$ sensitivities	$\pm 43$
IFP method with the $\sigma_n$ of $^1\text{H}$ in $\text{H}_2\text{O}$ sensitivities	$\pm 130$

Taking as reference the results obtained with the direct perturbation of the LEAPR parameters, there is in general an underestimation of the calculated uncertainty due to the  $^1\text{H}$  in  $\text{H}_2\text{O}$  using the IFP method in the TRIPOLI4 code. When calculating the sensitivities of the keff value to the scattering cross section,

the underestimation of the calculated uncertainty is close to 100 pcm. When the sensitivity to the thermal scattering function is studied, the underestimation is close to 200 pcm.

Only the direct propagation method is the approach that allows obtaining realistic uncertainties on the reactivity. The IFP method is an easy-to-use and robust uncertainty propagation technique that looks promising for practical applications. However, further analyses are needed in order to understand the origin of such differences with respect to the direct perturbation.

## 7.9 Preliminary conclusions

In this chapter it was done the uncertainties propagation on the parameters of the CAB model, corresponding to the water potential parameters and those of the JEFF-3.1.1 library, corresponding to the LEAPR parameters. The propagation method was the direct perturbation of the model parameters.

Due to the large size of the thermal scattering matrix, it was necessary to adopt a multigroup approach to perform the uncertainty propagation. As an example, it was presented the covariance matrices for 25 meV and 250 meV of energy transfer. The results achieved for the CAB model and for the JEFF-3.1.1 library are nearly similar.

Covariance matrices for the  $^1\text{H}$  in  $\text{H}_2\text{O}$  scattering cross section were also generated. The realistic uncertainties obtained illustrate the feasibility of the adopted methodology. Particularly, at the thermal neutron energy (25.3 meV), the calculated relative uncertainties for CAB and JEFF-3.1.1 are 3.3% and 5.0% respectively.

The contribution of the uncertainty due to the  $^1\text{H}$  bound to  $\text{H}_2\text{O}$  was evaluated as well for the MISTRAL-1 and MISTRAL-2 experiments. The uncertainty on the calculated reactivity was quantified at 20 °C and 80 °C. For the case of JEFF-3.1.1, an uncertainty around 130 pcm was obtained in MISTRAL-1. The results at 20 °C and 80 °C are very close. For the case of CAB model, at 20 °C the uncertainty on the reactivity is 70 pcm for the MISTRAL-1 case. At high temperature, the uncertainty is almost twice as room temperature. The same trend was found for the MISTRAL-2 configuration. The overall uncertainties are more significant than for the UOX core. The fact of using the same covariance matrix of the CAB model parameters (calculated at 20 °C) for the uncertainty propagation might induce a systematic error contribution when computing the uncertainty to the reactivity at 80 °C.

Finally, it was compared the direct perturbation method with the IFP method, implemented in the Monte Carlo code TRIPOLI4. The IFP method calculates the sensitivities of the keff value to the thermal scattering law or to the scattering cross section of  $^1\text{H}$  in  $\text{H}_2\text{O}$ . The test was done on the PST-001.1 benchmark of the ICSBEP database. Being the direct propagation method the reference case, the results derived using the IFP method underestimate severely the uncertainty on the calculated reactivity. Particularly, we have encounter problems in the convergence of the sensitivity coefficients which make difficult to assure the obtained results.

One breakthrough would be the calculation of the sensitivities of the keff to the parameters of the LEAPR module directly, avoiding the intermediate steps of generating covariance matrices of the thermal scattering function or of the scattering cross section. This latter option has not been implemented yet in the Monte Carlo code TRIPOLI4, but it would serve as a direct basis comparison with the direct propagation method.

# General conclusions and perspectives

It was studied, analyzed and compared the neutron thermal scattering models of light water of the JEFF-3.1.1 nuclear data library and of the CAB model. The first one is based on experimental measures of the double differential cross section to obtain the frequency spectrum of  $^1\text{H}$  in  $\text{H}_2\text{O}$ , while the second one derives from molecular dynamic simulations of the microscopic interaction between the molecules.

The shape of frequency spectrum of  $^1\text{H}$  in  $\text{H}_2\text{O}$  calculated with the CAB model differs significantly from the spectrum of JEFF-3.1.1. This yields sizable discrepancies at low energy exchange ( $<13$  meV) when calculating the thermal scattering function  $S(\alpha,\beta)$ . The calculation of the  $\text{H}_2\text{O}$  total cross section show an improvement of the CAB model when compared with the experimental data at the cold energy range ( $<1$  meV). The difference between the JEFF-3.1.1 and CAB cross sections at the thermal energy point is 5%.

The description of the low energy physics of the models was tested with the experimental measures of the double differential cross section done in the frame of this work. It was created a simplified model of the time-of-flight spectrometers in the Monte Carlo code TRIPOLI4 to compare the calculated cross sections of the CAB model and of JEFF-3.1.1. The results show the difficulties of this latter to reproduce the quasi-elastic peak of the distribution. The incorporation in CAB of a diffusion model to describe the low energy dynamics allows having a better agreement with the data.

Nevertheless, discrepancies were recognized in the amplitude of the quasi-elastic peak, whose origins were investigated. During the experiment, the background measures were done at a higher temperature than the light water measures due to temperature regulation drawbacks. The mean kinetic energy owing to the molecular thermal agitation will then differ, producing an attenuated intensity of the empty cell acquisition. At the level of the quasi-elastic peak, the background subtraction will be, consequently, underestimated. As regards the calculated double differential cross section, it might be possible that the approximation used to evaluate the thermal scattering function (the Gaussian approximation) is not appropriate for the cold neutron energy range. At this regime, the diffusion of the water molecules does not follow the classical Fick's law, and such an approximation is not able to account this complex behavior.

The impact on using two different neutron thermal scattering models for the light water was evaluated in a reactor calculation. The selected benchmark was the MISTRAL experiment, carried out in the zero power reactor EOLE of CEA Cadarache at cold reactor conditions (from  $10$  °C to  $80$  °C). It was quantified the difference in the calculated reactivity and the calculation error on the isothermal reactivity temperature coefficient (RTC).

For the UOX lattice, the calculated reactivity with the CAB model is  $+100$  pcm larger on average than with the JEFF-3.1.1 library, while for the MOX case is close to  $+180$  pcm. The latter result accounts the effect that plutonium-containing benchmarks are more sensitive to thermal scattering data due to the strong fission resonances in the  $0.3$  eV energy range.

The increase of the reactivity when using the TSL of CAB model might be attributed to the fact that the  $^1\text{H}$  absorption reaction rate calculated with JEFF-3.1.1 is larger in the energy range where the thermal flux is found. Consequently, there will be fewer neutrons to produce new fissions with the  $^{235}\text{U}$ , the  $^{239}\text{Pu}$  and the  $^{241}\text{Pu}$ . Examining the ratio of the JEFF-3.1.1 to CAB model of the capture to fission reaction rates of these three isotopes, we recognize that in all cases the fission rate is larger for the CAB model. The discrepancies are more accentuated for the plutonium isotopes; which explains the significant reactivity increase in the MOX configuration.

As regards, the bias in the reactivity temperature coefficient, improvements were identified with the CAB model in this safety parameter. In the temperature range from 10 °C to 80 °C, the calculation error on the RTC is  $-0.27 \pm 0.3$  pcm/°C and  $+0.05 \pm 0.3$  pcm/°C obtained with the JEFF-3.1.1 and with the CAB model respectively (UOX lattice). For the MOX core, the error on the RTC is  $-0.98 \pm 0.3$  pcm/°C and  $-0.72 \pm 0.3$  pcm/°C calculated with the JEFF-3.1.1 and with the CAB model respectively.

The uncertainties on the thermal scattering data were quantified creating covariance matrices between the parameters of the CAB model (the water potential parameters) and of the JEFF-3.1.1 library (the LEAPR module parameters) with the CONRAD code. In the case of JEFF-3.1.1, a large uncertainty was found for the parameter that describes the shape of the frequency spectrum of  $^1\text{H}$  in  $\text{H}_2\text{O}$ , mainly because of the disagreement with the total cross section measurements in the neutron thermal energy. Concerning the CAB model, the uncertainties for all the parameters of the water potential were produced. An approach that can be taken in mind for a future work could be to fit those parameters that show a high sensitivity to the selected experimental data. The uncertainty of the remaining parameters could be deduced from measures of the thermophysical properties of water (thermal conductivity, diffusion coefficient, enthalpy of vaporization, etc.).

By direct propagation, the covariance matrices between the parameters were propagated to produce covariance matrices for the thermal scattering function  $S(\alpha, \beta)$ . A challenging aspect regarding the  $S(\alpha, \beta)$  covariance matrix is the storage format due to the large amount of data to be handled. The multigroup approach represents a partial solution, but still there is no established method for storing the covariances in the current ENDF-6 format. The problematic remains open.

Covariance matrices of the  $^1\text{H}$  in  $\text{H}_2\text{O}$  scattering cross section were also produced for JEFF-3.1.1 and the CAB model. The marginalization technique in the CONRAD code allows obtaining realistic uncertainties on the cross section. At the neutron thermal energy the relative uncertainty is 5.0% and 3.3% for the JEFF-3.1.1 library and for the CAB model respectively.

The contribution of the uncertainty due to the  $^1\text{H}$  in  $\text{H}_2\text{O}$  thermal scattering data was evaluated for the MISTRAL-1 and MISTRAL-2 experiments. For the case of JEFF-3.1.1, an uncertainty on the calculated reactivity close to  $\pm 130$  pcm was obtained in MISTRAL-1 at 20 °C. At 80 °C a similar uncertainty was achieved. The uncertainty calculated with the CAB model at 20 °C reaches  $\pm 71$  pcm for the MISTRAL-1 core. At high temperature, the uncertainty is almost twice with respect to room temperature. The same trend was found for the MISTRAL-2 configuration, where the uncertainty on the reactivity at 20 °C is  $\pm 110$  pcm.

The covariance matrix of the CAB model parameters was calculated at 20 °C. The same matrix was used to propagate the uncertainties to the calculated reactivity at 80 °C. This might introduce larger uncertainties at high temperature.

Finally, it was investigated the possibility of performing the uncertainties propagation with the iterated fission probability method (IFP) implemented in the TRIPOLI4 code. The IFP method is an easy-to-use uncertainty propagation technique that computes the sensitivities of the keff value to other quantities like the thermal scattering function  $S(\alpha, \beta)$ . However, we have encountered problems in the convergence of the sensitivity coefficients. By using the IFP to determine the keff uncertainties on the PST-001.1 benchmark (ICSBEP), we obtained an uncertainty of 40 pcm, while the reference uncertainty is close to 245 pcm (calculated by direct perturbation).

A possible work to be done in the future could be to implement a module to calculate the sensitivities of the keff value to the parameters of the thermal scattering model, avoiding the intermediate step of generating a covariance matrix of the  $S(\alpha, \beta)$ . This option would serve to compare directly the results with the direct perturbation method.

# List of references

- [1] G. I. Bell and S. Glasstone, Nuclear Reactor Theory, Van Nostrand Reinhold Company, New York (1970).
- [2] M. B. Chadwick, M. Herman et al., Nuclear Data Sheets 112, 2887-2996 (2011).
- [3] A. Santamarina et al., The JEFF-3.1.1 Nuclear Data Library, JEFF Report 22, Nuclear Energy Agency (2009).
- [4] M. Mattes and J. Keinert, Thermal Neutron Scattering Data for the moderator Materials H<sub>2</sub>O, D<sub>2</sub>O and ZrHx in ENDF-6 Format and as ACE Library for MCNP(x) Codes. INDC (NDS)-0470 (2005).
- [5] J. I. Marquez Damian, J. R. Granada and D. C. Malaspina, Ann. Nucl. Energy 65, 280-289 (2014).
- [6] G. L. Squires, Introduction to the theory of thermal neutron scattering, Cambridge University Press, New York (1977).
- [7] R. E. MacFarlane et al., The NJOY Data Processing System, Version 2012, Los Alamos National Laboratory (2012).
- [8] V. Sears, "Neutron scattering lengths and cross sections", AECL Research, Chalk River Laboratory, Ontario, Canada (1968).
- [9] L. Van Hove, Phys. Rev. 95,1 (1954).
- [10] P. A. Egelstaff and P. Schofield, Nucl. Sc. Eng. 12, 260-270 (1962).
- [11] J. Keinert and M. Mattes, JEF-1 scattering law data, JEFDOC-41 (1984).
- [12] J. U. Koppel, "Neutron scattering by Hydrogenous moderators", GA-7055, Gulf General Atomic (1966).
- [13] B. C. Haywood, Journal of Nucl. Energy 21, 249-262 (1967).
- [14] B. Haywood and D. Page, Scattering Laws for Heavy Water at 540K and Light Water at 550K, Proc. of the Symp. on Neutron Thermalization and Reactor Spectra Vol. I, Ann Arbor (1967).
- [15] J. U. Koppel, J. R. TRIPLETT and Y. D. Naliboff, "Gasket, a Unified Code for Thermal Neutron Scattering", GA-7417, Gulf General Atomic (1966).
- [16] L. J. Esch and M. L/ Yeater, Nucl. Sci. Eng. 46, 223-235 (1971).
- [17] Y. Lisichkin, L. Saharova, J. Marti and A. Novikov, Mol. Sim. 31, 1019-1025 (2005).
- [18] Y. Abe et al., Nucl. Instrum. Method A 735, 568-573 (2014).

- [19] E. Farhi et al., Nucl. Sci. Tech. 52, 844-856 (2015).
- [20] D. Van Der Spoel et al., Journal of computational Chemistry 26, 1701-1718 (2005).
- [21] M. A. Gonzalez and J. L. F. Abascal, Jour. Chem. Phys. 135, 224516 (2011).
- [22] J. I. Marquez Damian, J. R. Granada and D. C. Malaspina, Journ. Chem. Phys. 139, 024504 (2013).
- [23] G Novikov, A., Lisichkin, Y.V., Fomichev, N.K., 1986. Russian Journal of Physical Chemistry 60, 1337 (1986).
- [24] F. Bischoff et al., Low Energy Neutron Inelastic Scattering, Rensselaer Polytechnic Institute report, RPI-328-87
- [25] K.N. Zaitsev et al., Sov. At. Energy 70, 238 (1991).
- [26] K. Heinloth, Z. Phys. 163, 218 (1961).
- [27] S. B. Herdade et al., Brazilian report to the I.N.D.C. No.2, p.22 (1973).
- [28] M. Drista, A. Kostikas [X4# 20038003] (1967).
- [29] <https://www.ill.eu/instruments-support/computing-for-science/data-analysis/nausicaa/>
- [30] <https://www.ill.eu/reactor-environment-safety/high-flux-reactor/technical-characteristics/>
- [31] Time-of-flight spectrometers IN4 and IN6, Guide to the Neutron Research Facilities, The Yellow Book, Institut Laue-Langevin, Grenoble, France (2008).
- [32] J. Vaibhav et al., Measurement of double differential cross section of light water at high temperature and pressure to generate  $S(\alpha, \beta)$  in : Proc. Int. Conf. on Nuclear Data for Science and technology, Bruges, Belgium (2016).
- [33] J. Mayers, Nucl. Instr. Meth. 221, 609-618 (1984).
- [34] B. Lebech et al., Nucl. Instr. Meth. 79, 51-54 (1970).
- [35] D. Richard, M. Ferrand, G.J. Kearley, J Neutron Res. 4, 33-39 (1996).
- [36] E. Brun et al., Ann. Nucl. Energy 82, 151 (2015).
- [37] Y. Abe and S. Tasaki, Ann. Nucl. Energy 83, 302-308 (2015).
- [38] P. Archier et al., Nucl. Data Sheets 118, 488 (2014).
- [39] J. P. Scotta, G. Noguere, D. Bernard, J. I. Marquez Damian and A. Santamarina, EPJ Nucl. Sci. Technol. 2, 28 (2016).

- [40] S. Cathalau, J. C. Cabrillat, J. P. Chauvin, P. J. Fink, P. Fougeras, G. Flamenbaum, H. Matura, M. Ueji, and T. Yamamoto, "MISTRAL: An Experimental Programme in the EOLE Facility Devoted to 100% MOX Core Physics", Proc. Int. Conf. PHYSOR'96, Break-through of Nuclear Energy by Reactor Physics, Mito, Japan, September 16–20, 1996, Vol. H, p. 84 (1996).
- [41] S. Cathalau, P. Fougeras, and A. Santamarina, "First Validation of Neutronic Lattice Parameters of Overmoderated 100% MOX Fueled PWR Cores on the Basis of the MISTRAL Experiment," Proc. Int. Conf. Physics of Reactors (PHYSOR'98), Long Island, New York (1998).
- [42] R.E. MacFarlane, A.C. Kahler, Nucl. Data Sheets 111, 2739 (2010).
- [43] G. Noguere, J-C. Sublet, Ann. Nucl. Energy 35, 2259 (2008).
- [44] A. Meister and A. Santamarina, "The Effective Temperature for Doppler Broadening of Neutron Resonances in UO<sub>2</sub>", Proc. Int. Conf. Physics of Reactors (PHYSOR'98), Long Island (1998).
- [45] Thermophysical properties database of materials for light water reactors and heavy water reactors, IAEA-TECDOC-1496 (2006).
- [46] L. Erradi et al., Nucl. Sci. Eng. 144, 47 (2003).
- [47] R. Sanchez et al., Nucl. Sci. Tech. 42, 474 (2010).
- [48] A. Santamarina, P. Blaise, L. Erradi and P. Fougeras, Ann. Nucl. Energy 48, 51 (2012).
- [49] D. Rochman and A. J. Koning, Nucl. Sci. Eng. 172, 287 (2012).
- [50] L. Erradi et al., Nucl. Sci. Eng. 144, 47 (2003).
- [51] L. Erradi, A. Santamarina, Analysis of the MISTRAL experiment on the reactivity temperature coefficient for UOX and MOX lattices using JEFF-3.1.1 nuclear data library, in Proc. Int. Conf. PHYSOR 2010, Advances in Reactor Physics to Power the Nuclear Renaissance, Pittsburgh, USA (2010).
- [52] B.K. Jeon et al., Nucl. Techn. 191, 1 (2015).
- [53] C. Mounier, "Contribution à l'étude du coefficient de température des réacteurs à eau légère," PhD Thesis, Université de Paris Sud Orsay (1993).
- [54] C. Lampoudis et al., Eur. Phys. J. Plus 128, 86 (2013).
- [55] G. Noguere et al., Phys. Rev. C 92, 014607 (2015).
- [56] M. B. Chadwick et al., Nucl. Data Sheets 118, 1 (2014).
- [57] L. Leal, E. Ivanov, G. Noguere, A. Plompen and S. Kopecky, EPJ Nuclear Sci. Technol. 2, 43 (2016).
- [58] J. J. Bair and F. X. Haas, Phys. Rev. C 7, 1356 (1973).

- [59] J. Taylor, "An introduction to error analysis: The study of uncertainties in physical measurements", University Science Books (1997).
- [60] D. Rochman, A. J. Koning, S. C. Van der Marck, A. Hogenbirk and C. M. Sciolla, *Ann. Nucl. Ener.* 38, 942-952 (2011).
- [61] T. Bayes, "An Essay Toward Solving a Problem in the Doctrine of Chances," *Philos. Trans. R. Soc. London*, 53, 370 (1763); reprinted in *Biometrik*, 45, 293 (1958).
- [62] C. Shannon, "A Mathematical Theory of Communication", *The Bell System Technical Journal*, 27:379-423 (1948).
- [63] D. Smith, *Probability, Statistics and Data Uncertainties in Nuclear Science and Technology*, volume 4. OECD-NEA Committee Series (1990).
- [64] C. De Saint Jean et al., *Nucl. Sci. Eng.* 161, 363 (2009).
- [65] B. Habert, C. De Saint Jean, G. Noguere, L. Leal and Y. Rugama, *Nucl. Sci. and Eng.* 166, 276–287 (2010).
- [66] G. Noguere, P. Archier, C. De Saint Jean and B. Habert, *Nucl. Sci. Eng.* 172, 164-179 (2012).
- [67] D. W. Muir, *Nucl. Inst. Meth A* 644, 55 (2011).
- [68] J. R. Beyster, J. C. Young, J. M. Neill and W. R. Mowry, *Differential Neutron Scattering from Hydrogenous Materials - Annual Summary Report (GA-6295)*. General Atomics Technical Report (1965).
- [69] A. G. Novikov, A. A. Vankov and L. S. Gosteva, *Jour. Struc. Chem.* 31, 77 (1990).
- [70] G. Noguere, J. P. Scotta, C. De Saint Jean and P. Archier., *Ann. Nucl. Ener.* 104, 132-145 (2017).
- [71] D. Neudecker et al., *Nucl. Inst. Methods A* 723, 163 (2013).
- [72] S. E. Lappi, B. Smith and S. Franzen, *Spectrochim. Acta Part A* 60, 2611-2619 (2004).
- [73] G. Truchet, P. Leconte, A. Santamarina, E. Brun, F. Damian and A. Zoia, *Ann. Nucl. Energy* 85, 17-26 (2015).
- [74] J. Briggs, *International Handbook of Evaluated Criticality Safety Benchmark Experiments*. Tech. rep., OECD/NEA (2010).

## Appendix A

*MISTRAL-2 core configurations used to compensate the reactivity loss due to the temperature*

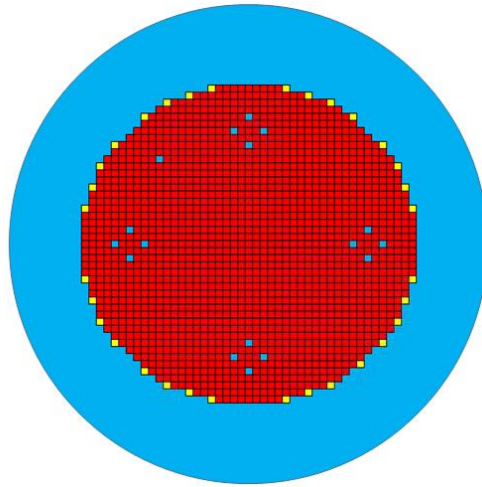


Fig. A1 MISTRAL-2 configuration at 10 °C and 15 °C.

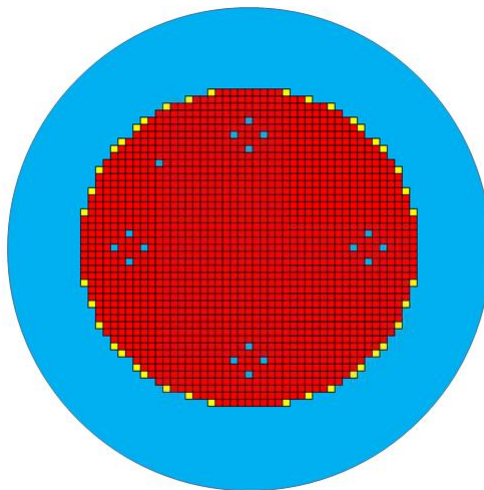


Fig. A2 MISTRAL-2 configuration at 20 °C.

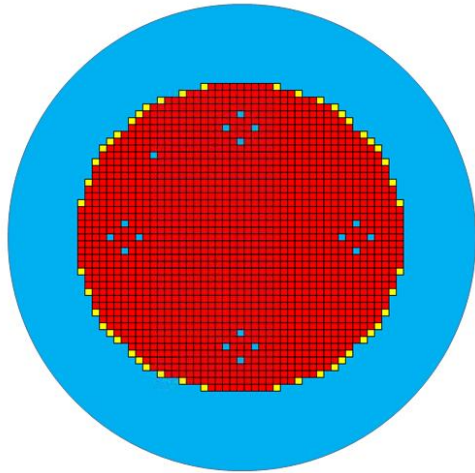


Fig. A3 MISTRAL-2 configuration at 25 °C.

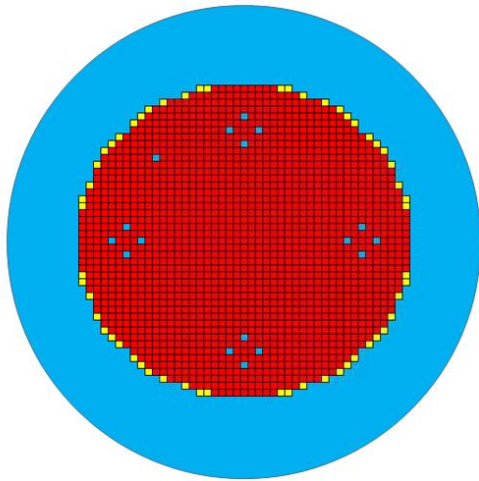


Fig. A4 MISTRAL-2 configuration at 30 °C.

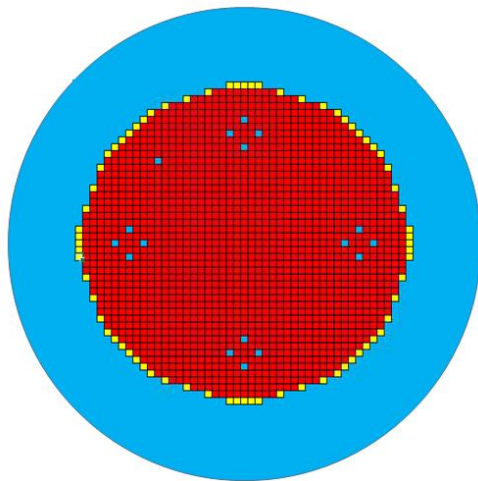


Fig. A5 MISTRAL-2 configuration at 40 °C.

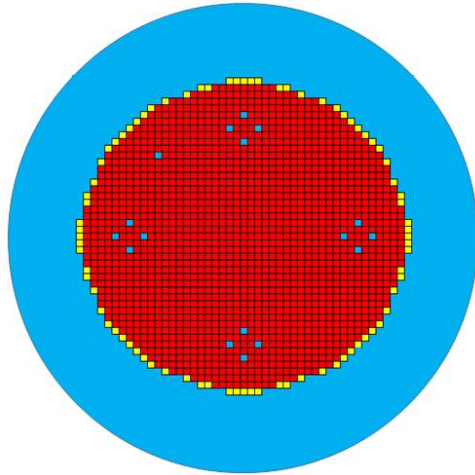


Fig. A6 MISTRAL-2 configuration at 45 °C.

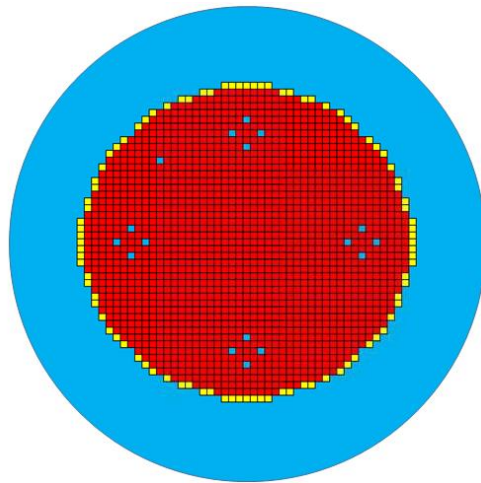


Fig. A7 MISTRAL-2 configuration at 50 °C.

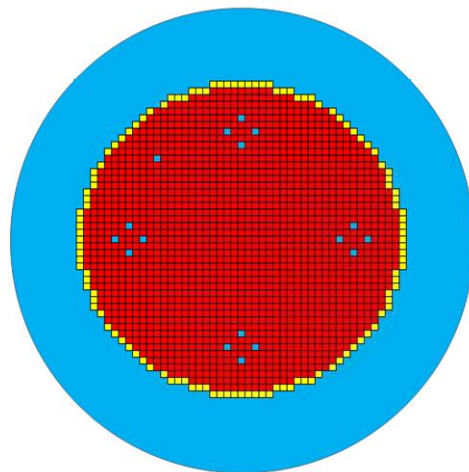


Fig. A8 MISTRAL-2 configuration at 60 °C.

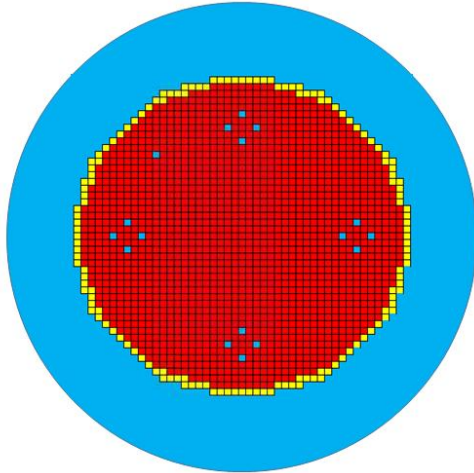


Fig. A9 MISTRAL-2 configuration at 65 °C.

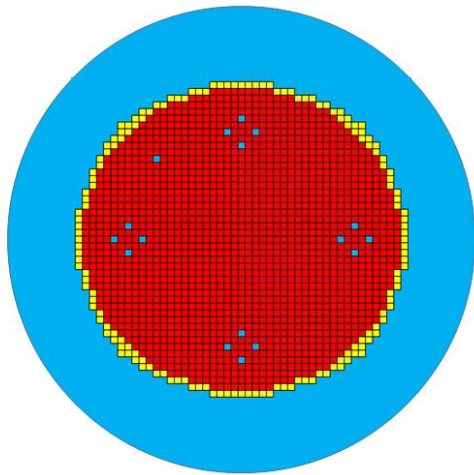


Fig. A10 MISTRAL-2 configuration at 70 °C.

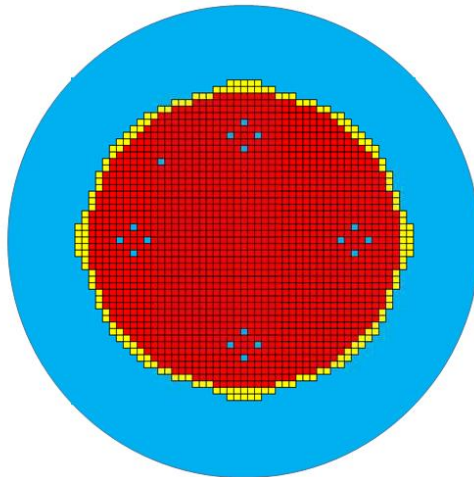


Fig. A11 MISTRAL-2 configuration at 75 °C.

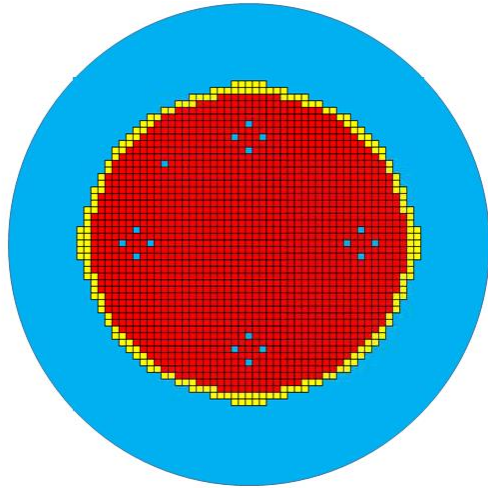


Fig. A12 MISTRAL-2 configuration at 80 °C.

# Appendix B

## *List of publications*

[1] J. P. Scotta, G. Noguere, D. Bernard, J. I. Marquez Damian and A. Santamarina, EPJ Nuclear Sci. Technol. 2, 28 (2016).

[2] J. P. Scotta, G. Noguere, D. Bernard and J. I. Marquez Damian, EPJ Web of conferences 111, 04001 (2016).

[3] J. P. Scotta, G. Noguere, D. Bernard, J. I. Marquez Damian and C. De Saint Jean, "Study on neutron scattering in light water in the MISTRAL experiments carried out in EOLE reactor at CEA Cadarache", Proc. Int. Conf. on Physics of Reactor (PHYSOR2016), Sun Valley, ID (USA), May 1-5 (2016).

[4] J. P. Scotta, G. Noguere and J. I. Marquez Damian, "Towards a covariance matrix of CAB model parameters for H(H<sub>2</sub>O)", Proc. Int. Conf. on Nuclear Data (ND2016), Bruges, Brussels, Sept 11-16 (2016).

[5] G. Noguere, J. P. Scotta, C. De Saint Jean and P. Archier, Ann. Nucl. Energy 104, 132-145 (2017).

# Acknowledgements

I cannot finish the present report without expressing my gratitude to those people who have a contribution and helped me to carry out this project.

I would like to thank firstly to the person who gave me the possibility to do this PhD, my director Gilles Noguere. We have shared three years and a half of hard work (including the internship), many meetings, workshops and several weeks in Grenoble doing experiments. Thank you for your patience in general and trusting on me.

In the same way, to all people from the LEPH laboratory who contributed to spend a nice time at work. A separate mention has to make to the “downstairs PhD students” whom I spent most of the time at the office and during lunch. Thanks for helping me distract from the stressing job.

I would like to thank as well to all my defense committee: Jose Busto, Luiz Leal, Cyrille de Saint Jean, Florencia Cantargi, Florent Réal and Yoann Calzavara. Most of them have traveled a long distance to attend my presentation, something I am very grateful for.

I mentioned before the experiments performed at the Institute Laue-Langevin, Grenoble. I’ve met there very helpful and nice people like Emmanuel Fahri, Alain Fillol, Jacques Olivier and Yoann as well. Thank you for teaching me how to measure the mysteries of water. I had the possibility to meet here Vaibhav Jaiswal, my processing data colleague from IRSN, very nice guy.

I would like to refer to the other two Argentineans at CEA Cadarache: Alfredo Vasile and Francisco Acosta. Thanks a lot for those nice launches and cool talks in Spanish. You do great empanadas Alfredo!

Last but not least, to Nacho Marquez from Centro Atomico Bariloche, whom I call him as my virtual tutor. Thanks for the emails, skypes and talks during meetings that helped me to clarify many concepts I will continue misunderstanding.